Adaptive Feedforward Cancellation Viewed from an Oscillator Amplitude Control Perspective

by

Joseph Harry Cattell

B.S., Mechanical Engineering (2000)
University of Pittsburgh

Submitted to the Department of Mechanical Engineering
in partial fulfillment of the requirements for the degree of

Master of Science

at the

MASSACHUSETTS INSTITUTE OF TECHNOLOGY

[June 2003]
May 2003

Author .....
Department of Mechanical Engineering
May 9, 2003

Certified by .....
David L. Trumper
Associate Professor of Mechanical Engineering
Thesis Supervisor

Accepted by .....
Ain A. Sonin
Chairman, Department Committee on Graduate Students

Adaptive Feedforward Cancellation Viewed from an Oscillator Amplitude Control Perspective

by
Joseph Harry Cattell

Submitted to the Department of Mechanical Engineering
on May 9, 2003, in partial fulfillment of the
requirements for the degree of
Master of Science

Abstract

This thesis presents methods of characterizing the convergence, error, stability, and robustness properties of Adaptive Feedforward Cancellation (AFC) for use on fast tool servos in high-precision turning applications. Previous work has shown that classical control techniques can be used to analyze the stability and robustness of an AFC loop. However, determination of the convergence and error properties of the closed-loop system to changes in the reference or disturbance signal is not an obvious output of these analyses. We have developed a method of viewing AFC from an oscillator amplitude control (OAC) perspective, which provides additional use of classical control techniques to determine the convergence and error properties of the closed-loop system.

AFC is a form of repetitive control that can be used to significantly improve periodic trajectory following/disturbance rejection. Fast tool servos used in high-precision turning applications commonly follow periodic trajectories and develop large errors, which usually occur at integer harmonics of the fundamental spindle rotation frequency. We have developed a loop-shaping approach to designing multiple resonator AFC controllers and have implemented this design on a commercially available piezoelectric (PZ) driven FTS using a PC-based digital control system.

Our view of Adaptive Feedforward Cancellation from an oscillator amplitude control perspective builds upon previous work in the literature. We use an averaging analysis to simplify the single resonator AFC system into two coupled single-input single-output (SISO) oscillator amplitude control loops and show that by using the correct rotation matrix, these loops are effectively decoupled. This simplification provides the use of classical control techniques to approximate the dynamics of the closed-loop output to changes in the amplitude or frequency of the reference/disturbance signal. The simulated and experimental results conform well to our analytical predictions for sufficiently low gain values.

Thesis Supervisor: David L. Trumper
Title: Associate Professor of Mechanical Engineering

Acknowledgments

I would first like to thank my advisor Professor David L. Trumper. He continually challenged me to work at my full potential, and helped me learn to look at things from a new perspective. It has been an honor working with him over the past two years. Next, I would like to thank all of my colleagues in the Precision Motion Control Lab. This includes Marten Byl, Katie Lilienkamp, Xiaodong Lu, Rick Montesanti, Vijay Shilpiekandula, Andrew Stein, and Dave Otten. I cannot single out any one of them, since each person helped me tremendously during my time here at MIT. It has also been an honor and privilege working with them and I wish them all the best in the future. Maggie Beucler and David Rodriguera were also a tremendous help with taking care all of the administrative needs I had.

For the times not spent in Lab, I am thankful for the friendships I developed with Ahmed Elmouelhi, John Mcbean, and I-hsiang Shu. I truly enjoyed the times I spent with each of them, even if we had to eat at Old Country Buffet. Also, I would like to thank Dr. Ivan Salgo. I will always remember the many conversations we had and the guidance he has given me. He has been a great friend, as well as one of my role models.

Finally, I would like to thank my family for all of their support and understanding over the past two years. My time here at MIT has been a bumpy ride and I don't think I would have made it without them. Most importantly, I would like to thank my fiancé April Kalix. For the past two years, MIT consumed almost all of my free time. Although in completely different locations, we were able to make it work. I am anxiously looking forward to spending the rest of my life with her.

For my Father, Harry Joseph Cattell

Contents

List of Figures

List of Tables

Chapter 1

Introduction

1.1 Project Summary

This thesis develops methods for characterizing the stability, convergence, and robustness properties of Adaptive Feedforward Cancellation (AFC) from an oscillator amplitude control (OAC) perspective. AFC is a form of repetitive control that can be used to provide increased control authority over a discrete set of frequencies. Examples of some control applications which can make use of AFC include hard disk and optical disk track following, vibration rejection in spindle and magnetic bearing systems, camshaft and piston machining, and fast tool servos for diamond turning [6]. In this thesis we focus primarily on the applicability of AFC for reducing/eliminating the steady-state tracking errors of fast tool servos in high-precision diamond turning applications.

We have experimentally applied AFC to control a commercially available fast tool servo (FTS). This system, the Variform FTS, was designed and manufactured by Kinetic Ceramics[1] and is shown in Figures 1-1 through 1-3. This particular FTS design consists of a tee-lever mechanism actuated by a double piezoelectric (PZ) stack arrangement coupled to two H-plate flexures, as illustrated in Figure 1-3. The tee-

[1]See Appendix K.

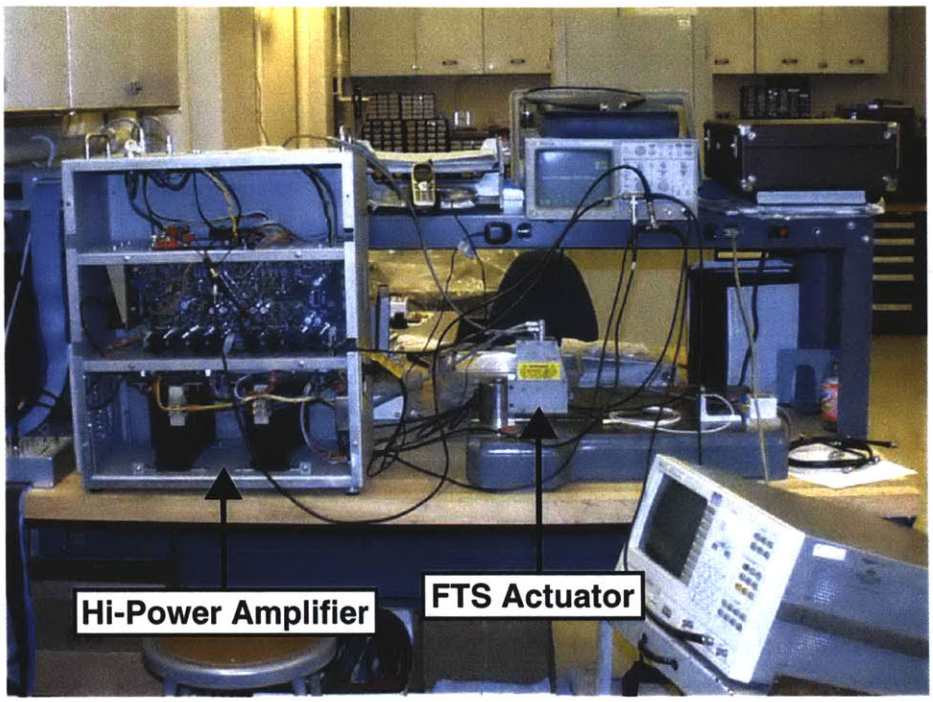

Figure 1-1: Variform FTS with hi-power amplifier and experimental hardware.

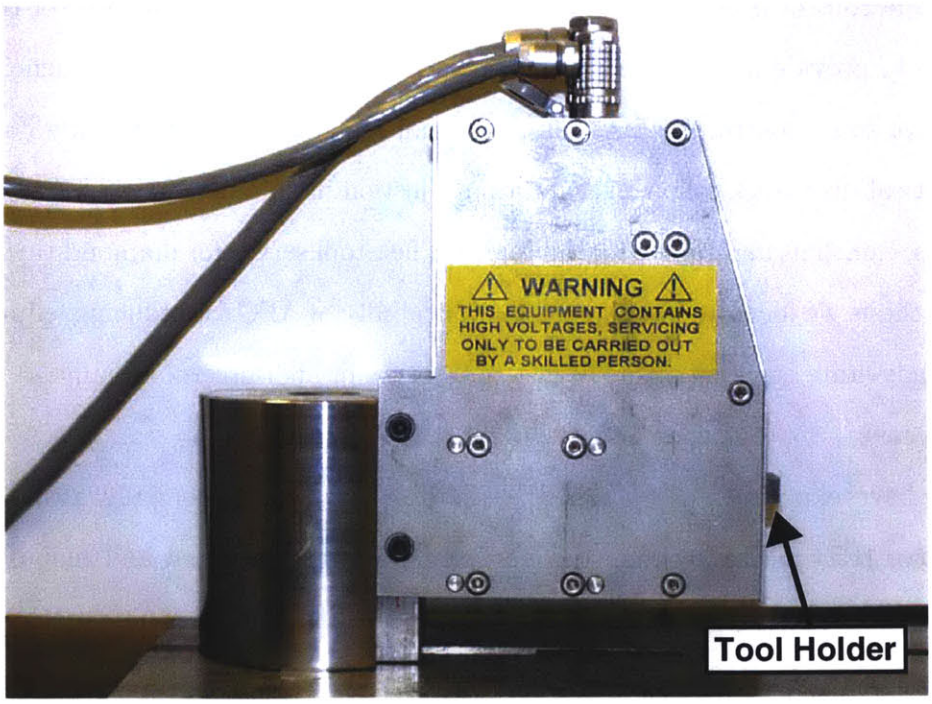

Figure 1-2: FTS piezoelectric actuator mounted on an experimental test base.

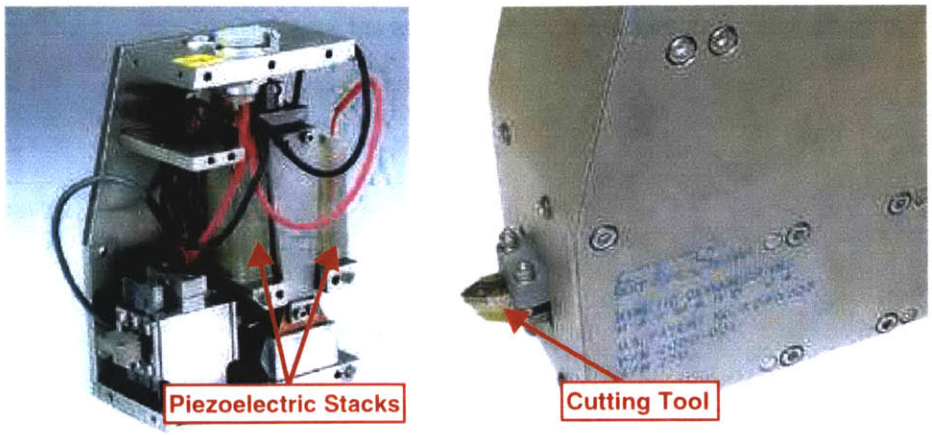

Figure 1-3: (left): FTS actuator with one of the side plates removed, illustrating the piezoelectric stacks. (right): FTS actuator with cutting tool attached to the tool holder. Figures adapted from Kinetic Ceramics [73].

lever amplifies the displacement from the PZ stacks by a factor of 13:1 while the flexures confine the action of the cutting tool to straight line motion. A high-power amplifier with an on-board digital feedback controller, as shown in Figure 1-1, drives the PZ stacks differentially to a maximum of ±400 V, which provides about a 200 Hz 0 dB crossover frequency with a total displacement of up to ±250 μm (±0.010").

It is well known that piezoelectric materials are inherently non-linear with respect to applied voltage. The Variform FTS controller takes advantage of an inner charge loop to minimize the PZ hysteresis curve along with an outer position feedback loop. During our experimental controller experiments, we utilized a PC-based digital control system. Therefore, we disabled the on-board controller and implemented our own control algorithms. A discussion of our implementation method is presented in Section 3.2. We designed a preliminary controller, as described in Section 3.3, and performed multiple closed-loop step responses where noticeable non-linear effects were observed. We speculate that these results are due to the hysteresis curve of the piezoelectric stacks. Thus, we re-enabled the inner charge loop, while bypassing the rest of the on-board controller, and developed several more conventional controller

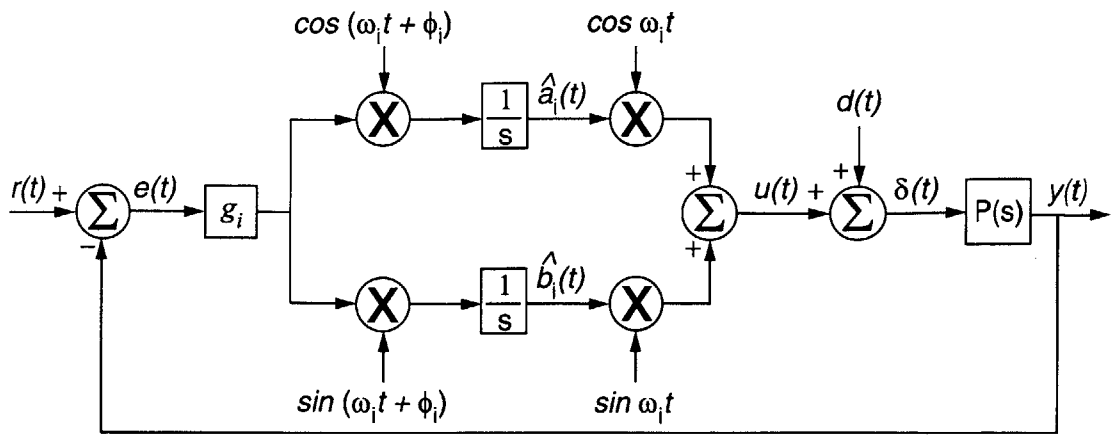

Figure 1-4: Single resonator AFC control loop with the phase advance parameter ϕ_i implemented. This system will exactly track or reject a signal with a single frequency ω_i.

designs (see Sections 3.4 and 3.5). The results of these experiments illustrate a significant attenuation of the non-linearities observed in Section 3.3. Finally, in Section 3.6, we performed several Adaptive Feedforward Cancellation experiments, which highlight the benefits of using AFC algorithms for reducing/eliminating the steady-state tracking errors of fast tool servos in high-precision diamond turning applications.

Figure 1-4 illustrates the loop configuration for a single resonator AFC controller, where P(s) is the transfer function of the plant being controlled. This closed-loop system is designed to provide zero steady-state error at the frequency ω_i. The internal dynamics of the AFC algorithm are linear time-varying (LTV) but in the literature it is shown that the input-output relationship from e(t) to u(t) is equivalent to a linear time-invariant (LTI) system [22]. The equivalent continuous-time transfer function is given by

$$C_i(s) = g_i \left[\frac{s \cos \phi_i + \omega_i \sin \phi_i}{s^2 + \omega_i^2} \right]. \tag{1.1}$$

Here g_i is a proportional gain and ϕ_i is a phase advance parameter that can be chosen to improve the closed-loop system's robustness. This LTI equivalence is a very powerful result, since it enables us to use classical control techniques (*i.e.*, Root Locus

plots, Nyquist diagrams, Bode plots, gain and phase margins, etc.) to determine the AFC system stability, robustness and performance characteristics.

In diamond turning applications, fast tool servos commonly follow near-periodic trajectories, since the tool motion is keyed to the fundamental spindle rotation frequency. The FTS axis can develop significant following errors, since conventional feedback loops only provide a finite controller gain. The FTS axis also experiences large disturbances (*e.g.*, cutting forces and spindle imbalance) which usually occur at integer harmonics of the spindle rotation frequency. As a result of all these effects, the error signal primarily consists of a summation of sinusoids of known frequencies and unknown Fourier coefficients of the form

$$e(t) = \sum_{n=1}^{N} [a_i cos(\omega_i t) + b_i sin(\omega_i t)]. \tag{1.2}$$

In order to be able to provide zero steady-state tracking error to multiple harmonics, several AFC resonators can be placed in parallel to form a multiple resonator AFC system. The general form of a multi-resonator AFC controller is given by

$$C(s) \quad = \quad \sum_{i=1}^{N} g_i \frac{s \cos \phi_i + \omega_i \sin \phi_i}{s^2 + \omega_i^2}. \tag{1.3}$$

In our lab at the Massachusetts Institute of Technology, Marten F. Byl, Dr. Steven J. Ludwick, and Professor David L. Trumper have developed a loop-shaping approach to designing these multiple resonator AFC systems for use in diamond turning applications [6]. Their complete design, as shown in Figure 1-5, includes a conventional inner-loop controller $G_c(s)$, command pre-shifting feedforward channel $P^{*-1}(j\omega_i)$, and multiple resonator AFC controller C(s). The inner-loop is designed to maximize closed-loop bandwidth and provide a well characterized frequency response for designing the outer AFC loop. $P^*(s)$ still suffers from magnitude and phase shift as a function of frequency though. Therefore, they implement command pre-shifting

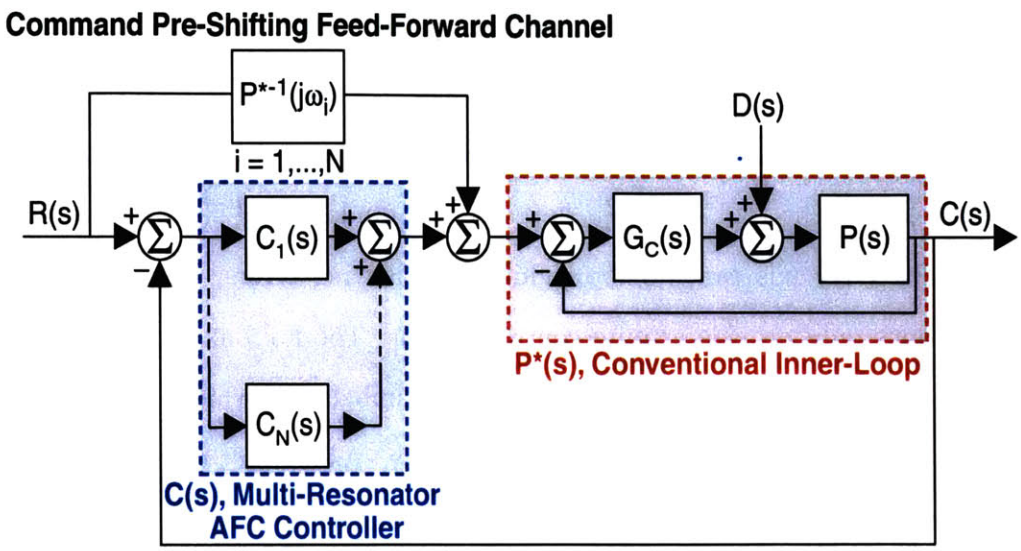

Figure 1-5: Control loop configuration used with the Variform FTS.

feedforward processing through the $P^{*-1}(j\omega_i)$ channel [6].

We use this loop-shaping approach and the controller configuration in Figure 1-5 to implement a ten resonator AFC system on the Variform FTS using a PC-based digital control system, as presented in Section 3.6. Since we are designing this loop for diamond turning applications, the trajectory reference signal contains integer harmonics of the fundamental spindle rotation frequency, which can be described by a Fourier series [1]. This means that the reference signal frequency components can be determined *a priori* and an inverse model of $P^*(s)$ is only required for this discrete set of frequencies. We can obtain the desired $P^{*-1}(s)$ magnitude and phase information from an experimental frequency response of the inner-loop $P^*(j\omega)$, which we then use to modify the feedforward command signal to the inner loop.

Figure 1-6 illustrates the calculated negative of the loop transmission frequency response for the Variform FTS with a multi-resonator AFC controller and conventional inner-loop integral compensator. The design of these loops is described in detail in Chapter 3. For the present, we want to highlight the experimental results obtained with the Variform FTS via the use of AFC control. This particular system

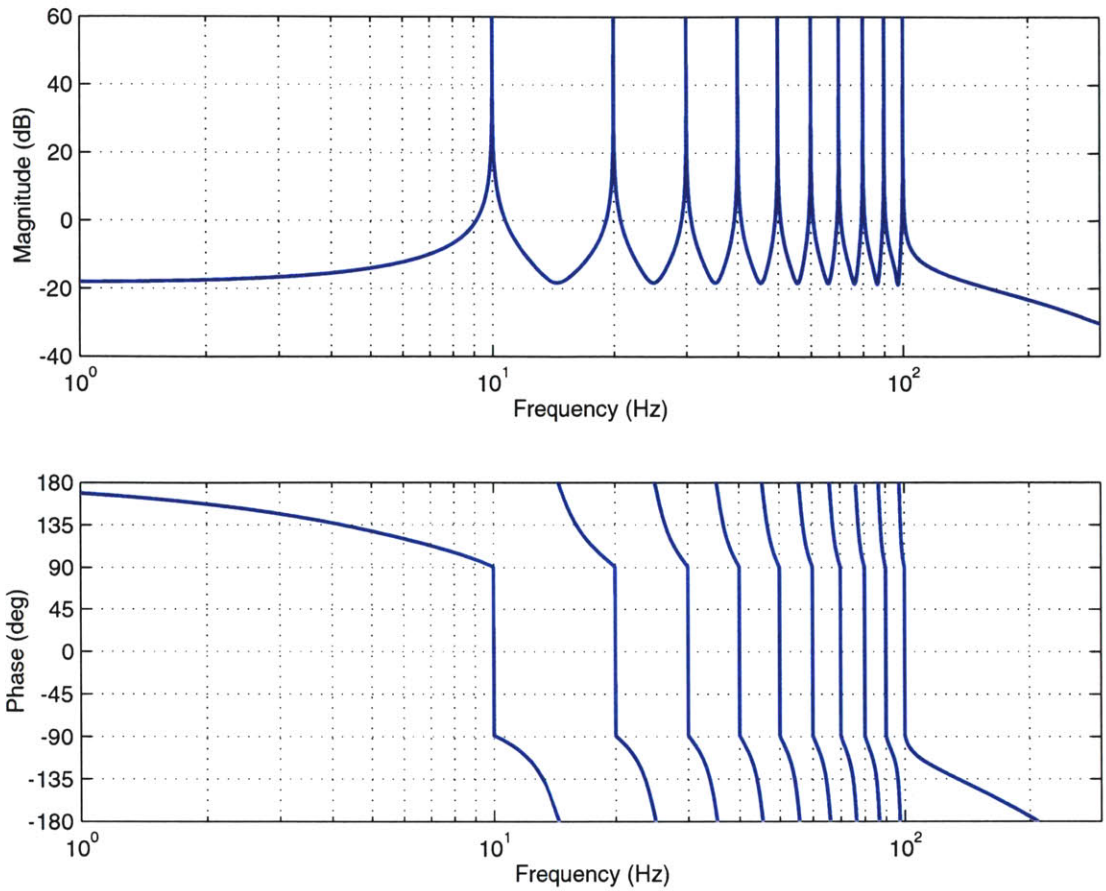

Figure 1-6: Calculated negative of the loop transmission frequency response for the Variform FTS with a ten resonator AFC controller.

is designed to provide zero steady-state error to a signal with up to ten harmonics at frequencies of

$$\omega_i = 10 \text{ Hz, } 20 \text{ Hz, } ..., \text{ and } 100 \text{ Hz.} \tag{1.4}$$

Figure 1-7 shows the experimentally measured ten-resonator AFC closed-loop system frequency response with the addition of the experimental command pre-shifting feed-forward loop. Note that the measured input-output transfer function passes through 0 dB and 0° of phase at each of the designed resonator frequencies, and thus that our AFC design works well in practice. A small amount of magnitude and phase shifting still exists at the in-between resonator frequencies, since the $\mathrm{P}^{*-1}(j\omega)$ magnitude

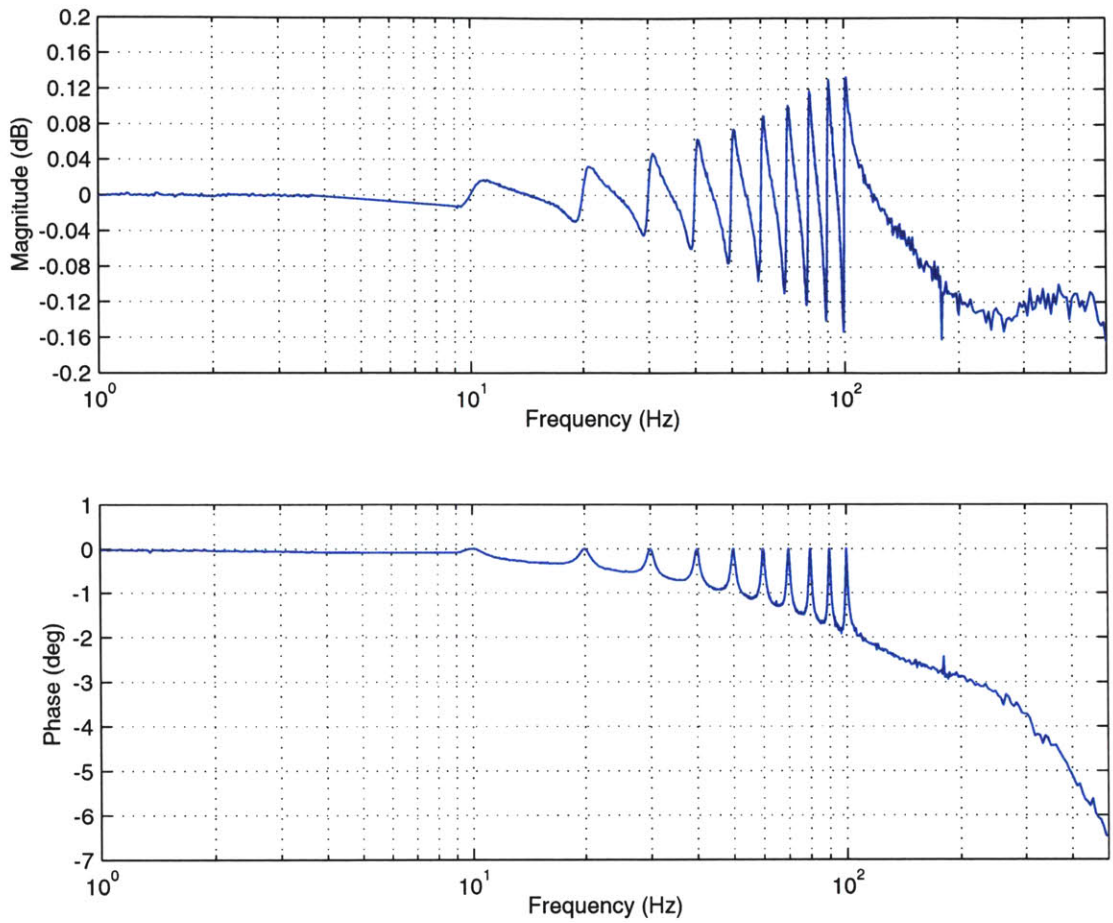

Figure 1-7: Experimental FTS closed-loop frequency response from reference to output with a ten resonator AFC controller and command pre-shifting feedforward channel.

and phase data is not 100% accurate relative to the actual system. However, up to approximately 100 Hz, the experimental results only show about a maximum 2% deviation from the 0 dB line in the Blot magnitude plot and 2° of phase lag.

Figure 1-8 shows the experimental Variform FTS closed-loop error signal during an air-cutting experiment with and without AFC control. The peak-to-peak system error without Adaptive Feedforward Cancellation, measured with the Variform FTS LVDT feedback sensor, amounts to approximately 15% of the trajectory reference signal, while the peak-to-peak system error with AFC control reduces to about 0.5%. It

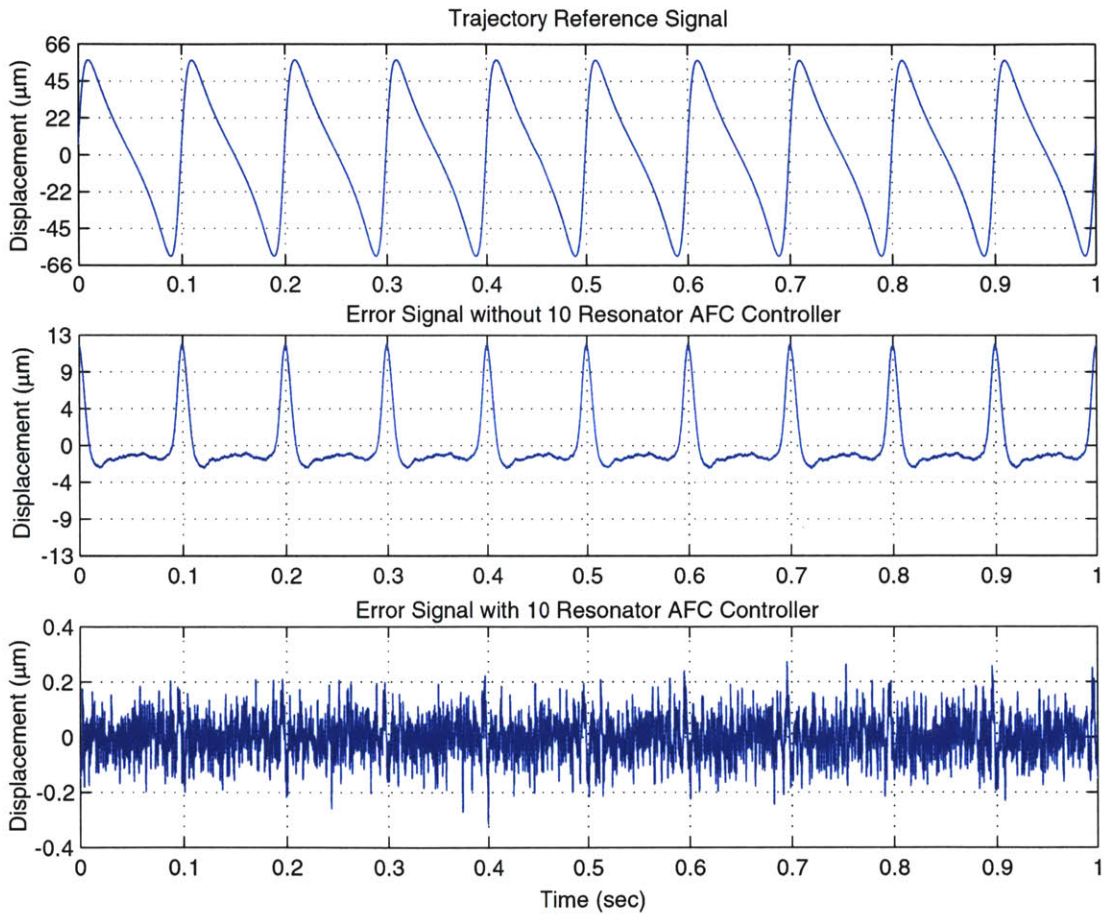

Figure 1-8: Comparison of the experimental closed-loop error signal with and without AFC Control.

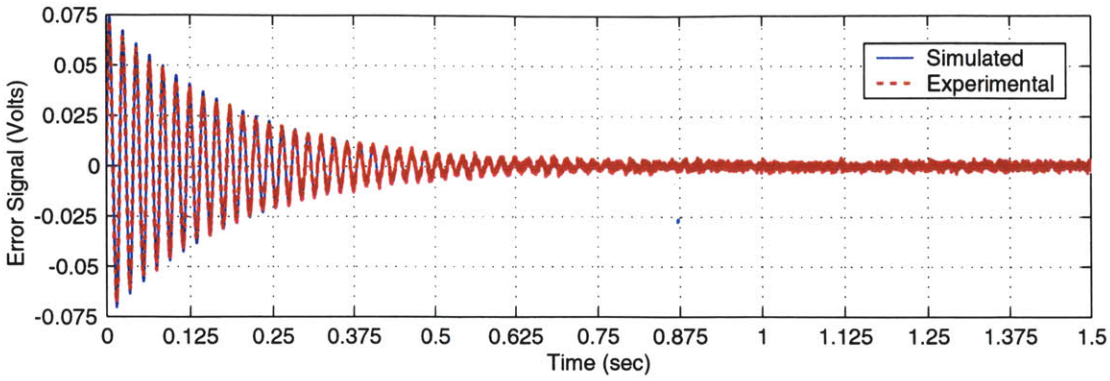

Figure 1-9: Experimental and simulated transient responses of a single resonator AFC system designed to follow a reference signal with $\omega_i = 50$ Hz.

should also be noted that the error signal with AFC control is dominated by the noise of the LVDT and there appears to be no apparent signal left that is correlated to the input reference signal. Therefore, the steady-state tracking error is essentially zero. Due to time and computer memory constraints, we were not able to implement the command pre-shifting channel during this particular test. Then again, we would have had trouble noticing any further improvements in the closed-loop response, since the addition of just the AFC controller apparently reduced the steady-state tracking error to less than the noise of the LVDT. These results illustrate a dramatic improvement in the FTS's steady-state tracking performance to constant amplitude periodic signals. However, determination of the convergence rate of the closed-loop system to changes in the reference or disturbance amplitude is not an obvious output of these analyses.

Figure 1-9 compares the simulated and experimental transient responses of a single resonator AFC closed-loop system designed to follow a signal at $\omega_i = 50$ Hz. This system provides approximately zero steady-state tracking error (if we ignore the noise of the LVDT sensor) but the amplitude of the error signal exhibits an exponential convergence rate. Hall and Wereley [53] and Bayard [64] state that this rate is approximately equal to the real part of the least damped closed-loop poles. These results provide a good measure of the time it takes the AFC controller to converge to a con-

stant amplitude reference or disturbance signal, but they do not provide an intuitive measure of the amplitude dynamics of an Adaptive Feedforward Cancellation system to sinusoids with slowly time-varying amplitudes or frequencies.

Roberge [46] showed that the amplitude of a sinusoidal oscillator can be stabilized by using an auxiliary feedback loop. He refers to this approach as an oscillator amplitude control system and states that if the bandwidth of this loop is much lower than the frequency of oscillation, then we can analyze the amplitude dynamics alone and ignore the sinusoidal portion of the loop. We provide a detailed discussion of Roberge's oscillator amplitude control system in Chapter 4 and use his work to simplify the single resonator AFC controller into a combination of oscillator amplitude control systems.

Chapter 5 describes our method of viewing Adaptive Feedforward Cancellation from an oscillator amplitude control (OAC) perspective, which provides an approximate measure of the amplitude dynamics of the closed-loop system. This perspective also allows the additional use of classical control techniques to determine an AFC loop's stability, convergence, and robustness properties. Our work builds upon that of Sacks *et al* [22], Hall and Wereley [53], and Tamisier *et al* [35]. We use an averaging analysis to simplify the single resonator AFC system from Figure 1-4 into two coupled single-input single-output (SISO) amplitude control loops and show that by setting the phase advance parameter ϕ_i equal to the phase of the inner closed-loop $P^*(\mathrm{s})$ at the resonator frequency ω_i, the loops are effectively de-coupled. This simplification is detailed in Section 5.4. An illustration of the single resonator AFC system viewed from an OAC perspective is shown in Figure 1-10, where a_{REF}, b_{REF}, a_{DIST}, and b_{DIST} refer to the input amplitudes of the periodic reference and disturbance signals and $\Psi_a(\mathrm{t})$ and $\Psi_b(\mathrm{t})$ equal the output amplitude envelopes of the cosine and sine channels of the single resonator AFC system.

As mentioned previously, viewing Adaptive Feedforward Cancellation from an

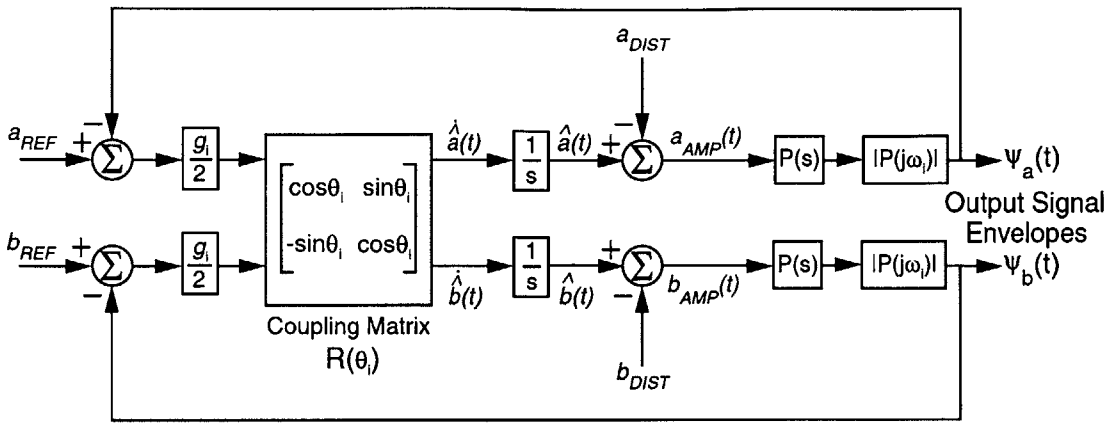

Figure 1-10: Closed-loop block diagram for the single resonator AFC system viewed as a multiple-input multiple-output (MIMO) oscillator amplitude control system.

oscillator amplitude control perspective enables the use of classical control techniques to approximate the dynamics of the AFC closed-loop system due to changes in the amplitude of the reference or disturbance signal. When $\phi_i = \angle P(j\omega_i)$, the coupling matrix in Figure 1-10 is diagonalized, which produces individual amplitude control loops for the sine and cosine channels of the single resonator AFC system. These loops effectively have the same dynamics (or an equivalent loop transmission) and the dominant OAC closed-loop pole approximates the amplitude dynamics of the AFC system output.

Figure 1-11 illustrates the closed-loop transient response of a single resonator AFC system designed to cancel a constant amplitude disturbance signal at $\omega_i = 180$ rad/sec. This figure compares the predicted AFC error signal to the approximate output using our oscillator amplitude control perspective. We see that since certain requirements are met, as discussed in Section 5.3, the OAC perspective predicts the response of the actual AFC system quite well. The approximate amplitude error envelope e_{AMP}(t), which is determined by the location of the dominant oscillator amplitude closed-loop pole, also predicts the convergence rate with and without the addition of the phase advance parameter reasonably well. See Chapter 5 for additional details on e_{AMP}(t).

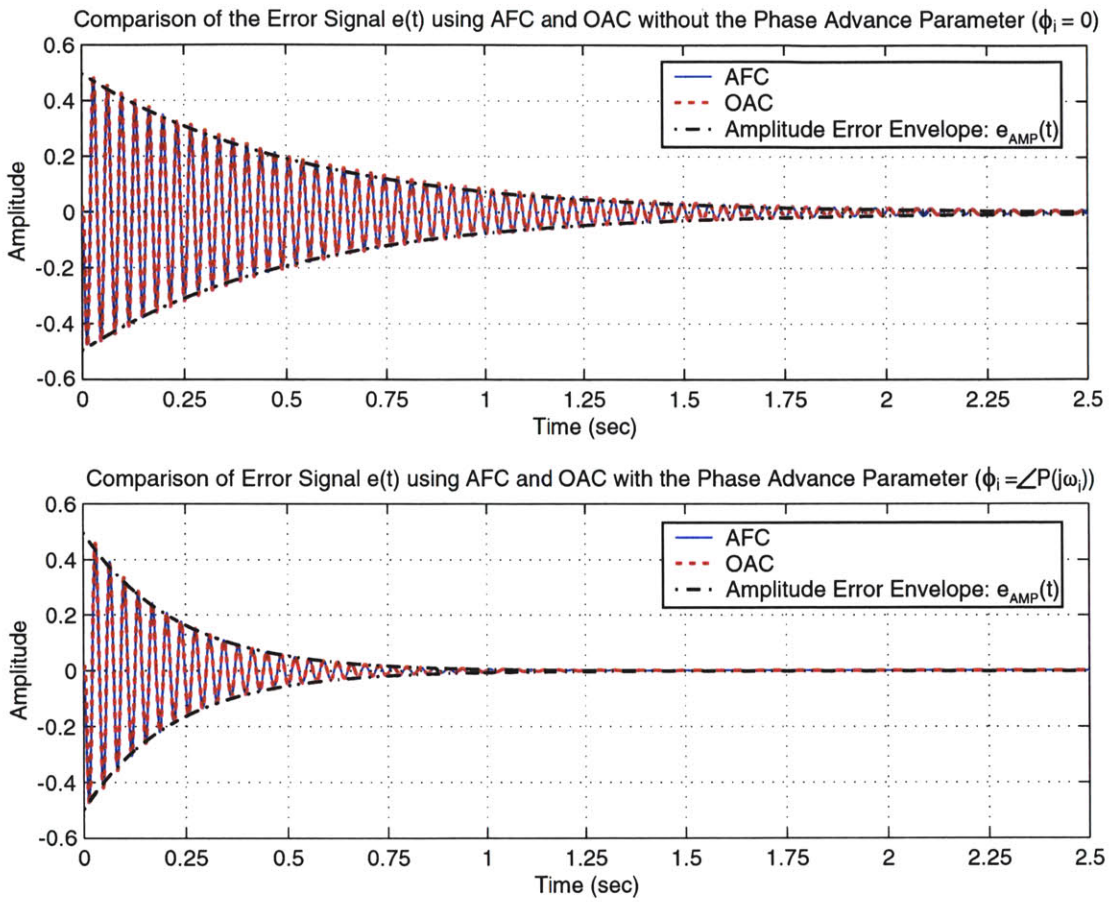

Figure 1-11: Simulated transient response of a single resonator AFC system designed to cancel a constant amplitude disturbance with $\omega_i = 180$ rad/sec. Included are the actual AFC system error signal, the approximate error signal using our OAC perspective, and the approximate amplitude error envelope, which is determined by the dominant oscillator amplitude closed-loop pole.

When the phase advance parameter is chosen properly, we can use the resulting negative of the loop transmission of the equivalent OAC loops to determine the stability and convergence properties of the single resonator AFC system. Also, when $\phi_i = \angle P(j\omega_i)$, the sine and cosine channels of the single resonator system both have 90° of phase margin and are robust to modelling errors in the plant transfer function. As long as any unmodelled plant dynamics do not contribute more than $\pm 90^o$ of additional phase lag to the negative of the loop transmission, the closed-loop system is stable but the convergence time increases and the AFC sine and cosine channels

become coupled, resulting in a MIMO control problem. An approximation of the coupled amplitude dynamics and increased convergence time can be determined with our oscillator amplitude control perspective, as shown in in Figure 1-11 and discussed in detail in Section 5.4.

1.2 Thesis Overview

The rest of this chapter presents the context and motivation for viewing Adaptive Feedforward Cancellation from an oscillator amplitude control perspective. Chapter 2 provides a background on repetitive control systems and develops the theory and design of Adaptive Feedforward Cancellation algorithms. We also present our complete multiple resonator AFC controller design for use on fast tool servos in diamond turning applications. In Chapter 3, we detail the complete design, implementation, and experimentation of several conventional control systems as well as our complete multiple resonator AFC controller design on the Variform FTS using a PC-based digital control system. Chapter 4 presents the background on oscillator amplitude control systems theory, while Chapter 5 develops our method of viewing Adaptive Feedforward Cancellation from an oscillator amplitude control perspective. Finally, in Chapter 6, we summarize the work presented and provide suggestions for future work.

1.3 Background

In this section, we present related prior work, in order to set the context for the results presented in this thesis. The section begins with a summary of the design and construction of a novel rotary fast tool servo for diamond turning, which uses a multiple resonator Adaptive Feedforward Cancellation controller to achieve increased control authority over a selected set of harmonics. Next, we summarize several repet-

itive controllers in the literature and their applications and show how they are related to the Adaptive Feedforward Cancellation algorithm. Finally, we discuss the Higher Harmonic Control and Automatic Vibration Rejection algorithm in depth, since we draw upon both of them in the development of our Adaptive Feedforward Cancellation viewed from an oscillator amplitude control perspective.

1.3.1 Rotary Fast Tool Servo for Diamond Turning of Asymmetric Optics

In our lab at MIT, Steven Ludwick, David Ma, David Chargin, and Joseph Calzaretta worked on the design and construction of a prototype diamond turning machine for the production of rotationally asymmetric spectacle lenses. This work is documented in the Doctoral thesis of Ludwick [1] and the Master's thesis of Ma [2] and Chargin [3], as well as [4] [5] and [6]. This machine uses a novel rotary fast tool servo design for cutting geometries with peak-to-peak amplitudes of up to 2 cm, which require a form accuracy of about 1 μm. Peak accelerations can be as high as 50g's (500 m/s^2) [6]. Thus, controlling this machine to meet such performance specifications is very challenging.

Conventional feedback systems cannot provide the required control authority to cut these asymmetric spectacle lenses, even when augmented with feedforward command processing [6]. Instead, Ludwick [1] investigates using a specialized control systems class, known collectively as repetitive control, to overcome the limits of the conventional algorithms. He relies on the fact that the trajectories on the fast tool servo can be represented as a summation of harmonics of the fundamental spindle rotation frequency, which is directly applicable to repetitive controllers. Ludwick's approach uses Adaptive Feedforward Cancellation (AFC), a form of repetitive control, to enhance the trajectory following capabilities of the closed-loop system for a selected set of harmonics. While following a 20 Hz sinusoid with a 1 cm peak-to-peak ampli-

tude, the experimental fast tool servo produced about a 20% peak-to-peak following error with a conventional lead-lag controller. The error is reduced to 1.2% peak-to-peak with feedforward command processing. With an AFC controller implemented, the experimental steady-state peak-to-peak tracking error reduced to approximately 0.01%.

Since Ludwick's implementation of a multiple-resonator AFC controller on the prototype rotary fast tool servo diamond turning machine, our lab has further investigated the use of Adaptive Feedforward Cancellation in asymmetric turning applications. Byl, Ludwick, and Trumper have developed a loop-shaping approach to designing multiple-resonator AFC systems, which provides rational tuning of the gain and phase parameters to minimize following errors yet still provide adequate stability margins [6]. This work shows that AFC provides excellent performance to disturbances with constant amplitude and frequency components, but it does not characterize the amplitude convergence properties of the closed-loop system or the response of Adaptive Feedforward Cancellation to sinusoids with time-varying amplitude or frequency components. In this thesis, we build upon the work of Byl, Ludwick, and Trumper to provide an approximate measure of the convergence properties and steady-state error characteristics of Adaptive Feedforward Cancellation systems to sinusoids with both constant and time-varying properties.

1.3.2 Self-Tuning Narrow-Band Trajectory Following & Disturbance Rejection Control Systems

The so-called "Adaptive Feedforward Cancellation" algorithm is just a form of self-tuning narrow-band trajectory following/disturbance rejection control. In the literature, several other algorithms have been proposed throughout the years under various titles (*i.e.*, Active Balancing System, Higher Harmonic Control, Automatic Vibration Rejection, Adaptive Sinusoidal Interference Canceller, etc.) but they are

all related. These algorithms effectively place resonators in the forward or feedback path of the control loop and adaptively adjust to the amplitude and/or phase of the components which the system is attempting to follow/reject. The following sections summarize several self-tuning narrow-band trajectory following/disturbance rejection control system applications. Also, the theory of techniques called Higher Harmonic Control and Automatic Vibration Control are presented.

Applications of Self-Tuning Narrow-Band Trajectory Following & Disturbance Rejection Control Systems

One of the earliest works in the field of self-tuning narrow-band trajectory following/disturbance rejection appears to have been by Glover [68]. In this work, he presents a discrete-time adaptive noise cancellation (ANC) algorithm for eliminating sinusoidal interference signals. This control system includes LTV equations but if the proper choice of parameters are used, the resulting controller can be approximated by an LTI system. Glover's algorithm essentially creates an adaptive notch filter located directly at the frequency of the sinusoidal interference. The researcher So [69] also proposed a discrete-time adaptive algorithm for the removal of a 50 Hz sinusoidal interference in the recording of electrocardiograms (ECG). He refers to this method as the Adaptive Sinusoidal Interference Canceller (ASIC) algorithm and simulates the complete removal of a sinusoidal waveform after transients. He also provides an approximate convergence rate of his ASIC algorithm, which predicts the time it takes for the system to eliminate a sinusoidal interference.

Other algorithms have been proposed for use in the field of active vibration suppression. Several papers have been published (*e.g.*, [51] [52] [53] [54]) on Higher Harmonic Control, which is designed to cancel vibrations in helicopters due to rotor blade aerodynamic loads. Tamisier *et al* [35] published a paper on a control method which suppresses unbalance vibrations in active magnetic bearing (AMB) systems,

while Li *et al* [36] also remove unbalance vibrations in an AMB system with a variation of the Adaptive Feedforward Cancellation algorithm. Scribner, Sievers, and von Flotow [61] describe a self-tuning frequency following algorithm for general uses in the noise and vibration isolation of machinery.

Sievers and von Flotow [62] provide an excellent comparison of several narrow-band disturbance rejection control systems. Their work includes a review of the Internal Model Principle [7] [8], modern control, and discrete-time based controllers. Although each of these algorithms vary significantly in their approach and design, all of them come to the same basic conclusion. A feedback system which provides zero steady-state error to a disturbance of frequency ω_i usually places a resonator in the loop transmission at ω_i.

The work presented herein is motivated by the Adaptive Feedforward Cancellation algorithm. Several papers on AFC were published in the mid 90's by Bodson, Kholsa, Messner, and Sacks [20] [21] [22] [23] [24] [25]. This work formed the basis for Ludwick's rotary fast tool servo controller approach. In Sacks *et al* [21] [22] [23] an experimental single and multiple-resonator AFC controller was applied to a computer hard disk drive (HDD) to reduce the periodic disturbance components of the position error signal (PES). An averaging analysis was also performed in [22], which provides an approximation of the convergence properties of an AFC closed-loop system from the locations of the AFC averaged system eigenvalues. We use these results as one of the baselines for our development of the Oscillator Amplitude Control perspective. Other researchers (*e.g.*, [57] [58] [59]) have also successfully used AFC controllers to reduce repeatable run-out (RRO) errors in hard disk drives.

In the following sections, we provide the background theory on the Higher Harmonic Control and Automatic Vibration Rejection algorithms. Both of these structures are fundamentally the same as Adaptive Feedforward Cancellation although they make use of slightly different approaches in their formulation and implementa-

tion. We also utilize both of these representations in the development of our oscillator amplitude control perspective.

Higher Harmonic Control

Higher Harmonic Control (HHC) is a type of self-tuning narrow-band disturbance rejection system that is designed to cancel vibrations in helicopters due to variations in the rotor blade aerodynamic loads. These vibrations, which reduce pilot and passenger comfort as well as increase maintenance and operating costs, are located predominantly at the fundamental rotor rotation frequency and its harmonics [53] [54]. Since these frequencies are well known, they can be used to create a modulation/demodulation controller structure with integrators to estimate the Fourier coefficients of the disturbance signal. The HHC algorithm then uses these estimates to create an inverse estimate of the disturbance, which is used to cancel the existing helicopter vibrations. McHugh and Shaw [51] and Shaw and Albion [52] developed the first discrete-time HHC algorithm, which was later expanded upon by Hall and Wereley [53] by viewing HHC in the continuous-time. In this section, we focus on the work of Hall and Wereley, as their continuous-time view of HHC corresponds more directly to the Adaptive Feedforward Cancellation algorithm.

Helicopter vibration suppression can be a rather complex control problem, since the dynamics of the plant are LTV, due to the periodically varying rotor blade aerodynamics. In order to simplify the problem, two assumptions can be made. First, the controller bandwidth is much lower than the plant's natural frequency. In this case, the plant be can treated as quasi-steady. Second, the effects of the periodicity are small enough that the system can be accurately represented by an LTI model. Assuming that the periodic helicopter dynamics are relatively small, Hall and Wereley analyze the HHC algorithm by modelling the plant as an LTI system with transfer function G(s). By keeping the controller bandwidth sufficiently low, they ignore the

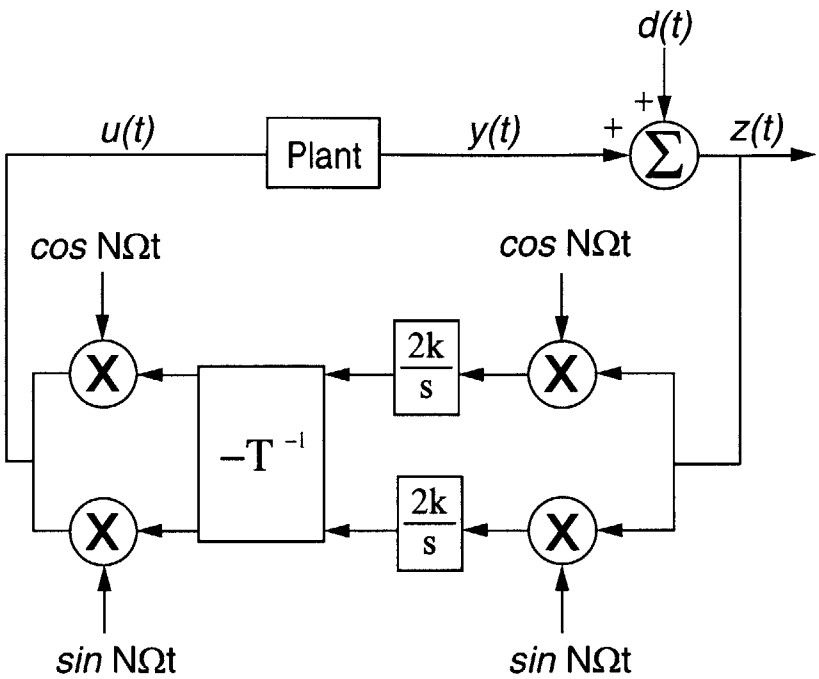

Figure 1-12: HHC closed-loop block diagram. Figure adapted from Hall and Wereley [53].

transient plant dynamics and model the plant with McHugh and Shaw's constant control response matrix, which is given by

$$\mathbf{T} = \begin{bmatrix} T_{cc} & T_{cs} \\ T_{sc} & T_{ss} \end{bmatrix}, \tag{1.5}$$

where

$$T_{cc} = T_{ss} = \mathrm{Re}\left[G(jN\Omega)\right], \tag{1.6}$$

$$T_{cs} = -T_{sc} = \mathrm{Im}\left[G(jN\Omega)\right]. \tag{1.7}$$

Figure 1-12 illustrates the continuous-time Higher Harmonic Control controller block diagram. This particular system provides zero steady-state error to a disturbance signal with frequency $\omega = N\Omega$. The closed-loop is also robust to small

fluctuations in the disturbance frequency, since Ω is the experimentally measured fundamental rotor frequency that is used to create the sine and cosine modulators, as shown in Figure 1-12.

Analogous to the AFC algorithm, the internal structure of the HHC controller consists of linear time-varying equations but the input-output relationship from z(t) to u(t) is linear time-invariant. The resulting HHC controller transfer function is

$$H(s) = -\frac{U(s)}{Z(s)} = \frac{2k(as + bN\Omega)}{s^2 + (N\Omega)^2}, \tag{1.8}$$

where k is a constant proportional gain. The proper choices for the parameters of the zero in (1.8) are given by

$$a = \frac{\mathrm{Re}[\mathrm{G}(jN\Omega)]}{|G(jN\Omega)|^2}, \tag{1.9}$$

$$b = \frac{\mathrm{Im}\,[\mathrm{G}(jN\Omega)]}{|G(jN\Omega)|^2}. \tag{1.10}$$

where $\mathrm{G}(jN\Omega)$ is the frequency response of the plant transfer function evaluated at $\mathrm{s} = jN\Omega$.

One of the main differences between the AFC and HHC algorithm is the method in which closed-loop stability is ensured. Typical AFC algorithms use a phase advance parameter to increase the system's robustness to plant variations while HHC incorporates the inverse control response matrix $\mathbf{T}^{-1}$. The similarity of (1.1) and (1.8) shows that although these methods take different viewpoints, they essentially produce the same results. We provide a more detailed comparison between both of these methods in Chapter 2.

Since HHC is equivalent to an LTI system, we can use classical controls techniques to evaluate the closed-loop stability and robustness. Hall and Wereley show that if the parameters of the zero are chosen as defined in (1.9) and (1.10) and the

quasi-steady approximation holds (*e.g.*, the plant dynamics are at least an order of magnitude further into the left hand s-plane), then the departure angles of the poles in (1.8) are at 180°. This essentially means that the negative of the loop transmission has approximately 90° of phase margin. However, if the quasi-steady assumption is violated, the HHC controller poles may depart directly into the right half plane and the loop will be unstable.

When the quasi-steady assumption is valid, the HHC system has closed-loop poles located approximately at

$$s_{1,2} = -k \pm jN\Omega, \tag{1.11}$$

and the convergence rate[2] is proportional to

$$\alpha \sim \frac{1}{k}. \tag{1.12}$$

For example, Hall and Wereley analyze the transient response of the HHC closed-loop system to a disturbance input given by

$$d(t) = \sin(N\Omega t), \tag{1.13}$$

and determine that the output is

$$z(t) = \frac{N\Omega}{\sqrt{(N\Omega)^2 - k^2}} e^{-kt} \sin \sqrt{(N\Omega)^2 - k^2} t. \tag{1.14}$$

This response is a sinusoid of frequency $\left(\sqrt{(N\Omega)^2 - k^2}\right)$ modulated with an exponentially decaying amplitude envelope, where the envelope time constant is $\tau = \frac{1}{k}$. Therefore, the convergence properties of the HHC system can be determined by the

[2]time it takes for the HHC closed-loop system to eliminate the disturbance signal d(t).

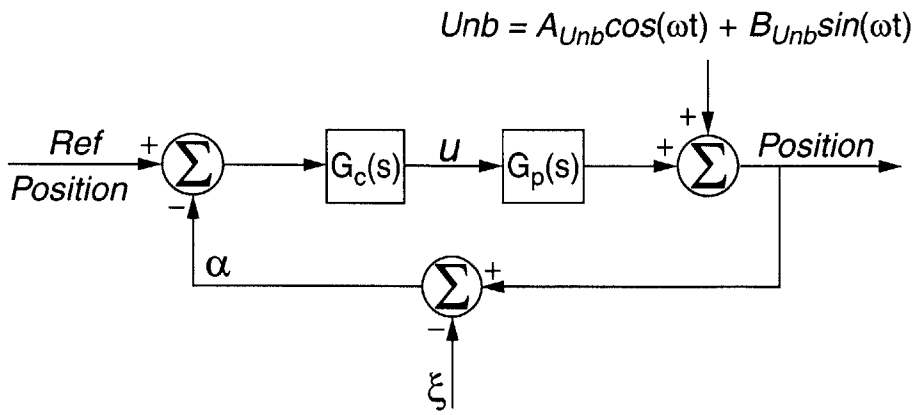

Figure 1-13: Active Magnetic Bearing closed-loop block diagram with Automatic Vibration Rejection. Figure adapted from Tamisier *et al* [35].

amplitude dynamics of output signal alone. Our oscillator amplitude control perspective builds upon this concept, modelling the amplitude dynamics of AFC systems specifically to characterize the closed-loop stability, convergence, and robustness properties of the Adaptive Feedforward Cancellation algorithm.

Automatic Vibration Rejection

Tamisier *et al* [35] have developed and apparently patented a self-tuning narrow-band disturbance rejection system for use on Active Magnetic Bearings (AMB), which is based on the unbalance control algorithm called Automatic Balancing System (ABS). They call their algorithm Automatic Vibration Rejection (AVR), since it is designed to cancel periodic unbalance vibrations from the feedback signal of rotating machinery with AMB systems. These vibrations develop from the difference between the axis of inertia of the rotor and the geometrical axis determined by the magnetic bearings.

Figure 1-13 illustrates the AMB closed-loop block diagram, where $G_c(s)$ and $G_p(s)$ represent conventional controller and plant transfer functions, respectively. The signal Unb(t) is the unbalance vibration, while ξ(t) refers to the control output of the AVR

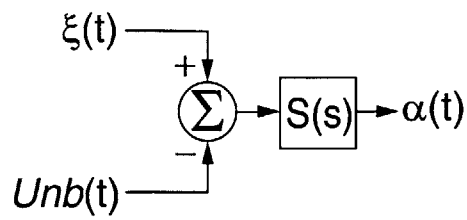

Figure 1-14: Summary of Automatic Vibration Rejection in block diagram form. Figure adapted from Tamisier *et al* [35].

system. Tamisier *et al* define a transfer function

$$\frac{Unb}{\alpha}(s) = \frac{\xi}{\alpha}(s) = \frac{1}{1 + G_c(s)G_p(s)} = S(s), \tag{1.15}$$

which they summarize with the block diagram in Figure 1-14. In essence, the AVR system produces an estimate of the inverse of the disturbance signal and will eliminate Unb(t) from α(t) when

$$\xi(t) = Unb(t). \tag{1.16}$$

Assuming the following equations,

$$\alpha(t) = A_\alpha \cos(\omega t) + B_\alpha \sin(\omega t), \tag{1.17}$$

$$\xi(t) = A_\xi \cos(\omega t) + B_\xi \sin(\omega t), \tag{1.18}$$

$$Unb(t) = A_{Unb} \cos(\omega t) + B_{Unb} \sin(\omega t), \tag{1.19}$$

the algorithm in which Tamisier *et al* propose to achieve such cancellation is shown in Figure 1-15. If viewed from a different perspective, the AVC configuration is exactly the same as the AFC and HHC control approach. Figure 1-13 can be re-arranged into an equivalent block diagram, as shown in Figure 1-16, while Figure 1-17 illustrates the resulting AVC algorithm.

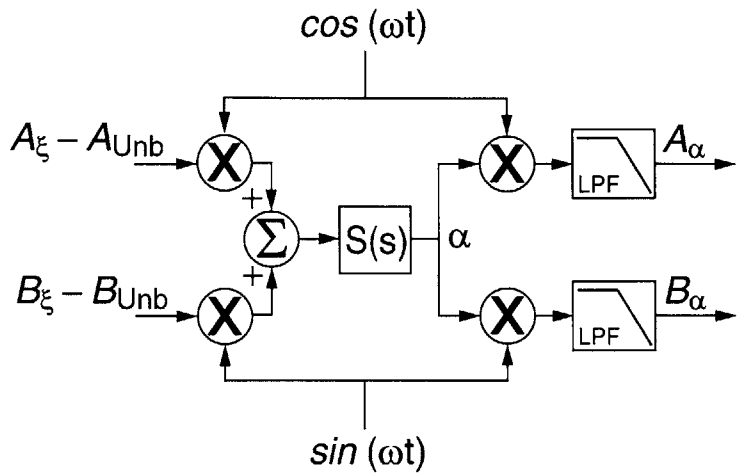

Figure 1-15: Automatic Vibration Rejection algorithm. Figure adapted from Tamisier *et al* [35]

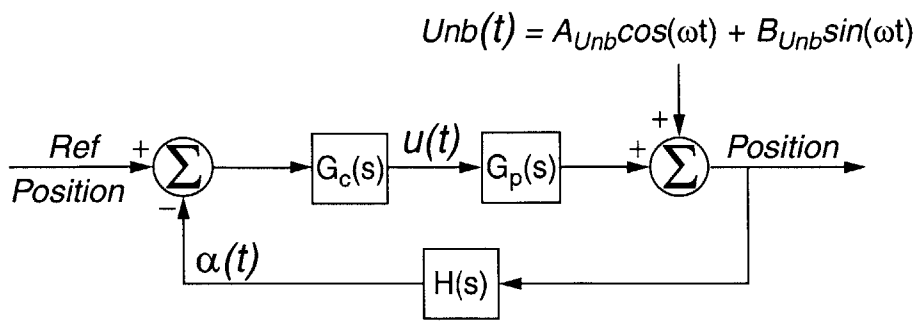

Figure 1-16: Active Magnetic Bearing closed-loop block diagram with Automatic Vibration Rejection converted into an AFC equivalent form. H(s) represents the resulting AVC algorithm.

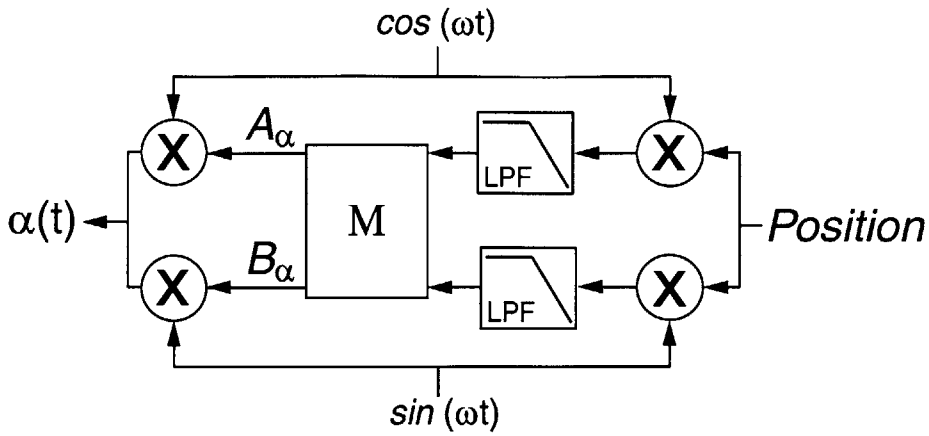

Figure 1-17: Automatic Vibration Rejection algorithm in an AFC equivalent form. This controller is represented by H(s) in Figure 1-16.

Tamisier *et al* state that low-pass filters with an associated proportional gain are used to achieve the desired control authority but they do not provide any specific details. For purposes of discussion, we will assume, based on the structure of the AFC and HHC algorithms, that they are also using integrators to filter the Position signal of the closed-loop system. Under this assumption, the low-pass filter blocks in Figure 1-16 become

$$LPF = \frac{K_p}{s}, \tag{1.20}$$

where K_p is a constant gain. The resulting AVC algorithm is equivalent to an LTI system, which is given by

$$H(s) = \frac{\alpha(s)}{Position(s)} = K_p \left[\frac{X_M s + Y_M \omega}{s^2 + \omega^2} \right]. \tag{1.21}$$

This system's stability and robustness is dependent upon K_p and the location of the H(s) zero, which is dependent on the choice of X_M and Y_M. These values are

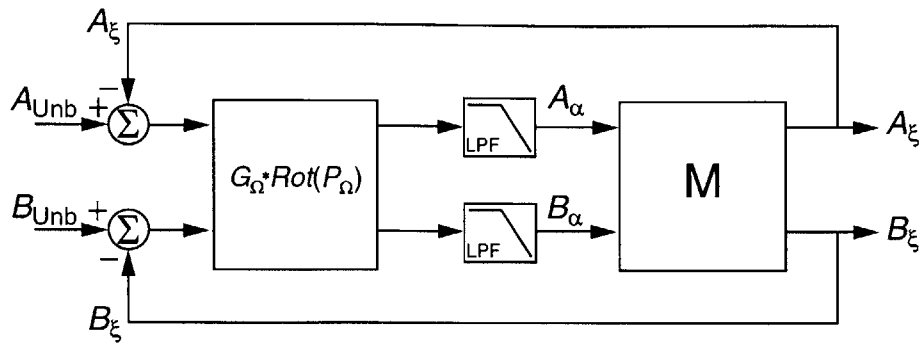

Figure 1-18: Principle of the AVR unbalance compensation algorithm. Figure adapted from Tamisier [35].

determined by a 2X2 rotation matrix of the form

$$\mathrm{M} = \begin{bmatrix} \cos\psi & -\sin\psi \\ \sin\psi & \cos\psi \end{bmatrix}. \tag{1.22}$$

In order to achieve the same level of stability and robustness as the AFC and HHC controllers, Tamisier *et al* state that the compensation angle ψ should be set equal to the phase of (1.15) at the frequency of the vibration ω,

$$\psi = \angle S(j\omega). \tag{1.23}$$

Equation (1.23) is equivalent to the phase of the sensitivity transfer function evaluated at s = $j\omega$, if H(s) is removed from the loop transmission of Figure 1-16.

Automatic Vibration Rejection thereby produces an adaptive notch filter located directly at the frequency of the unbalance vibration. When $\xi(t) = Unb(t)$, the unbalance vibration is eliminated from the feedback signal in Figure 1-16 and thus the conventional controller G_c(s) will not attempt to compensate for Unb(t). As a result, the AMB rotor experiences a repeatable run-out (due to the mass unbalance) but the power requirements of the electronics which control the current into the magnetic

bearings is minimized, as is the unbalance force injected into the machine support structure.

During their analysis, Tamisier *et al* provide an interesting perspective on their AVC algorithm. They illustrate the basic principle of Automatic Vibration Rejection in the manner shown in Figure 1-18. This view simplifies the analysis by eliminating the modulation/demodulation structure as shown in Figure 1-15, and focuses only on the dynamics of the Fourier coefficients of (1.17), (1.18), and (1.19). Also, the $G_\Omega * Rot(P_\Omega)$ block is given by

$$G_\Omega * Rot(P_\Omega) = \begin{bmatrix} Z_{11} & Z_{12} \\ Z_{21} & Z_{22} \end{bmatrix}, \tag{1.24}$$

where

$$Z_{11} = Z_{22} = \mathrm{Re}\left[\mathrm{S}(j\omega)\right], \tag{1.25}$$

$$Z_{12} = -Z_{21} = \mathrm{Im}\left[\mathrm{S}(j\omega)\right]. \tag{1.26}$$

We see that (1.24) is fundamentally equivalent to Shaw's HHC constant control response matrix. Therefore, Tamisier *et al* apparently also assume quasi-steady conditions. This perspective also provides a starting point in the development of our Adaptive Feedforward Cancellation viewed from an oscillator amplitude control perspective though we perform a more detailed analysis on the dynamics of the estimates of the Fourier coefficients.

In summary, there are several trajectory following/disturbance rejection controllers in the literature that are related to the Adaptive Feedforward Cancellation algorithm. Each of them provide their own applications and analysis tools, but in this thesis we utilize the loop-shaping approach developed by Byl, Ludwick, and Trumper [6] to design a multiple resonator AFC controller for use on the Variform

FTS. The following chapter provides a detailed background on the Adaptive Feedforward Cancellation algorithm. We illustrate the design and performance of the single resonator AFC system with several simulations. Also, we summarize Byl, Ludwick, and Trumper's multi-resonator AFC work and illustrate their tuning method with additional simulations.

Chapter 2

Adaptive Feedforward Cancellation Systems Theory

This chapter investigates the analysis and design of feedback control systems used for the tracking and disturbance rejection of periodic signals with a selected set of harmonics. These types of control systems, known collectively as *repetitive controllers*, have applicability for hard disk and optical disk track following, vibration rejection in spindle systems, camshaft and piston machining, and fast tool servos used in high-precision turning applications [6]. In this thesis we focus primarily on Adaptive Feedforward Cancellation (AFC), a form of repetitive control, to reduce/eliminate the steady-state tracking errors of fast tool servos for diamond turning.

In diamond turning applications, fast tool servos commonly follow periodic trajectories and with conventional controllers can develop large followings errors. With most part shapes, the tool position command is dominated by components which are harmonics of the fundamental spindle rotation frequency. Thus, the error signal primarily consists of a summation of sinusoids of known frequencies and unknown

Fourier coefficients of the form

$$e(t) = \sum_{n=1}^{N} [a_i cos(\omega_i t) + b_i sin(\omega_i t)]. \tag{2.1}$$

Classical feedback systems (*i.e.*, Proportional-plus-Integral-plus-Derivative (PID) and lead-lag controllers) are generally used in the industry to control fast tool servos. These controllers are relatively straightforward in design and provide excellent performance to applications with constant inputs and disturbances but they cannot provide zero steady-state error to periodic signals, even when command pre-shifting feedforward is included [6]. Therefore, controllers based on the Internal Model Principle [7] [8] can be used to enhance the closed-loop performance.

The rest of this chapter is organized as follows. Section 2.1 provides a background on repetitive control systems. This includes a brief review of classical controls, description of the Internal Model Principle of control theory, and analysis of several repetitive controller structures. In Section 2.2, we discuss the theory of Adaptive Feedforward Cancellation and present our complete AFC controller design for use on fast tool servos in diamond turning.

2.1 Background

2.1.1 Review of Classical Control

Figure 2-1 illustrates the classical closed-loop block diagram without a noise input, where $G_c(s)$, $G_p(s)$, and $H(s)$ are the transfer functions of the feedback controller, plant being controlled, and feedback or measurement function, respectively [43]. The loop transmission is defined as

$$\text{Loop Transmission} = L(s) = -G_c(s)G_p(s)H(s), \tag{2.2}$$

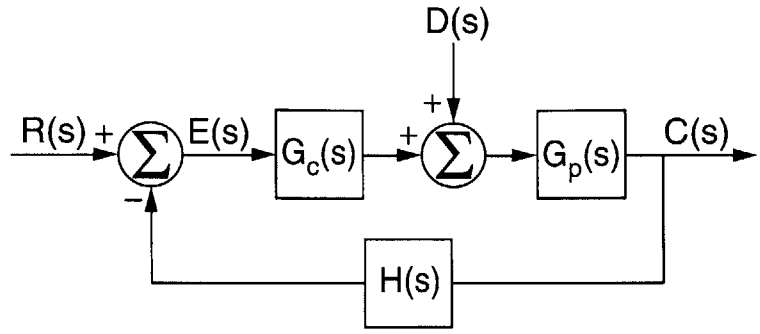

Figure 2-1: Classical feedback system closed-loop block diagram.

and the closed-loop output and disturbance rejection transfer functions are

$$\text{Closed-Loop Output} = \frac{C(s)}{R(s)} = \frac{G_c(s)G_p(s)}{1 - L(s)}, \tag{2.3}$$

$$\text{Disturbance Rejection} = \frac{C(s)}{D(s)} = \frac{G_p(s)}{1 - L(s)}. \tag{2.4}$$

Using block diagram manipulation, we can convert Figure 2-1 into an equivalent unity feedback closed-loop block diagram, as shown in Figure 2-2. Assuming that the measurement function output is $H(s) \approx 1$ for the frequencies of interest, the resulting loop transmission is of the form

$$L(s) \approx -G_c(s)G_p(s), \tag{2.5}$$

and when $|L(j\omega)| \gg 1$, the closed-loop and disturbance rejection transfer functions are approximately equal to

$$\frac{C(s)}{R(s)} \approx 1, \tag{2.6}$$

$$\frac{C(s)}{D(s)} \approx 0. \tag{2.7}$$

Classical PID and lead-lag controllers are only able to provide high gains ($|L(j\omega)| \gg$

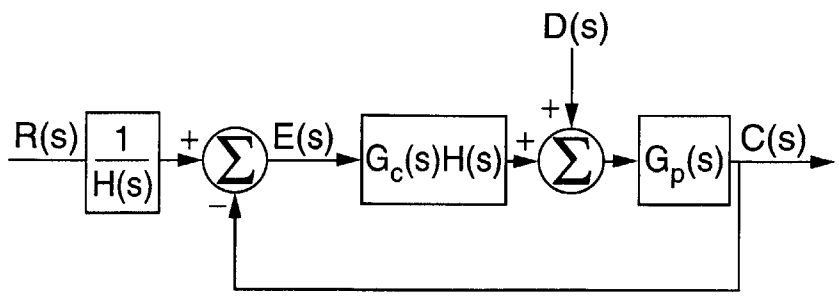

Figure 2-2: Closed-loop block diagram manipulated into a unity feedback notation.

1) for a limited range of frequencies. The resulting closed-loop systems thus cannot drive the steady-state error to zero for an input with non-zero frequency components. Figure 2-2 shows an example of a typical lead-lag compensator frequency response. Here, an integrator is located in the forward path of the feedback loop. Thus, $|L(j0)| = \infty$ and the closed-loop system will provide zero steady-state error to a constant reference or disturbance input. By extension, if we desire zero steady-state error to an input signal with frequency ω_i, the magnitude of the loop transmission must be infinite for that particular frequency as well. As shown in Figure 2-2, PID and lead-lag controller designs do not provide this type of infinite control authority at non-zero frequency. For this reason we design a controller based on the Internal Model Principle to meet these specifications.

Internal Model Principle

The Internal Model Principle, developed by Francis and Wonham [7] [8], states that in order for a feedback system to be able to provide zero steady-state error to a known reference signal, the controller must include a model of that particular signal. For example, consider a controller that includes an integrator. The resulting closed-loop system provides zero steady state error to a step input [9], since the Laplace transform of an integrator equals $\frac{1}{s}$ while the Laplace transform of a step input also equals $\frac{1}{s}$.

In order to achieve zero steady-state error to a periodic signal with frequency

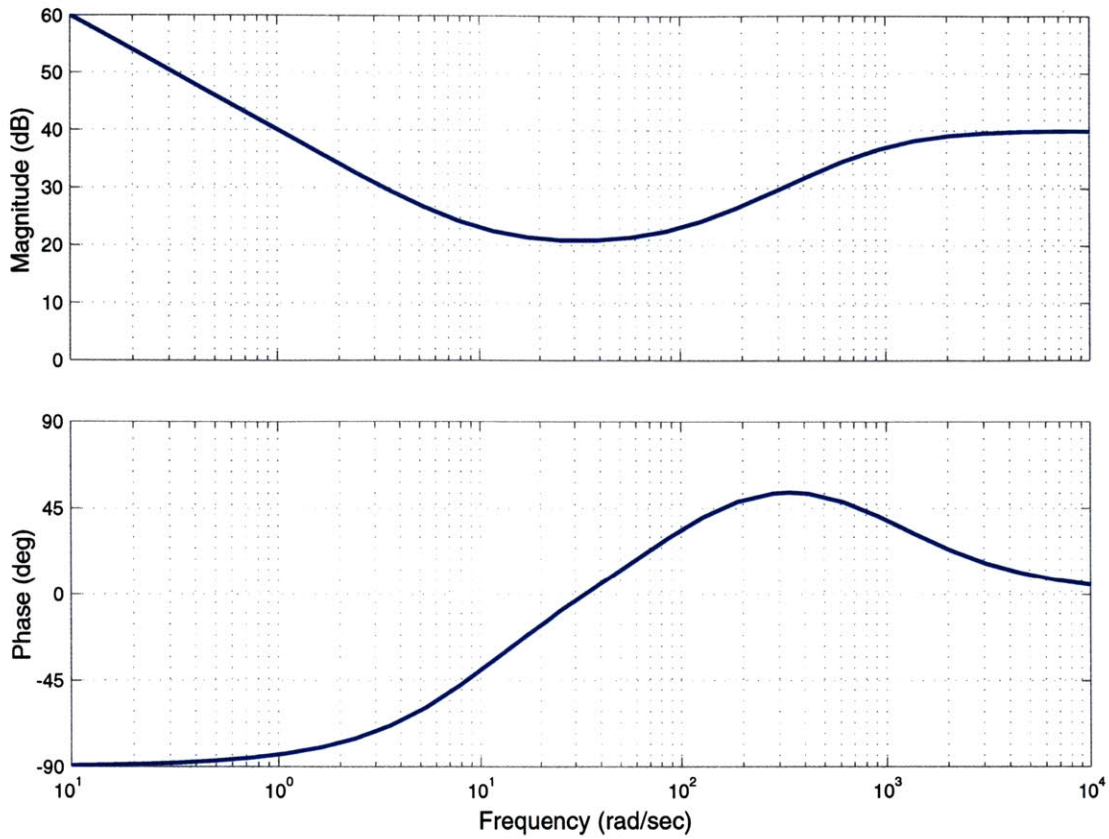

Figure 2-3: Example frequency response for lead-lag compensator with lag pole at the origin (s=0).

ω_i, the Internal model principle states that a controller must include a signal generator with the same fundamental period (*i.e.*, place poles on the imaginary-axis at $s = \pm j\omega_i$). Repetitive controllers are based on the Internal Model Principle and can be used for the tracking and rejection of periodic signals with known frequency content [18]. We briefly discuss several repetitive controller systems in the following sections.

2.1.2 Repetitive Control Systems

Messner and Bodson [24] state that repetitive control is the term used for describing a control methodology designed specifically to compensate for periodic disturbances

or to track periodic reference trajectories with some known period. The majority of these designs are based on the Internal Model Principle, which use marginally stable poles to provide increased control authority over a set of narrow frequency bands. In the following sections, we describe two types of repetitive control systems. The first algorithm consists of a real-axis zero and two imaginary-axis poles, which provides increased control authority about a single frequency. The second controller is based on placing a pure time delay in a positive feedback loop. The resulting closed-loop system yields an infinite number of imaginary-axis poles, which ultimately provides increased control authority to multiple frequencies.

Internal Model Principle Controller

In [24], Messner and Bodson propose a controller transfer function of the form

$$G_c(s) = \frac{\alpha(s+\beta)}{s^2+\omega_i^2}. \tag{2.8}$$

to reject sinusoidal disturbances in data storage systems. They refer to this design as the Internal Model Principle (IMP) controller, since (2.8) places marginally stable poles at $s = \pm j\omega_i$. When this compensator is placed into a feedback loop, the resulting closed-loop system produces zero steady-state error to periodic disturbances or reference trajectories with frequency ω_i. Figure 2-4 illustrates the simulated controller frequency response. In (2.8), ω_i sets the resonator frequency, β adjusts the location of the zero, and the gain α controls the system bandwidth. Sievers and von Flotow [62] also provide an excellent description of this linear time-invariant (LTI) controller design. They state that this loop configuration will be stable as long as the negative of the loop transmission is phase stable ($|\angle \mathrm{L}(j\omega_i)| < 180^o$) within the bandwidth of the compensator, since the system is gain stabilized for all frequencies outside of the bandwidth.

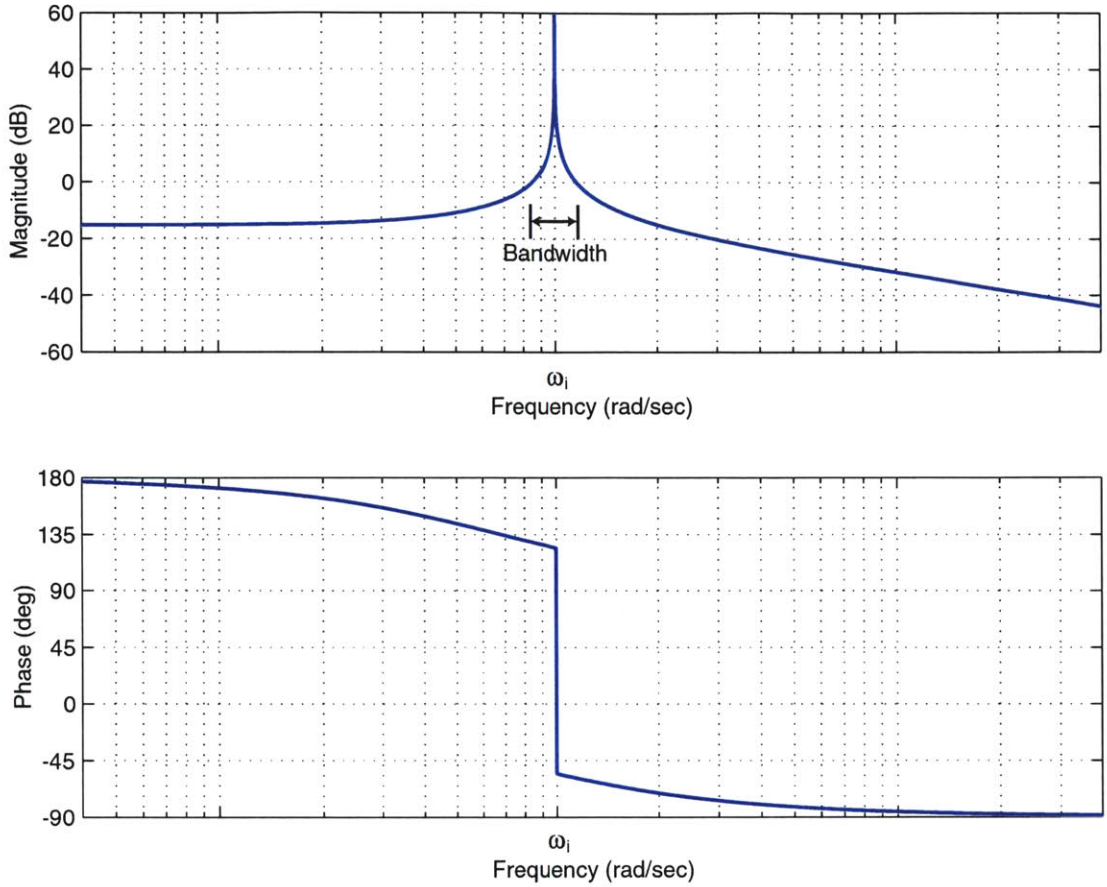

Figure 2-4: Example of the frequency response of an Internal Model Principle controller for cancelling errors with frequency ω_i.

We can maximize the robustness of the closed-loop system by selecting the location of the IMP controller zero so as to maximize the phase margin of the negative of the loop transmission. Assuming an accurate plant model, if we choose the proper value of β, root locus plots show that the departure angles of the marginally stable poles are equal to 180°. The optimal β value, derived by Messner and Bodson [24], is given by

$$\beta = \omega_i \tan(\phi_i), \tag{2.9}$$

where

$$\phi_i = \angle P(j\omega_i). \tag{2.10}$$

From a loop-shaping perspective, this means that the negative of the loop transmission has a phase margin of approximately 90° at the two magnitude crossings of unity gain in the vicinity of ω_i. Thus, the loop is robust to modelling errors in the plant phase by as much as $\pm 90^o$ before the system goes unstable. If the phase of the actual plant varies by more than $\pm 90^o$, then damping can be added to the poles of the IMP controller. This will increase the system's relative stability but the controller now violates the Internal Model Principle for reducing/eliminating constant amplitude signals with frequency ω_i. The resulting closed-loop system thus will not provide zero steady-state error. However, an IMP controller with added damping can be used to provide zero steady-state error to a different type of input signal, which we discuss in Section 2.2.3.

In diamond turning applications, the reference signal typically consists of multiple harmonics of the fundamental spindle frequency. Building on the previous results, we can place several IMP controllers in parallel to provide zero steady-state tracking error to each of the individual frequency components. Figure 2-5 illustrates the negative of the loop transmission frequency response for a controller that places ten IMP resonant controllers in parallel. The resulting closed-loop system will provide zero steady-state error for a references/disturbance signal with any combination of these ten frequency components.

Theoretically, we can add N IMP controllers in parallel to produce a closed-system which eliminates N frequency components. It is, however, not clear how to design these systems to ensure sufficient gain and phase margins. In Section 2.2.6, we present a loop-shaping approach to tuning systems with N IMP controllers in parallel that provides a rational selection process for the parameters in (2.8) to maximize the closed-loop performance and robustness.

One of the drawbacks to the IMP controller is the location of the marginally stable poles. Equation (2.8) provides infinite gain directly $s = j\omega_i$ but if the actual

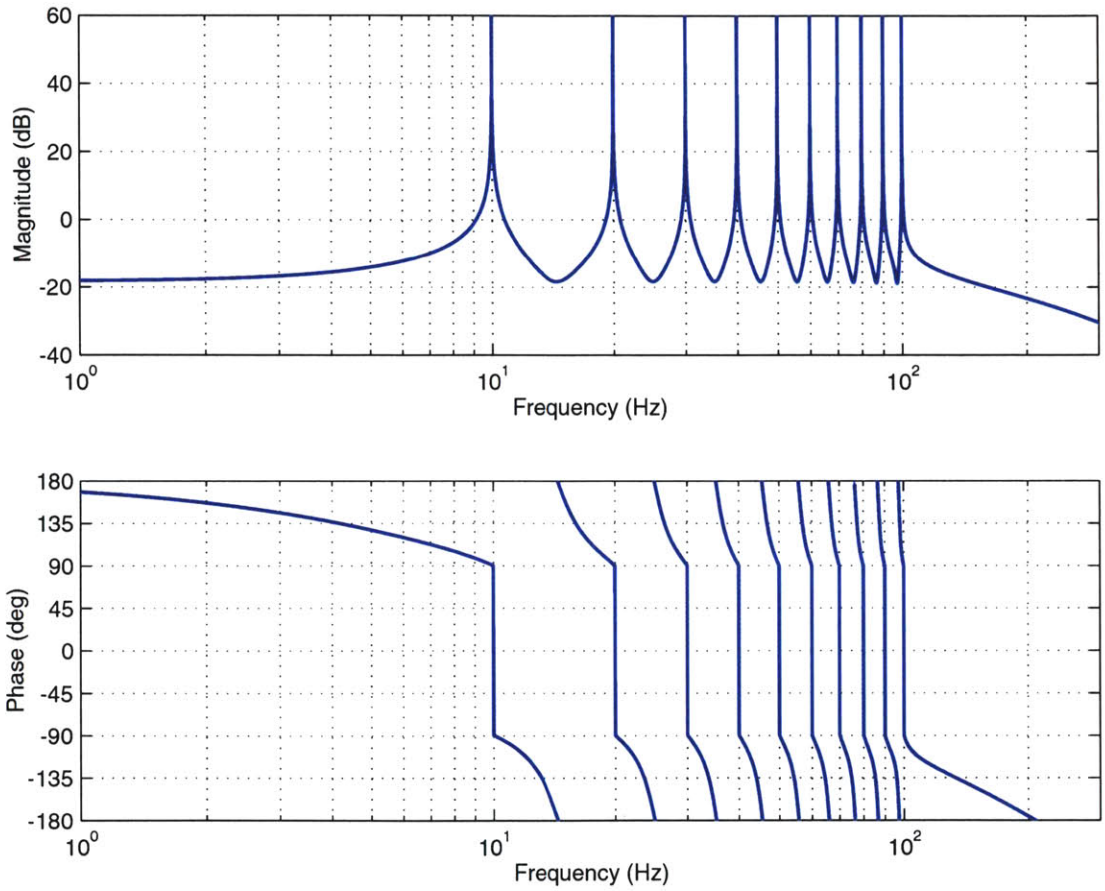

Figure 2-5: Calculated negative of the loop transmission frequency response with ten IMP controllers placed in parallel.

disturbance frequency differs from the designed value (*e.g.*, $\omega_{actual} = \omega_i \pm \epsilon$), then an undesirable steady-state error may occur. Fluctuations in the fundamental spindle rotation speed are typical in diamond turning applications. Therefore, a better controller design would continuously change the locations of the marginally stable poles to match the frequency of the disturbance signal. We can achieve this type of tracking control authority with Adaptive Feedforward Cancellation, as will be shown in Section 2.2.

Time-Delay Repetitive Control Systems

Hara *et al* [9] shows that we can generate a periodic signal with period (L) by the initial condition response of a pure time-delay in a positive feedback configuration, as shown in Figure 2-6. The resulting transfer function is given by

$$G_{TD}(s) = \frac{1}{1 + e^{-Ls}}, \tag{2.11}$$

which places an infinite number of poles on the imaginary axis at s = $j\omega_k$, where

$$\omega_k = \frac{2\pi k}{L} \qquad k = 0, \pm 1, \pm 2, \ . \ . \ . \ , \pm\infty. \tag{2.12}$$

This particular transfer function, if placed in the loop transmission of a conventional feedback system, theoretically provides zero steady-state tracking error to a signal with fundamental period (L) and its harmonics. However, since physical systems suffer from magnitude and phase shift as a function of frequency, equation (2.11) creates stability issues for the closed-loop system [10].

As mentioned previously, this pure time-delay arrangement places an infinite number of poles on the imaginary-axis. From a loop-shaping perspective, equation (2.11) yields an infinite number of narrow-band resonant peaks, as shown in Figure 2-7. This means that the resulting negative of the loop transmission will have an infinite num-

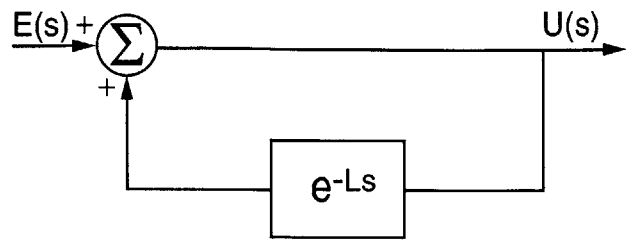

Figure 2-6: Simple repetitive controller periodic signal generator.

ber of crossover frequencies and thus is essentially impossible to stabilize. To solve this problem, Hara *et al* [9] proposed an altered repetitive controller structure with a low-pass filter q(s), as shown in Figure 2-8, where the altered repetitive controller transfer function is given by

$$G_{TD_Q}(s) = 1 + \frac{q(s)e^{-Ls}}{1 + q(s)e^{-Ls}}. \tag{2.13}$$

This controller structure increases the closed-loop stability and robustness but (2.13) violates the Internal Model Principle for constant amplitude periodic signals, since the so-called "q-filter" moves the marginally stable repetitive controller poles from the imaginary-axis into the LHP. Equation (2.13) improves the periodic trajectory following/disturbance rejection characteristics of a conventional feedback loop but G_{TD_Q}(s) will not produce zero steady-state error to a constant amplitude periodic signal. An example of a frequency response for (2.13) with a low-pass q-filter is shown in Figure 2-7. We see that the q-filter attenuates the higher frequency resonant peaks, which yields a finite number of crossover frequencies and a much easier system to stabilize.

Time-delay repetitive controllers are most practically designed and implemented in discrete-time using z-transforms, although considerable intuition can be obtained by looking at the structure in continuous-time. Moon *et al* [11] provide an excellent description of the stability and synthesis of the continuous-time time-delay algorithm

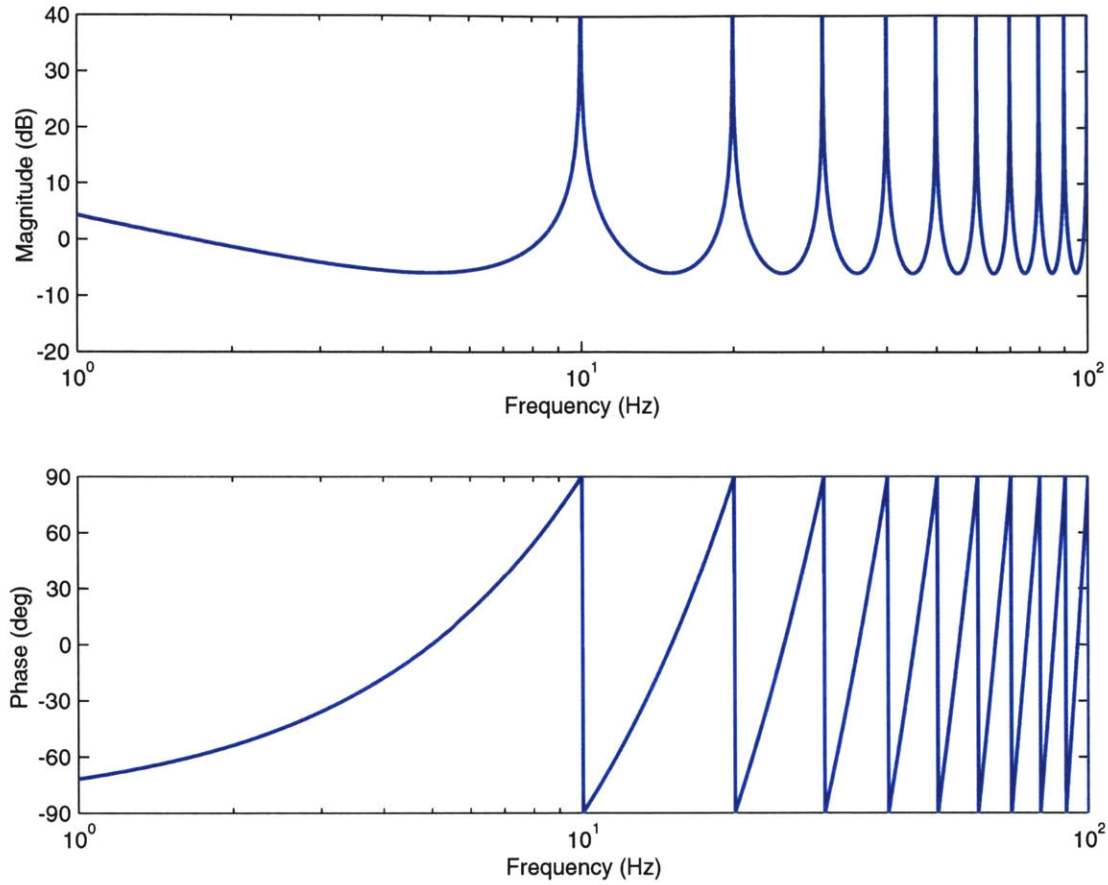

Figure 2-7: Example of a frequency response for a time-delay repetitive control system with period L = 0.1 seconds. The frequency range has been limited to only 100 Hz. The resonant peaks actually continue to s = $j\infty$.

while several variations of the discrete-time structure can be found in [12] [13] [14] and [15]. Several successful applications of time-delay repetitive controllers have been documented in the literature. Some of these examples include periodic disturbance rejection in hard disk drives [10] [11], improvements in camshaft turning [16] and diamond turning [17], and improvements in disturbance rejection for continuous casting processes [18]. A much more inclusive description of the time-delay repetitive system in continuous and discrete-time, with numerous other cited references, is presented in Ludwick [1].

The use of the low-pass filter q(s) in (2.13) increases the robustness of the closed-

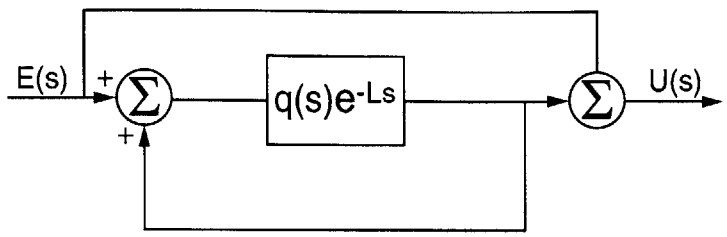

Figure 2-8: Altered repetitive controller periodic signal generator block diagram with a low-pass filter q(s).

loop system by filtering the high-frequency gain. Ideally, we would like q(s) to provide unity gain and zero degrees of phase up to the desired crossover frequency of the negative of the loop transmission, and then completely filter out any higher frequency components. The resulting closed-loop system would place N signal generators in the loop transmission, providing zero steady-state error to a selected set of N harmonics. However, such a controller structure is not practically done with a time-delay system. An even more ideal control structure would place marginally stable poles in the negative of the loop transmission directly at the frequencies contained in the reference/disturbance signal [1]. We can achieve this tailored pole placement design with Adaptive Feedforward Cancellation, as shown in the following sections.

2.2 Adaptive Feedforward Cancellation

Adaptive Feedforward Cancellation (AFC) is a form of repetitive control that can also be viewed from an adaptive control perspective, as presented in this section. Adaptive control is defined as the methodology used to control systems with known dynamic structure, but unknown constant or slowly-varying parameters [45]. Assuming a plant with transfer function P(s) has a single frequency disturbance input of the form

$$d(t) = a_i \cos(\omega_i t) + b_i \sin(\omega_i t), \tag{2.14}$$

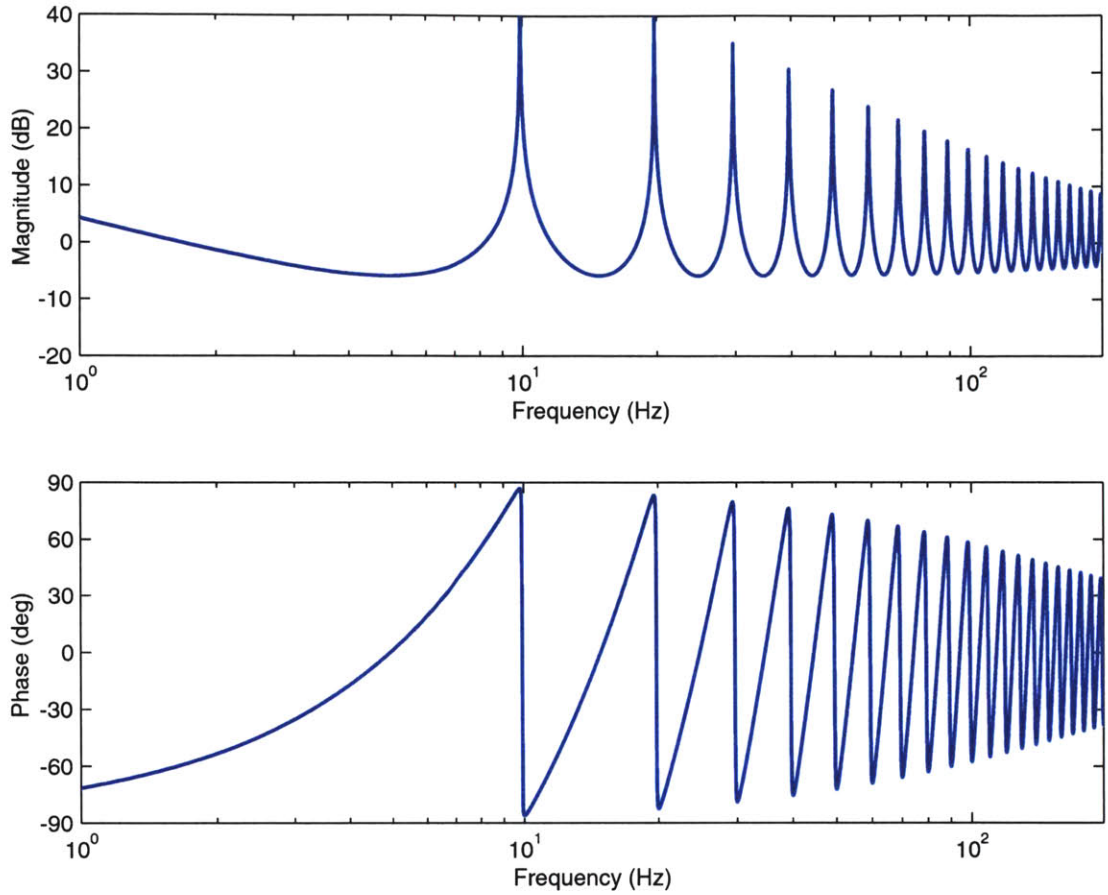

Figure 2-9: Example of a frequency response for a time-delay repetitive control system with a q-filter. The q-filter is a low-pass filter with a break frequency at 1000 rad/sec and period L = 0.1 seconds. The frequency range has been limited to only 100 Hz. The resonant peaks actually continue to s = $j\infty$ but the magnitude of the resonant peaks monotonically decrease as a function of frequency.

as shown in Figure 2-10, we want to design a controller that will reduce/eliminate the steady-state error (adapted from Bodson *et al* [20]).

The AFC algorithm creates a control output signal that adapts to the values of a_i and b_i and produces an estimate of the disturbance signal given by

$$\hat{d}(t) = \hat{a}_i(t)\cos(\omega_i t) + \hat{b}_i(t)\sin(\omega_i t), \tag{2.15}$$

which when added with an opposite sign to (2.14) effectively eliminates the distur-

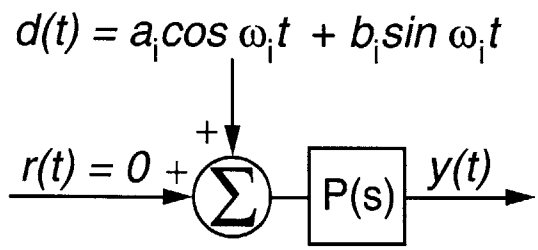

Figure 2-10: Plant transfer function P(s) with a periodic disturbance input d(t).

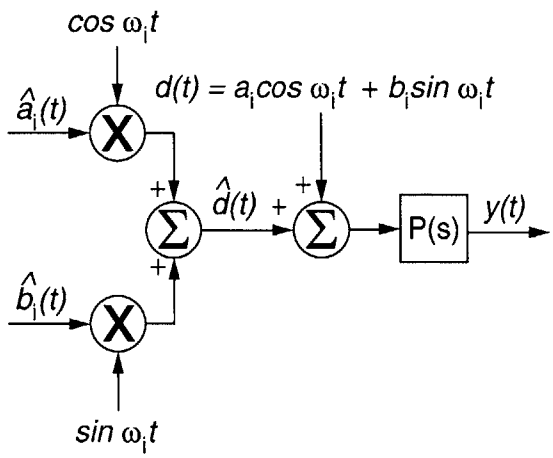

Figure 2-11: Adaptive periodic disturbance rejection block diagram. Figure adapted from Bodson *et al* [20].

bance when

$$\hat{a}_i(t) = a_i, \tag{2.16}$$

$$\hat{b}_i(t) = b_i. \tag{2.17}$$

An illustration of this in block diagram form is shown in Figure 2-11.

The main components of the Adaptive Feedforward Cancellation algorithm are the equations for estimates of the Fourier coefficients, which are based on the adaptive gradient algorithm [64]. Note, in this thesis, we restrict ourselves to discussing Adaptive Feedforward Cancellation from a continuous-time perspective. AFC is most

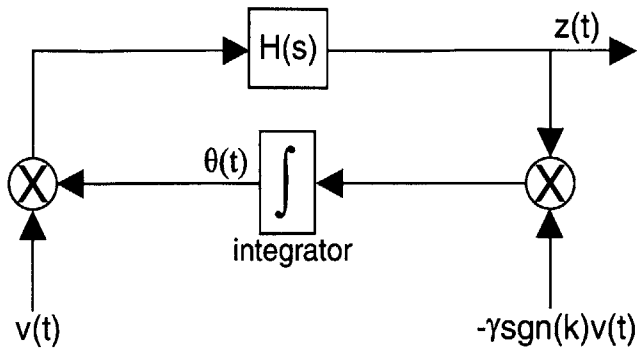

Figure 2-12: System containing a Strictly Positive Real transfer function. Figure adapted from Slotine and Li [45].

practically implemented though in discrete-time via a PC-based digital control system. The adaptive gradient algorithm, when converted into a discrete-time equivalent, is given by the least mean-squares (LMS) algorithm [64]. Some of the papers that have been published on the LMS algorithm include [60] [62] [65] [66] [67] [69] and [70], while several successful applications are shown in [22] [52] [58] and [68]. The interested reader is referred to these papers for additional details. In the following section, we use Lyapunov theory and Barbalat's Lemma [45] to derive the equations describing $\hat{a}_i(\mathrm{t})$ and $\hat{b}_i(\mathrm{t})$.

2.2.1 Derivation of the Estimates of the Fourier Coefficients

The equations for the estimates of the Fourier coefficients can be derived from Lemma (8.1) in [45]. Here, Slotine and Li consider two signals z(t) and $\theta(\mathrm{t})$, as shown in Figure 2-12, which are related by

$$z(t) = \mathrm{H}[k\theta^{\mathbf{T}}(\mathbf{t})\mathbf{v}(\mathbf{t})], \tag{2.18}$$

where $\mathrm{H}[k\theta^{\mathbf{T}}(\mathbf{t})\mathbf{v}(\mathbf{t})]$ is the Laplace transform of h(t) operating on the product of k, $\theta^{\mathbf{T}}(\mathrm{t})$, and $\mathbf{v}(\mathrm{t})$. The state-space representation of (2.18) is given by

$$\dot{\mathbf{x}} = \mathbf{A}\mathbf{x} + \mathbf{b}[\mathbf{k}\theta^{\mathbf{T}}\mathbf{v}], \tag{2.19}$$

$$\mathbf{z(t)} = \mathbf{c^T x}, \tag{2.20}$$

where k is some unknown constant with known sign and

$$\mathbf{v(t)} = \begin{bmatrix} \cos(\omega_i t) \\ \sin(\omega_i t) \end{bmatrix}, \tag{2.21}$$

$$\theta(\mathbf{t}) = \begin{bmatrix} \hat{a}_i(t) \\ \hat{b}_i(t) \end{bmatrix}. \tag{2.22}$$

If the transfer function H(s) is Strictly Positive Real (SPR), then from the Kalman-Yakubovich Lemma [45], for some symmetric positive definite (p.d.) matrix $\mathbf{Q}$, there will exist some symmetric p.d. matrix $\mathbf{P}$ such that

$$\mathbf{A^T P} + \mathbf{PA} = -\mathbf{Q}, \tag{2.23}$$

$$\mathbf{Pb} = \mathbf{c}. \tag{2.24}$$

The transfer function H(s) is a Strictly Positive Real transfer function if

$$\mathrm{Re}[\mathrm{H}(j\omega_i)] > 0 \ \ \forall\ \omega_i, \tag{2.25}$$

which is equivalent to saying

$$-90^o < \angle \mathrm{H}(j\omega_i) < 90^o \ \ \forall\ \omega_i. \tag{2.26}$$

Slotine and Li propose a p.d. Lyapunov Function of the form

$$V[\mathbf{x}, \theta] = \mathbf{x^T P x} + \frac{|\mathbf{k}|}{\gamma}\theta^{\mathbf{T}}\theta, \tag{2.27}$$

whose derivative along the trajectories of (2.19) and (2.20) is given by

$$\begin{aligned}\dot{V}[\mathbf{x},\theta] &= \mathbf{x^T(PA + A^TP)x + 2x^TPb(k\theta^Tv) - 2\theta^T(kzv)},\\ &= \mathbf{-x^TQx \leq 0}.\end{aligned} \tag{2.28}$$

If the derivative of $\theta(\mathbf{t})$ is defined as

$$\dot{\theta}(t) = -\gamma sgn(k)z(t)\mathbf{v(t)}, \tag{2.29}$$

where γ is some constant adjustable adaptive gain, then (2.18) and (2.29) imply that z(t) and $\theta(\mathbf{t})$ are globally bounded, and since $\mathbf{v(t)}$ is bounded, $\dot{\mathbf{x}}(\mathbf{t})$ is also bounded. These results imply that $\dot{V}$ is uniformly continuous, since the second derivative of V is of the form

$$\ddot{V}[\mathbf{x},\phi] = \mathbf{-2xQ\dot{x}}, \tag{2.30}$$

which is also bounded. Therefore, it can be deduced from Barbalat's Lemma [45] that

$$z(t) \rightarrow 0 \;\; as \;\; t \rightarrow \infty.$$

Substituting (2.21) and (2.22) into (2.29),

$$\dot{\theta}(t) = -\gamma sgn(k)z(t)\mathbf{v(t)} \longrightarrow \begin{bmatrix}\dot{\hat{a}}_i(t)\\ \dot{\hat{b}}_i(t)\end{bmatrix} = -\gamma\mathbf{sgn(k)z(t)}\begin{bmatrix}\cos(\omega_i t)\\ \sin(\omega_i t)\end{bmatrix}, \tag{2.31}$$

then the equations for the estimates of the Fourier coefficients are

$$\dot{\hat{a}}_i(t) = -\gamma sgn(k)z(t)\cos(\omega_i t), \tag{2.32}$$

$$\dot{\hat{b}}_i(t) = -\gamma sgn(k)z(t)\sin(\omega_i t). \tag{2.33}$$

Defining the unknown constant k in front of the modulator in Figure 2-12 as unity k = 1, redefining the output of transfer function H(s) as the plant output y(t), and redefining the adjustable adaptive gain γ as g_i, equations (2.32) and (2.33) become

$$\frac{d}{dt}\hat{a}_i(t) = -g_i y(t)\cos(\omega_i t), \tag{2.34}$$

$$\frac{d}{dt}\hat{b}_i(t) = -g_i y(t)\sin(\omega_i t). \tag{2.35}$$

Equations (2.34) and (2.35) are the well-known definitions for the estimates of the Fourier coefficients $\hat{a}_i$(t) and $\hat{b}_i$(t) used in repetitive control [6] [20] [22] [24] [25].

The top of Figure 2-13 re-illustrates the adaptive disturbance rejection block diagram from Figure 2-11, where we redefine the estimate of the disturbance signal $\hat{d}(t)$ as the AFC control output signal u(t) and label the input to the plant as

$$\delta(t) = [u(t) - d(t)]. \tag{2.36}$$

The implementation of the equations for the estimates of the Fourier coefficients in block diagram form is shown in the middle of Figure 2-13, while the bottom of Figure 2-13 illustrates the resulting AFC closed-loop system. The modulator/integrator structure in the Adaptive Feedforward Cancellation closed-loop block diagram at the bottom of the figure represents the complete AFC algorithm.

Up to this point, Adaptive Feedforward Cancellation has only been viewed as a periodic disturbance rejection control system. If we place the AFC algorithm in the forward path of the feedback loop, as shown at the bottom of Figure 2-13, the resulting closed-loop system will adapt to follow a reference and/or reject a disturbance with frequency ω_i. This particular structure forms the basis for our AFC controller design, as will be discussed in the following sections.

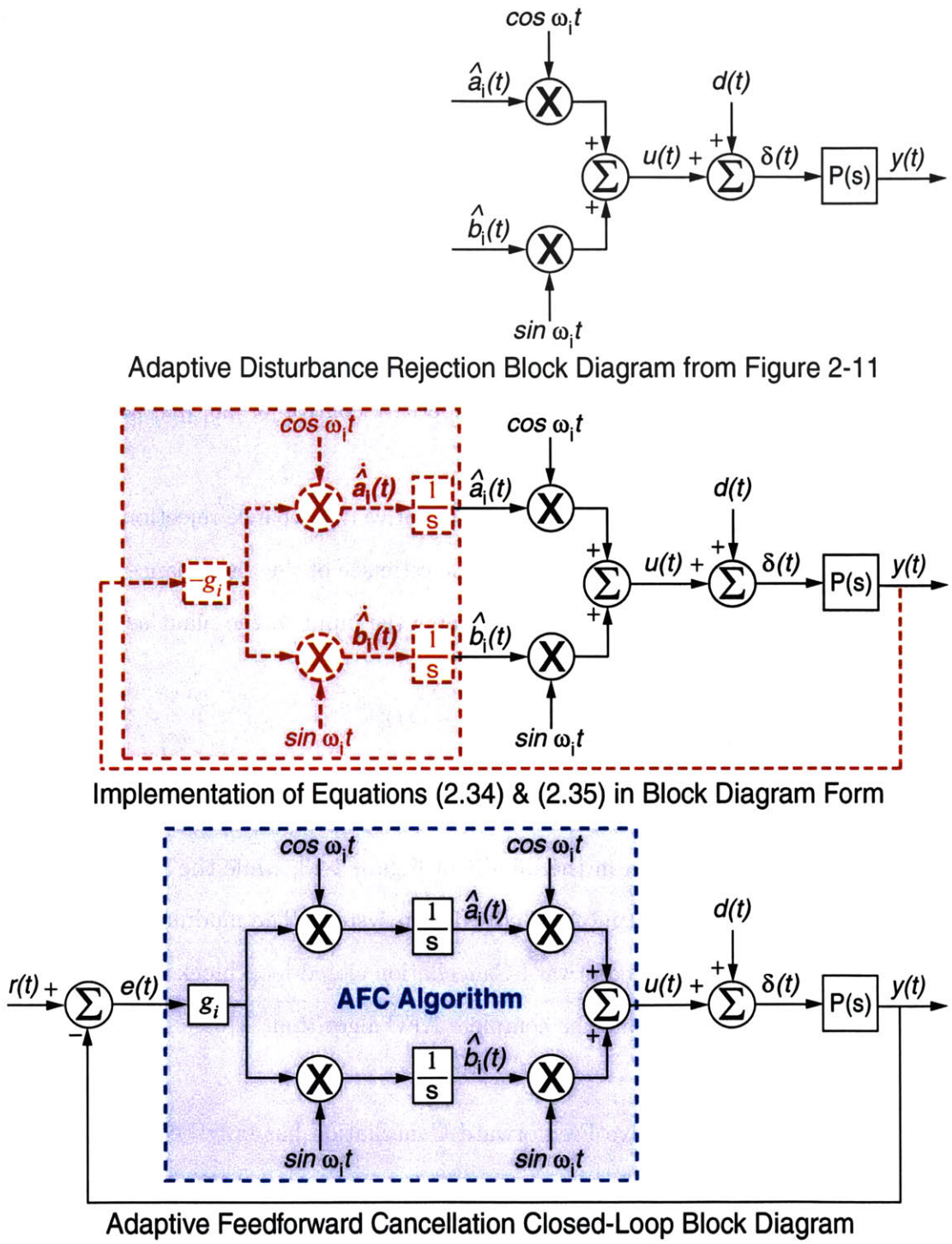

Figure 2-13: Altered adaptive disturbance rejection figure with the block diagram implementation of the equations for the estimates of the Fourier coefficients $\hat{a}_i(\mathrm{t})$ and $\hat{b}_i(\mathrm{t})$.

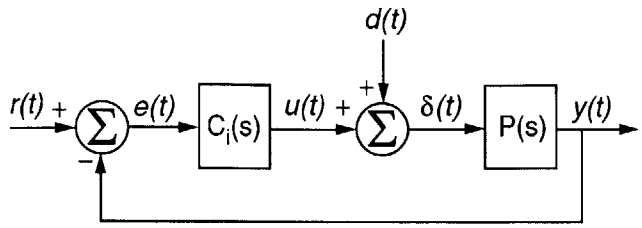

Figure 2-14: LTI equivalent single resonator AFC controller closed-loop block diagram.

2.2.2 Equivalence of the AFC Algorithm to an LTI System

The estimates of the Fourier coefficients in the AFC algorithm are described by linear time-varying (LTV) equations (see (2.34) and (2.35)) but the literature has shown that the input-output relationship from e(t) to u(t) in the block of gray at the bottom of Figure 2-13 is equivalent to a linear time-invariant (LTI) system [1] [20] [25] [53] [63]. This is a very powerful result, since it enables us to use classical control techniques (*i.e.*. Root Locus plots, Nyquist diagrams, Bode plots, gain and phase margin, etc.) to determine the closed-loop stability, robustness and performance characteristics. The resulting continuous-time AFC transfer function equals

$$C_i(s) = \frac{U(s)}{E(s)} = g_i \left[\frac{s}{s^2 + \omega_i^2} \right], \tag{2.37}$$

which includes a zero at the origin and marginally stable poles at

$$s_{1,2} = \pm j\omega_i. \tag{2.38}$$

We refer to (2.38) as a single resonator AFC controller, since the algorithm effectively places a resonator in the loop transmission with an undamped natural frequency of ω_i. As a result, $C_i(s)$ obeys the Internal Model Principle and will provide zero steady-state error to a constant amplitude periodic reference or disturbance signal with a frequency component at ω_i. Figure 2-14 illustrates the LTI equivalent single resonator

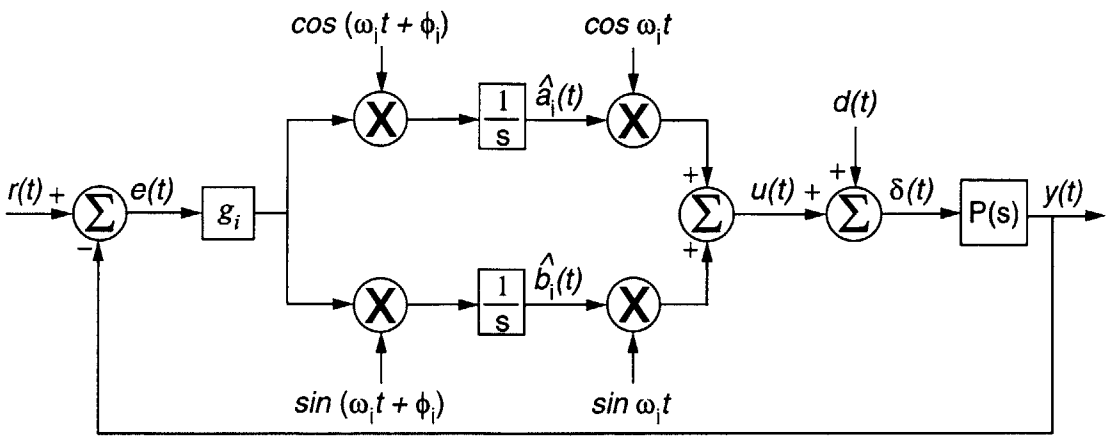

Figure 2-15: Single resonator AFC controller closed-loop block diagram with the phase advance parameter ϕ_i implemented. This system is designed to follow and/or reject a periodic signal with a single frequency component at ω_i.

AFC closed-loop block diagram.

Sacks *et al* [22] improve the robustness properties of the AFC algorithm by introducing an altered set of equations for the estimates of Fourier coefficients. They add a phase advance parameter ϕ_i to (2.34) and (2.35), which reduces the closed-loop system's sensitivity to the phase of the plant being controlled. The resulting equations are of the form

$$\frac{d}{dt}\hat{a}_i(t) = g_i e(t)\cos(\omega_i t + \phi_i), \tag{2.39}$$

$$\frac{d}{dt}\hat{b}_i(t) = g_i e(t)\sin(\omega_i t + \phi_i). \tag{2.40}$$

where the negative of the plant output -y(t) in (2.34) and (2.35) has been changed to the error signal e(t). This is due to the fact that the single resonator AFC controller is now located in the forward path of the feedback loop, where

$$e(t) = [r(t) - y(t)]. \tag{2.41}$$

The altered single resonator AFC closed-loop block diagram is shown in Figure 5-1,

where the new LTI equivalent single resonator AFC controller is

$$C_i(s) = \frac{U(s)}{E(s)} = g_i \left[\frac{s \cos \phi_i + \omega_i \sin \phi_i}{s^2 + \omega_i^2} \right]. \tag{2.42}$$

Equation (2.42) also places marginally stable poles at $s_{1,2} = \pm j\omega_i$ but the pure differentiator (zero at s=0) in (2.37) has changed into a real-axis zero located at

$$s_{zero} = -\omega_i \tan \phi_i. \tag{2.43}$$

This is a very interesting result, since (2.42) is essentially identical to the IMP controller transfer function described in Section 2.1.2. For (2.42), the choice of ϕ_i affects the closed-loop stability, while the variable gain g_i dictates the controller bandwidth, as shown in Figure 2.1.2. We expand upon these findings in the following sections.

There are several approaches to proving the LTI equivalence of the AFC algorithm with and without addition of the phase advance parameter ϕ_i. In this section, we restrict ourselves to providing the derivations of (2.37) and (2.42) through two methods that utilize the time and frequency domain.

Derivation of LTI Equivalence using the Frequency Domain Method

The following derivation uses the frequency domain and the modulation, integration, time-shifting, and frequency-shifting properties of the Laplace transform [47] to show the equivalence of the Adaptive Feedforward Cancellation algorithms in Figure 2-13 and Figure 5-1 to linear time-invariant systems. This derivation is taken from [1] but includes the addition of the phase advance parameter ϕ_i and relies heavily on [28].

We know from Section 2.2.1 that the equations for the estimates of the Fourier

coefficients for the single resonator AFC controller are

$$\frac{d}{dt}\hat{a}_i(t) = g_i e(t)\cos(\omega_i t), \tag{2.44}$$

$$\frac{d}{dt}\hat{b}_i(t) = g_i e(t)\sin(\omega_i t). \tag{2.45}$$

With the addition of the phase advance parameter ϕ_i, equations (2.44) and (2.45) become

$$\frac{d}{dt}\hat{a}_i(t) = g_i e(t)\cos(\omega_i t + \phi_i), \tag{2.46}$$

$$\frac{d}{dt}\hat{b}_i(t) = g_i e(t)\sin(\omega_i t + \phi_i). \tag{2.47}$$

Using the following Laplace transform pairs

$$\mathcal{L}\{f(t)\} = F(s), \tag{2.48}$$

$$\mathcal{L}\{f(t)e^{s_0 t}\} = F(s - s_0), \tag{2.49}$$

$$\mathcal{L}\{f(t - t_o)\} = F(s)e^{-j\omega t_o}, \tag{2.50}$$

and Euler's formulas

$$e^{\pm j\theta} = \cos\theta \pm j\sin\theta, \tag{2.51}$$

$$\cos(\omega_i t) = \left(\frac{e^{j\omega_i t} + e^{-j\omega_i t}}{2}\right), \tag{2.52}$$

$$\sin(\omega_i t) = \left(\frac{e^{j\omega_i t} - e^{-j\omega_i t}}{2j}\right), \tag{2.53}$$

the Laplace transform of the sine and cosine modulators with the phase advance

parameter ϕ_i are given by

$$\cos(\omega_i t + \phi_i) = \frac{e^{j\phi_i}}{2} e^{j\omega_i t} + \frac{e^{-j\phi_i}}{2} e^{-j\omega_i t}, \tag{2.54}$$

$$\sin(\omega_i t + \phi_i) = \frac{e^{j\phi_i}}{2j} e^{j\omega_i t} - \frac{e^{-j\phi_i}}{2j} e^{-j\omega_i t}. \tag{2.55}$$

Thus, the Laplace transforms of the estimates of the Fourier coefficients $\hat{a}_i$(t) and $\hat{b}_i$(t) are

$$\hat{A}_i(s) = \frac{g_i e^{j\phi_i}}{2} \frac{E(s - j\omega_i)}{s} + \frac{g_i e^{-j\phi_i}}{2} \frac{E(s + j\omega_i)}{s}, \tag{2.56}$$

$$\hat{B}_i(s) = \frac{g_i e^{j\phi_i}}{2j} \frac{E(s - j\omega_i)}{s} - \frac{g_i e^{-j\phi_i}}{2j} \frac{E(s + j\omega_i)}{s}. \tag{2.57}$$

The output of the single resonator AFC controller is of the form

$$u(t) = \hat{d}(t) = \hat{a}_i(t)\cos(\omega_i t) + \hat{b}_i(t)\sin(\omega_i t), \tag{2.58}$$

where the Laplace transform is

$$U(s) = \frac{\hat{A}_i(s - j\omega_i)}{2} + \frac{\hat{A}_i(s + j\omega_i)}{2} + \frac{\hat{B}_i(s - j\omega_i)}{2j} - \frac{\hat{B}_i(s + j\omega_i)}{2j}. \tag{2.59}$$

Substituting (2.56) and (2.57) into (2.59) yields

$$\begin{aligned} U(s) = \frac{g_i}{4} \Bigg[& e^{j\phi_i} \frac{E(s - 2j\omega_i)}{s - j\omega_i} + e^{j\phi_i} \frac{E(s)}{s + j\omega_i} + e^{-j\phi_i} \frac{E(s)}{s - j\omega_i} + e^{-j\phi_i} \frac{E(s + 2j\omega_i)}{s + j\omega_i} \\ - & e^{j\phi_i} \frac{E(s - 2j\omega_i)}{s - j\omega_i} + e^{j\phi_i} \frac{E(s)}{s + j\omega_i} + e^{-j\phi_i} \frac{E(s)}{s - j\omega_i} - e^{-j\phi_i} \frac{E(s + 2j\omega_i)}{s + j\omega_i} \Bigg], \end{aligned} \tag{2.60}$$

which can be simplified to

$$U(s) = \frac{g_i}{2} \left[\frac{e^{j\phi_i}}{s + j\omega_i} + \frac{e^{-j\phi_i}}{s - j\omega_i} \right] E(s). \tag{2.61}$$

Equation (2.61) can be rearranged to have a common denominator of the form

$$U(s) = \frac{g_i}{2}\left[\frac{e^{j\phi_i}(s - j\omega_i) + e^{-j\phi_i}(s + j\omega_i)}{(s + j\omega_i)(s - j\omega_i)}\right] E(s), \tag{2.62}$$

and after grouping like terms

$$U(s) = \frac{g_i}{s^2 + \omega_i^2}\left[s\left(\frac{e^{j\phi_i} + e^{-j\phi_i}}{2}\right) + \omega_i\left(\frac{e^{j\phi_i} - e^{-j\phi_i}}{2j}\right)\right] E(s). \tag{2.63}$$

Using Euler's formulas again, the transfer function describing the input-output relationship of the single resonator AFC controller with the phase advance parameter ϕ_i equals

$$\frac{U(s)}{E(s)} = g_i\left[\frac{s\cos\phi_i + \omega_i \sin\phi_i}{s^2 + \omega_i^2}\right]. \tag{2.64}$$

To determine the input-output relationship of the single resonator AFC controller without the addition of the phase advance parameter, we set $\phi_i = 0$ and (2.64) becomes

$$\frac{U(s)}{E(s)} = g_i\left[\frac{s}{s^2 + \omega_i^2}\right]. \tag{2.65}$$

Derivation of LTI Equivalence using the Time Domain Method

The following derivation uses the time domain and the definition of the convolution integral to show the equivalence of the Adaptive Feedforward Cancellation algorithms in Figures 2-13 and 5-1 to linear time-invariant systems. This work also relies heavily on [28].

Looking at Figure 5-1, the signals entering the integrators are

$$g_i e(t)\cos(\omega_i t + \phi_i), \tag{2.66}$$

$$g_i e(t)\sin(\omega_i t + \phi_i), \tag{2.67}$$

and the linear time-varying estimates of the Fourier coefficients $\hat{a}_i(\mathrm{t})$ and $\hat{b}_i(\mathrm{t})$ are of

the form

$$\hat{a}_i(t) = \int_0^t g_i e(\tau) \cos(\omega_i \tau + \phi_i) \, d\tau, \tag{2.68}$$

$$\hat{b}_i(t) = \int_0^t g_i e(\tau) \sin(\omega_i \tau + \phi_i) \, d\tau. \tag{2.69}$$

For this dervation, we assume that the integrators begin with zero initial conditions. The AFC control output $u(t)$ is the summation of the estimates of the Fourier coefficients modulated by sinusoids. Therefore, substituting (2.68) and (2.69) into (2.58) yields

$$u(t) = \left(\int_0^t g_i e(\tau) \cos(\omega_i \tau + \phi_i) \, d\tau \right) \cos \omega_i t + \left(\int_0^t g_i e(\tau) \sin(\omega_i \tau + \phi_i) \, d\tau \right) \sin \omega_i t. \tag{2.70}$$

Equation (2.70) can be rearranged into the form

$$u(t) = g_i \int_0^t e(\tau) \left[\cos(\omega_i \tau + \phi_i) \cos \omega_i t + \sin(\omega_i \tau + \phi_i) \sin \omega_i t \right] \, d\tau, \tag{2.71}$$

and using the trigonometric identity

$$\cos(\alpha \pm \beta) = \cos \alpha \cos \beta \mp \sin \alpha \sin \beta, \tag{2.72}$$

this reduces to

$$u(t) = g_i \int_0^t e(\tau) \cos(\omega_i [t - \tau] - \phi_i) \, d\tau. \tag{2.73}$$

The definition of the convolution integral equals

$$x(t) * h(t) = \int_{-\infty}^{+\infty} x(\tau) h(t - \tau) \, d\tau. \tag{2.74}$$

Thus, the output of the single resonator AFC controller in (2.73) can be reduced to

$$u(t) = g_i \int_0^t e(\tau)\cos(\omega_i[t-\tau] - \phi_i)\ d\tau = g_i\left[e(t) * \cos(\omega_i t - \phi_i)\right]. \tag{2.75}$$

Taking the Laplace transform of both sides of (2.75), noting that convolution in the time domain corresponds multiplication in the frequency domain, yields

$$U(s) = g_i E(s)\frac{s\cos\phi_i + \omega\sin\phi_i}{s^2+\omega_i^2} \longrightarrow \frac{U(s)}{E(s)} = g_i\left[\frac{s\cos\phi_i + \omega\sin\phi_i}{s^2+\omega_i^2}\right]. \tag{2.76}$$

Without the implementation of the phase advance parameter (*i.e.*. $\phi_i = 0$), equation (2.76) becomes

$$\frac{U(s)}{E(s)} = g_i\left[\frac{s}{s^2+\omega_i^2}\right]. \tag{2.77}$$

2.2.3 Phase Advance Parameter ϕ_i

It has been shown that the single resonator AFC controller without the phase advance parameter ϕ_i is exponentially stable for all resonator frequencies if the plant transfer function is SPR [22]. However, when the plant transfer function P(s) is non-SPR, the closed-loop system as shown in Figure 2-13 will only be stable for resonators frequencies where

$$-90^o < \angle \mathrm{P}(j\omega_i) < 90^o. \tag{2.78}$$

Sacks *et al* [22] prove this result through an averaging analysis. For an open-loop stable plant and sufficiently small g_i levels, they show that the single resonator AFC closed loop-system without the phase advance parameter will be stable if

$$\mathrm{Re}[\mathrm{P}(j\omega_i)] > 0. \tag{2.79}$$

resonator AFC closed-loop system to the phase of the plant being controlled. In the following sections, we study the effects ϕ_i has on single resonator AFC systems. We begin our analysis by examining the methods in which ϕ_i can be implemented. Next, we study the effects ϕ_i has on the pole-zero plot and frequency response of the single resonator AFC controller. Finally, we determine the choice of ϕ_i that maximizes the system phase margin. Note, the majority of the work presented herein is discussed by Byl *et al* [6] but is presented again here for completeness. This work is followed by demonstrating related results for multi-resonator systems.

Methods of Implementation

We can increase the robustness of the single resonator AFC closed-loop system by adding a phase advance parameter to the AFC algorithm. One method of implementation involves time shifting the first sine and cosine modulators by ϕ_i, as shown in Figure 5-1. This particular arrangement provides the desired control output signal but the phase advance parameter creates a synchronous modulation/demodulation configuration which requires generating phase shifted sines and cosines. We can avoid this additional computation by implementing ϕ_i through a rotation matrix, as was done for example in the works of McHugh and Shaw [51] and Shaw and Albion [52] for use in the Higher Harmonic Control algorithm. Tamisier [35] also utilized a rotation matrix to provide synchronous unbalance cancellation control to an Active Magnetic Bearing system on an air turbine compressor. Both of these systems are essentially equivalent to the Adaptive the Feedforward Cancellation algorithm. The reader is referred to Section 1.3.2 for a background on both of these approaches.

Figure 2-17 illustrates a self-tuning frequency following algorithm that Scribner *et al* describe for the isolation of machinery noise from resonant substructures [61].

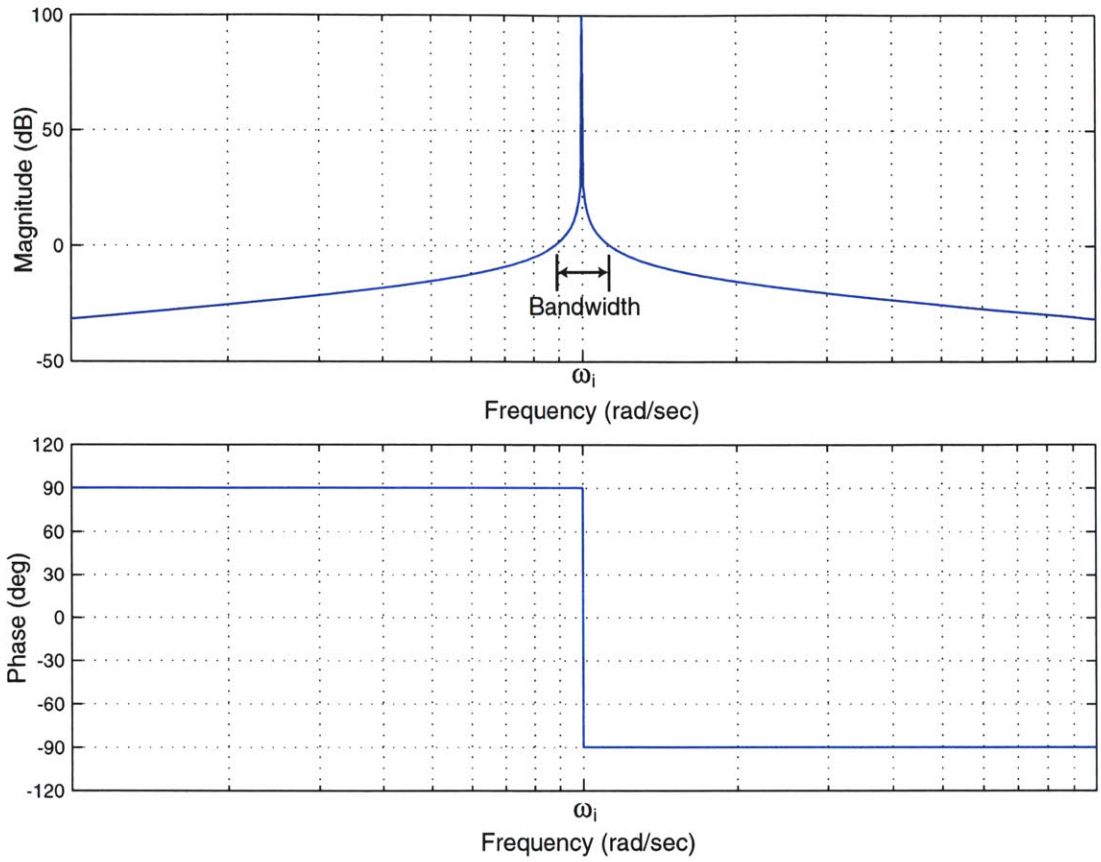

Figure 2-16: Example of a frequency response for a single resonator AFC controller without the phase advance parameter ϕ_i.

This can also be interpreted by looking at the frequency response of (2.37), as shown in Figure 2-16. Assuming the plant transfer function has unity DC gain and a monotonically decreasing magnitude as a function of frequency, the phase of the plant only has to fulfil the requirements of (2.78) over the bandwidth of the single resonator AFC controller. In other words, the negative of loop transmision only requires a positive phase margin over the frequencies of the compensator bandwidth. Outside of this narrow frequency band, the system is gain-stabilized.

Most physical systems are non-SPR. Thus, care must be taken to make sure the dynamics of the plant do not cause loop instability problems. The implementation of the phase advance parameter, however, greatly increases the robustness of the single

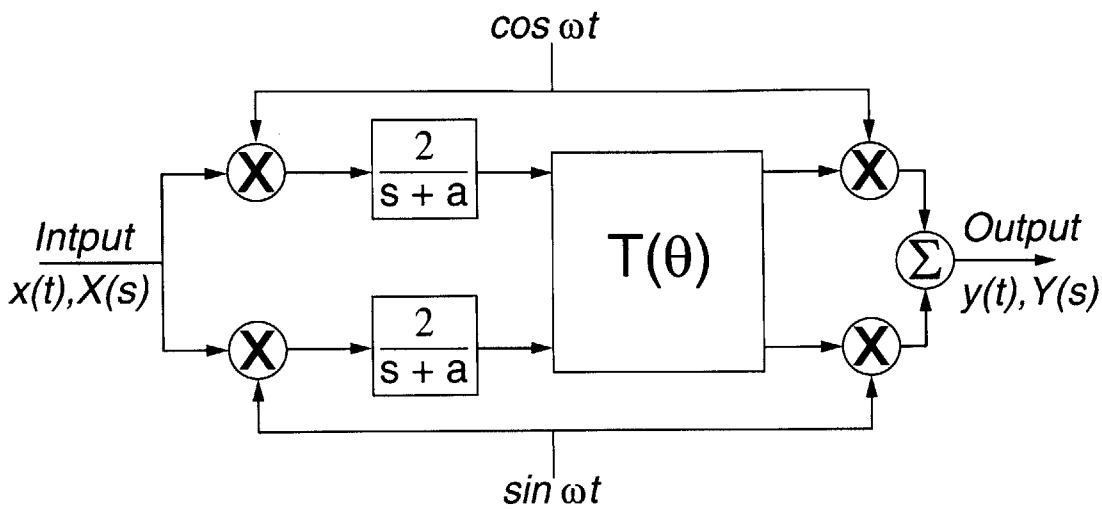

Figure 2-17: Frequency following compensator: x, input signal: y, output signal; s, Laplace variable: a, corner frequency of low-pass filter: ω, reference frequency; $T(\theta)$, rotation matrix. Figure adapted from Scribner *et al* [61].

With a rotation matrix of the form

$$\mathbf{T}(\theta) = \begin{bmatrix} \cos\theta & -\sin\theta \\ \sin\theta & \cos\theta \end{bmatrix}, \tag{2.80}$$

the frequency following algorithm's LTI equivalent transfer function is given by

$$\frac{Y(s)}{X(s)} = \left[\frac{(s+a)\cos\theta + \omega\sin\theta}{(s+a)^2 + \omega_i^2}\right]. \tag{2.81}$$

Equation (2.81) places poles at

$$s_{1,2} = -a \pm j\omega_i, \tag{2.82}$$

and a zero at

$$s_{zero} = -\left[a \pm \omega\tan\theta\right]. \tag{2.83}$$

We see that this controller is also equivalent to the single resonator AFC controller

in (2.42), except the integrators have been changed into low-pass filters. Ludwick [1] refers to this particular configuration as Adaptive Feedforward Cancellation with finite damping. According to the Internal Model Principle, equation (2.81) will provide zero steady-state tracking error to a system with exponentially decaying sinusoidal inputs.

Extending these results, we observe that the phase advance parameter ϕ_i can be implemented in the AFC algorithm through a rotation matrix of the form

$$\mathbf{R}(\phi_i) = \begin{bmatrix} \cos\phi_i & -\sin\phi_i \\ \sin\phi_i & \cos\phi_i \end{bmatrix}. \tag{2.84}$$

Figure 2-18 compares the phase advance parameter implementation by using the time shifting and rotation matrix method. The equations for the estimates of the Fourier coefficients from the rotation matrix approach are given by

$$\frac{d}{dt}\hat{a}_i(t) = [\alpha_i \cos(\omega_i t)\cos\phi_i - \beta_i \sin(\omega_i t)\sin\phi_i], \tag{2.85}$$

$$\frac{d}{dt}\hat{b}_i(t) = [\alpha_i \cos(\omega_i t)\sin\phi_i + \beta_i \sin(\omega_i t)\cos\phi_i]. \tag{2.86}$$

We know from Figure 2-18 that

$$\alpha_i = \beta_i = g_i e(t), \tag{2.87}$$

and substituting (2.87) into (2.85) and (2.86) gives

$$\frac{d}{dt}\hat{a}_i(t) = g_i e(t)\,[\cos(\omega_i t)\cos\phi_i - \sin(\omega_i t)\sin\phi_i], \tag{2.88}$$

$$\frac{d}{dt}\hat{b}_i(t) = g_i e(t)\,[\cos(\omega_i t)\sin\phi_i + \sin(\omega_i t)\cos\phi_i]. \tag{2.89}$$

Using the trigonometric identities

$$\cos(\alpha \pm \beta) = \cos\alpha\cos\beta \mp \sin\alpha\sin\beta, \tag{2.90}$$

$$\sin(\alpha \pm \beta) = \sin\alpha\cos\beta \pm \cos\alpha\sin\beta, \tag{2.91}$$

these reduce to

$$\frac{d}{dt}\hat{a}_i(t) = g_i e(t)\cos(\omega_i t + \phi_i), \tag{2.92}$$

$$\frac{d}{dt}\hat{b}_i(t) = g_i e(t)\sin(\omega_i t + \phi_i). \tag{2.93}$$

We see that (2.92) and (2.93) are equivalent to the equations for $\hat{a}_i$(t) and $\hat{b}_i$(t) derived with the time shifting approach (see Section 2.2.2) and thus the rotation matrix creates the same effect as time shifting the sine and cosine modulators.

Effect on the Pole-Zero Plot and Frequency Response

As shown previously in Section 2.2.2, the LTI equivalent transfer function of the single resonator AFC controller with the phase advance parameter is

$$C_i(s) = \frac{U(s)}{E(s)} = g_i\left[\frac{s\cos\phi_i + \omega_i\sin\phi_i}{s^2 + \omega_i^2}\right]. \tag{2.94}$$

The choice of ϕ_i affects the closed-loop stability by setting the location of the AFC real-axis zero located at

$$s_{zero} = -\omega_i\tan\phi_i. \tag{2.95}$$

Figure 2-19 illustrates the effect the phase advance parameter has on the zero location as ϕ_i is varied between $-\frac{\pi}{2}$ and $\frac{\pi}{2}$ and resonator frequency is set equal to $\omega_i = 20\pi$ rad/sec. We see that when $-\frac{\pi}{2} < \phi_i < 0$, the AFC controller produces a real-axis RHP zero. If $-\frac{3\pi}{2} < \phi_i < -\pi$, the AFC zero is also placed in the RHP, but the resulting

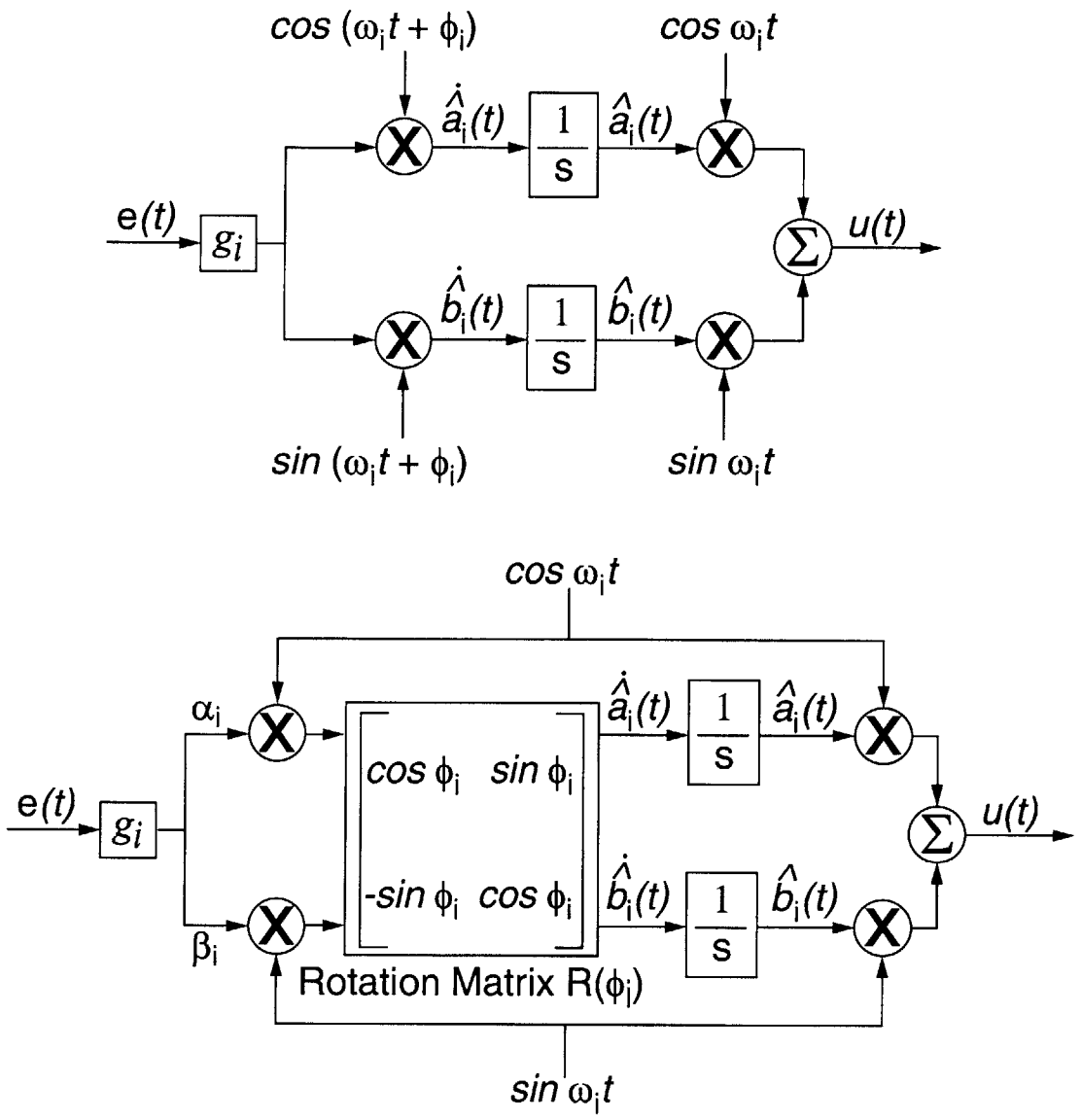

Figure 2-18: Comparison of the single resonator AFC controller with the phase advance parameter ϕ_i implemented through the time shifting (top) and an equivalent technique utilizing a rotation matrix $R(\phi_i)$ (bottom).

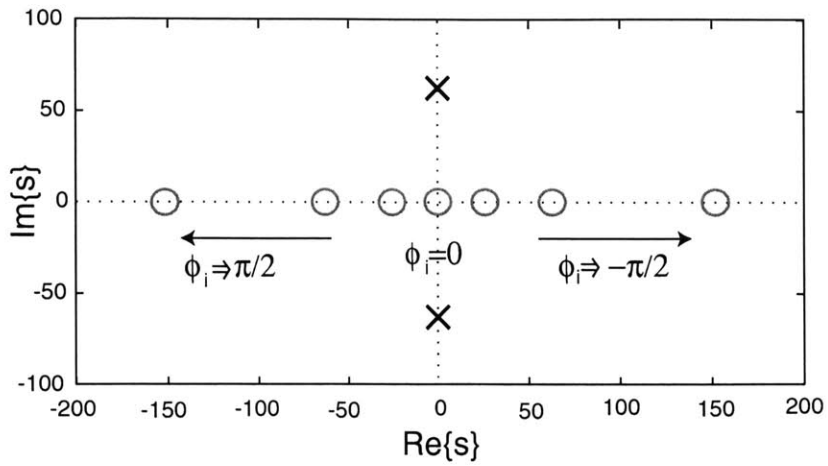

Figure 2-19: Pole-zero map of a single resonator AFC controller as the phase advance parameter is varied between $-\frac{\pi}{2} < \phi_i < \frac{\pi}{2}$. Figure adapted from Byl *et al* [6].

feedback of the closed-loop system is effectively positive, since the coefficient of the linear term in the transfer function is negative [6]. When $0 < \phi_i < \frac{\pi}{2}$, the AFC zero rests on the LHP real-axis. Finally, if $-\pi < \phi_i < -\frac{\pi}{2}$, the zero also rests in the LHP, but the resulting AFC algorithm once again creates a positive feedback system.

It seems counter intuitive to use a compensator that produces positive feedback and results in a RHP zero. However, for appropriately chosen g_i values, these results actually improve the stability, robustness, and performance of single resonator AFC closed-loop systems. A summary of the possible AFC zero locations is illustrated in Figure 2-20, while Section 2.2.4 provides single resonator AFC controller examples where the phase of the plant is in the fourth and third quadrant.

The corresponding frequency responses for $-\frac{\pi}{2} < \phi_i < 0$ and $0 < \phi_i < \frac{\pi}{2}$ are shown in Figure 2-21 and Figure 2-22 . We see that as ϕ_i is varied between $-\frac{\pi}{2}$ and $\frac{\pi}{2}$, the shapes of the Bode magnitude and phase curve are noticeably affected. First, we analyze the effects ϕ_i has on the magnitude curve. For $-\frac{\pi}{2} < \phi_i < \frac{\pi}{2}$, the slope of the Bode magnitude curve changes before and after the resonator frequency.

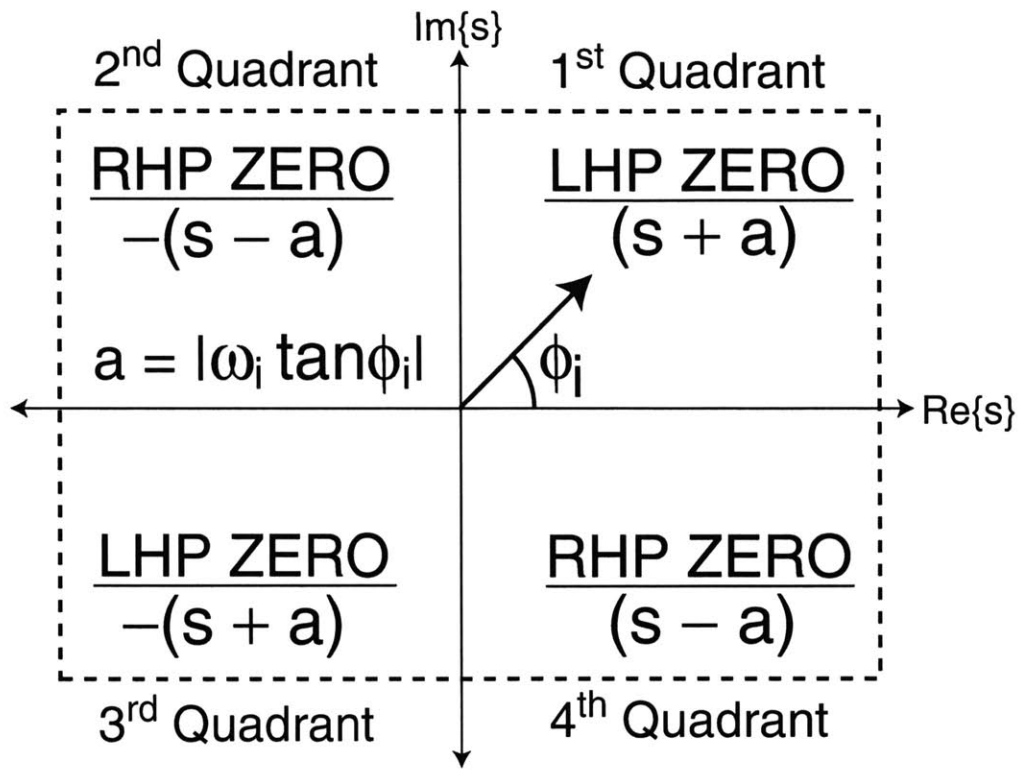

Figure 2-20: Illustration of the locations of the AFC zero as the phase advance parameter is varied between $0 < \phi_i < 2\pi$. The AFC zero is located in the LHP when ϕ_i is placed in the 1st or 3rd quadrant. When ϕ_i is in the 2nd of 4th quadrant, the AFC zero rests in the RHP. Along the same lines, when ϕ_i is located in the 2nd or 3rd quadrant, the AFC algorithm effectively creates a positive feedback system.

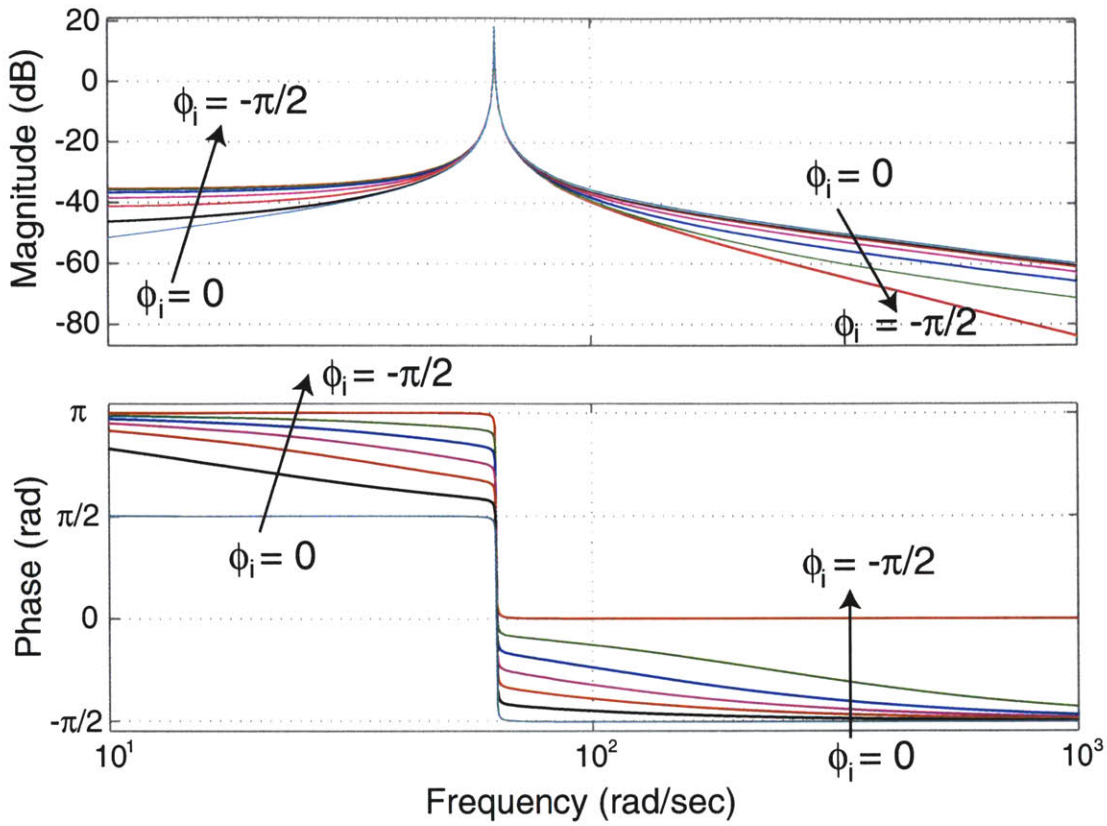

Figure 2-21: Bode plot illustrating the effect the phase advance parameter has on the single resonator AFC controller for $-\frac{\pi}{2} < \phi_i < 0$. The resonant peak is centered on $\omega_i = 62.8$ rad/sec (10 Hz). Figure adapted from Byl *et al* [6].

However, it appears that ϕ_i has a negligible effect on the shape of the AFC resonant peak. We confirm this intuition by perturbing (2.94) about ω_i, following an approach presented in Byl *et al* [6].

Defining the perturbed resonator frequency as

$$\omega_\epsilon = \omega_i(1 + \epsilon), \tag{2.96}$$

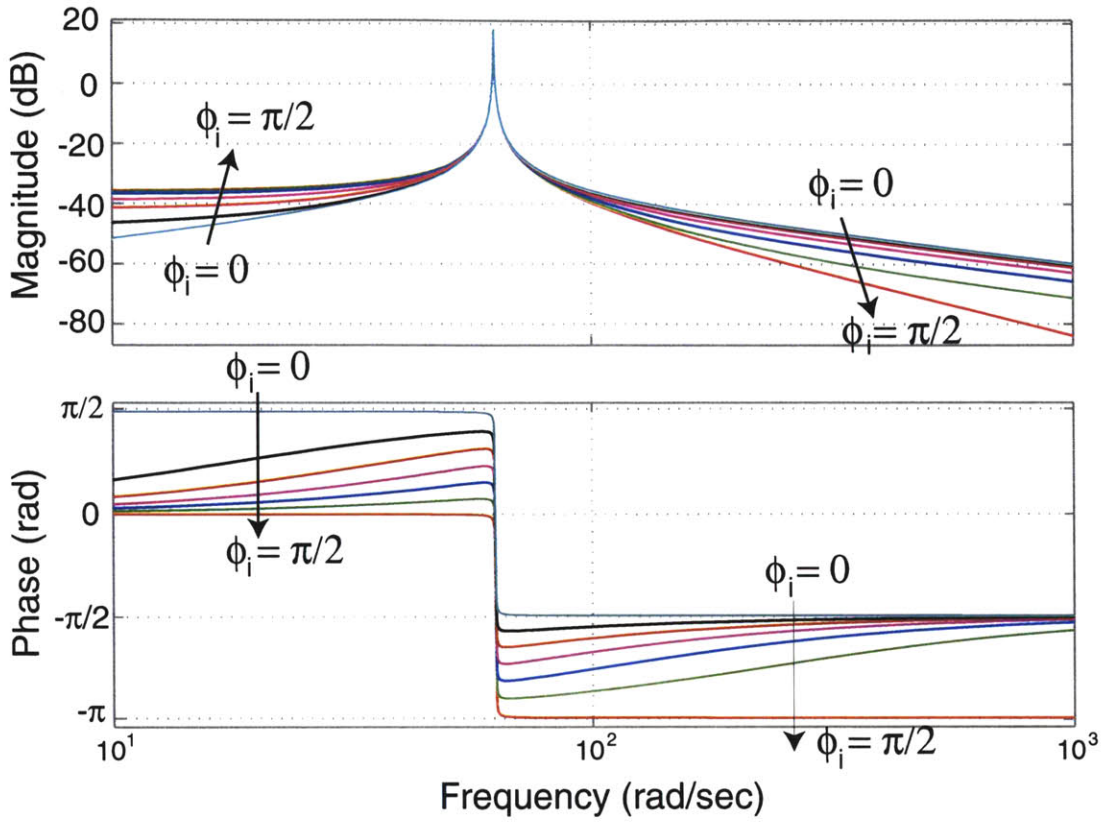

Figure 2-22: Bode plot illustrating the effect the phase advance parameter has on the single resonator AFC controller for $0 < \phi_i < \frac{\pi}{2}$. The resonant peak is centered on ω_i = 62.8 rad/sec (10 Hz). Figure adapted from Byl *et al* [6].

the magnitude of the single resonator AFC controller at s = $j\omega_\epsilon$ is given by

$$\begin{aligned} |C_i(j\omega_\epsilon)| &= g_i \left| \frac{\omega_i(1+\epsilon)\cos\phi_i + \omega_i \sin\phi_i}{s^2 - (1+\epsilon)^2\omega_i^2} \right|, \\ &= g_i \frac{\omega_i \sqrt{(1+2\epsilon+\epsilon^2)\cos^2\phi_i + \sin^2\phi_i}}{|\omega_i^2(2\epsilon+\epsilon^2)|}. \end{aligned} \tag{2.97}$$

Performing a first order approximation, we drop the ϵ^2 terms and (2.97) becomes

$$|C_i(j\omega_\epsilon)| \approx g_i \frac{\omega_i \sqrt{(1+2\epsilon)\cos^2\phi_i + \sin^2\phi_i}}{2\omega_i^2|\epsilon|}. \tag{2.98}$$

Using the following trigonometric relationship

$$\sin^2\theta + \cos^2\theta = 1, \tag{2.99}$$

the term inside the square root in the numerator of (2.98) reduces to

$$\begin{aligned}(1+2\epsilon)\cos^2\phi_i + \sin^2\phi_i &= 2\epsilon\cos^2\phi_i + \cos^2\phi_i + \sin^2\phi_i, \\ &= 2\epsilon\cos^2\phi_i + 1, \end{aligned} \tag{2.100}$$

Substituting (2.99) into (2.98) yields

$$|C_i(j\omega_\epsilon)| \approx g_i \frac{\omega_i\sqrt{1+2\epsilon\cos^2\phi_i}}{2\omega_i^2|\epsilon|}. \tag{2.101}$$

Next, we consider the approximation

$$\sqrt{1+\Delta} \approx \left(1+\frac{\Delta}{2}\right) \quad \text{for} \quad \Delta \ll 1. \tag{2.102}$$

As a result,

$$\begin{aligned}|C_i(j\omega_\epsilon)| &\approx g_i\left(\frac{1}{2\omega_i|\epsilon|} + \frac{\epsilon\cos^2\phi_i}{|\epsilon|\omega_i}\right), \\ &\approx g_i\left(\frac{1}{2\omega_i|\epsilon|} + sgn(\epsilon)\frac{\cos^2\phi_i}{\omega_i}\right), \end{aligned} \tag{2.103}$$

which reduces to

$$|C_i(j\omega_\epsilon)| \approx \left(\frac{g_i}{2\omega_i|\epsilon|}\right) \quad \text{for} \quad |\epsilon| \ll 1. \tag{2.104}$$

Thus, equation (2.104) confirms the observation that the magnitude of the single resonator AFC controller, in the vicinity of ω_i, is unaffected by the choice of ϕ_i.

The variation of the phase advance parameter between $-\frac{\pi}{2}$ and $\frac{\pi}{2}$ has a greater ef-

fect on the Bode phase curve of the single resonator AFC controller. We see that if $-\frac{\pi}{2} < \phi_i < 0$, the AFC zero is placed into the RHP and $\angle C_i(j\omega) = 0^o$ for $\omega = 0$ rad/sec. As the frequency increases, the phase curve decreases to $(\frac{\pi}{2} - \phi_i)$ as $\omega \longrightarrow \omega_i$. At the resonator frequency, $\angle C_i(j\omega)$ drops by π to $(-\phi_i - \frac{\pi}{2})$ and asymptotically approaches $-\frac{\pi}{2}$ as $\omega \longrightarrow \infty$. Similarly, when $-\frac{\pi}{2} < \phi_i < 0$, the AFC zero rests in the LHP and $\angle C_i(j\omega) = 0^o$ for $\omega = 0$ rad/sec. As the frequency increases, the phase curve increases to $(\frac{\pi}{2} - \phi_i)$ as $\omega \longrightarrow \omega_i$. At the resonator frequency, $\angle C_i(j\omega)$ drops by π to $(-\phi_i - \frac{\pi}{2})$ and also asymptotically approaches $-\frac{\pi}{2}$ as $\omega \longrightarrow \infty$.

Choice of Phase Advance Parameter

Since the Adaptive Feedforward Cancellation algorithm is equivalent to an LTI system, we can view the single resonator AFC closed-loop system from a classical controls perspective to determine the choice of ϕ_i that will maximize the closed-loop system's stability, performance, and robustness to variations in system parameters. Messner and Bodson [24] state that ϕ_i should be selected as the phase of the plant at the resonator frequency

$$\phi_i = \angle P(j\omega_i). \tag{2.105}$$

We confirm these results from choosing the phase advance parameter to maximize the phase margin of the negative of the loop transmission. Reviewing the effects the phase advance parameter has on the single resonator AFC controller, as shown in Figure 2-21 and Figure 2-22, we see that the $-\pi$ phase discontinuity is always centered on $-\phi_i$. We prove this mathematically by analyzing the phase of (2.94), again following an approach presented in Byl *et al* [6].

If we define the transfer function for the single resonator controller as

$$C_i(s) = g_i \left[\frac{s\cos\phi_i + \omega_i \sin\phi_i}{s^2 + \omega_i^2} \right] = g_i \left[\frac{N(s)}{D(s)} \right], \tag{2.106}$$

then the phase of (2.106) evaluated at s = $j\omega_i$ is given by

$$\angle C_i(j\omega_i) = \angle N(j\omega_i) - \angle D(j\omega_i). \tag{2.107}$$

The transfer function for the numerator of (2.106) evaluated at s = $j\omega_i$ is

$$\begin{aligned} N(j\omega_i) &= j\omega_i \cos\phi_i + \omega_i \sin\phi_i = j\omega_i(\cos\phi_i - j\sin\phi_i), \\ &= j\omega_i e^{-j\phi_i} = \omega_i e^{j\frac{\pi}{2}} e^{-j\phi_i} = \omega_i e^{j(\frac{\pi}{2}-\phi_i)}, \end{aligned} \tag{2.108}$$

and the phase of (2.108) is given by

$$\angle N(j\omega_i) = \frac{\pi}{2} - \phi_i. \tag{2.109}$$

Since the phase of the denominator of the single resonator AFC controller is discontinuous at ω_i, we define $\angle \bar{D}(j\omega_i)$ as the average phase of the denominator as ω is swept through ω_i. This means that in the vicinity before and after the resonance, the average phase of the denominator is given by

$$\begin{aligned} \angle \bar{D}(j\omega_i-) &= 0, \\ \angle \bar{D}(j\omega_i+) &= \pi, \end{aligned} \tag{2.110}$$

where

$$\begin{aligned} (\omega_i-) &= (\omega_i - \epsilon), \\ (\omega_i+) &= (\omega_i + \epsilon). \end{aligned} \tag{2.111}$$

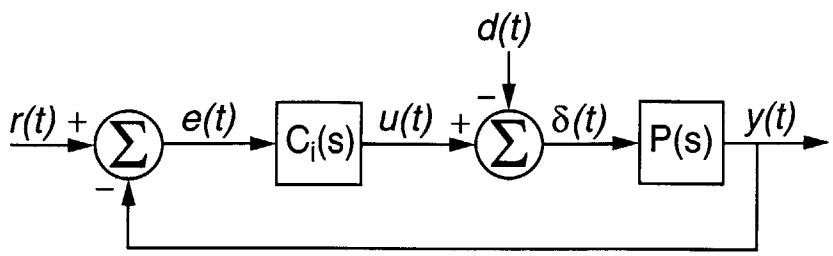

Figure 2-23: LTI equivalent closed-loop block diagram for the single resonator AFC controller.

Thus, the average denominator phase at s = $j\omega_i$ becomes

$$\begin{aligned}\angle\bar{D}(j\omega_i) &= \frac{(\angle\bar{D}(j\omega_i^-) + \angle\bar{D}(j\omega_i^+))}{2} = \frac{(0+\pi)}{2}, \\ &= \frac{\pi}{2}, \end{aligned} \tag{2.112}$$

and after combining (2.109) and (2.112), the average phase of the single resonator AFC controller evaluated at $s = j\omega_i$ is given by

$$\begin{aligned}\angle\bar{C}(j\omega_i) &= \angle N(j\omega_i) - \angle\bar{D}(j\omega_i), \\ &= \left(\frac{\pi}{2} - \phi_i\right) - \frac{\pi}{2}, \\ &= -\phi_i. \end{aligned} \tag{2.113}$$

Figure 2-23 illustrates the LTI equivalent single resonator AFC closed-loop block diagram. The resulting negative of the loop transmission is given by

$$-L(s) = C_i(s)P(s). \tag{2.114}$$

Thus, the average phase of the negative of the loop transmission is of the form

$$\angle - L(j\omega_i) = \angle\bar{C}_i(j\omega_i) + \angle P(j\omega_i). \tag{2.115}$$

In order to maximize the phase margin, we want to center the phase discontinuity in Figure 2-21 and Figure 2-22 about 0°. This will give the negative of the loop transmission approximately 90° of phase margin (depending on the size of g_i). Using (2.115), the average phase of the negative of the loop transmission evaluated at s = $j\omega_i$ is

$$-\angle L(j\omega_i) = \angle \bar{C}_i(j\omega_i) + \angle P(j\omega_i) = -\phi_i + \angle P(j\omega_i). \tag{2.116}$$

Thus, in order to center the phase discontinuity of $-L(s)$ about 0° (place the phase discontinuity between $\pm\frac{\pi}{2}$), we must set the phase advance parameter equal to the phase of the plant at s = $j\omega_i$

$$\phi_i = \angle P(j\omega_i). \tag{2.117}$$

This result is equivalent to the result determined by Messner and Bodson [24], as shown in (2.105).

The phase advance parameter essentially inverts the phase of the plant directly at the frequency we are attempting to follow/reject. For sufficiently small g_i values, the negative of the loop transmission exhibits a 90° phase margin and maximum robustness to modelling errors in the plant transfer function. Assuming we have a relatively accurate model of the plant, it does not matter what the phase of the plant is at the resonator frequency. For any phase values between 0 and 360°, choosing $\phi_i = \angle P(j\omega_i)$ will always center the $-\pi$ discontinuity about 0° for the single resonator AFC system, ensuring a stable and robust closed-loop AFC system. Also, in diamond turning applications, the resonator and reference input frequency is keyed to the fundamental spindle rotation frequency through the modulator/demodulator structure in the AFC algorithm. As a result, the closed-loop system is also robust to small fluctuations in the speed of the spindle carrying the part being turned. In the following section, we detail the design of two single resonator AFC controllers and simulate the closed-loop

transient response to constant amplitude periodic disturbance signals.

2.2.4 Example of Single Resonator AFC Controller Implementation

In this section we study the design and implementation of two single resonator AFC controllers in the context of a simplified plant model. Assuming a transfer function of the form

$$P(s) = \frac{\omega_n^2}{s^2 + 2\zeta\omega_n s + \omega_n^2}, \tag{2.118}$$

where the parameters are selected as $\omega_n = 250$ rad/sec and $\zeta = \frac{\sqrt{2}}{2}$, we analyze the AFC closed-loop transient response to a periodic disturbance input of the form

$$d(t) = \frac{1}{4}\cos(\omega_i t) + \frac{1}{2}\sin(\omega_i t), \tag{2.119}$$

where the frequencies are chosen as $\omega_1 = 70\pi$ rad/sec and $\omega_2 = 110\pi$ rad/sec. The magnitude and phase of the plant at ω_1 and ω_2 are

$$|P(j70\pi)| = 0.79\ (-2.04\ \text{dB}), \tag{2.120}$$

$$\angle P(j70\pi) = -1.39\ \text{rad}\ (-79.7^o), \tag{2.121}$$

$$|P(j110\pi)| = 0.46\ (-6.67\ \text{dB}), \tag{2.122}$$

$$\angle P(j110\pi) = -2.01\ \text{rad}\ (-115^o). \tag{2.123}$$

Initially, we design the single resonator AFC closed-loop system to cancel the disturbance signal with $\omega_i = \omega_1$. Since the input/output relationship of the AFC algorithm is equivalent to the IMP controller, we will use AFC equivalent transfer functions throughout the rest of the section.

The single resonator AFC controller without proper choice of the phase advance

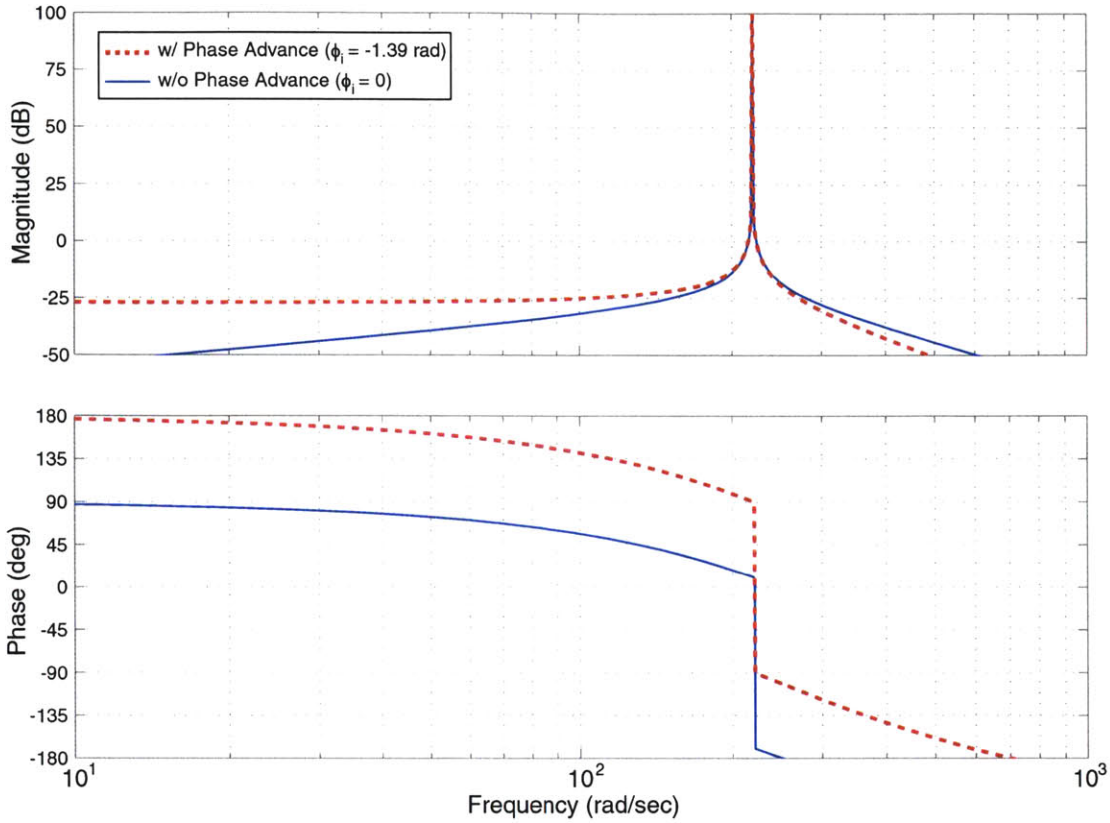

Figure 2-24: Comparison of negative of the loop transmission frequency responses for a single resonator AFC system designed to follow/reject a 70π rad/sec sinusoid with the phase advance parameter (ϕ_i = -1.39 rad) and ($\phi_i = 0$), and $g_i = 10$.

parameter ($\phi_i = 0$) is

$$C_1(s) = g_i \left[\frac{s}{s^2 + 4900\pi^2} \right], \tag{2.124}$$

while after changing to $\phi_i = \angle P(j70\pi)$ = -1.39 rad, the single resonator AFC controller becomes

$$C_{1_{\phi i}}(s) = g_i \left[\frac{0.1789s - 216.36}{s^2 + 4900\pi^2} \right]. \tag{2.125}$$

Figure 2-24 compares the negative of the loop transmission frequency responses with and without the phase advance parameter and $g_i = 10$. We see that both of these systems are stable but the negative of the loop transmission with $\phi_i = 0$ only has approximately 10° of phase margin. Once ϕ_i is set equal to $\angle P(j70\pi)$ ($\phi_i =$

-1.39 rad), the $-\pi$ phase discontinuity is centered about 0° and the resulting negative of the loop transmission has approximately 90° of phase margin.

Root locus techniques can also be used to demonstrate the stability and robustness of the AFC loop. Messner and Bodson [24] and Hall and Wereley [53] showed that once the phase advance parameter is properly implemented, the departure angles of the marginally stable AFC poles are 180° (*i.e.*, into the LHP perpendicular to the imaginary-axis). Figure 2-25 illustrates the resulting root locus plots. With (ϕ_i = 0), the locus of the marginally stable poles briefly move into the LHP but the departure angles are only approximately 100°. Also, the system is not very robust to any modelling errors in the plant transfer function. With the addition of the proper phase advance parameter, the departure angles are at 180° and the closed-loop poles move much further into the LHP, which remain stable for a larger range of gains. Both of these systems are unstable for large gains but the root locus plots clearly show how the addition of a RHP zero actually improves the closed-loop stability and robustness if ϕ_i is chosen properly.

Figure 2-26 compares the transient responses of $\hat{a}$(t), $\hat{b}$(t), and the plant output y(t) to the disturbance input. We see that both of these systems provide zero steady-state error to d(t), though the responses experience significantly different dynamics. With (ϕ_i = 0), the estimates of the Fourier coefficients have a rather oscillatory response before settling to their final steady-state values and the plant output has a long convergence time. With the addition of the proper phase advance parameter, the estimates appear to follow a first order response, as we would expect with a 90° phase margin. Also, $\hat{a}$(t), $\hat{b}$(t), and y(t) converge to their final values considerably faster.

When the disturbance frequency equals $\omega_i = \omega_2$, the single resonator controllers

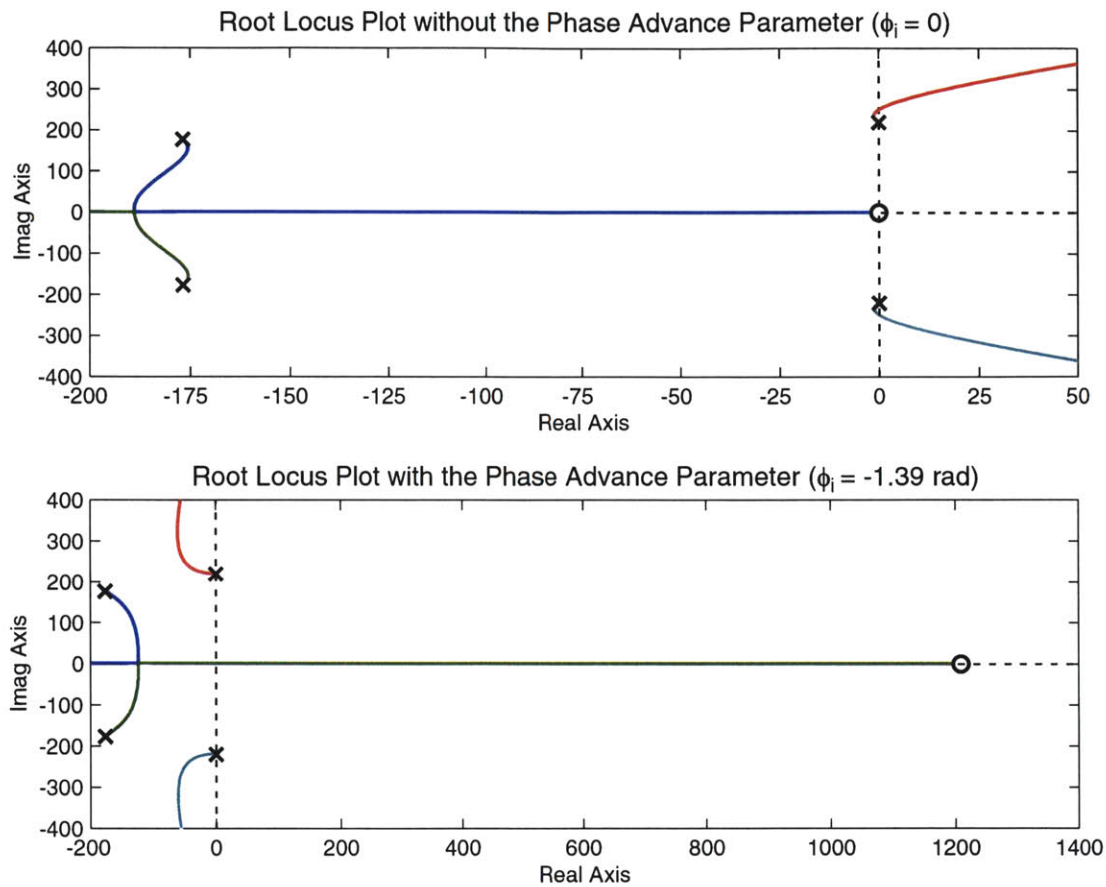

Figure 2-25: Root locus plots of the negative of the loop transmission for the single resonator AFC system designed to follow/reject a 70π rad/sec sinusoid.

with and without the phase advance parameter become

$$C_2(s) = g_i \left[\frac{s}{s^2 + 12100\pi^2} \right], \tag{2.126}$$

$$C_{2_{\phi i}}(s) = -g_i \left[\frac{(0.422s + 313.25)}{s^2 + 12100\pi^2} \right]. \tag{2.127}$$

Figure 2-27, Figure 2-28, and Figure 2-29 illustrate the accompanying negative of the loop transmission frequency responses, root locus plots, and transient responses of $\hat{a}$(t), $\hat{b}$(t), and y(t) when the variable gain $g_i = 10$. Since $\angle P(j110\pi)$ is more negative than -90°, as shown in (2.123), the system with ($\phi_i = 0$) is unstable for all gains. The estimates of the Fourier coefficients diverge and the plant output diverges

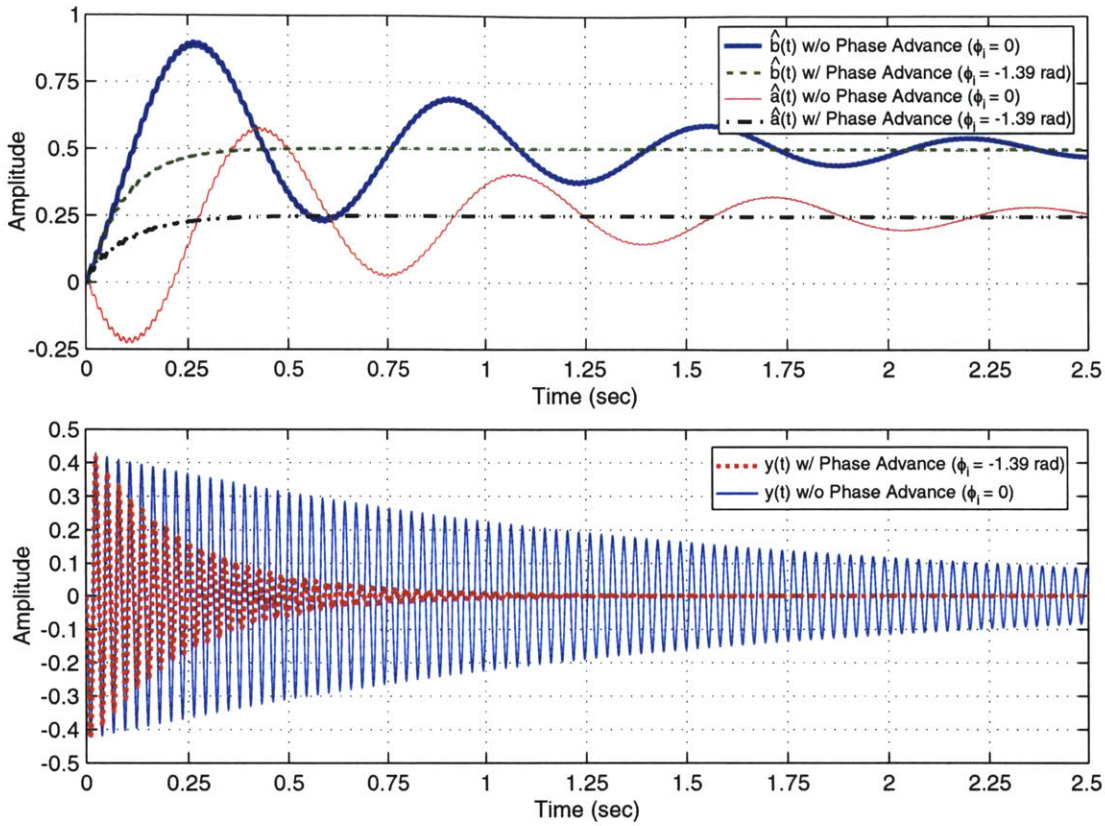

Figure 2-26: Comparison of the transient responses of $\hat{a}$(t), $\hat{b}$(t) and y(t) with the phase advance parameter (ϕ_i = -1.39 rad) and (ϕ_i = 0), and g_i = 10.

to infinity. However, with the addition of the correct phase advance parameter (ϕ_i = -2.01 rad), the system exhibits approximately 90° of phase margin, 180° departure angles, and reasonable $\hat{a}$(t), $\hat{b}$(t), and y(t) convergence rates.

2.2.5 Convergence Properties of Adaptive FeedForward Cancellation

The results of the examples in the previous section highlight some very interesting characteristics of the AFC algorithm. We use these results to interpret the convergence properties for a single resonator AFC closed-loop system. Also, we present the averaging analysis of Sacks *et al* [22], which also provides a measure of the AFC

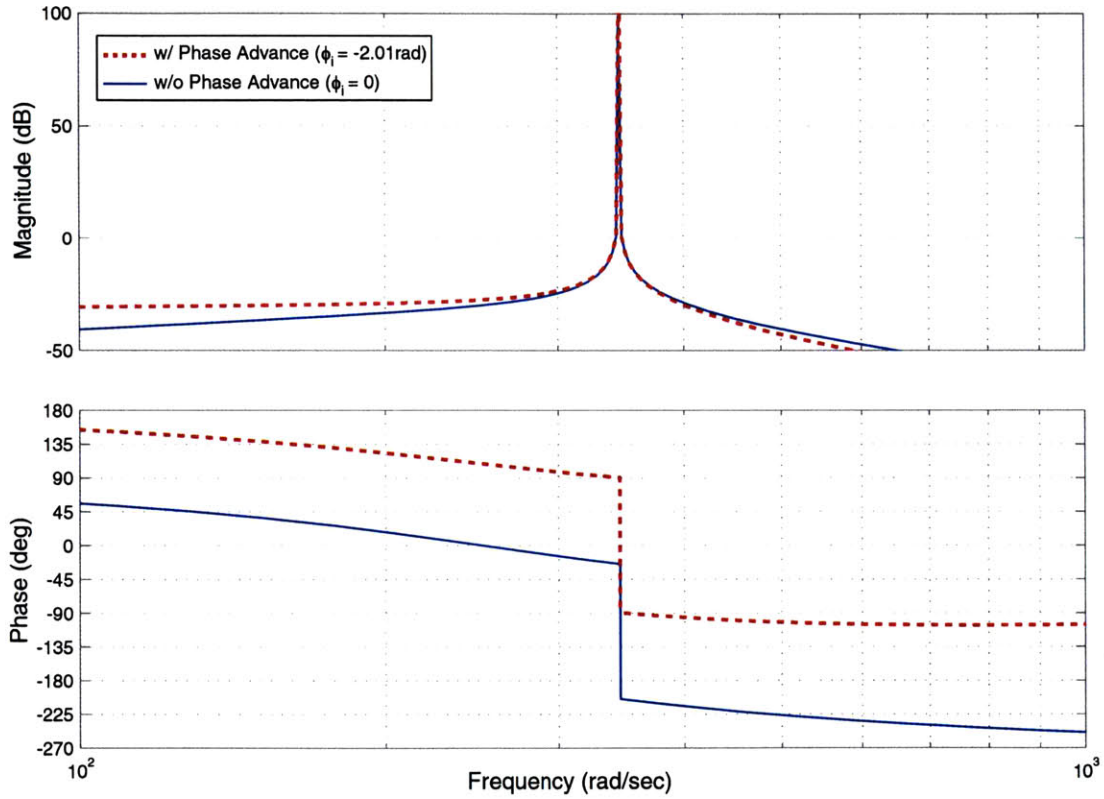

Figure 2-27: Comparison of negative of the loop transmission frequency responses for a single resonator AFC system designed to follow/reject a 110π rad/sec sinusoid with the phase advance parameter (ϕ_i = -2.01 rad) and ($\phi_i = 0$), and $g_i = 10$.

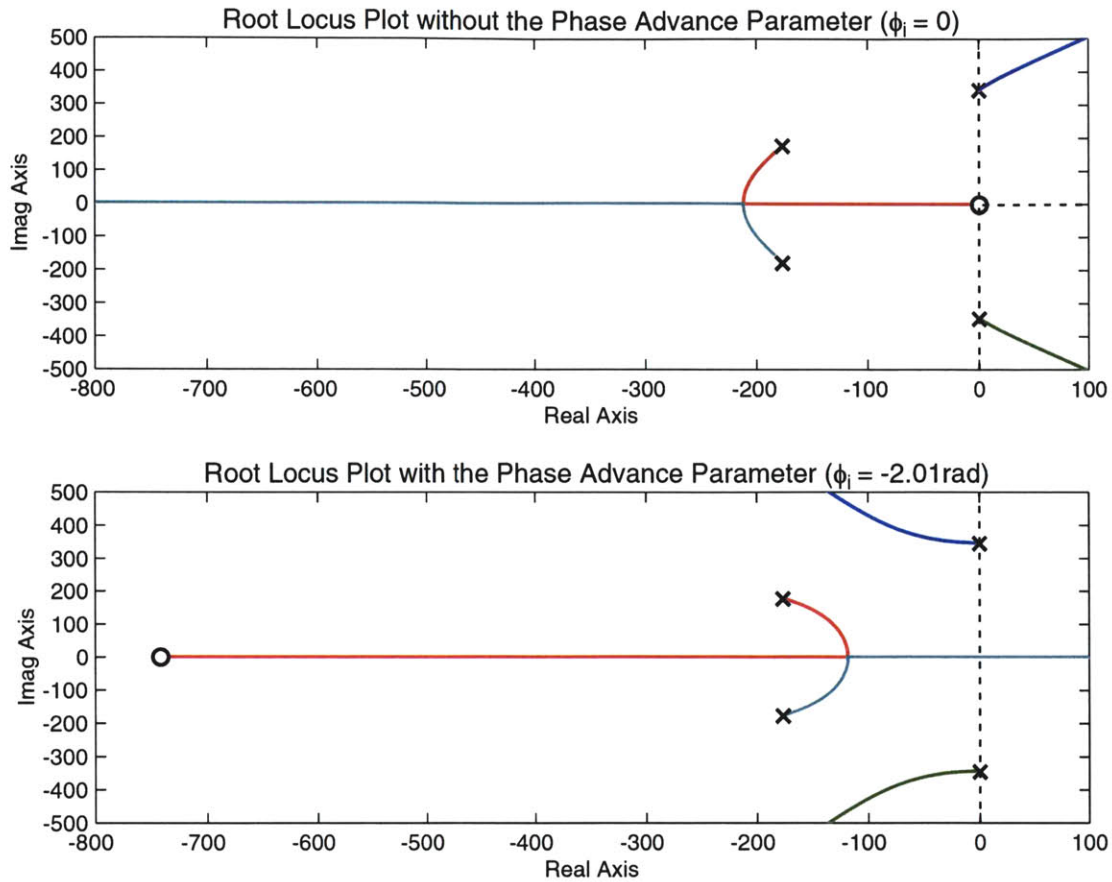

Figure 2-28: Root locus plots of the negative of the loop transmission for the single resonator AFC system with $\omega_i = \omega_2$.

closed-loop convergence rate.

Figure 2-26 compares the transient responses of a single resonator AFC system designed to follow a signal at $\omega_i = 35$ Hz with and without the phase advance parameter. We see that when $\phi_i = 0$ the resulting closed-loop system is stable, since $|\angle \mathrm{P}(j\omega_i)| < \frac{\pi}{2}$, but the convergence rate is much slower than when $\phi_i = \angle \mathrm{P}(j\omega_i)$. Hall and Wereley [53] and Bayard [64] state that these convergence rates are approximately equal to the real part of the least damped AFC closed-loop poles. Sacks, Bodson, and Khosla also determined an approximate measure of the convergence rate for the single resonator AFC system. Their results are based on an averaging analysis

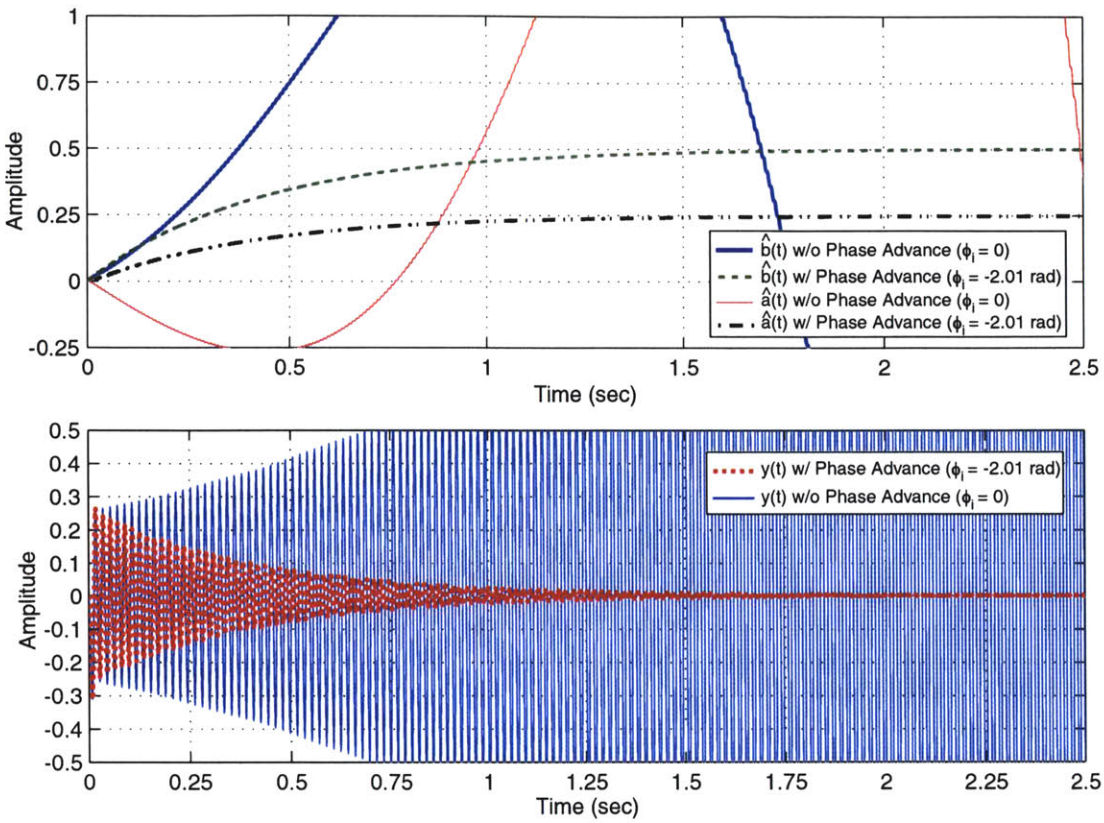

Figure 2-29: Comparison of the transient responses of $\hat{a}$(t), $\hat{b}$(t), and y(t) for a single resonator AFC system designed to follow/reject a 110π rad/sec sinusoid with the phase advance parameter (ϕ_i = -2.01 rad) and ($\phi_i = 0$), and $g_i = 10$.

of the entire feedback loop, as presented below.

Averaging Analysis of the Single Resonator Adaptive Feedforward Cancellation System

Sacks, Bodson, and Khosla [22] perform an averaging analysis on the single resonator AFC closed-loop system which leads to the form

$$\dot{\varphi}_{av} = A_{av}\varphi_{av}, \tag{2.128}$$

where

$$\varphi = \begin{bmatrix} \hat{a}_i(t) - a_i \\ \hat{b}_i(t) - b_i \end{bmatrix}. \tag{2.129}$$

Looking at Figure 2-13, without the addition of the phase advance parameter ϕ_i, they define a regressor vector as

$$v = \begin{bmatrix} cos(\omega_i t) \\ \sin(\omega_i t) \end{bmatrix}, \tag{2.130}$$

and the control input into the plant P(s) is given by

$$\delta(t) = u(t) - d(t) = v^T \varphi. \tag{2.131}$$

Thus, the plant output is

$$y(t) = P[v^T \varphi], \tag{2.132}$$

where P[xy] is the Laplace Transform of the plant P(s) operating on the product of x(t) and y(t). Bodson [19] defines the averaged system as

$$\dot{\varphi}_{av} = -g_i AVG[vP[v^T]]\varphi_{av}, \tag{2.133}$$

where the averaging equation is of the form

$$AVG[x] = \lim_{T \to \infty} \int_0^T x(t)dt. \tag{2.134}$$

Sacks, Bodson, and Khosla show that in the steady-state,

$$P[v] = \begin{bmatrix} \mathrm{Re}[P(j\omega_i)]\cos(\omega_i t) - \mathrm{Im}[P(j\omega_i)]\sin(\omega_i t) \\ \mathrm{Re}[P(j\omega_i)]\sin(\omega_i t) - \mathrm{Im}[P(j\omega_i)]\cos(\omega_i t) \end{bmatrix}, \tag{2.135}$$

where

$$\begin{aligned}\mathrm{Re}[P(j\omega_i)] &= |P(j\omega_i)|\cos(\angle P(j\omega_i)), &(2.136)\\ \mathrm{Im}[P(j\omega_i)] &= |P(j\omega_i)|\sin(\angle P(j\omega_i)). &(2.137)\end{aligned}$$

Therefore, the averaged system A_{av} matrix is

$$A_{av} = -g_i AVG[\upsilon P[\upsilon^T]], \tag{2.138}$$

with $\upsilon P[\upsilon^T]$ given by

$$\upsilon P[\upsilon^T] = \begin{bmatrix} \Omega_R\cos^2(\omega_i t) - \Omega_I\sin(\omega_i t)\cos(\omega_i t) & \Omega_R\sin(\omega_i t)\cos(\omega_i t) + \Omega_I\cos^2(\omega_i t) \\ \Omega_R\sin(\omega_i t)\cos(\omega_i t) - \Omega_I\sin^2(\omega_i t) & \Omega_R\sin^2(\omega_i t) + \Omega_I\sin(\omega_i t)\cos(\omega_i t) \end{bmatrix}, \tag{2.139}$$

where

$$\begin{aligned}\Omega_R &= \mathrm{Re}[P(j\omega_i)], &(2.140)\\ \Omega_I &= \mathrm{Im}[P(j\omega_i)]. &(2.141)\end{aligned}$$

Using the following trigonometric relations

$$\begin{aligned}\sin\alpha\cos\beta &= \frac{1}{2}[\sin(\alpha-\beta)+\sin(\alpha+\beta)], &(2.142)\\ \cos^2\theta &= \frac{1}{2}(1+\cos 2\theta), &(2.143)\\ \sin^2\theta &= \frac{1}{2}(1-\cos 2\theta), &(2.144)\end{aligned}$$

equation (2.139) reduces to

$$\upsilon P[\upsilon^T] = \frac{1}{2}\begin{bmatrix} \Omega_R(1+\cos(2\omega_i t)) - \Omega_I\sin(2\omega_i t) & \Omega_R\sin(2\omega_i t) + \Omega_I(1+\cos(2\omega_i t)) \\ \Omega_R\sin(2\omega_i t) - \Omega_I(1-\cos(2\omega_i t)) & \Omega_R(1-\cos(2\omega_i t)) + \Omega_I\sin(2\omega_i t) \end{bmatrix}. \tag{2.145}$$

After averaging (2.145) over one period, the averaged system A_{av} matrix in (2.138) becomes

$$A_{av} = -\frac{g_i}{2}\begin{bmatrix} \mathrm{Re}[P(j\omega_i)] & \mathrm{Im}[P(j\omega_i)] \\ \mathrm{Im}[P(j\omega_i)] & \mathrm{Re}[P(j\omega_i)] \end{bmatrix}, \tag{2.146}$$

and the resulting averaged system eigenvalues are given by

$$\lambda_{1,2} = -\frac{g_i}{2}\left[\mathrm{Re}[P(j\omega_i)] \pm j\mathrm{Im}[P(j\omega_i)\right], \tag{2.147}$$

or,

$$\lambda_{1,2} = -\left(\frac{g_i|P(j\omega_i)|}{2}\right)\left[\cos(\angle P(j\omega_i)) \pm j\sin(\angle P(j\omega_i))\right]. \tag{2.148}$$

With the addition of the proper phase advance parameter ($\phi_i = \angle P(j\omega_i)$) to the Adaptive Feedforward Cancellation algorithm, Sacks, Bodson, and Khosla define a new regressor vector

$$\mu = \begin{bmatrix} \cos(\omega_i t + \phi_i) \\ \sin(\omega_i t + \phi_i) \end{bmatrix}, \tag{2.149}$$

and the resulting averaged system becomes

$$\dot{\varphi}_{av} = -g_i AVG[\mu P[v^T]]\varphi_{av}. \tag{2.150}$$

The new averaged A matrix is

$$A_{av} = -g_i AVG[\mu P[v^T]], \tag{2.151}$$

where

$$\mu P[v^T] = \left(\frac{|P(j\omega_i)|}{2}\right)\begin{bmatrix} X_{11} & X_{12} \\ X_{21} & X_{22} \end{bmatrix}, \tag{2.152}$$

and

$$
\begin{aligned}
X_{11} &= \left[(1+\cos(2\omega_i t))\cos^2\phi_i - 2\sin(2\omega_i t)\sin\phi_i\cos\phi_i\right. \\
&+ \left.(1-\cos(2\omega_i t))\sin^2\phi_i\right], \qquad (2.153) \\
X_{12} &= \left[(1+\cos(2\omega_i t))\sin\phi_i\cos\phi_i - \sin(2\omega_i t)\sin^2\phi_i + \sin(2\omega_i t)\cos^2\phi_i\right. \\
&- \left.(1-\cos(2\omega_i t))\sin\phi_i\cos\phi_i\right], \qquad (2.154) \\
X_{21} &= \left[(1+\cos(2\omega_i t))\sin\phi_i\cos\phi_i - \sin(2\omega_i t)\sin^2\phi_i + \sin(2\omega_i t)\cos^2\phi_i\right. \\
&- \left.(1-\cos(2\omega_i t))\sin\phi_i\cos\phi_i\right], \qquad (2.155) \\
X_{22} &= \left[2\sin(2\omega_i t)\sin\phi_i\cos\phi_i + (1+\cos(2\omega_i t))\sin^2\phi_i\right. \\
&+ \left.(1-\cos(2\omega_i t))\cos^2\phi_i\right]. \qquad (2.156)
\end{aligned}
$$

After averaging (2.152) over one period, the new averaged system A_{av} matrix, with the phase advance parameter ϕ_i set equal to the phase of the plant, is

$$
A_{av} = -\frac{g_i}{2}\begin{bmatrix} |P(j\omega_i)|(\cos^2\phi_i + \sin^2\phi_i) & 0 \\ 0 & |P(j\omega_i)|(\cos^2\phi_i + \sin^2\phi_i) \end{bmatrix}. \qquad (2.157)
$$

Using the trigonometric relation

$$
\left(\cos^2\phi_i + \sin^2\phi_i\right) = 1, \qquad (2.158)
$$

the resulting eigenvalues are given by

$$
\lambda_{1,2} = -\frac{g_i}{2}|P(j\omega_i)|. \qquad (2.159)
$$

In [22], Sacks, Bodson, and Khosla note that in order to perform an averaging analysis on the single resonator AFC system, the plant transfer function P(s) must be open-loop stable and the AFC gain g_i must be sufficiently small. For the purposes

of discussion, we assume both criterions are met and thus see that the proper choice of the phase advance parameter reduces the convergence rate of the feedback-loop to a constant amplitude signal with frequency ω_i. Using (2.148) and (2.159), we define the approximate convergence rate of the single resonator AFC system (for sufficiently small g_i levels) as

$$\alpha \approx \frac{2}{g_i|P(jw_i)|\cos(\theta_C)}, \tag{2.160}$$

where

$$\theta_C = \angle \mathrm{P}(j\omega_i) - \phi_i. \tag{2.161}$$

When ϕ_i is chosen properly, equation (2.160) shows that the closed-loop system, for a given proportional gain g_i, maximizes the convergence rate. As the difference between the phase of the plant at s $= j\omega_i$ and ϕ_i approaches $\pm 90^o$, the convergence becomes increasingly slower, as shown in Figure 2-26. When $|\theta_C| > 90^o$, the system becomes unstable and the closed-loop output diverges to infinity, as shown in Figure 2-29.

Byl *et al* [6] show an example of a single resonator AFC system with the phase advance parameter, designed with a resonator frequency $\omega_i = 20$ rad/sec and various proportional gain g_i levels. They assume a second order system given by (2.118), where the parameters are selected as $\omega_n = 1200$ rad/sec and $\zeta = \frac{\sqrt{2}}{2}$. Figure 2-30 illustrates the resulting plant frequency response, while Figure 2-31 shows the time response of the percent following error for the AFC closed-loop system to an input signal with frequency $\omega_r = 20$ rad/sec and $g_i = 0$ (essentially no AFC control), and $g_i = 1, 5, 10$.

When $g_i = 0$, the steady-state peak-to-peak following error is 2.3%, while all the other levels provide zero steady-state tracking error. As (2.160) predicts, the larger the g_i level, the faster the convergence rate. Byl *et al* speculate that the small ripple observed in Figure 2-31 for $g_i = 5$ and $g_i = 10$ is due to numerical issues in the simulation.

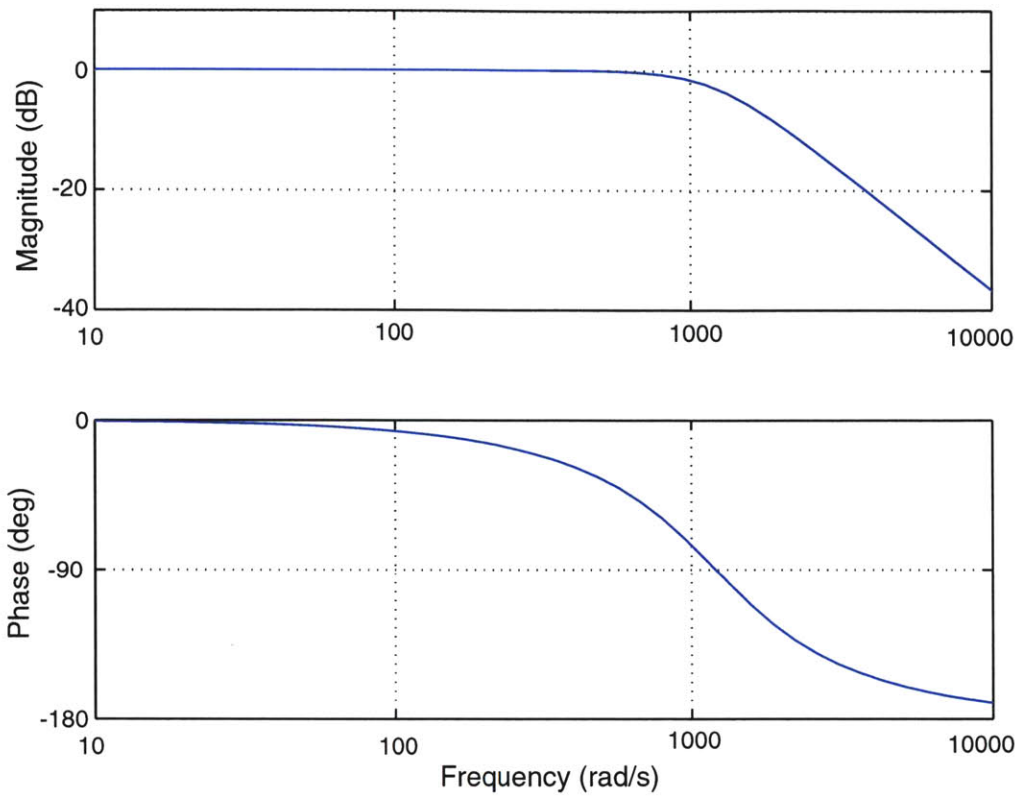

Figure 2-30: Bode Plot for second order system P(s) used to simulate the effect of the proportional gain g_i on the closed-loop system response. Figure adapted from Byl *et al* [6].

They repeat this simulation, but perturb the input signal frequency by setting ω_r equal to 19.5 rad/sec. The results of these simulations are shown in Figure 2-32. We see that since the reference frequency does not equal the designed resonator frequency, the closed-loop system cannot provide zero steady-state tracking error. However, we observe that the size of the steady-state error is inversely proportional to the size of g_i, which can be explained by a simple magnitude of the loop transmission argument [6].

The work of Hall and Wereley [53], Bayard [64], and Sacks *et al* [22], as mentioned previously, provide a good measure of the time it takes an AFC system to achieve zero-steady state error to a constant amplitude input with frequency ω_i. However, only Hall and Wereley provide an analysis of the steady-state error properties to an

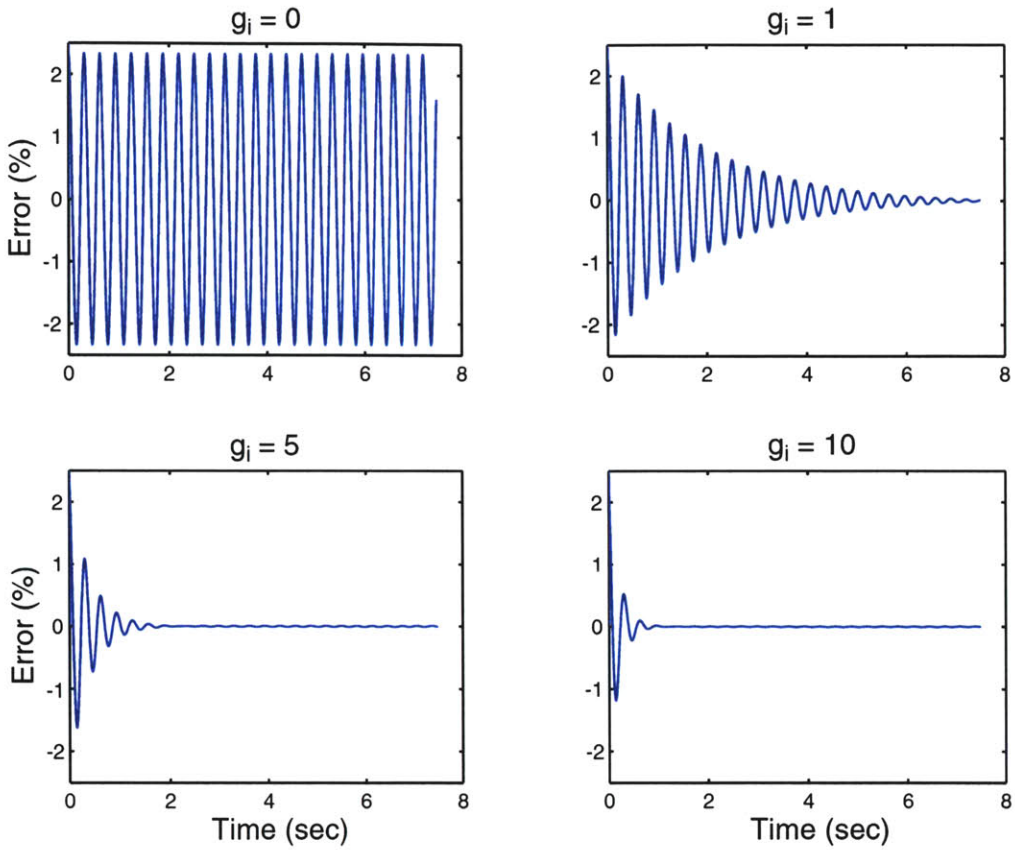

Figure 2-31: Percent error tracking a sinusoidal reference trajectory with $\omega_r = 20$ rad/sec with an AFC resonator tuned to $\omega_i = 20$ rad/s for resonator gains g_i =0, 1, 5, and 10, respectively. Figure adapted from Byl *et al* [6].

input with slowly time-varying amplitude and frequency components. They state that in practice, the Higher Harmonic Control algorithm is only able to reject between 25 to 90% of the periodic vibrations. Several speculations are presented as the possible sources of the unpredicted error, but they provide a detailed analysis of the error signal to an input with random frequency content.

In [53], Hall and Wereley consider the possibility of a disturbance signal with random frequency content. They model this disturbance as a random process with power spectral density centered about the resonator frequency, as shown in Figure 2-32. The spread (width) of the disturbance spectrum is inversely proportional to the

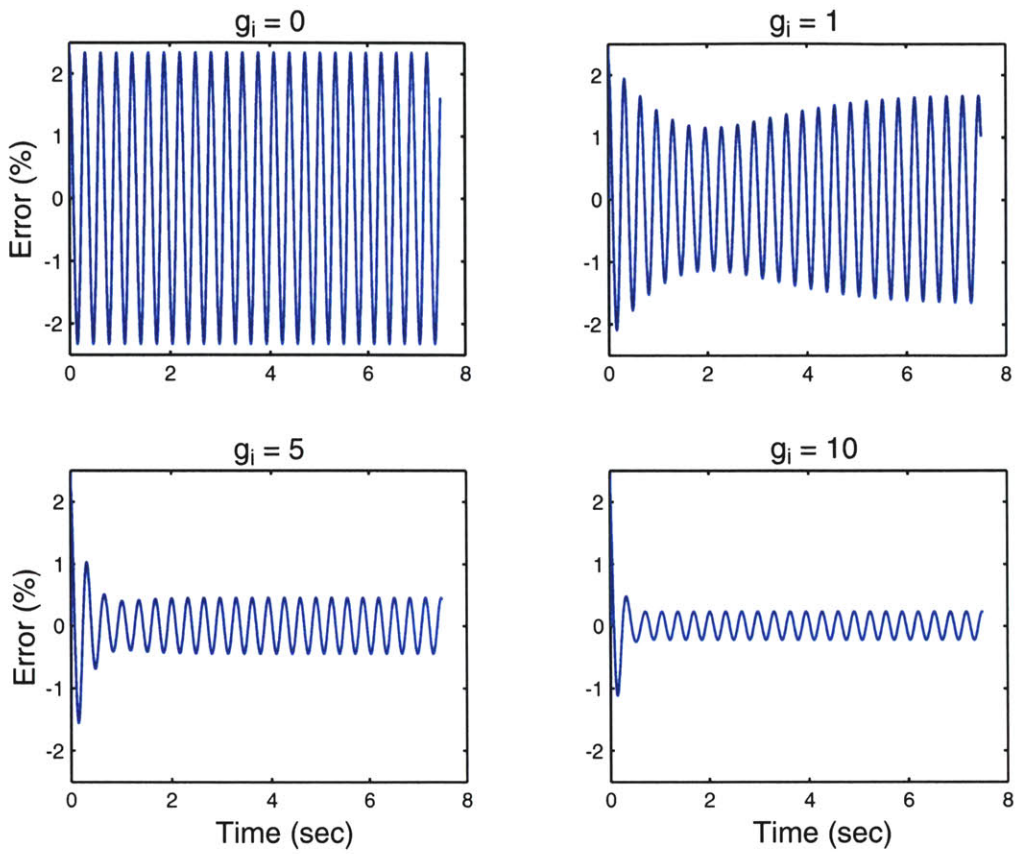

Figure 2-32: Percent error tracking a sinusoidal trajectory with $\omega_r = 19.5$ rad/sec and an AFC resonator tuned to $\omega_i = 20$ rad/sec for resonator gains $g_i = 0$, 1, 5, and 10, respectively. Figure adapted from Byl *et al* [6].

correlation time τ_c, where τ_c refers to any time variation in the periodic disturbance input (*e.g.*, time constant of wind turbulence, average time between flight maneuvers, etc.) to the helicopter rotor blades. For diamond turning applications, τ_c could correspond to the time variation of the reference/disturbance frequency, changes in the size of the reference/disturbance Fourier coefficients, or magnitude and phase shifting of the plant transfer function.

Hall and Wereley use two methods to determine an approximate relationship between the open and closed-loop root-mean-squared (RMS) vibration levels, which include a Gauss-Markov process with an autocorrelation function and a random walk

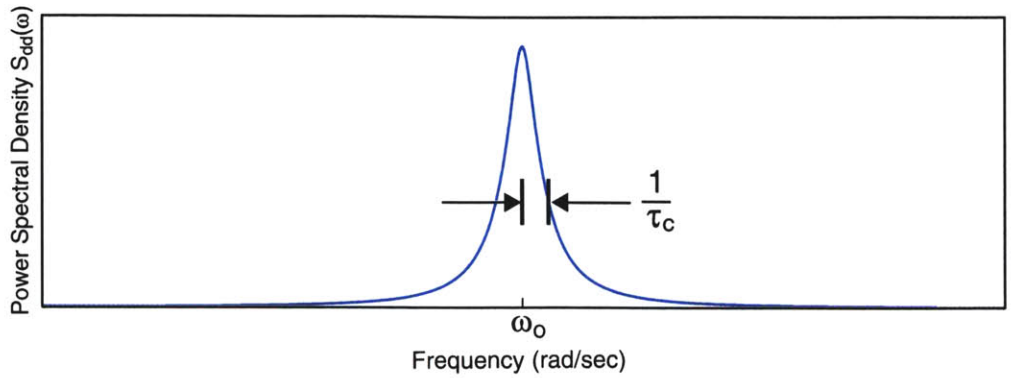

Figure 2-33: Power spectral density of a spread spectrum disturbance signal, centered about the resonator frequency ω_i. The spread of the disturbance spectrum is characterized by the correlation time τ_c. Figure adapted from Hall and Wereley [53].

disturbance model. It turns out, however, that their results are nearly identical for both models. They determined

$$\frac{\sigma_z}{\sigma_d} \approx \frac{1}{k\tau_c}, \tag{2.162}$$

where k is the proportional gain of the HHC algorithm and σ_z and σ_d are the closed-loop and open-loop RMS vibration levels, respectively. Adapting these results to the single resonator AFC system, we see that the steady-state RMS tracking error decreases as the variable gain g_i or correlation time increases. In Chapter 5, we build upon the results of Hall and Werely and Byl *et al* with our Adaptive Feedforward Cancellation viewed from an oscillator amplitude control perspective. The following section expands the theory presented thus far to Adaptive Feedforward Cancellation systems with multiple resonators.

2.2.6 Multiple Resonator Adaptive Feedforward Cancellation Systems

In diamond turning applications, fast tool servos commonly follow near-periodic trajectories, since the tool motion is keyed to the fundamental spindle rotation frequency.

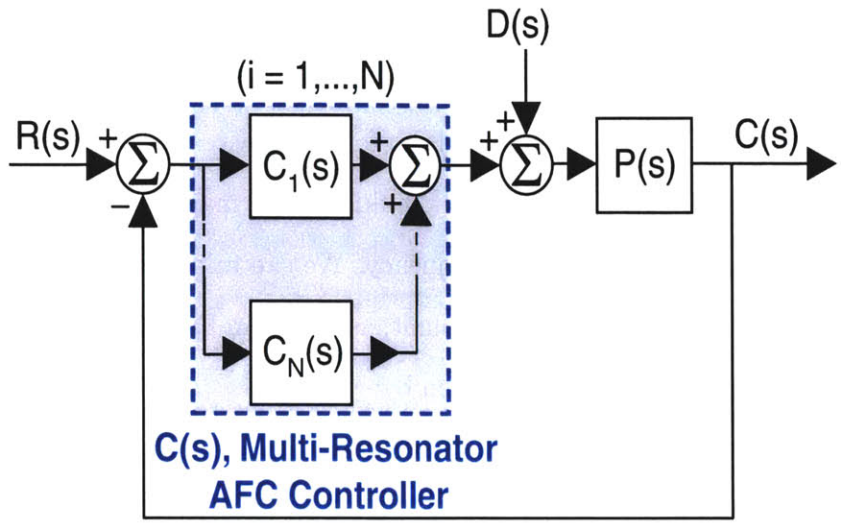

Figure 2-34: LTI equivalent closed-loop block diagram with an N resonator Adaptive Feedforward Cancellation controller.

The FTS axis can develop significant following errors, since conventional feedback loops only provide a finite controller gain. The FTS axis also experiences large disturbances (*e.g.*, cutting forces and spindle imbalance) which usually occur at integer harmonics of the spindle rotation frequency. As a result of all these effects, the error signal primarily consists of a summation of sinusoids of known frequencies and unknown Fourier coefficients of the form

$$e(t) = \sum_{n=1}^{N} [a_i cos(\omega_i t) + b_i sin(\omega_i t)]. \tag{2.163}$$

In order to be able to provide zero steady-state tracking error to these multiple harmonics, several AFC resonators can be placed in parallel to form a multiple resonator AFC system. The general form of a multi-resonator AFC controller is given by

$$C(s) \;=\; \sum_{i=1}^{N} g_i \left(\frac{s \cos \phi_i + \omega_i \sin \phi_i}{s^2 + \omega_i^2} \right), \tag{2.164}$$

where the resulting LTI equivalent closed-loop block diagram is shown in Figure 2-34.

In most practical systems (*e.g.*, the Variform FTS), the plant being controlled with Adaptive Feedforward Cancellation does not provide a desirable frequency response over the frequencies of harmonics we desire to follow/reject. Also, the plant P(s) may experience non-linear effects, which results in fluctuating magnitude and phase values as a function of input amplitude and frequency. We can minimize these problems by simply closing an inner-loop around the plant, as shown in Figure 2-35. The resulting inner closed-loop transfer function is given by

$$P^*(s) = \frac{G_c(s)P(s)}{1 + G_c(s)P(s)}, \tag{2.165}$$

where G_c(s) is a conventional compensator. This configuration attenuates any plant non-linearities and provides a well-characterized frequency response for designing the outer AFC loop. Ideally, we would like (2.165) to have as high of closed-loop bandwidth as possible, so the inner-loop provides negligible magnitude and phase shifting over the harmonics of interests. Now, the proper choice of the phase advance parameter is

$$\phi_i = \angle \mathrm{P}^*(j\omega_i), \tag{2.166}$$

and the negative of the loop transmission and closed-loop transfer functions for the entire AFC system, as shown in Figure 2-35, are given by

$$-L(s) = C(s)P^*(s) = C(s)\left(\frac{G_c(s)P(s)}{1 + G_c(s)P(s)}\right), \tag{2.167}$$

$$\begin{aligned}\frac{C(s)}{R(s)} &= \frac{L(s)}{1 + L(s)} = \frac{C(s)P^*(s)}{1 + C(s)P^*(s)} = \frac{C(s)\left(\frac{G_c(s)P(s)}{1+G_c(s)P(s)}\right)}{1 + C(s)\left(\frac{G_c(s)P(s)}{1+G_c(s)P(s)}\right)}, \\ &= \frac{C(s)G_c(s)P(s)}{1 + G_c(s)P(s) + C(s)G_c(s)P(s)}. \end{aligned} \tag{2.168}$$

Figure 2-36 illustrates the calculated negative of the loop transmission frequency

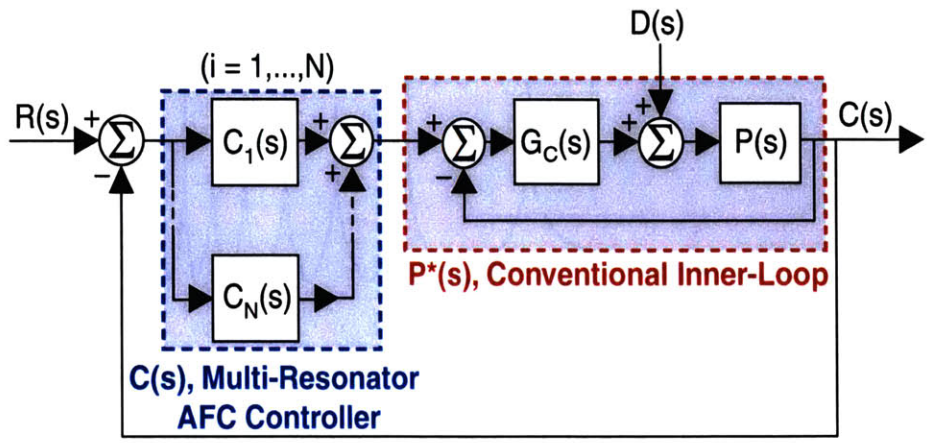

Figure 2-35: LTI equivalent closed-loop block diagram with an N resonator Adaptive Feedforward Cancellation controller C(s) and conventional inner-loop compensator G_c(s).

response for the Variform FTS (Appendix B includes the state-space matrices for this plant model P(s) = G_{p_1}(s)) with a multi-resonator AFC controller and conventional inner-loop integral compensator. A loop-shaping approach to designing the multiple resonator controller is presented later in this section, while the details of the experimental C(s) and G_c(s) transfer functions for the Variform FTS are described in Chapter 3. For the present, we note that the proper choice of the phase advance parameter for each resonator still equals the phase of the plant evaluated at s = $j\omega_i$, or $\angle$P$^*(j\omega_s)$ when an inner-loop is used. This centers the $-\pi$ discontinuities of all the AFC resonators about 0°, as shown in Figure 2-36, which provides a stable and robust closed-loop system. We designed the multiple resonator AFC system for the Variform FTS to provide zero steady-state error to an input with up to ten harmonics at frequencies of

$$\omega_i = 10 \text{ Hz, } 20 \text{ Hz, ..., and } 100 \text{ Hz.} \tag{2.169}$$

We see in Figure 2-36 that -L(s) produces infinite gain at all ten of these frequencies, thus the closed-loop system will yield zero-steady state error to a constant amplitude input with any combination of these values.

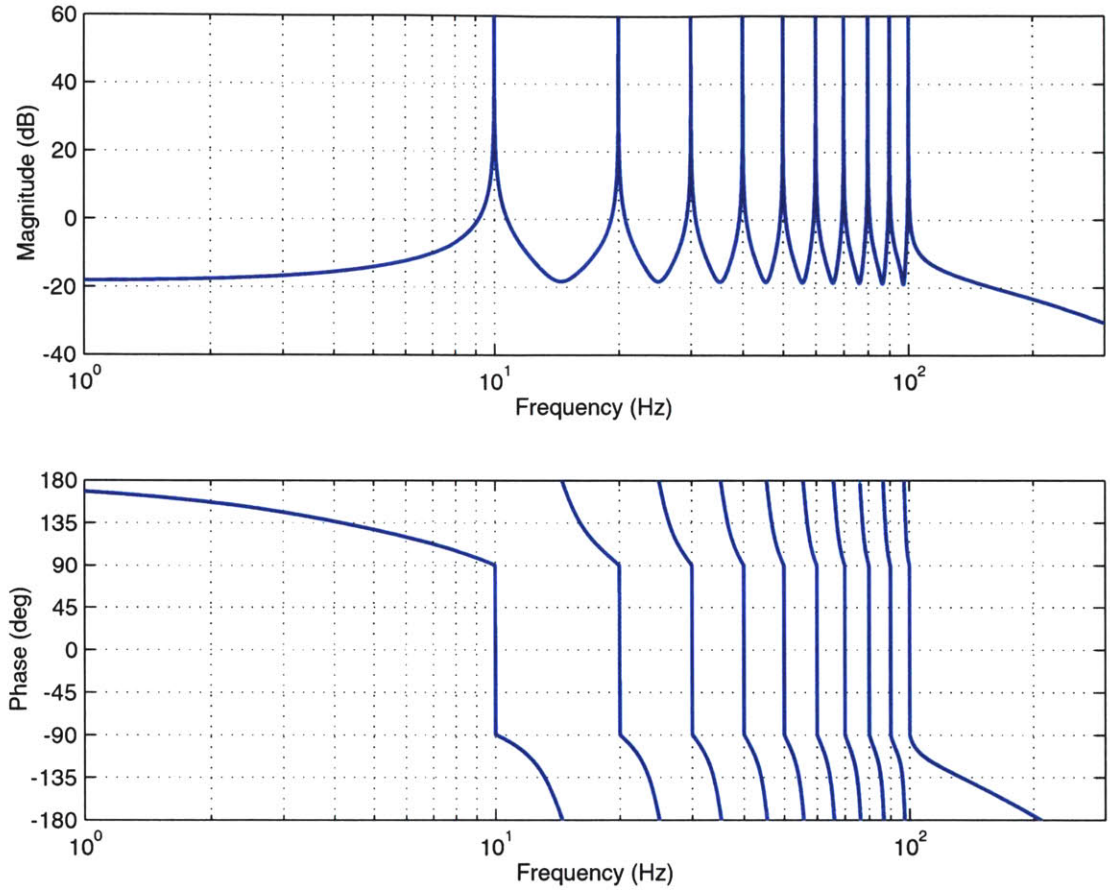

Figure 2-36: Calculated negative of the loop transmission frequency response for the Variform FTS with a multiple resonator AFC controller and conventional inner-loop integral compensator.

Figure 2-37 shows the calculated closed-loop frequency response for the Variform FTS with the ten-resonator AFC controller and conventional inner-loop integral compensator. This system does provide 0 dB and 0° of phase at all of the resonator frequencies but the closed-loop performance in-between these frequencies is rather poor. In particular, the slope of the Bode phase plot is very undesirable, since any frequency components in the reference or disturbance signal other than the ten AFC resonator frequencies will cause significant following errors.

We can improve the closed-loop performance by using an altered AFC controller configuration, as shown in Figure 2-38. The resulting closed-loop system still provides

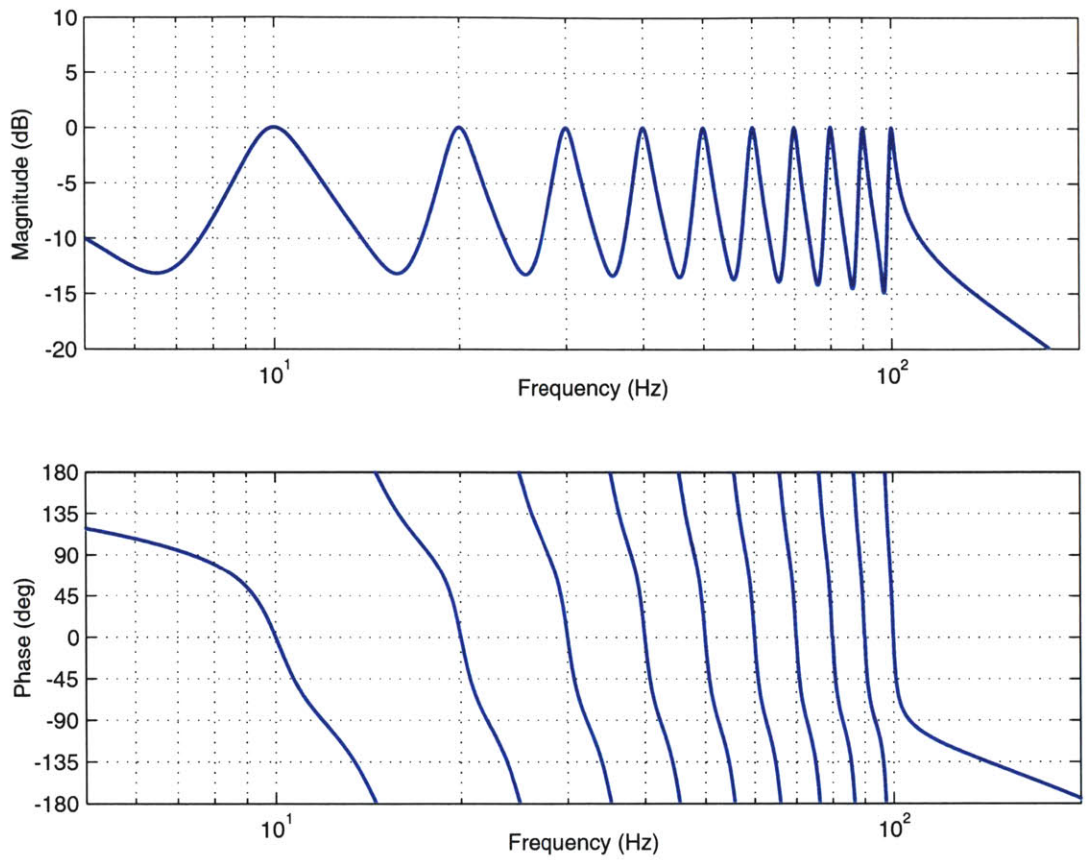

Figure 2-37: Calculated closed-loop frequency response for the Variform FTS with a multiple resonator AFC controller and conventional inner-loop integral compensator.

zero steady-state error at all of the resonator frequencies, but it dramatically improves the rest of the closed-loop frequency response. The resulting negative of the loop transmission and closed-loop transfer functions are given by

$$-L(s) = G_c(s)P(s)\left(1 + C(s)\right), \tag{2.170}$$

$$\begin{aligned} \frac{C(s)}{R(s)} &= \frac{L(s)}{1 + L(s)} = \frac{G_c(s)P(s)\left(1 + C(s)\right)}{1 + G_c(s)P(s)\left(1 + C(s)\right)}, \\ &= \frac{G_c(s)P(s) + C(s)G_c(s)P(s)}{1 + G_c(s)P(s) + C(s)G_c(s)P(s)}, \end{aligned} \tag{2.171}$$

and the choice of the phase advance parameter which maximizes closed-loop stability

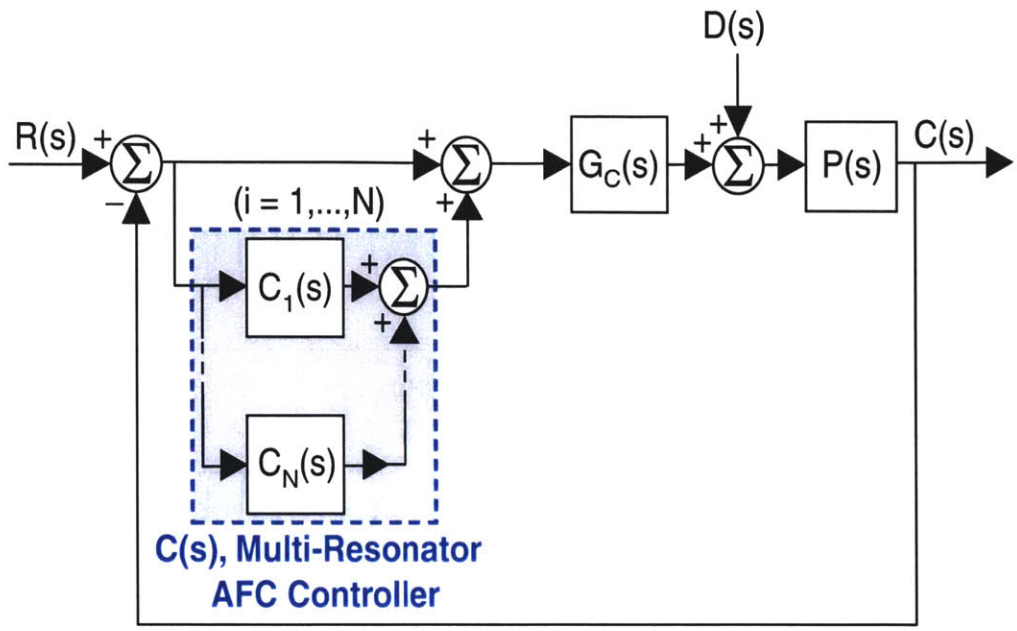

Figure 2-38: Altered block diagram for the Variform FTS with a multiple resonator AFC controller and conventional integral compensator.

and robustness is still given by

$$\phi_i = \angle \mathrm{P}^*(j\omega_s) \tag{2.172}$$

where the transfer function P*(s) is

$$\mathrm{P}^*(s) \quad = \quad \frac{G_c(s)P(s)}{1 + G_c(s)P(s)}. \tag{2.173}$$

The proper selection of ϕ_i is not intuitively obvious from the closed-loop block diagram in Figure 2-38. However, we can manipulate the altered AFC configuration into an equivalent closed-loop block diagram. Figure 2-39 illustrates the equivalent closed-loop system for the altered AFC configuration, which is simply the closed-loop block diagram in Figure 2-35 with the addition of a unity feedforward channel.

Figure 2-40 illustrates the classical closed-loop block diagram with a feedforward

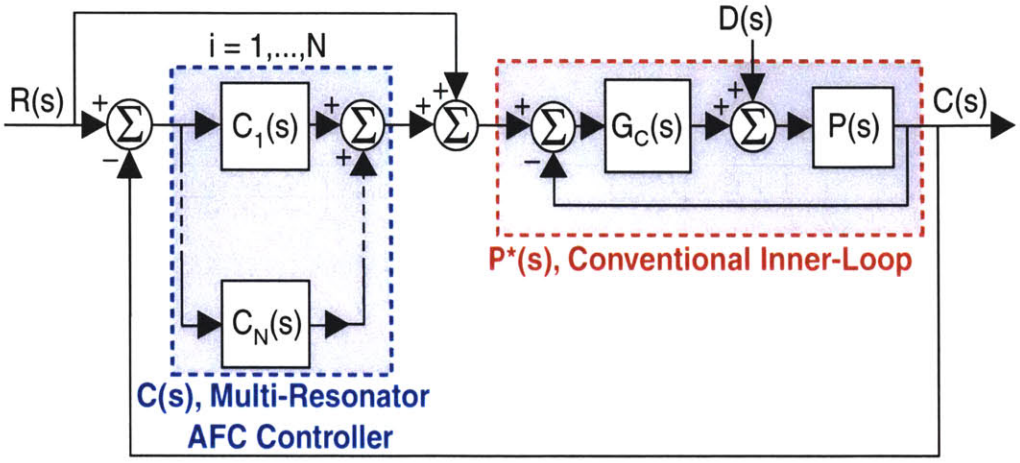

Figure 2-39: Altered block diagram for the Variform FTS with a multiple resonator AFC controller, conventional inner-loop integral compensator, and feedforward channel.

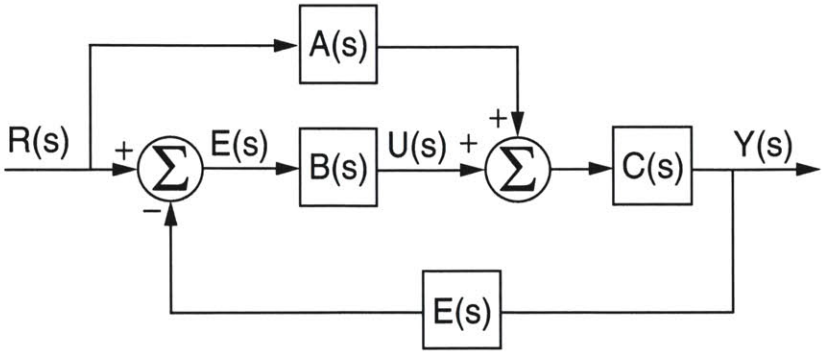

Figure 2-40: Classical closed-loop block diagram with an additional feedforward channel. Figure adapted from Ludwick [1].

channel, where the closed-loop transfer function is given by

$$\frac{Y(s)}{R(s)} = \frac{A(s)C(s) + B(s)C(s)}{1 + B(s)C(s)E(s)}. \tag{2.174}$$

Therefore, the closed-loop transfer function for the AFC system in Figure 2-39 is

$$\begin{aligned}\frac{C(s)}{R(s)} &= \frac{P^*(s) + C(s)P^*(s)}{1 + C(s)P^*(s)} = \frac{\left(\frac{G_c(s)G_p(s)}{1+G_c(s)G_p(s)}\right) + C(s)\left(\frac{G_c(s)G_p(s)}{1+G_c(s)G_p(s)}\right)}{1 + C(s)\left(\frac{G_c(s)G_p(s)}{1+G_c(s)G_p(s)}\right)}, \\ &= \frac{G_c(s)G_p(s) + C(s)G_c(s)G_p(s)}{1 + G_c(s)G_p(s) + C(s)G_c(s)G_p(s)}. \end{aligned} \tag{2.175}$$

We see that (2.175) is equivalent to (2.171), thus both feedback configurations provide the same closed-loop frequency response.

There are several advantages to the controller configuration in Figure 2-39 when compared to the initial altered AFC closed-loop block diagram in Figure 2-38. First, it is clear what the proper choice is for the phase advance parameter. Since the feedforward channel does not contribute to the stability of the feedback loop, the phase of C(s) should be chosen as to cancel the phase of the inner-loop evaluated at $s = j\omega_i$. In other words,

$$\angle \mathrm{C}(j\omega_i) + \angle \mathrm{P}^*(j\omega_i) = 0. \tag{2.176}$$

We know from Section 2.2.3 that the average phase of C(s) at a resonator frequency is

$$\angle \bar{C}(j\omega_i) = -\phi_i. \tag{2.177}$$

Therefore, substituting (2.177) into (2.176), the proper choice of the phase advance parameter is given by

$$\phi_i = \angle \mathrm{P}^*(j\omega_i). \tag{2.178}$$

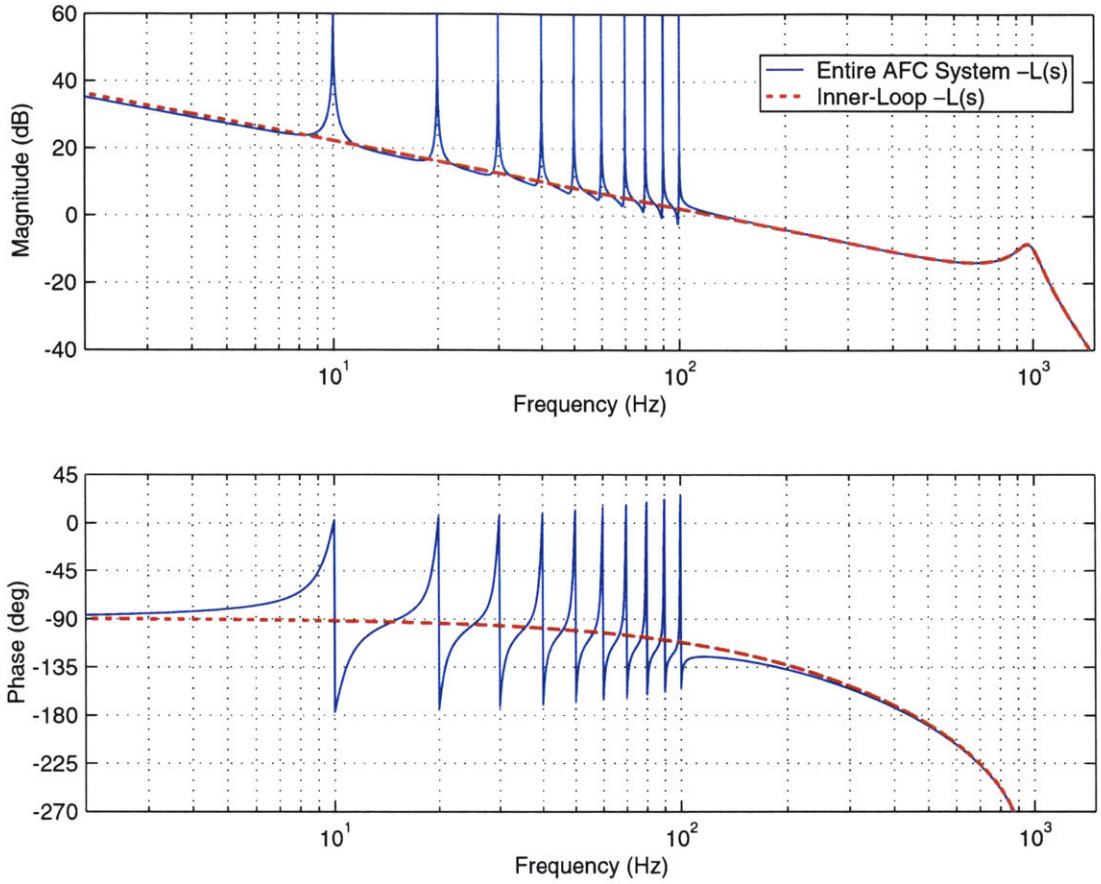

Figure 2-41: Comparison of the calculated negative of the loop transmission frequency responses for the altered closed-loop configuration in Figure 2-38 and the conventional inner-loop.

Another advantage of the controller configuration in Figure 2-39 is resulting feedforward channel. This channel can be used to feedforward a magnitude and phase shifted input signal to the inner-loop P*(s) (known collectively as *command pre-shifting*), which improves the AFC closed-loop frequency response for the in-between resonator frequencies. We expand upon this concept later in this section.

Figure 2-41 compares the calculated negative of the loop transmission frequency responses for the entire altered AFC system and the conventional inner-loop. We see that -L(s) for the entire AFC loop, with an N AFC resonator controller, is essentially equal to the negative of the loop transmission for the inner-loop with N infinite peaks

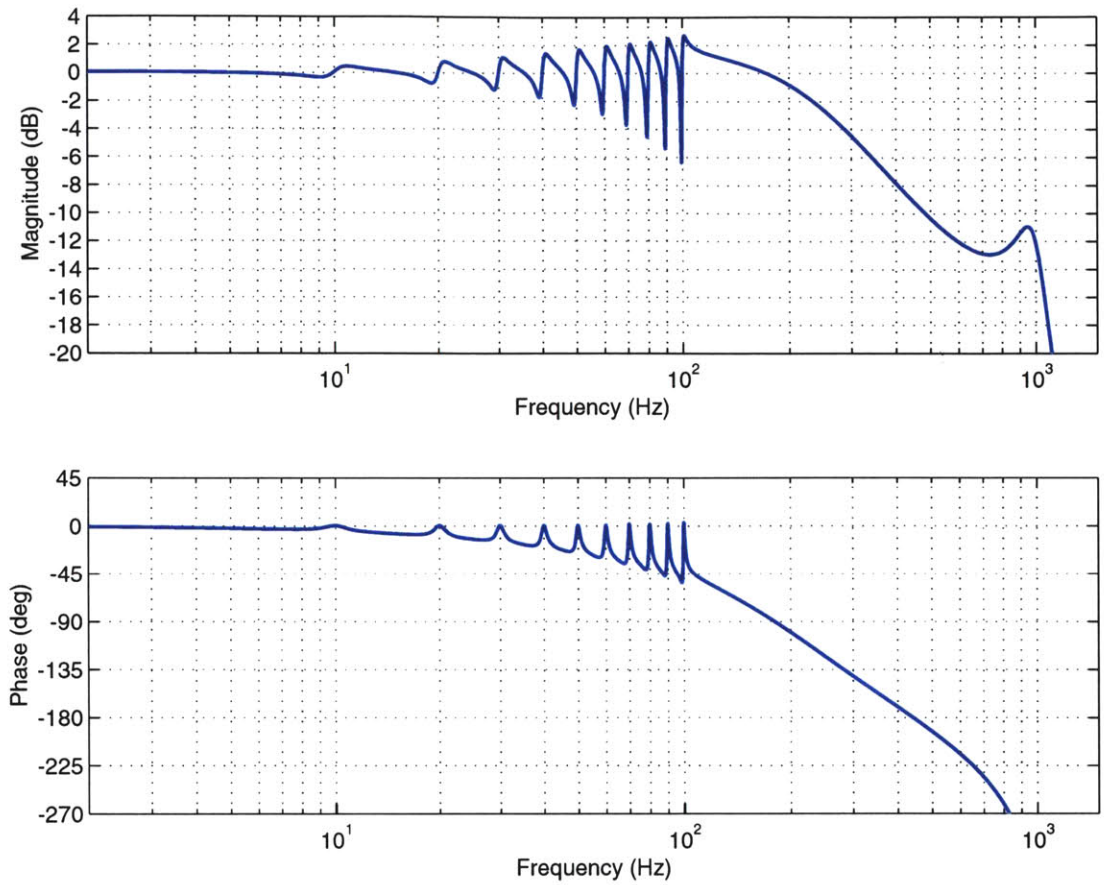

Figure 2-42: Calculated closed-loop frequency responses for the altered AFC configuration with a conventional inner-loop and unity feedforward channel.

and N $-\pi$ phase discontinuities at s=$j\omega_i$. As a result of these findings, the inner-loop should be designed to provide adequate trajectory following/disturbance rejection properties at the non-resonator frequencies, while the N AFC resonator controller provides zero-steady tracking error for the selected set of harmonics. In the vicinity surrounding the higher frequency AFC resonators, there are small notches in the Bode magnitude plot. These are due to the phase characteristics between the individual components in (2.175). We can correct for this through the feedforward channel, as will be discussed shorty.

Figure 2-42 shows the calculated closed-loop frequency response for the Variform FTS with the altered multiple resonator AFC system. We observe a noticeable im-

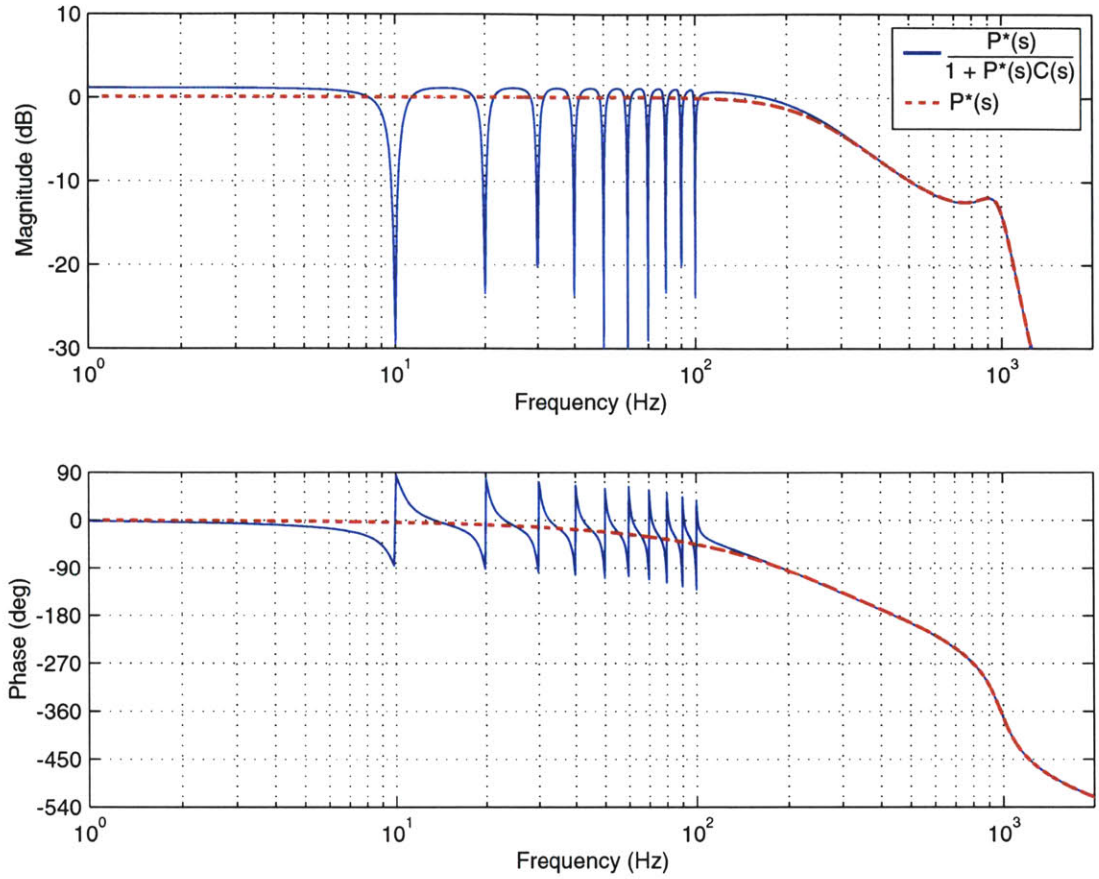

Figure 2-43: Comparison of the simulated frequency responses for Part A of (2.179) ($\frac{P^*(s)}{1+C(s)P^*(s)}$) and the conventional inner-loop $P^*(s)$.

provement in the closed-loop performance, simply with the addition of the unity feedforward channel. However, the Bode magnitude and phase curves still illustrate undesirable in-between resonator frequency performance, due to the magnitude notches and phase characteristics in the negative of the loop transmission. We can explain this waviness by looking at (2.175) as a summation of two separate transfer functions.

The closed-loop transfer function of the multi-resonator AFC controller, with a unity feedforward channel, can be written as

$$T_{FF}(s) = \frac{C(s)}{R(s)} = \underbrace{\frac{P^*(s)}{1+C(s)P^*(s)}}_{PartA} + \underbrace{\frac{C(s)P^*(s)}{1+C(s)P^*(s)}}_{PartB}. \tag{2.179}$$

The first part of (2.179) (Part A) provides a frequency response that is approximately equal to the shape of the conventional inner-loop $P^*(s)$ but with notches centered at the AFC resonator frequencies, as shown in Figure 2-43. The second part of of (2.179) (Part B) is equivalent to the closed-loop transfer function without a feed-forward loop, see (2.168). We observe that at the resonator frequencies, the gain of (Part A) is essentially $-\infty$ dB while (Part B) is 0 dB. When the two transfer functions are added together, (2.179) provides 0 dB and 0° of phase directly at the AFC resonator frequencies. The reduction in closed-loop performance, at the in-between resonator frequencies, is a direct result of magnitude and phase shift from the presence of $P^*(s)$ in the numerator of (Part A).

Figure 2-44 compares the frequency response of the individual components in (2.179), while Figure 2-45 shows the same Bode plot magnitude and phase plots in the vicinity of the 40 Hz AFC resonator. We see that (Part A) dominates the closed-loop system except for the small range of frequencies surrounding each resonator. As the frequency approaches ω_i, the phase difference between (Part A) and (Part B) decreases from π to $(\frac{\pi}{2} + \angle P(j\omega_i))$. Directly after each resonator frequency, this phase difference decreases from $(-\frac{\pi}{2} + \angle P(j\omega_i))$ to $-\pi$. As a result of this difference, for the frequencies directly before each AFC resonator, (Part B) is always subtracting from (Part A). Directly after each AFC resonator, (Part B) adds to (Part A) until the phase difference is less than $-\frac{\pi}{2}$. Figure 2-45 clearly illustrates these results. The resulting $\mathrm{T}_{FF}(j\omega)$ Bode magnitude curve becomes less than 0 dB before the AFC resonator frequency and then overshoots the 0 dB line after ω_i, gradually approaching 0 dB as the phase difference between (Part A) and (Part B) approaches $-\pi$.

We can greatly attenuate the magnitude and phase shifts by incorporating an inverse model of the inner-loop to the unity feedforward channel. Even simply adding $\angle \mathrm{P}^{*-1}(j\omega)$ would center the $-\pi$ phase discontinuities of (Part A) about 0°, which would lead to a constant $|\frac{\pi}{2}|$ phase difference between (Part A) and (Part B) in the

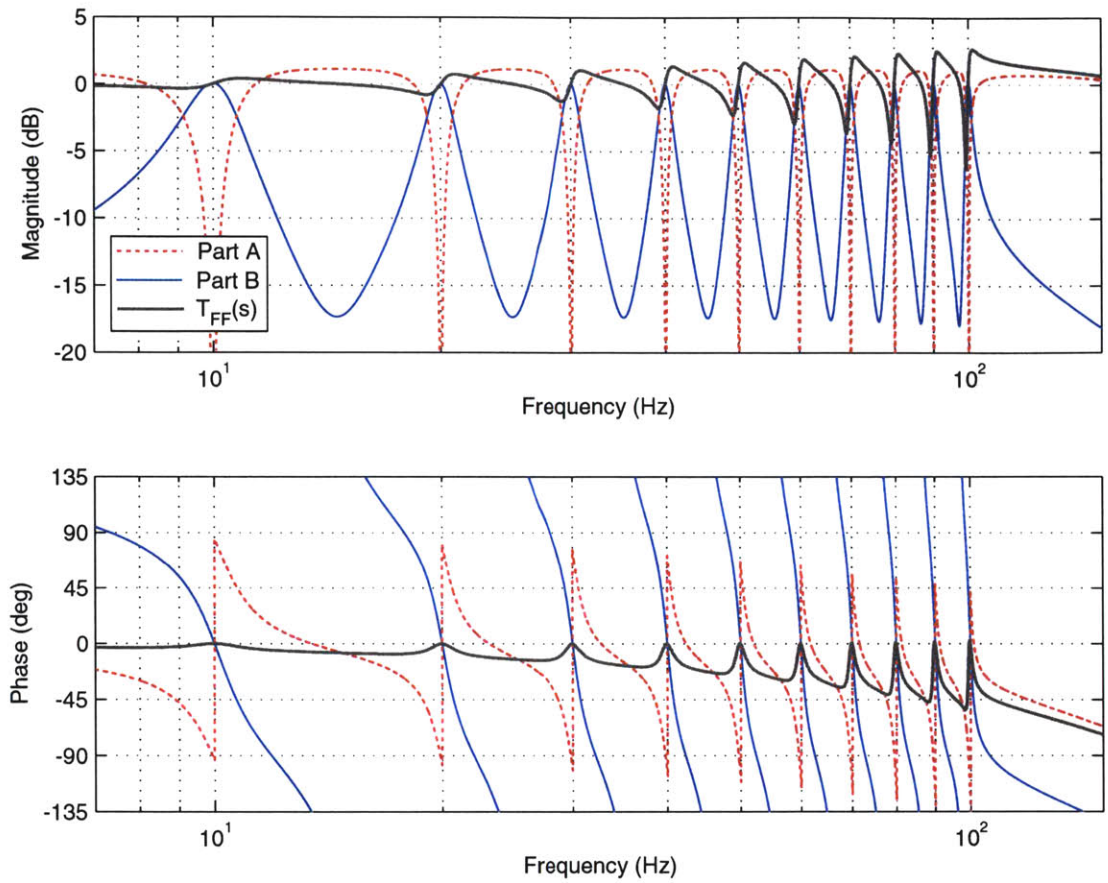

Figure 2-44: Comparison of the the simulated frequency responses for Part A, Part B and the complete AFC closed-loop transfer function $T_2(s)$ with a unity feed-forward loop.

vicinity of ω_i and improved closed-loop performance. If we add an inverse model of the inner-loop to the unity feedforward channel, the resulting closed-loop transfer function becomes

$$\frac{C(s)}{R(s)} = \frac{P^{*-1}(s)P^*(s) + C(s)P^*(s)}{1 + C(s)P^*(s)} \approx \frac{1 + C(s)P^*(s)}{1 + C(s)P^*(s)}. \tag{2.180}$$

Theoretically, we can invert the parametric model of the inner-loop and cancel the effects of P^*(s) in the numerator of (Part A) in (2.179), which leads to a closed-loop system with 0 dB and 0° for all frequencies. This is not practically done with

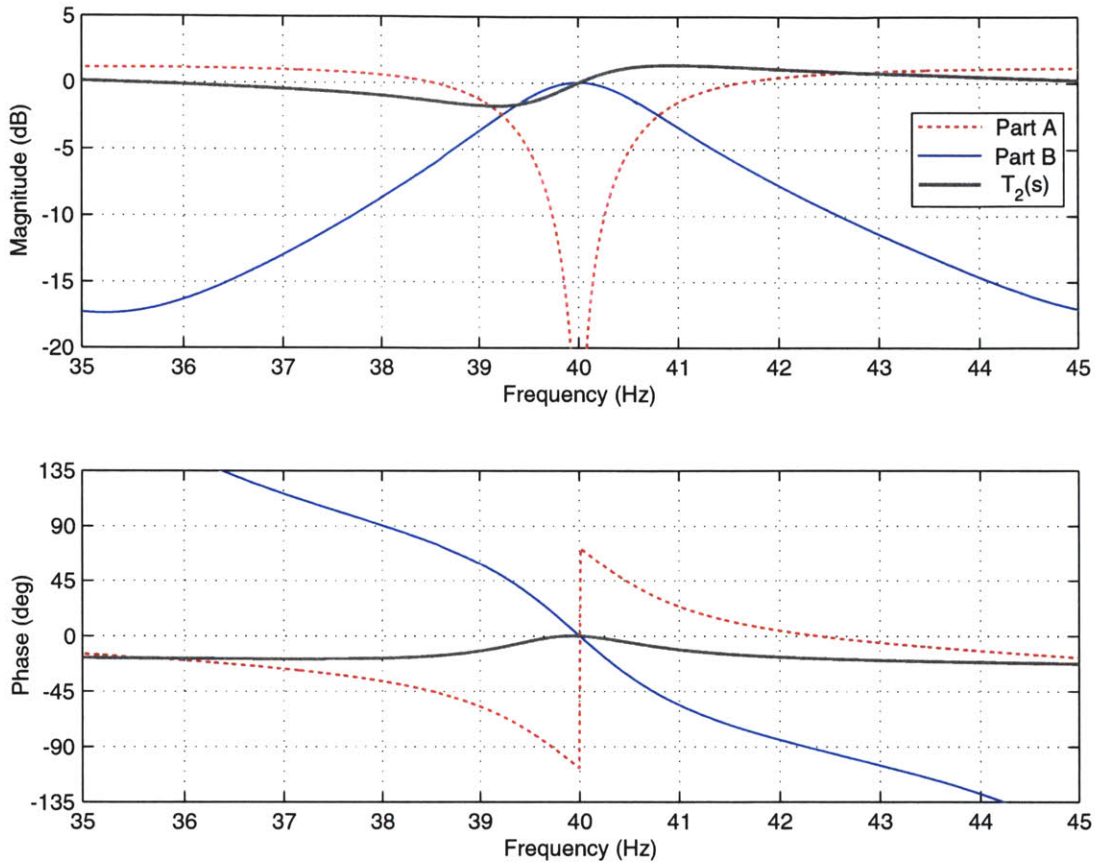

Figure 2-45: Comparison of the the calculated frequency responses for (Part A), (Part B) and entire closed-loop transfer function $T_{FF}(s)$ in the vicinity of the 40 Hz AFC resonator.

real-world systems though, since it is impossible to achieve a 100% perfect model of $P^{*-1}(s)$.

Figure 2-46 illustrates the predicted closed-loop frequency response if we assume 95% correct magnitude and phase information. The resulting closed-loop frequency response greatly improves, especially with the correct phase information. However, if the inner-loop includes non-minimum phase zeros, when we invert the parametric model they will become unstable poles [1]. Tomizuka [32] addressed this issue with his Zero Phase Error Tracking Controller (ZPETC) design. Also, we do not want a flat closed-loop frequency response past the highest frequency we are attempting to

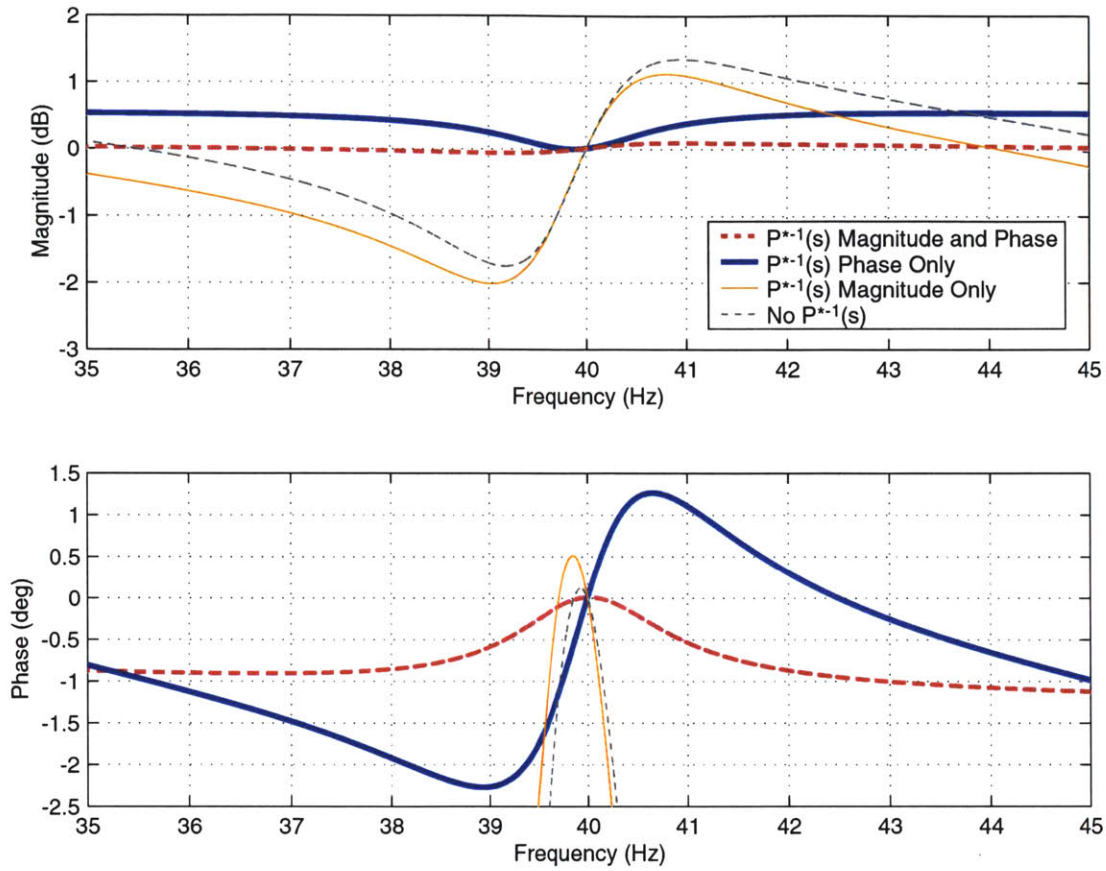

Figure 2-46: Comparison of several AFC closed-loop frequency responses in the vicinity of the 40 Hz resonator frequency with information from $P^{*-1}(s)$ added to the feedforward channel. We assume the inverse model contains 95% correct information.

follow. This will lead to the propagation of high-frequency system noise. Thus, we take advantage of command pre-shifting feedforward processing.

Since this particular multiple resonator AFC controller is meant for diamond turning applications, the trajectory reference signal contains integer harmonics of the fundamental spindle rotation frequency, which can be described by a Fourier series [1]. This means that the reference signal frequency components can be determined *a priori* and an inverse model of $P^*(s)$ is only required for this selected set of harmonics. We can obtain the desired $P^{*-1}(s)$ magnitude and phase information from an experimental frequency response of the inner-loop $P^*(j\omega)$, which we

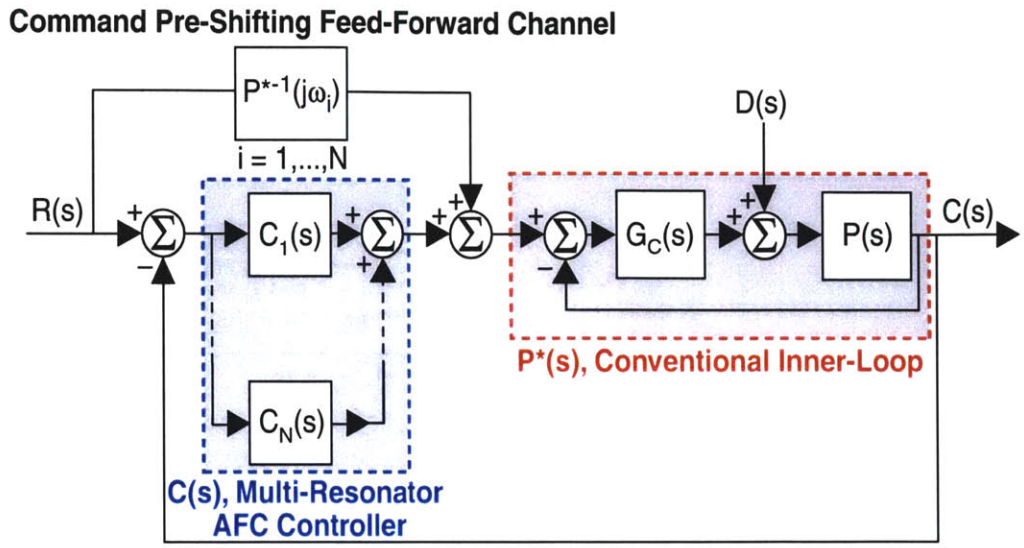

Figure 2-47: Our complete multiple resonator AFC closed-loop system for fast tool servos in diamond turning.

can then use to modify the feedforward channel to the inner-loop. This particular type of feedforward control, known as command pre-shifting, appears to have first been applied to the Large Optics Diamond Turning Machine (LODTM) for machining a non-axisymmetric phase corrector [31] and later adapted by Ludwick [1] for use in machining rotationally asymmetric spectacle lenses with a rotary FTS. We provide experimental closed-loop frequency response results of the Variform FTS with command pre-shifting in Section 3.6. For a more in depth discussion of command pre-shifting and feedforward control, the interested reader is referred to [1].

In summary, our final multiple resonator AFC closed-loop system for fast tool servos in diamond turning is shown in Figure 2-47. This system includes a conventional inner-loop controller $G_c(s)$, command pre-shifting feedforward channel $P^{*-1}(j\omega_i)$, and multiple resonator AFC controller C(s). The inner-loop is used to provide a well-characterized closed-loop frequency response for designing the outer AFC loop, with as high a closed-loop bandwidth as possible. The AFC controller provides zero steady-state error for a selected set of harmonics. Finally, since $P^*(s)$ still suffers from

magnitude and phase shift as a function of frequency, command pre-shifting to the inner-loop is provided through the $P^{*-1}(j\omega_i)$ channel.

Multiple Resonator Adaptive Feedforward Cancellation Controller Design

In our lab at the Massachusetts Institute of Technology, Marten F. Byl, Dr. Steven J. Ludwick, and Professor David L. Trumper have developed a loop-shaping approach to designing multiple resonator AFC systems [6]. We use this approach, along with the controller configuration in Figure 2-47, to experimentally implement a ten resonator AFC system on the Variform FTS using a PC-based digital control system, as presented in Section 3.6. In this section, we provide a summary of the tuning rules Byl, Ludwick, and Trumper use to maximize the AFC closed-loop performance yet still provide adequate stability margins.

An AFC controller with N resonators in parallel results in 2N design parameters, a proportional gain and phase advance parameter for each resonator, which must be adjusted to maximize closed-loop performance [6]. When placed in series with the inner-loop $P^*(s)$, the resulting negative of the loop transmission frequency response produces N resonator peaks, N-1 Bode magnitude local minima between the resonator frequencies, and N $-\pi$ phase discontinuities. We have determined in Section 2.2.3 that the phase advance parameters ϕ_i should be set equal to the phase of $P^*(s)$ evaluated at $s = j\omega_i$. This choice centers all of the $-\pi$ phase discontinuities about 0°, as shown in Figure 2-36, and maximizes the closed-loop phase margin for sufficiently low gain levels. Next, we need to determine the g_i levels to set the gain margin associated with each of the N-1 Bode magnitude local minima.

Byl *et al* have determined that the frequencies of the Bode magnitude local minima are located approximately at the geometric mean of the adjacent resonator frequencies

and can be expressed as

$$\omega_{min} \approx \sqrt{\omega_i \omega_{i+1}}. \tag{2.181}$$

We see from Figure 2-36 that the negative of the loop transmission with an AFC controller changes by $\pm 180^o$ in the vicinity of ω_{min}. This means that to ensure closed-loop stability, the N-1 local minima should be kept below the 0 dB line. We also know from Section 2.2.5 that the AFC closed-loop convergence rate and steady-state following errors are inversely proportional to the size of g_i. Thus we want the proportional gains to be as large as possible, especially for the dominating harmonics in the closed-loop error signal.

In the development of their gain selection method, Byl *et al* employ two approximations. First, they assume that the magnitude of the local minimum may be controlled by simply adjusting the proportional gains of the local resonators, since the Bode magnitude curve is dominated by the nearest resonators. This approximation greatly reduces the complexity of the gain selection process, and works quite well for the low resonator frequencies. However, Byl *et al* state that this approximation breaks down for the higher resonator frequencies, where the harmonics are more closely spaced on the logarithmic frequency axis. Next, they assume that the local minima are located at ω_{min} but go on to note that it is not particulary difficult to determine the exact frequency of the local minimum. However, this assumption provides a rapid way to get a good estimate of the system gain margin. Byl *et al* also state that this assumption works well when adjacent resonators only have small differences in their g_i values. For large gain differences, the local minima shifts towards the resonator with the lower gain, since the side bands of the higher gain resonator dominates the sum of both resonators over a larger frequency range. Byl, Ludwick, and Trumper summarize their AFC loop-shaping approach as followed:

1. Set ϕ_i for each resonator to the phase of the inner closed loop $\angle P^*(j\omega_i)$ to maximize phase margin.

2. Set initial resonator gains g_i to unity.

3. Using the previously determined values, compute the negative of the loop transmission -$L(j\omega) = C(j\omega)P(j\omega)$ and determine the local loop transmission minimum with the least gain margin.

4. Choose a desired gain margin.

5. Determine the ratio between the minimum gain margin found in step 3 and the desired gain margin.

6. Scale all of the resonator gains by the ratio found in the previous step.

7. Recompute and plot $C(j\omega)P(j\omega)$ to verify stability margins.

8. Adjust the gain margins of the local minima as desired by adjusting the gains of the adjacent resonators to trade robustness for control authority.

In the following section, we illustrate the loop-shaping tuning method for multiple resonator AFC systems with an example that is also adapted from Byl, Ludwick, and Trumper [6].

Example of a Multiple Resonator AFC System Design

Figure 2-48 illustrates the calculated closed-loop frequency response for the novel rotary fast tool servo developed in our lab, as mentioned previously in Section 1.3.1. The feedback controller consists of a conventional lead-lag compensator, which is detailed in the Doctoral work of Ludwick [1]. The state-space matrices for the entire closed-loop system are shown in Appendix E. Byl *et al* use this parametric model as

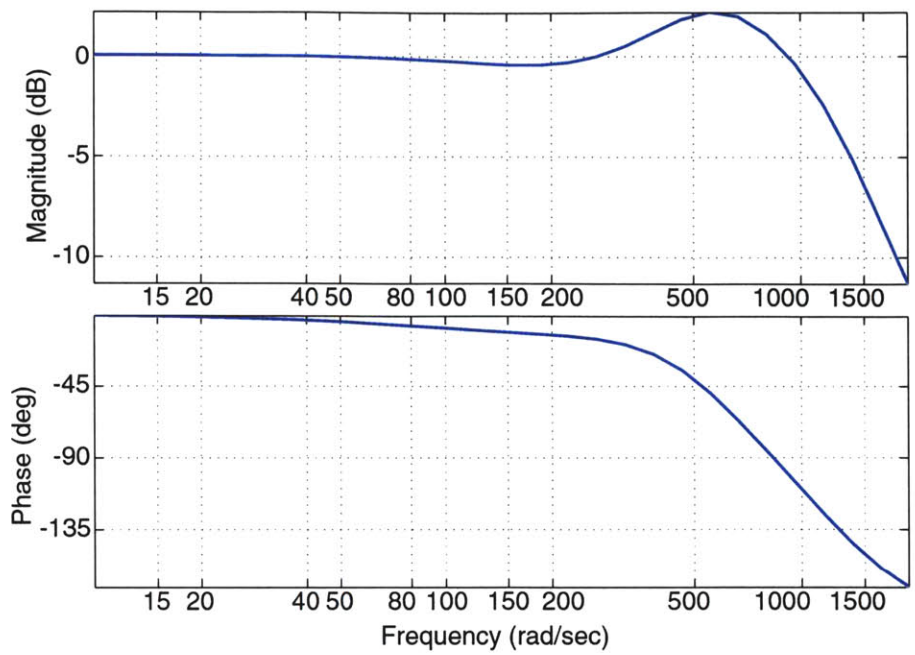

Figure 2-48: Calculated closed-loop frequency response for the rotary fast tool servo with a lead-lag compensator, from position reference input to measured position output. Figure adapted from Byl *et al* [6].

the inner closed-loop $P^*(s)$ and design a ten-resonator AFC controller at frequencies of

$$\omega_i = 20 \text{ Hz, } 40 \text{ Hz, ..., and } 200 \text{ Hz.} \tag{2.182}$$

Figure 2-49 illustrates the calculated negative of the loop transmission for the rotary FTS with the ten resonator AFC system, where the phase advance parameters $\phi_i = 0$ and the gains g_i are listed in Table F.2. We see that without the use of the phase advance parameter, the $-\pi$ phase discontinuities are centered at $\angle P^*(j\omega_i)$ and since $P^*(s)$ is not SPR, the resulting closed-loop system is unstable.

Figure 2-50 shows the negative of the loop transmission frequency response when the proper phase advance parameters are chosen and all of the gains are set equal to unity. We see that all of the $-\pi$ phase discontinuities are now centered about 0°, which results in approximately 84° of phase margin. The minimum gain margin

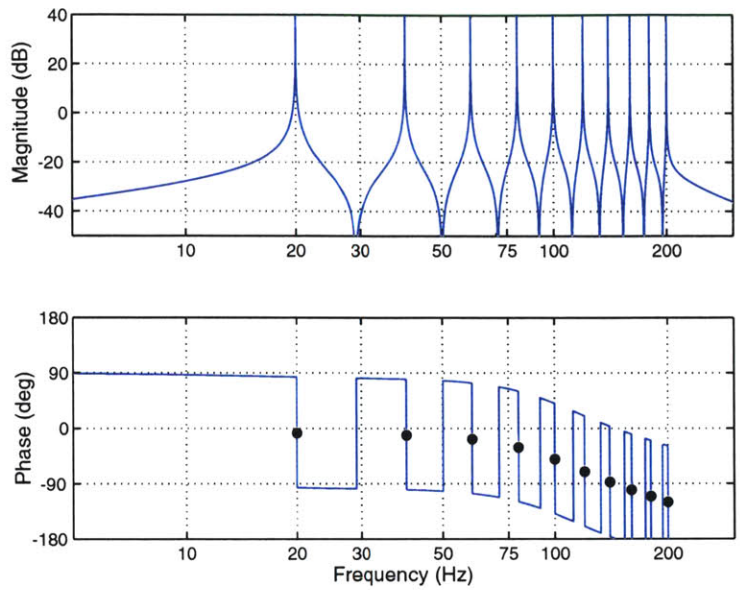

Figure 2-49: Calculated negative of the loop transmission frequency response $C_i(j\omega)P(j\omega)$ for the rotary FTS with ten AFC resonators. $\phi_i = 0$, while g_i and ω_i are listed in Table F.2 in Appendix F. The dots mark the center of the phase discontinuity. Figure adapted from Byl *et al* [6].

is about 34 dB and occurs at the local minimum between the fifth and sixth AFC resonator. Byl *et al* note that the frequency response tends to follow that of $P^*(j\omega_i)$ and the gain margin is a little conservative. Thus, they increase all of the gains to 5.18, resulting in approximately 20 dB of gain margin. Figure 2-51 the resulting negative of the loop transmission frequency response. We see that the local minimum between the fifth and sixth AFC resonator yields the minimum 20 dB gain margin but the low- and high-frequency local minima still yield excessive gain margin. Byl *et al* note that the low-frequency harmonics will dominate the error signal when machining asymmetric spectacle lenses. Therefore, they individually hand-tuned each resonator gain to achieve the final controller design.

The final negative of the loop transmission frequency response, after hand tuning the low- and high-frequency resonators to a target gain margin of 20 dB, is shown in Figure 2-52. All of the ϕ_i, g_i, and ω_i parameters for this system are summarized

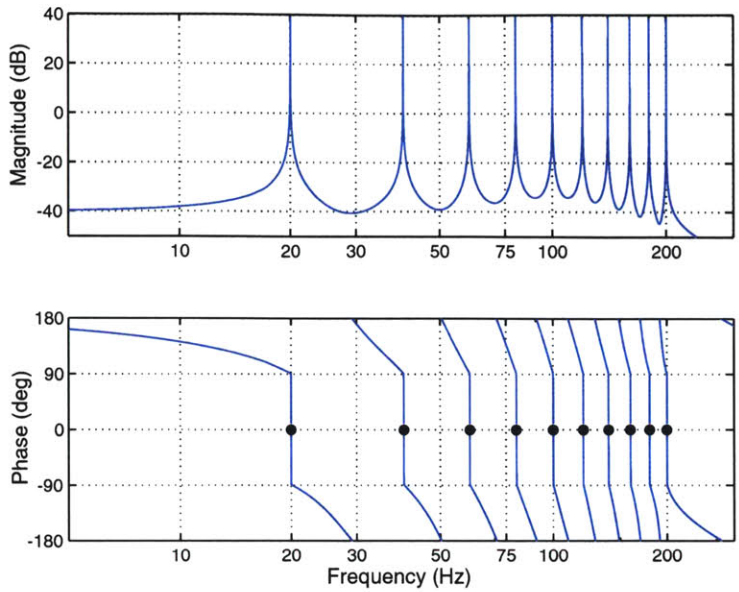

Figure 2-50: Calculated negative of the loop transmission frequency response $C_i(j\omega)P(j\omega)$ for the rotary FTS with 10 AFC resonators. The ϕ_i, g_i, and ω_i values are summarized in Table F.1 in Appendix F. Figure adapted from Byl *et al* [6].

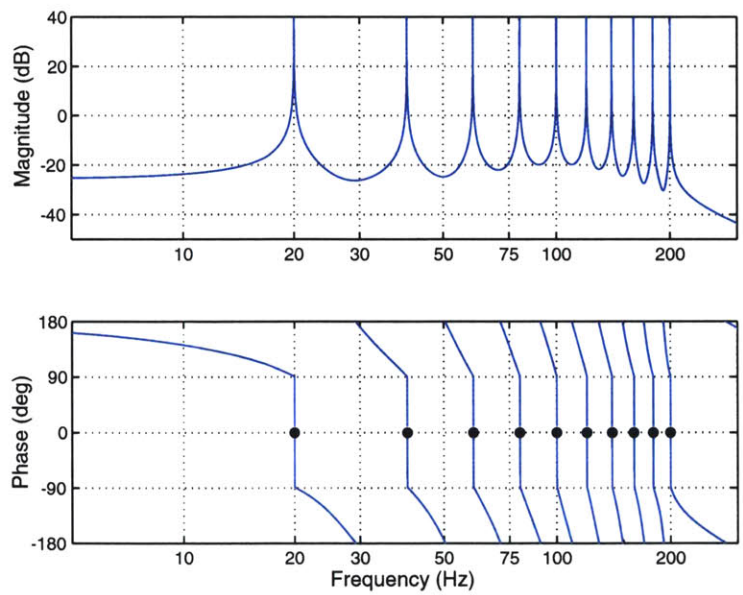

Figure 2-51: Calculated negative of the loop transmission frequency response $C_i(j\omega)P(j\omega)$ for the rotary FTS with 10 AFC resonators. The ϕ_i, g_i, and ω_i values are summarized in Table F.2 in Appendix F. Figure adapted from Byl *et al* [6].

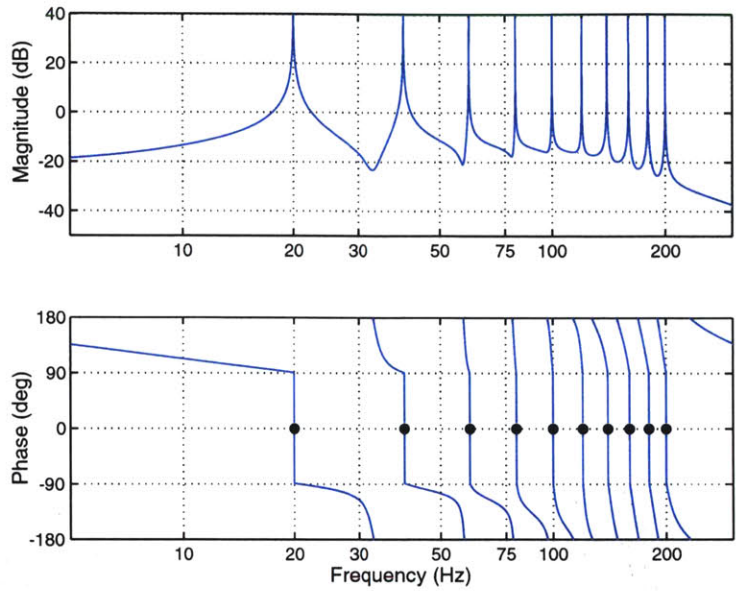

Figure 2-52: Calculated negative of the loop transmission frequency response $C_i(j\omega)P(j\omega)$ for the rotary FTS with 10 AFC resonators. The ϕ_i, g_i, and ω_i values are summarized in Table F.3 in Appendix F. Figure adapted from Byl *et al* [6].

in Table F.3 in Appendix F. We see that the low-frequency gain has been increased by a factor of 6, while the minimum gain margin (still located at the local minimum between the fifth and sixth AFC resonator) is only reduced to approximately 16 dB. This multiple resonator system provides a stable and robust closed-loop system, which provides particulary good closed-loop performance for the low-frequency harmonics.

Byl *et al* experimentally implemented the ten-resonator AFC system on the rotary fast tool servo while cutting a 0x4 diopter toric shape in CR39 (an acrylic plastic commonly used to make spectacle lenses) at a radius of 30 mm with a fundamental single rotation speed of 600 RPM [6]. The entire closed-loop system consisted of an inner-loop with a conventional lead-lag compensator, the final hand-tuned ten-resonator AFC controller, and a command pre-shifting feedforward channel. The resulting RMS following error was 1.2 μm, as shown in Figure 2-53, which equates to only 0.06% of the peak command amplitude.

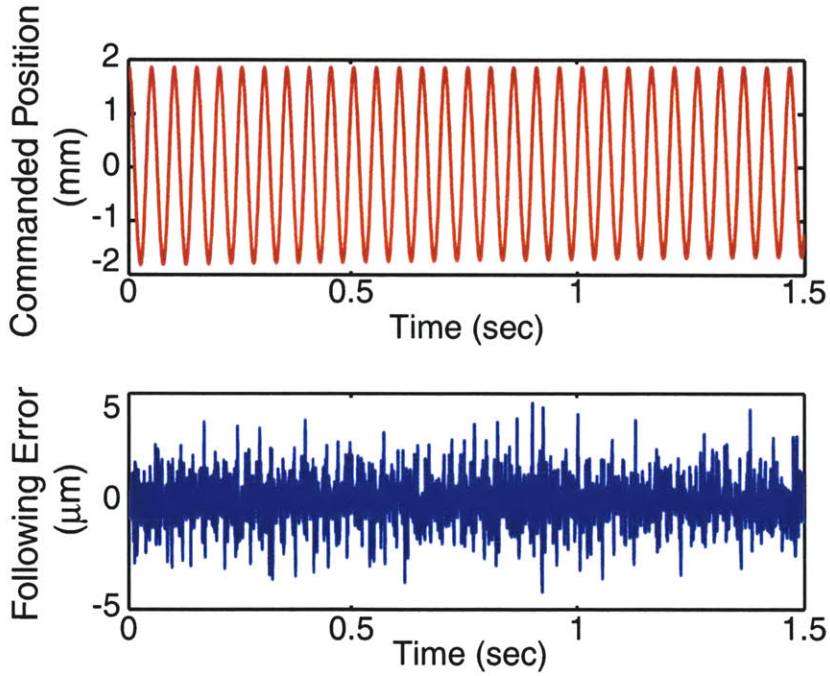

Figure 2-53: Measured error with both AFC and command pre-shifting while cutting a 0x4 toric in CR39 at 600 RPM. Data taken at a radius on the part of 30 mm. Figure adapted from Byl *et al* [6].

2.3 Adaptive Feedforward Cancellation Summary

In summary, Adaptive Feedforward Cancellation is a power control strategy for reducing/eliminating following errors in systems with periodic reference or disturbance inputs. Although internally linear time-varying, the AFC algorithm has an LTI equivalent transfer function, which provides an intuitive measure of the stability margins through classical control techniques. We can achieve increased control authority over a selected set of harmonics with a parallel array of N AFC resonators. To ensure a well characterized system, we should also close an inner-loop around the plant with a conventional compensator.

Our complete controller design for fast tool servos in diamond turning applications consists of a multiple resonator AFC controller, conventional inner closed-loop, and a command pre-shifting feedforward channel, as shown in Figure 2-47. This system is relatively straightforward to design, as long as the loop-shaping approach developed by Byl *et al* is followed. For additional details on this method and Adaptive Feedforward Cancellation background theory, the interested reader is referred to [6]. In the following chapter, we experimentally implement several conventional compensators on the Variform FTS. Then, we use one of these designs as an inner-loop and implement several simple AFC controller designs. Finally, we experimentally implement a ten-resonator AFC controller with a command pre-shifting feedforward channel.

Chapter 3

Experimental Controller Design

The Lawrence Livermore National Laboratory (LLNL) Engineering Division purchased a Variform Fast Tool Servo (FTS) from HiTek Power[1] in September of 1999. A part cutting study was designed and performed at LLNL using the FTS to determine the system's performance and feasibility as a precision manufacturing machine tool. One of these tests included cutting a section of a 1.5 m radius sphere and resulted in extremely high surface roughness. It was speculated that this result is due to a firmware error in the FTS on-board controller and/or the unconventional method used to cut the part. Recommendations by LLNL to improve the surface finish included using a machine that can execute larger part programs, implementing the on-board FTS inner charge loop, decreasing the noise in the LVDT feedback path and filtering the command signal. Due to the resulting poor surface finish, LLNL decided to cease any further testing. Rick Montesanti, currently a Ph.D. candidate in the Precision Motion Control (PMC) Laboratory at the Massachusetts Institute of Technology on a sponsored leave-of-absence from LLNL, brought the Variform FTS to MIT for further investigation.

In this chapter, we present the complete design and implementation of Adaptive Feedforward Cancellation algorithms on the Variform Fast Tool Servo. Section 3.1

[1]See Appendix K.

provides an overview of the as-received condition of the FTS hardware and offers a few recommendations to the observed hardware problems. Section 3.2 describes our method of controller implementation. Section 3.3 details the design and implementation of a conventional cascade controller after placing the FTS on-board controller into an open-loop configuration. Section 3.4 incorporates the FTS on-board inner charge loop in a second preliminary experimental controller design. In Section 3.5, we build upon the preliminary controller designs and increase the closed-loop bandwidth. Finally, in Section 3.6, we detail several Adaptive Feedforward Cancellation controller designs, as well as our complete multi-resonator AFC controller design with command pre-shifting feedforward channel.

3.1 Hardware Evaluation

When the Variform FTS was brought to MIT, minimal documentation was included describing the various internal components and operating parameters. Therefore, we purchased a Variform (9000-064 REVE) Technical Manual from Kinetics Ceramics[2]. This manual provides the operating instructions and details of the Variform FTS mechanism, high-power amplifier, and on-board FTS closed-loop controller.

In order to perform the various controller experiments, we removed one of the metal side plates from the high-power amplifier and constructed a new Plexiglas shield to expose the amplifier interface (I/F) board yet still provide protection from the high voltage components. The I/F board provides full access to the FTS inputs and outputs that are required to perform the AFC controller experiments. Figure 3-1 through Figure 3-4 show the FTS and experimental hardware as well as a closeup of the amplifier I/F board.

When testing began on the FTS, there was a problem with it blowing fuses. Before the system came to MIT, Bussman type GDC 6.3 amp slow blow fuses were placed in

[2]See Appendix K.

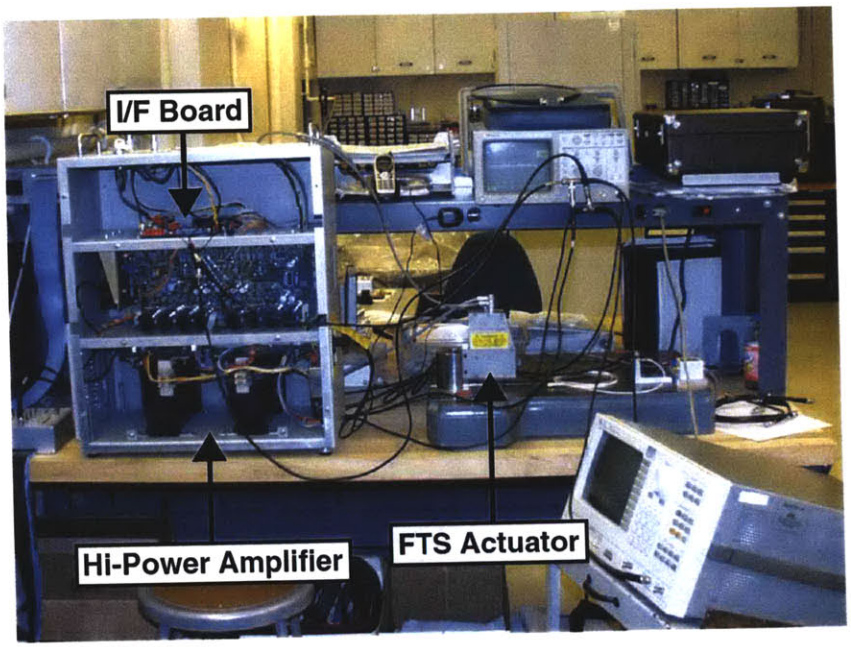

Figure 3-1: Variform FTS and experimental hardware.

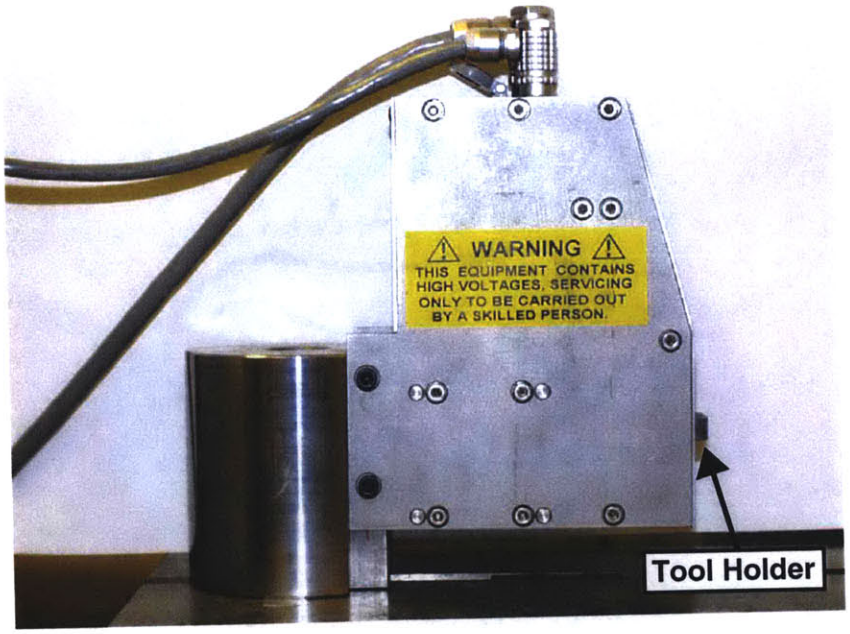

Figure 3-2: FTS piezoelectric actuator mounted on an experimental test base. Diamond tool mounted at lower right.

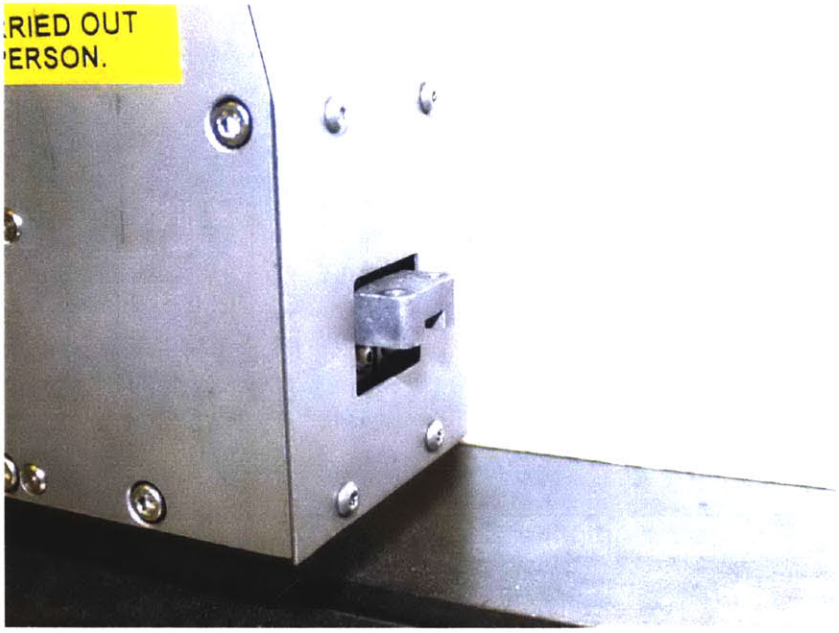

Figure 3-3: Variform FTS piezoelectric actuator tool holder.

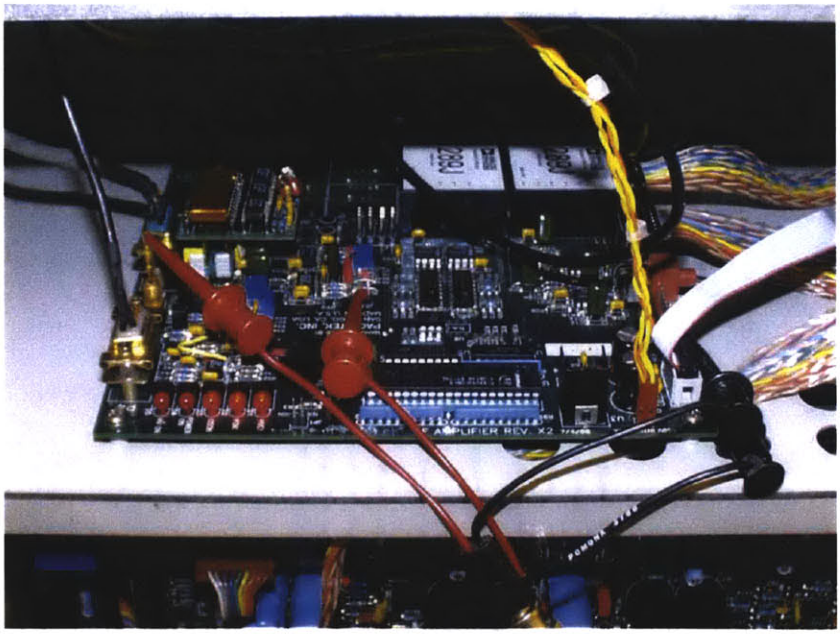

Figure 3-4: Variform Fast Tool Servo amplifier interface (I/F) board.

the fuse holder. These fuses are not large enough to survive repeated power cycling of the amplifier and will eventually fail. The Variform (9000-064 REVE) Technical Manual recommends using an 10 amp slow blow fuse. Therefore, Bussman type GMC 10 amp slow blow fuses were placed into the amplifier and the problem appears to have been solved. The manual also recommends that whenever the AC power is turned off, a one-minute wait period must be observed in order for the reset of the inrush current limiter. This particular current limiter utilizes a Negative Temperature Coefficient (NTC) thermistor to limit the inrush current, which requires a one-minute wait period for the thermistor to cool off and thus rise to a safe level.

Included in the limited Variform FTS literature from LLNL were several experimental closed-loop frequency responses. According to these plots, successful closed-loop frequency response tests were performed in February of 2000. We attempted our own experimental closed-loop frequency response to verify these results and make sure the hardware was still in proper working order. Within several seconds of turning the FTS amplifier on, the system made a buzzing sound and the high voltage portion shut down. This behavior indicates that the controller on the FTS amplifier I/F board is out of calibration and requires adjustments to stabilize the servo loop.

To eliminate the on-board controller instability problem, the LDVT SET UP procedure in the Variform (9000-064 REVE) Technical Manual should be followed. However, a copy of an e-mail in the FTS literature from Mike Macklin of HiTek Power states that an offset circuit was added to the LVDT assembly board on newer Variform FTS models so the DC offset voltage can be removed electronically. A call to HiTek Power resulted in acquiring the updated LVDT assembly wiring schematic (see Figure 3-5) and instructions on how to wire the offset circuit.

Mike Macklin provided the following directions. Two 47 kΩ 1/8 W 1% resistors and one multi-turn (15 turn minimum) 20 kΩ potentiometer are used to bias the offset voltage. The 47 kΩ resistors are to be attached to each end of the potentiometer while

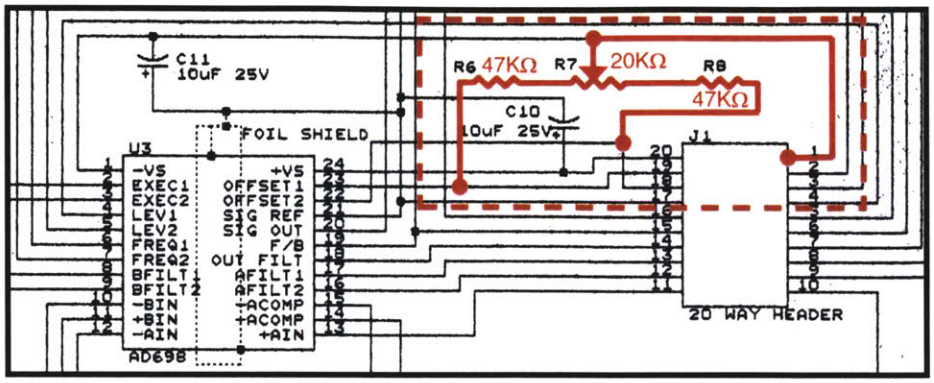

Figure 3-5: Updated LVDT assembly board wiring schematic. (Note, the LVDT DC Voltage Offset Circuit is highlighted in RED.) Components shown are on the amplifier interface board.

the potentiometer wiper output is connected to pin 1 of the 20-pin header. The other ends of the resistors are then connected to pin 18 and 19 of the 20-pin header while the potentiometer may be secured to the LVDT interface circuit with any general form of epoxy. Figure 3-5 highlights the locations of all three offset circuit components on the updated LVDT assembly board wiring diagram. This circuit allows adjustments of up to $\pm$ 2 V DC but if the voltage is outside of this range, the piezoelectric actuator must be opened and the LVDT mechanical zero adjusted as stated in the LDVT SET UP procedure.

The Variform FTS uses a small Linear Variable Differential Transformer (LVDT) located inside of the piezoelectric actuator housing as the feedback sensor for the on-board controller. We speculate that during shipment from LLNL to MIT, the LVDT's mechanical zero shifted from the nominal position and is causing the instability problem. When we received the FTS hardware, a 0.34 lb cutting tool adapter was still attached to piezoelectric actuator's tool holder, as shown in Figure 3-6. This relatively large mass and the random road vibrations during shipment could have easily dislodged the LVDT mechanical zero.

Due to time constraints, the work presented in this chapter does not include im-

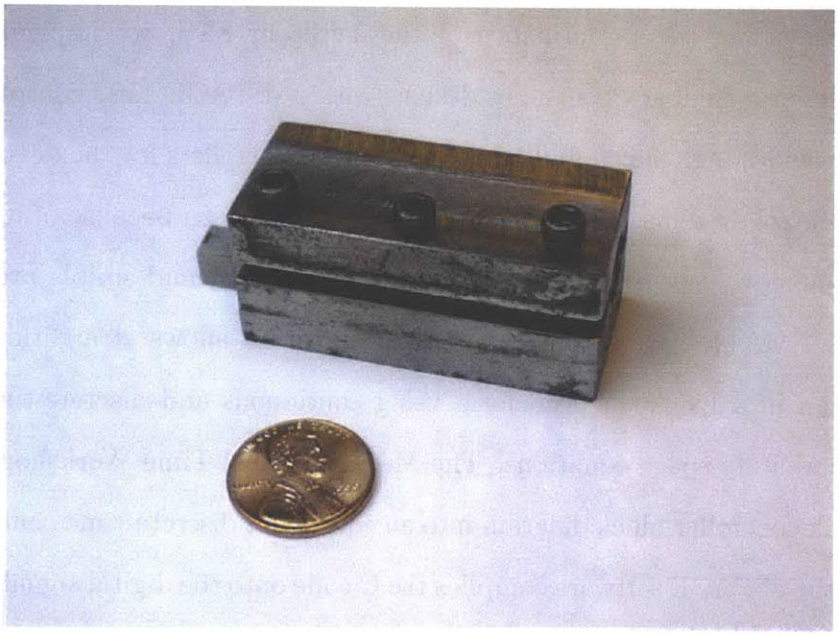

Figure 3-6: 0.34 lb. cutting tool adapter attached to the Variform Fast Tool Servo tool holder during shipment from the Lawrence Livermoore National Laboratory to the Precision Motion Control Lab at the Massachusetts Institute of Technology. This Holder is far too massive for use as a payload for the FTS.

plementing the LVDT offset circuit to fix the closed-loop instability problem. Instead, we bypass the controller on the amplifier I/F board, as shown in Figure 3-26, and a utilize a dSPACE[3]-based digital controller to implement our own conventional control systems as well as Adaptive Feedforward Cancellation controller designs.

3.2 Control System Implementation

While investigating the performance of the Varfirom FTS, we implemented several experimental feedback controller designs with a dSPACE 1102 controller board. dSPACE provides high-speed multi-variable digital controllers for the development of real-time control systems. This particular model was chosen because of its availability within our lab, user-friendly interface with MATLAB[4] and simple programming capabilities. MATLAB's graphical Simulink[5] software allows straightforward controller design in a block diagram form using continuous and discrete-time transfer functions and state-space equations. The MATLAB Real Time Workshop translates the Simulink controller block diagram into an equivalent discrete-time controller algorithm and the dSPACE software compiles the C code onto the digital signal processing board, interfacing the physical hardware with the 1102 controller board [26]. Using dSPACE ControlDesk software, we can create interactive control panels for monitoring the inputs and outputs of the position servo-loop and adjusting the controller parameters in real-time.

As mentioned previously, after determining the apparent instability of the on-board FTS controller, we decided to completely bypass the controller on the amplifier I/F board and create our own dSPACE-based feedback controllers (see Figure 3-7). Initially, we designed several conventional cascade controllers to close a feedback loop around the FTS hardware and then implemented a multiple-resonator Adaptive Feed-

[3]See Appendix K.
[4]See Appendix K.
[5]See Appendix K.

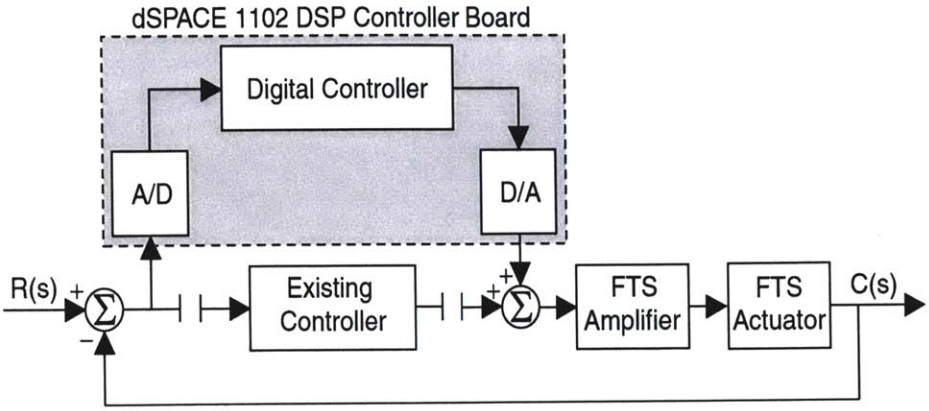

Figure 3-7: dSPACE digital controller implementation bypassing the FTS controller on the amplifier interface board.

forward Cancellation controller with a command pre-shifting feed-forward loop. This requires altering the jumper configurations on the amplifier I/F board to completely bypass the on-board controller and place the FTS into an open-loop configuration.

There are numerous jumpers located on the amplifier I/F board that are used to enable and disable the various FTS hardware components and on-board closed-loop controller. The Variform (9000-064 REVE) Technical Manual provides the names and locations of all the jumpers that are required to disable the on-board controller and permit the implementation of the dSPACE 1102 controller board. Appendix A includes a schematic of the I/F board with all pertinent jumper locations highlighted. In order to obtain an open-loop configuration, we need to place the jumpers at locations JP5 and JP7 in the (a-b) position (see Figure 3-8) and remove the jumpers at locations JP10, JP15 and JP18. Once this is completed, we are ready to design the dSPACE-based feedback controllers.

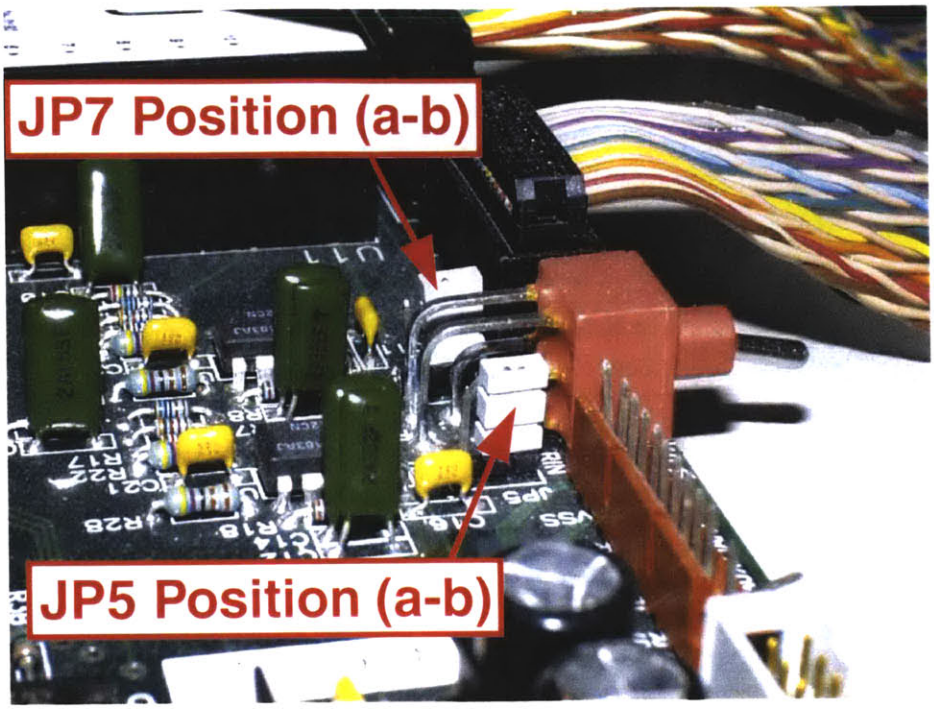

Figure 3-8: Amplifier interface board illustrating the JP5 and JP7 position (a-b) jumper locations.

3.3 Preliminary Controller Design

With the Variform FTS in an open-loop configuration, we begin designing a preliminary dSPACE-based feedback controller. The first step to obtaining satisfactory closed-loop performance is to measure an open-loop frequency response on the as-received hardware. We use a Hewlett Packard (HP) model #35665A Dynamic Signal Analyzer (DSA) to collect this data, inputting a 100 mV_{p-p} sinusoidal signal from the HP DSA to the FTS through JP15 (pin b) on the amplifier I/F board with ground referenced to JP2 (pin 2) while monitoring the FTS output from the LVDT at JP9 with reference again at JP2 (pin 2). Figure 3-4 illustrates all of these connections on the amplifier I/F board (Appendix A includes closeup pictures of the individual connections), while the results of the experimental open-loop frequency response are shown in Figure 3-9. We import this data into MATLAB and are able to well-model

the plant as a sixth order transfer function of the form

$$\frac{V_{out}}{V_{in}}(s) \triangleq G_{p_1}(s) = \frac{-0.54325}{(\frac{s}{2600}+1)(\frac{s}{18850}+1)(\frac{s^2}{\omega_1^2}+\frac{2\zeta_1 s}{\omega_1}+1)(\frac{s^2}{\omega_2^2}+\frac{2\zeta_2 s}{\omega_2}+1)}\left[\frac{V}{V}\right], \quad (3.1)$$

where the parameters as selected as $\omega_1 = 6085$ rad/sec, $\zeta_1 = 0.085$, $\omega_2 = 6283$ rad/sec, and $\zeta_2 = 0.051$ (Appendix B includes the State Space Matrices for $G_{p_1}(s)$).

$G_{p_1}(s)$ contains poles at -517.23±6063j, -3204.3±5404.5j, -2600 and -18850 rad/sec. The fourth order complex conjugate pole pairs are apparently due to the natural resonance of the FTS piezoelectric stacks and tee-lever/tool-beam mechanism at approximately 1 kHz while the LVDT has a built-in first order low-pass filter with a breakpoint at 3 kHz ($\approx$ 18850 rad/sec). We speculate that the pole at -2600 rad/sec is due to either the I/F board or LVDT electronics. The minus sign in the numerator of (3.1) is due to a 180° phase difference between the reference input and LVDT output signal, which we discuss further in the chapter. Figure 3-9 includes the simulated Bode plot of $G_{p_1}(s)$, illustrating how well the parametric model agrees with the experimental data for the frequencies of interest.

During the initial stages of testing, we bypass the LVDT sensor and implement a Kaman Instrumentation[6] inductive sensor to measure the displacement of the FTS, in order to test with simpler dynamics. This requires attaching a flat aluminum target to the piezoelectric actuator tool holder, as seen in Figure 3-10. Figure 3-11 shows the implementation of the Kaman sensor and aluminum target on the FTS hardware, while Figure 3-12 compares the resulting experimental open-loop frequency response to the simulated Bode plot for $G_{p_1}(s)$. The experimental FTS open-loop frequency response with the Kaman Instrumentation sensor illustrates the 1 kHz resonance but the curves do not show the additional low-pass filtering as seen with the LVDT output. These results support the speculation that the pole at -2600 rad/sec is due to the

[6]See Appendix K.

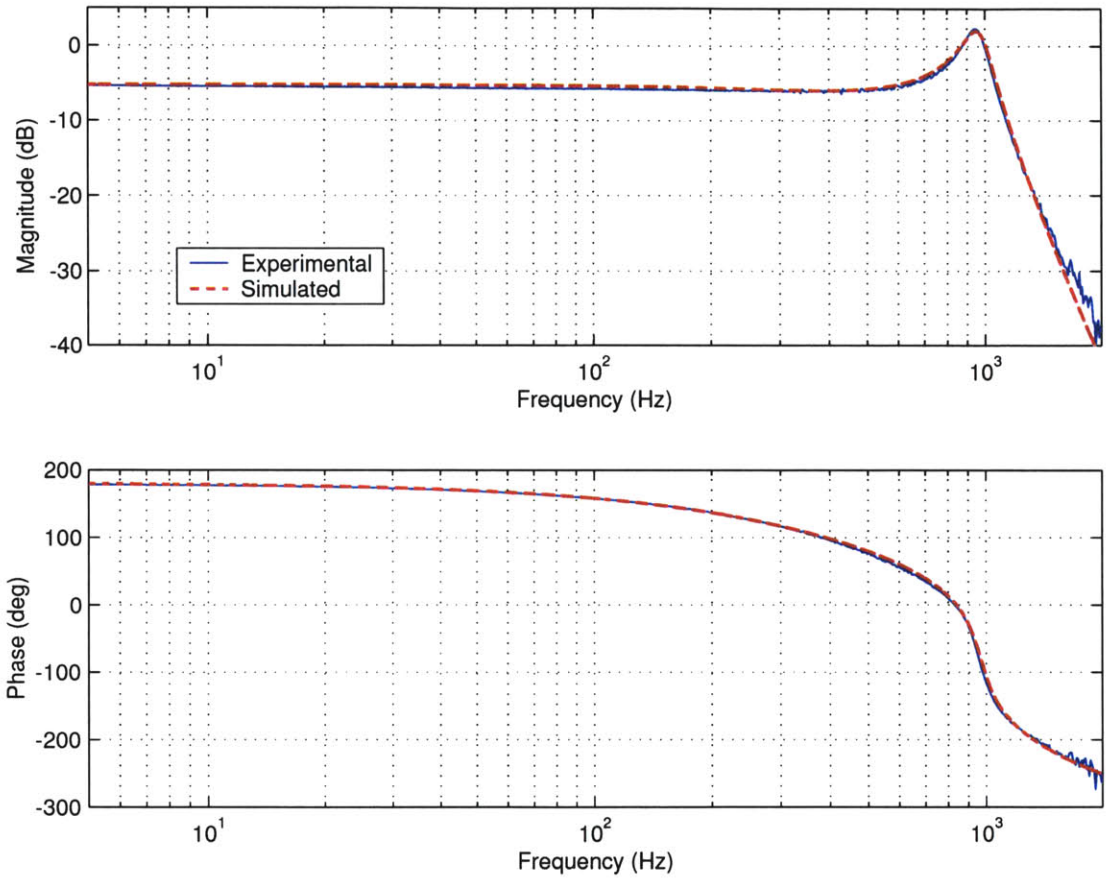

Figure 3-9: Comparison of the experimental and fitted FTS hardware open-loop frequency responses with $G_{p_1}(s)$. (Note, the Bode phase plots as shown are shifted by 180°, since a positive change in the command voltage results in a negative change in FTS displacement.)

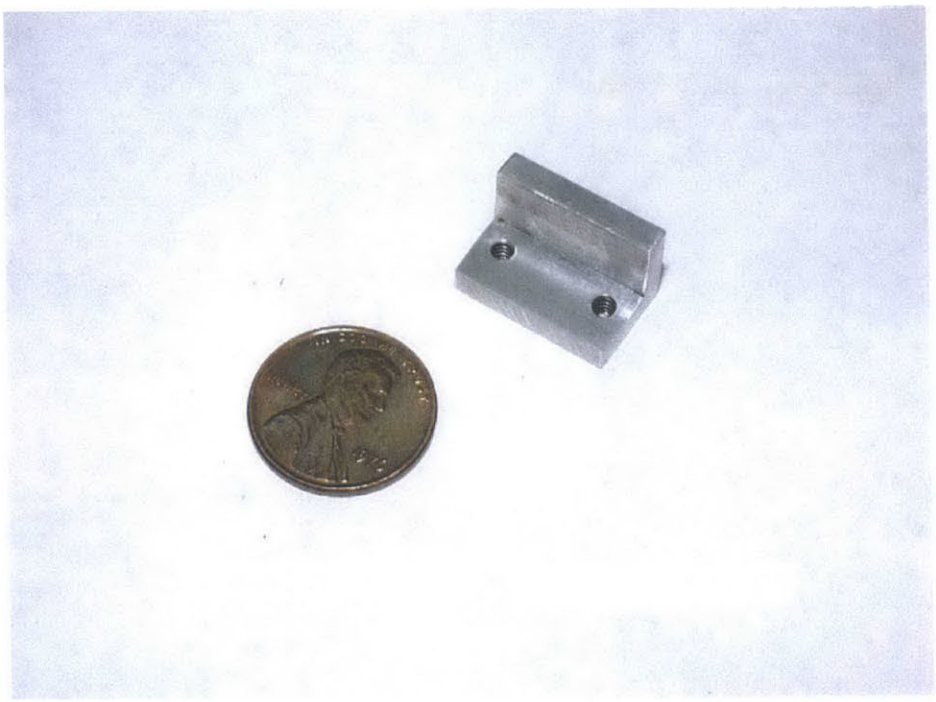

Figure 3-10: 0.006 lb aluminum target used for initial open-loop frequency response testing with the Kaman Instrumentation inductive sensor.

dynamics of either the I/F board or LVDT electronics. The system with the Kaman sensor is easier to control due to less negative phase shift.

However, in order to take advantage of the Kaman Instrumentation sensor and also be able to attach a cutting tool to the front of FTS, the inductive sensor would have to be placed inside the piezoelectric actuator housing. This is not an easy modification, and so we decided to revert back to the LVDT as the feedback sensor and design the preliminary dSPACE controller with $G_{p_1}(s)$, despite the additional negative phase shift.

The preliminary continuous-time controller transfer function is given by

$$G_{c_1}(s) = \frac{K_p}{s}, \tag{3.2}$$

which consists of an integrator with an associated gain K_p. We use (3.2) to close a

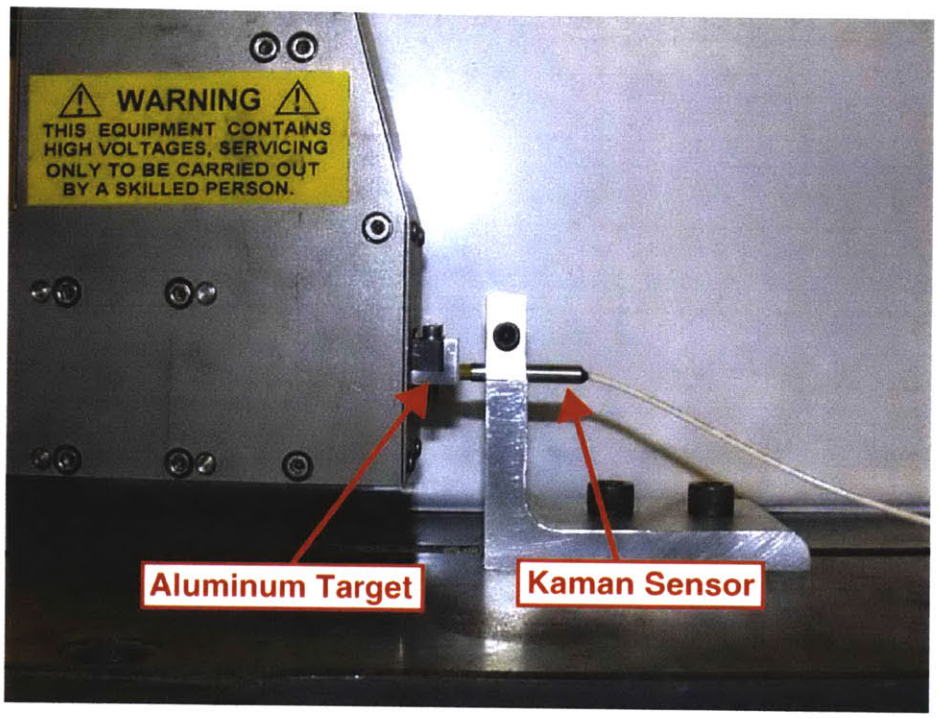

Figure 3-11: Variform FTS piezoelectric actuator with an aluminum target connected to the tool holder and Kaman Instrumentation induction sensor.

preliminary feedback loop around the FTS hardware in order to get a basic dSPACE-based controller working and see how well the simulated model predicts the experimental results. An even simpler controller would only use a proportional gain but the plant's flat low-frequency Bode magnitude curve and 1 kHz resonant peak makes the system essentially impossible to achieve a stable 0 dB crossover frequency with proportional control.

Without introducing additional controller dynamics, the resonant peak (and therefore the rest of the Bode magnitude curve) must stay below the 0 dB line to keep the feedback loop from going unstable. Thus, we add an integrator to the controller, which increases the low-frequency gain of the negative of the loop transmission $-L(s)$ and provides a -20 dB/decade slope below 1 kHz. Figure 3-13 illustrates the preliminary closed-loop system block diagram.

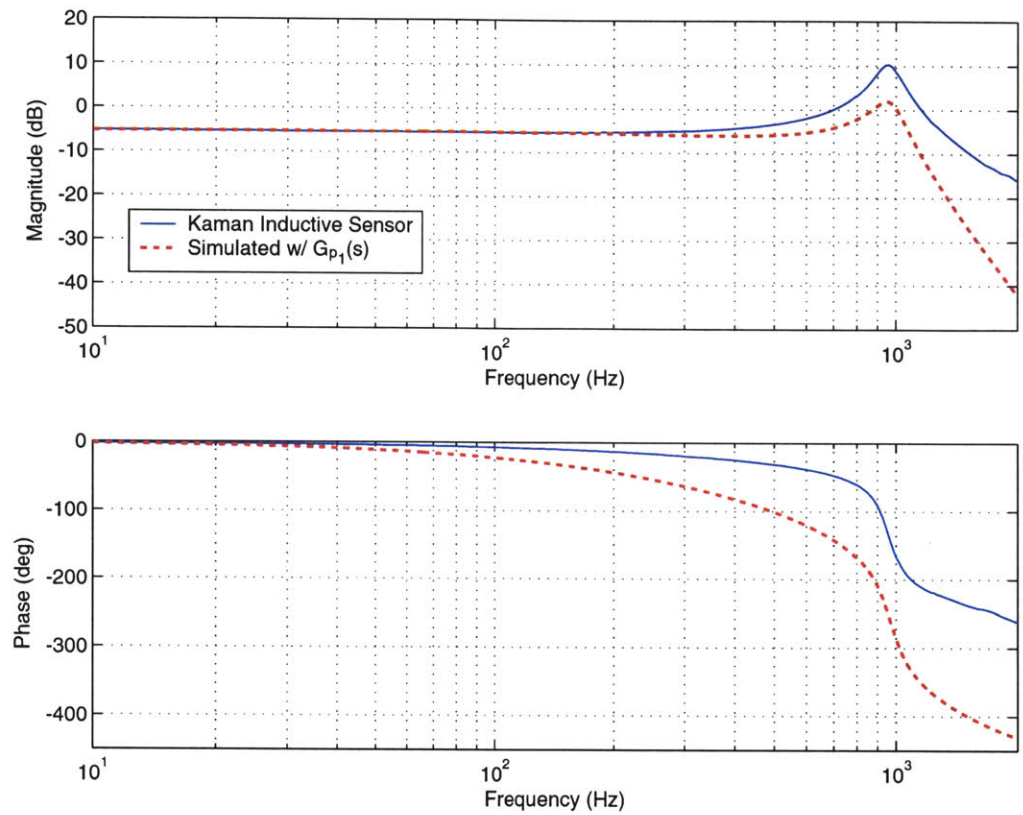

Figure 3-12: Comparison of the simulated $G_{p_1}(s)$ Bode plot and experimental FTS open-loop frequency response with the Kaman Instrumentation inductive sensor replacing the built-in LVDT.

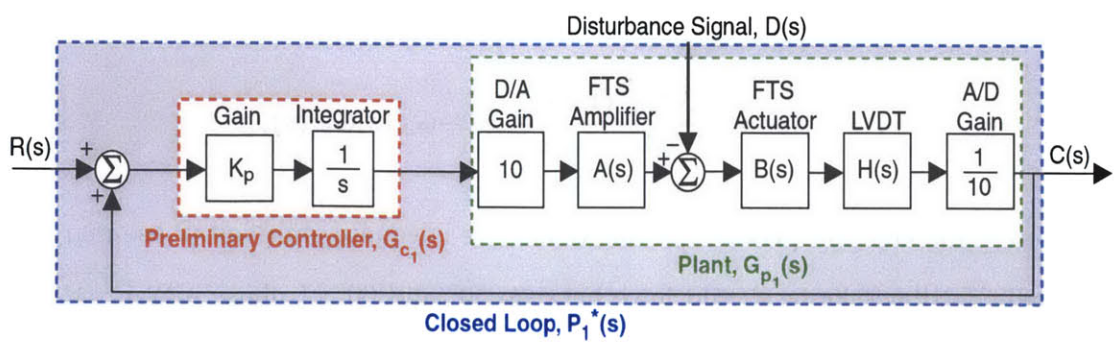

Figure 3-13: Preliminary FTS closed-loop system block diagram with an integral controller. A plus sign has been placed next to the feedback signal instead of the conventional negative feedback nomenclature, since the output C(s) is 180° out of phase with respect to the reference input R(s). This sign change is required to ensure closed-loop stability.

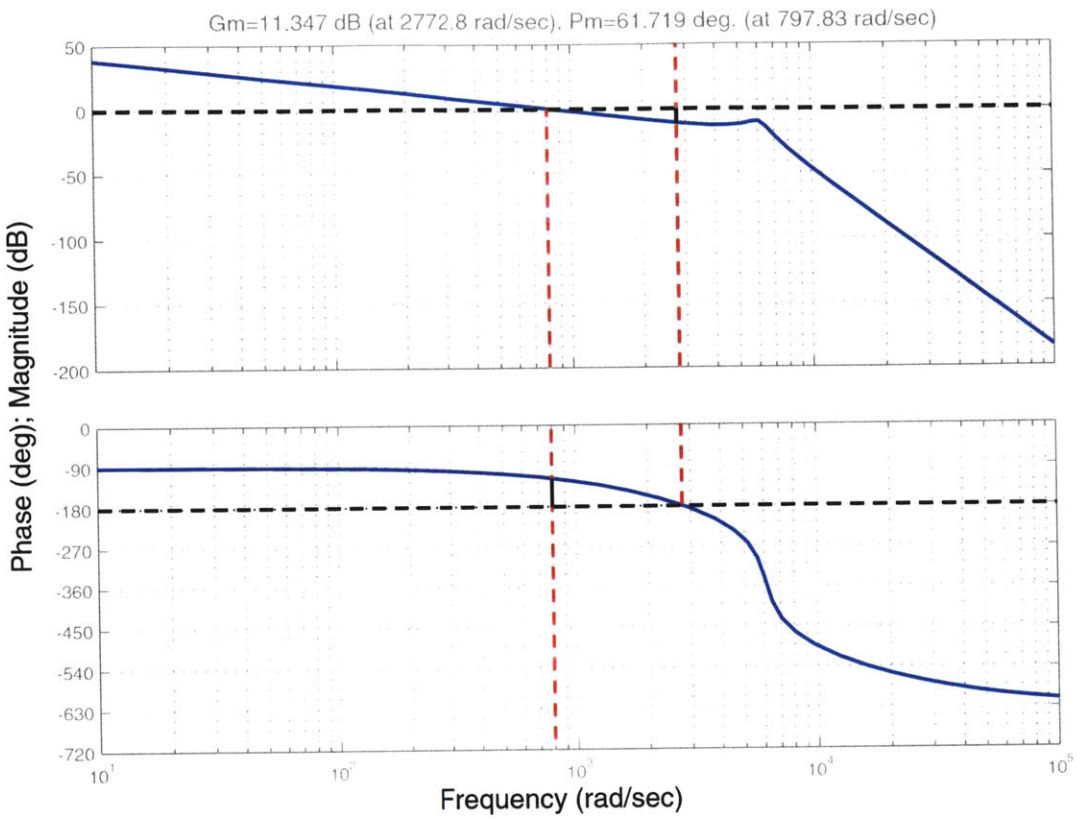

Figure 3-14: Simulated negative of the loop transmission Bode plot indicating the gain and phase margin for the Variform FTS with the preliminary controller $G_{c_1}(s)$.

We simulate the resulting negative of the loop transmission

$$-L_1(s) = \frac{\text{LVDT Output}}{\text{I/F Board Input}} = -G_{c_1}(s)G_{p_1}(s), \tag{3.3}$$

and determine an appropriate K_p value to achieve adequate gain and phase margins. Typically, feedback loops should have between 30° and 60° of phase margin (P.M.), more than 6 dB of gain margin (G.M.) and a slope of about -20 dB/decade at the 0 dB crossover frequency [50]. This ensures a sufficiently stable and robust closed-loop performance. The simulated negative of the loop transmission with the gain K_p set equal to 1500, measured from the input of $G_{c_1}(s)$ to the feedback of the LVDT, predicts an 11 dB gain margin, 62° phase margin and 798 rad/sec ($\approx$ 125 Hz)

0 dB crossover frequency (see Figure 3-14), while the simulated closed-loop transfer function

$$P_1^*(s) = \frac{C(s)}{R(s)} = \frac{L_1(s)}{1 + L_1(s)} = \frac{G_{c_1}(s)G_{p_1}(s)}{1 - G_{c_1}(s)G_{p_1}(s)}, \tag{3.4}$$

predicts a 1620 rad/sec ($\approx$ 250 Hz) -3 dB bandwidth.

We perform the preliminary dSPACE-based controller experiments by converting $G_{c_1}(s)$ into an equivalent z-transform and download the discrete-time algorithms onto the dSPACE 1102 controller board. The complete experimental Simulink block diagram we use to conduct closed-loop testing, as shown in Figure 3-15, includes an integrator, variable gain, on/off switch, DC offset, saturation, A/D convertor, D/A convertor and Dynamic Signal Analyzer block.

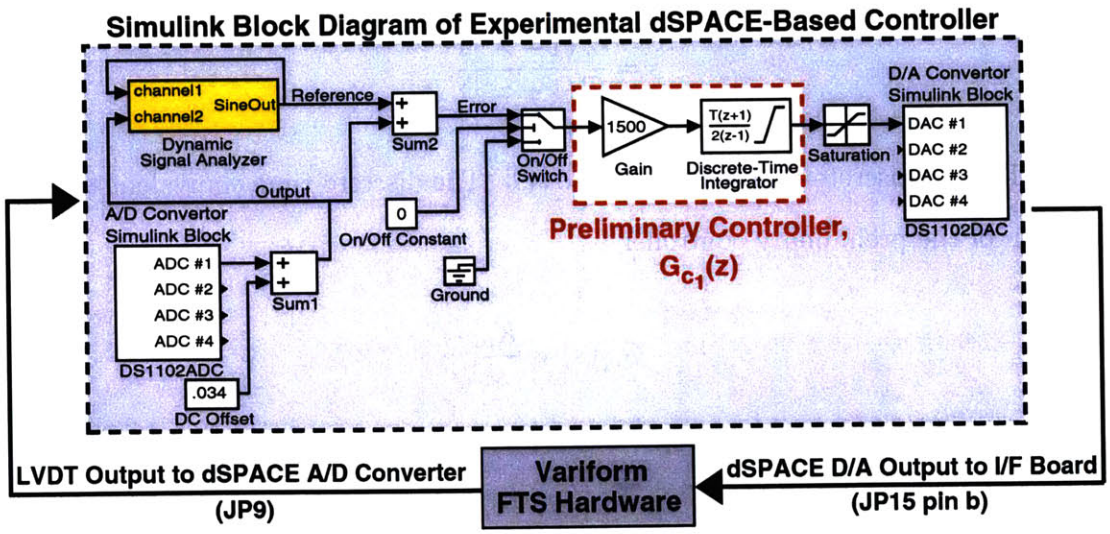

Figure 3-15: Preliminary experimental Simulink closed-loop block diagram with the experimental controller G_{c_1}(z).

As mentioned previously in Section 3.2, dSPACE controllers can be designed with continuous-time transfer functions but the experimental algorithms are ultimately implemented in discrete-time on the dSPACE 1102 controller board. To reduce the complexity of the Simulink controller models and achieve the fastest sampling rates possible, we convert all of the continuous-time controller designs into discrete-time

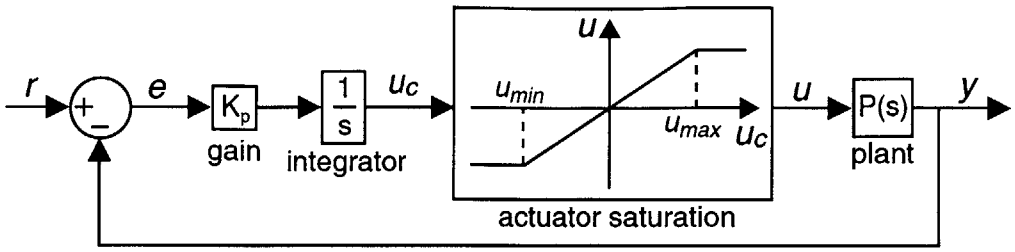

Figure 3-16: Closed-loop block diagram with an integrator and actuator saturation. Figure taken from Franklin, Powell, and Emami-Naeini [49].

transfer functions using the Tustin transformation [41].

The Tustin transformation, or bilinear approximation, approximates the continuous-time transfer function with a discrete-time z-transform by setting

$$s = \frac{2}{T}\frac{(1 - z^{-1})}{(1 + z^{-1})}, \tag{3.5}$$

where T is the discrete-time sampling rate [49]. The discrete-time equivalent transfer function of the preliminary controller

$$G_{c_1}(s) = \frac{K_p}{s}, \tag{3.6}$$

sampled at 25 kHz, is given by

$$G_{c_1}(z) = \frac{0.03z + 0.03}{z - 1}. \tag{3.7}$$

Figure 3-15 illustrates a discrete-time integrator Simulink block in place of a discrete-time transfer function block. This particular block provides the bilinear approximation to a continuous-time integrator but also includes integration saturation limits. We utilize this adjustable form of integral anti-windup throughout all of the applicable dSPACE-based FTS controller experiments.

Integral anti-windup keeps a feedback loop with an integrator in the controller

from accumulating an excessive control signal. Consider a closed-loop system, as shown in Figure 3-16, which includes an integrator and actuator saturation. If a large reference input is commanded, the control input to the plant saturates at u_{max}. The integrator will accumulate the resulting error signal but since the system has saturated, increasing u_c has no additional effect on the control authority. Depending on how long the system remains saturated, the accumulated error signal can become quite large and cause excessive overshooting and control effort. One way to eliminate this problem involves turning off the integral action as soon as the system saturates [49]. This is known collectively as integral *anti-windup*. Both the continuous and discrete-time MATLAB Simulink integrator blocks provide integration saturation limits which provide a form of integral anti-windup. Since we place a saturation block into the experimental closed-loop block diagram to keep the control input to the amplifier I/F board below a certain threshold, the integral anti-windup option should also be implemented.

The Dynamic Signal Analyzer block in Figure 3-15 was designed by Katie Lilienkamp, another graduate student in the PMC Lab. She developed this Simulink block and corresponding MATLAB software[7] to work with dSPACE to extract the magnitude and phase of a system using swept sine excitation. This software provides a very convenient method for obtaining experimental Bode plots but the measurement bandwidth is limited to half the sampling rate of the dSPACE 1102 board [30]. Also, the implementation via digital signal processing (DSP) produces discrepancies between the simulated and experimental model. These additional features are seen by the digital controller as well, and so should be included.

The discrepancies between the simulated and experimental frequency responses conducted with the dSPACE DSA are largely due to the pure time delay T_d that the dSPACE board introduces into the feedback loop. The transfer function for a pure

[7]The associated software is available for download from the Precision Motion Control Laboratory's website, http://web.mit.edu/pmc/www/Links/download/download.html.

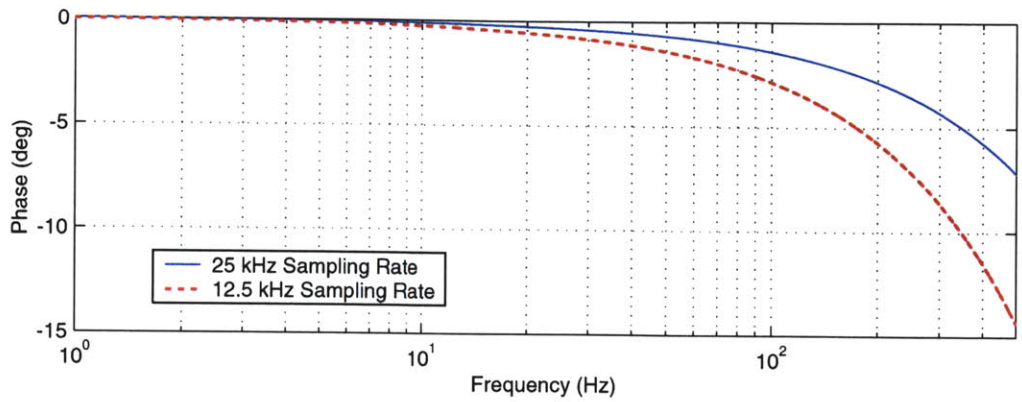

Figure 3-17: Bode phase plot for the phase lag $\psi_{lag}(j\omega)$ from the dSPACE 1102 controller board for a 12.5 kHz and 25 kHz sampling rate.

time delay is

$$H_{delay}(s) = e^{-T_d s}, \tag{3.8}$$

which produces a frequency dependent phase lag given by

$$\psi_{lag}(j\omega) = -\omega T_d. \tag{3.9}$$

We assume that the dSPACE 1102 controller board requires approximately half of one sampling period to process the controller algorithms while the digital-to-analog (D/A) convertor's zero-order-hold (ZOH) produces an additional half-sample delay [26]. Therefore, with a 25 kHz sampling rate, dSPACE introduces an approximate $T_d = 4 \times 10^{-5}$ second pure time delay. Figure 3-17 illustrates the Bode phase plot of (3.8) for a 25 and 12.5 kHz sampling rate.

Figure 3-18 compares the simulated open-loop frequency response of $G_{p_1}(s)$ to an experimental response taken with the dSPACE DSA. The Bode magnitude curves match quite well but the experimental phase curve shows additional negative phase shift due to the resulting pure time-delay. We do not see this phase lag in Figure 3-9, since this particular frequency response was conducted with the Hewlett Packard DSA. We will be using the dSPACE DSA to perform all of the experimental closed-

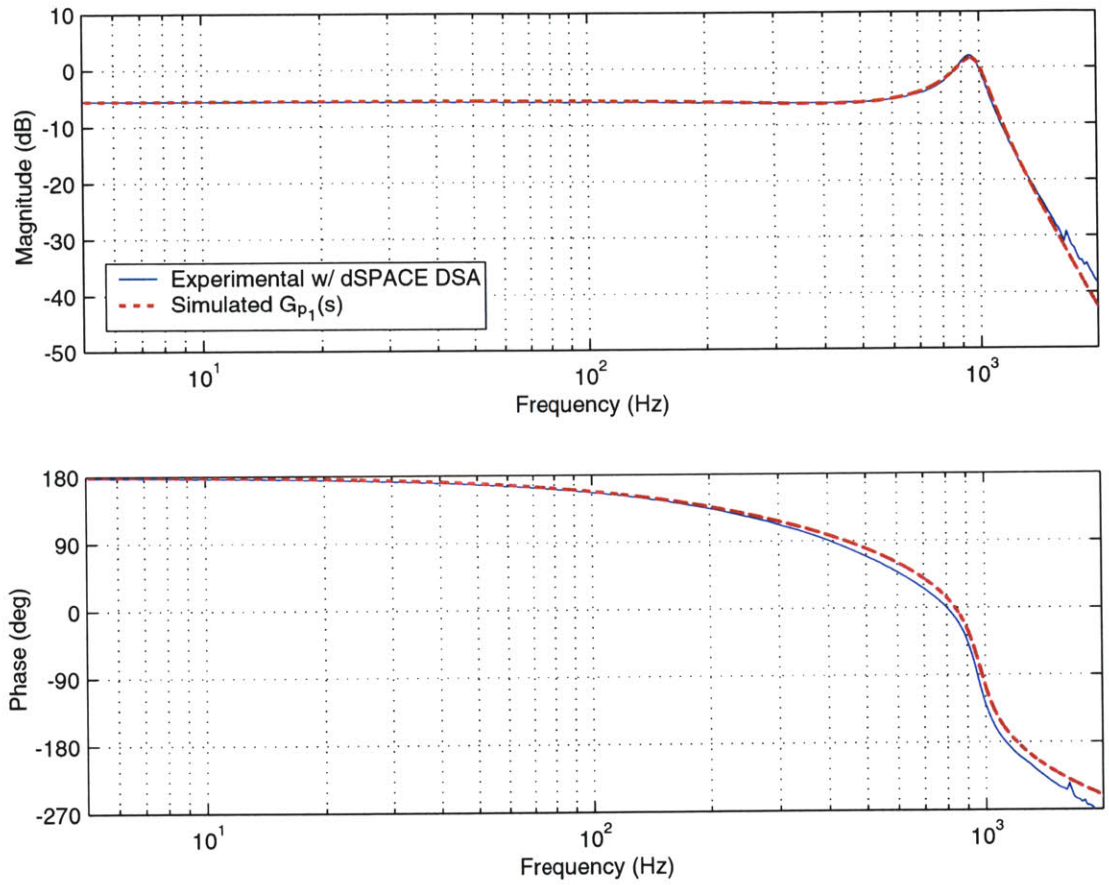

Figure 3-18: Comparison of the experimental and fitted FTS hardware open-loop frequency responses with $G_{p_1}(s)$. The experimental frequency response was conducted with the dSPACE DSA, resulting in the additional phase lag. (Note, the Bode phase plots as shown are shifted by 180°, since a positive change in the command voltage results in a negative change in FTS displacement.)

loop frequency responses. Thus, we decided to modify the open-loop plant model in (3.1) by adding a model of the dSPACE pure time delay. The corresponding fitted plant model is given by

$$G_{p_1DELAY}(s) = \frac{-0.54325e^{-4\times10^{-5}s}}{(\frac{s}{2600}+1)(\frac{s}{18850}+1)(\frac{s^2}{\omega_1^2}+\frac{2\zeta_1 s}{\omega_1}+1)(\frac{s^2}{\omega_2^2}+\frac{2\zeta_2 s}{\omega_2}+1)}\left[\frac{V}{V}\right], \qquad (3.10)$$

where the natural frequency and damping ratio parameters are defined earlier with (3.1). Figure 3-19 compares the experimental frequency response taken with the dSPACE DSA to the simulated open-loop response for the fitted plant model $G_{p_1DELAY}(s)$. With the pure time delay taken into account, the experimental and predicted curves match quite well.

It should be noted that we did not use (3.10) to predict the gain and phase margin for the negative of the loop transmission with a 125 Hz crossover frequency, since we did not account for the dSPACE time delay during the initial controller design. The addition of the pure time delay will reduce the predict closed-loop performance, but since we operated the dSPACE-based controller with a 25 kHz sampling rate, the resulting additional phase lag only amounts to a few degrees. This will have an insignificant effect on the closed-loop performance for the frequencies of interest.

The saturation block in Figure 3-15 was used to protect the Variform FTS hardware. The FTS literature states that the amplifier I/F board can input a maximum ±10 V but when input signals have excitation frequencies greater than 1 kHz, the input voltage must stay below 10% of the maximum level. If this voltage level is exceeded, the piezoelectric discs inside the FTS actuator can become dangerously hot and damage the RTV that encapsulates them. Throughout the experimental dSPACE controller testing, we performed numerous open and closed-loop frequency responses with excitation frequencies of up to 2 kHz. Therefore, we initially set the saturation block to limit the output to ± 300 mV, guaranteeing that the output signal from the

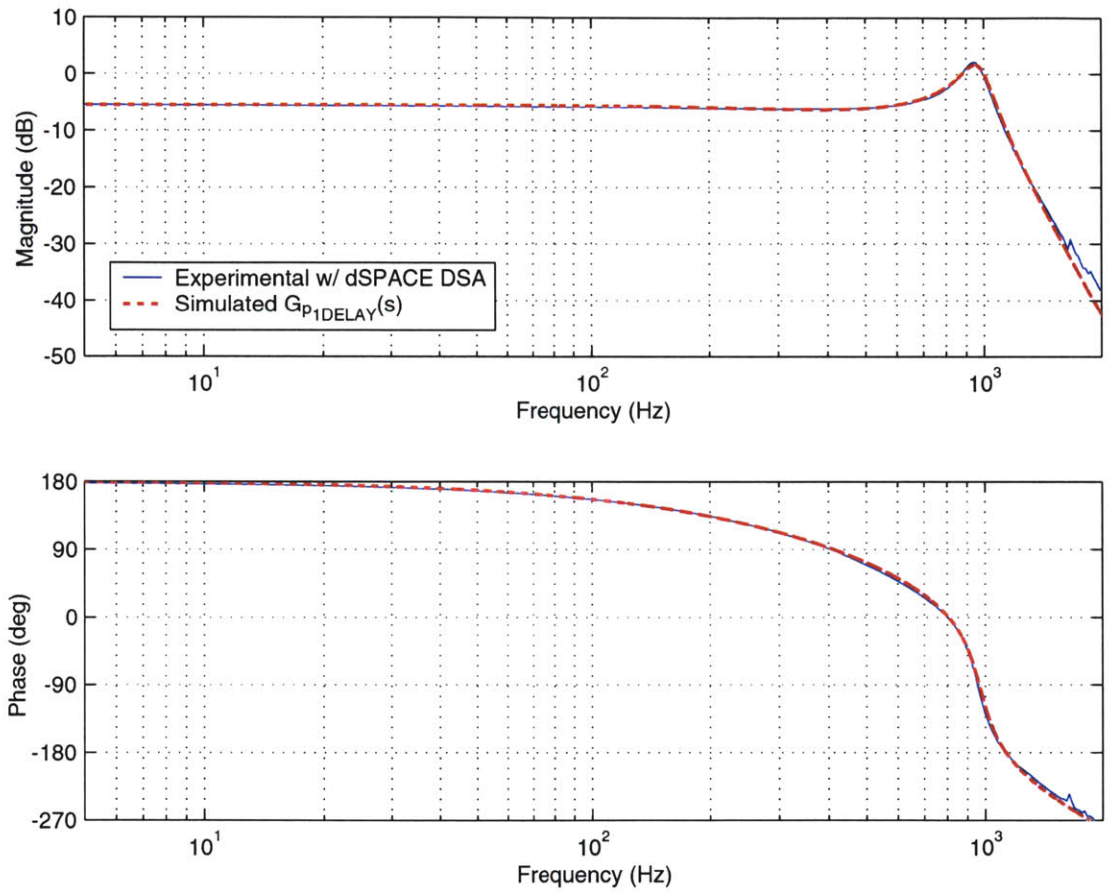

Figure 3-19: Comparison of the experimental and fitted FTS hardware open-loop frequency responses with $G_{p_{1DELAY}}(s)$. The experimental frequency response was conducted with the dSPACE DSA. (Note, the Bode phase plots as shown are shifted by 180°, since a positive change in the command voltage results in a negative change in FTS displacement.)

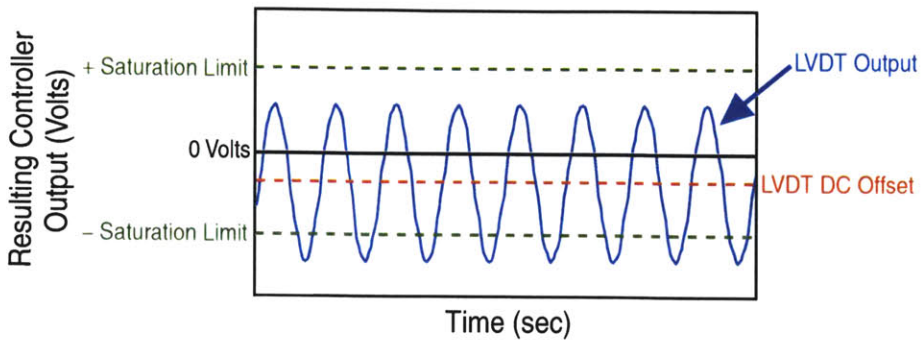

Figure 3-20: Illustration of the DC offset LVDT output signal.

dSPACE controller to the amplifier I/F board does not exceed ± 1 V.

During the initial experimental frequency response testing, the dSPACE controller experienced instability problems. We narrowed the problem down to the sensor output signal and determined that the LVDT produces a DC offset voltage which yields a shifted sinusoidal control system output that is greater than one of the experimental saturation limits. An illustration of this is shown in Figure 3-20. To eliminate this problem, we place a DC voltage offset of 0.034 V into the Simulink model, as shown in Figure 3-15, thereby centering the LVDT output back at approximately 0 V and placing the controller output signal within the boundaries of the experimental saturation limits. We speculate that this offset voltage is also the cause of the on-board FTS controller instability problems. As mentioned previously in Section 3.1, due to time constraints and the methods in which we are conducting the controller experiments, we did not implement the LVDT offset circuit to solve the on-board controller instability problems. We simply bypass the on-board controller and use the dSPACE 1102 board to implement all of our own controller algorithms.

The output of the Sum2 summation block, as shown in Figure 3-15, represents the closed-loop error signal. Conventionally, the error signal equals the difference between the feedback and reference input (see Figure 2-1) but there is a 180° phase shift from the amplifier I/F input to the LVDT output. This is due to a negative

change in the FTS displacement for a given positive change in the reference input. To prevent positive feedback and closed-loop instability, the minus sign in front of the feedback signal must be changed to a plus sign. During the dSPACE-based controller experiments, we arbitrarily chose a plus sign in front of the input reference signal. This resulted in a 180^0 phase shift of the closed-loop response, as shown in Figure 3-23, which is also due to the 180° phase shift from the input reference signal to the LVDT output. Changing the sign of the reference will not affect stability, since this signal is not part of the feedback loop. Thus, if we place a minus sign in front of the reference input, the 180° phase shift will be removed from the experimental frequency responses.

The final preliminary experimental Simulink controller element shown in Figure 3-15 is a virtual on/off switch. We implement this component as an additional safety device to protect the Variform FTS hardware, controlling the switching process through the dSPACE ControlDesk software. Ideally, we should have added an additional on/off switch between the saturation and D/A Convertor block, which would directly control the D/A output to high-power amplifier I/F board. Figure 3-21 illustrates one of the ControlDesk layouts we use to perform the closed-loop experiments. In this layout, we can continuously monitor and adjust the gain K_p, integration and control input saturation limits, and reference signal amplitude and frequency levels.

Figure 3-22 compares the experimental and simulated negative of the loop transmission frequency responses while Figure 3-23 compares the experimental and simulated closed-loop frequency responses. By using (3.10) to model the Variform FTS hardware, both of these figures show close agreement between the experimental results and the simulated model. Figure 3-24 compares the experimental and simulated preliminary controller closed-loop step responses. For this particular test, we changed the saturation limits to ± 5 V and initially commanded a 300 mV step input. As Figure 3-24 illustrates, the experimental curve follows the general shape of the sim-

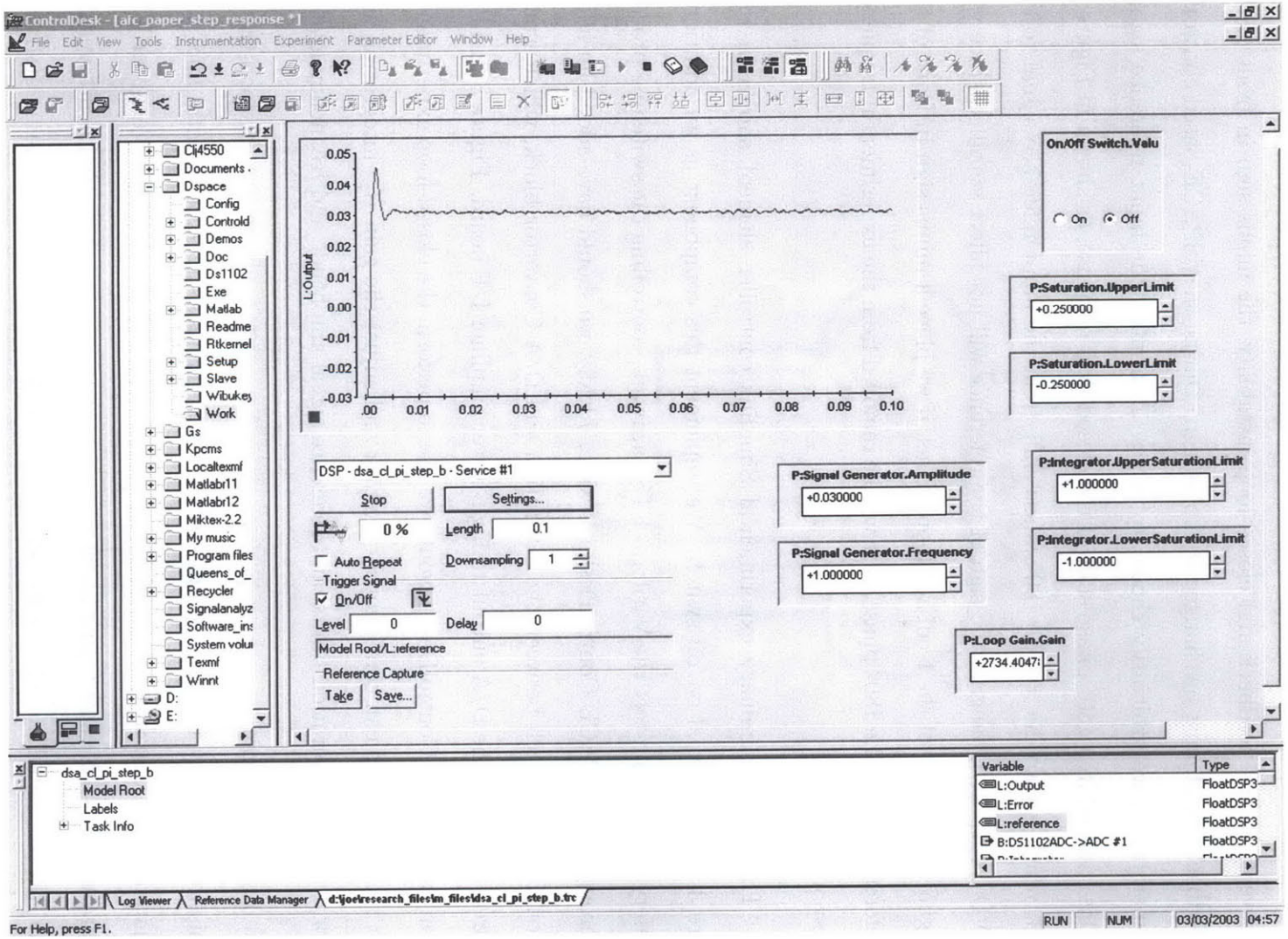

Figure 3-21: Picture of one of the ControlDesk layouts we used for performing experimental closed-loop step responses.

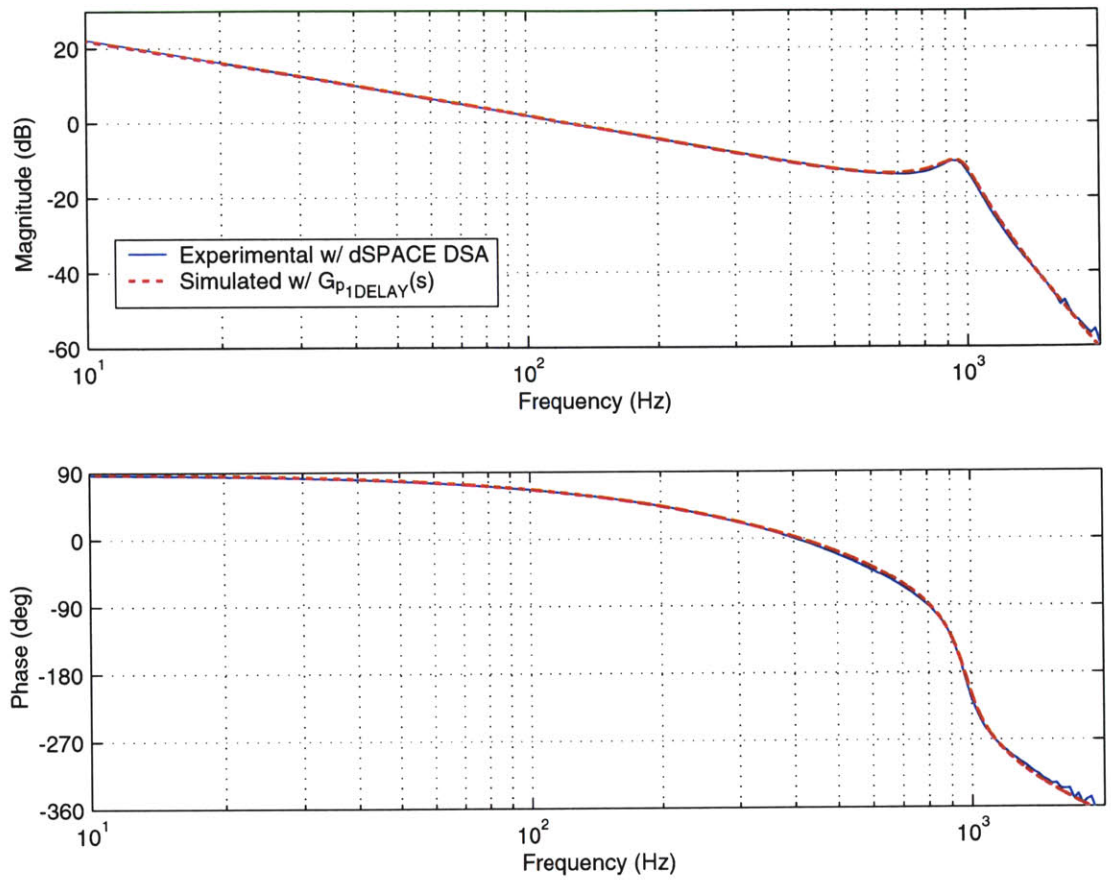

Figure 3-22: Comparison of the experimental and simulated negative of the loop transmission frequency responses with the preliminary dSPACE controller $G_{c_1}(z)$. (Note, the Bode phase plots as shown are shifted by 180°, since a positive change in the command voltage results in a negative change of the FTS displacement.)

ulated response but exhibits a 4% larger peak overshoot and reduced peak time. It appears from Figure 3-19 and the results in Figure 3-24 that the fitted plant model $G_{p_{1DELAY}}(s)$ captures the governing FTS dynamics reasonably well. Therefore, we decided to investigate possible non-linear effects.

To study the non-linear effects, we conducted several more step responses at various input amplitudes. Figure 3-25 compares several experimental closed-loop step responses, clearly illustrating a non-linear behavior. As the input voltage increases, the resulting percent overshoot increases and effective damping decreases. These re-

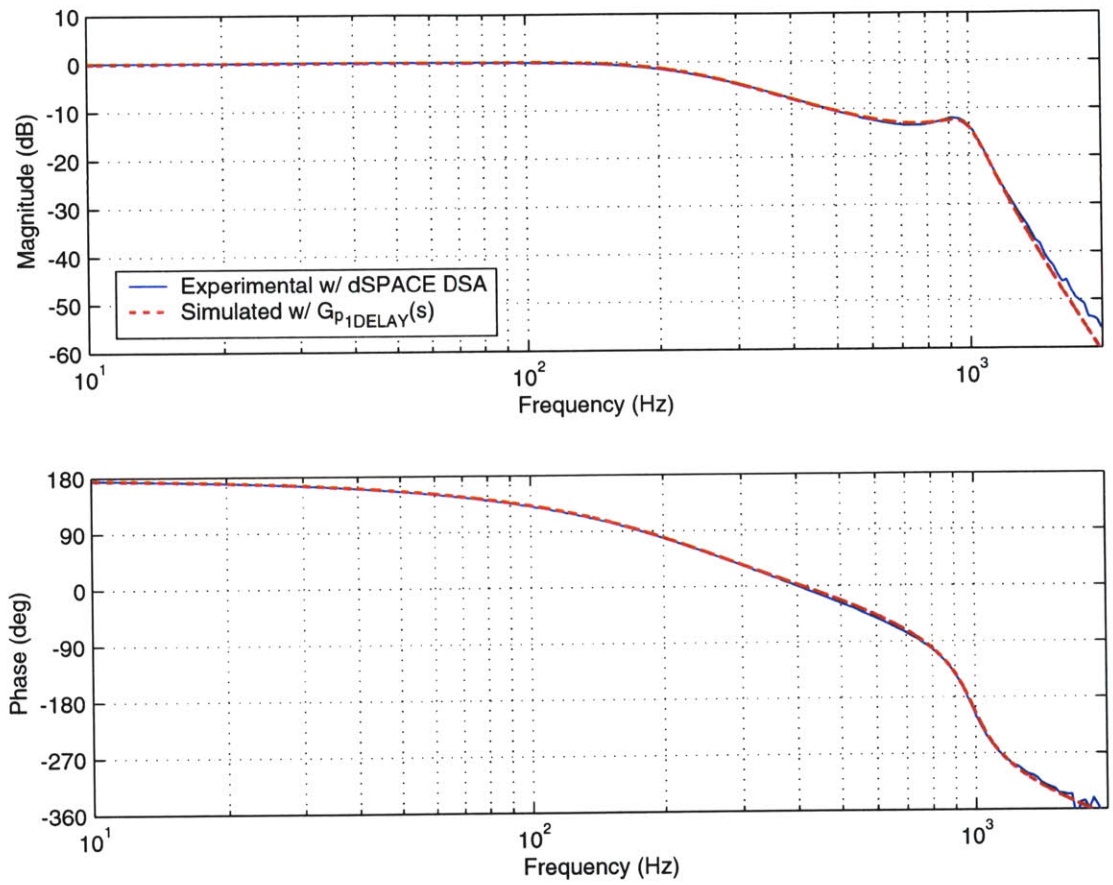

Figure 3-23: Comparison of the experimental and simulated closed-loop frequency responses with the preliminary dSPACE controller $G_{c_1}(z)$. (Note, the Bode phase plots as shown are shifted by 180°, since a positive change in the command voltage results in a negative change of the FTS displacement.)

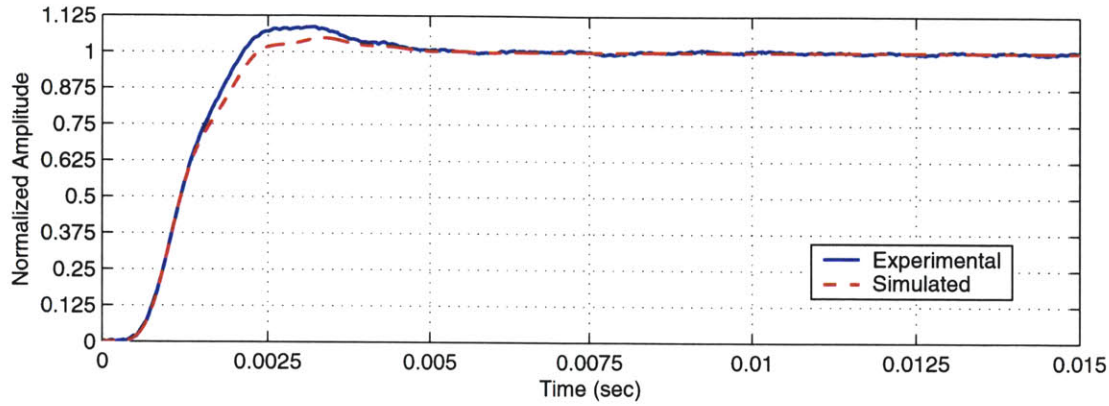

Figure 3-24: Comparison of the experimental and simulated closed-loop step responses with the preliminary dSPACE controller $G_{c_1}(z)$. For ease of comparison, the experimental response has been normalized to unity final value.

sults are probably not due to controller saturation, since we used relatively small reference input signals and continuously monitored the control output to the I/F board with a Tektronix[8] model TDS 420 digital oscilloscope, where we did not observe any saturation effects. Thus, we speculate that this characteristic is probably due to the piezoelectric stacks in the Variform FTS actuator.

The Variform FTS literature states that the piezoelectric actuator is inherently non-linear with respect to applied voltage and exhibits a hysteresis curve that can be as much as 20% of the total displacement. The FTS on-board controller optionally utilizes an inner charge loop that reduces this hysteresis curve while the outer position loop linearizes the displacement with respect to the commanded reference signal. Since we completely bypass the on-board controller and use the dSPACE 1102 board for the preliminary dSPACE-based controller experiments, the inner charge loop is also disabled. In the following section, we re-enable the inner charge loop and evaluate the improvements on the outer position servo loop.

[8]See Appendix K.

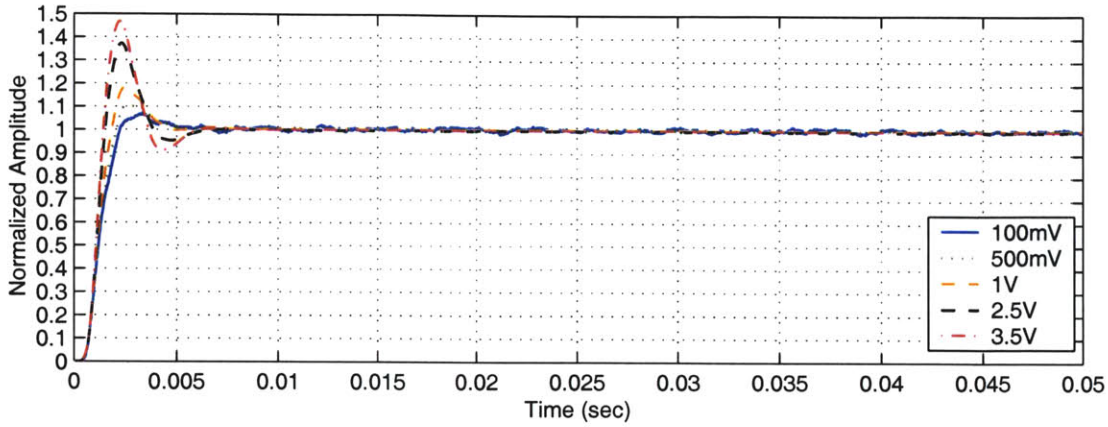

Figure 3-25: Comparison of the experimental closed-loop step responses with various input amplitudes. For ease of comparison, all the experimental step responses have been normalized to unity final value.

3.4 Preliminary Controller Design with Inner Charge Loop

In this section, we design another preliminary feedback controller but also include the on-board controller inner charge loop in the overall design. This involves altering the jumpers on the amplifier I/F board again, which affects the dynamics of the open-loop plant and requires a new experimental open-loop frequency response. We move the jumpers at positions JP5 and JP7 from the a-b positions, as shown in Figure 3-8, and place them into the b-c positions. Figure 3-26 illustrates the new experimental controller configuration while Figure 3-27 compares the resulting experimental and fitted open-loop frequency responses.

We fit a model for the altered plant dynamics as a seventh order transfer function

$$\frac{V_{out}}{V_{in}}(s) \triangleq G_{p_2}(s) = \frac{-9.114(\frac{s}{18.85}+1)}{s(\frac{s}{2600}+1)(\frac{s}{18850}+1)(\frac{s^2}{\omega_3^2}+\frac{2\zeta_3 s}{\omega_3}+1)(\frac{s^2}{\omega_4^2}+\frac{2\zeta_4 s}{\omega_4}+1)}\left[\frac{V}{V}\right], \quad (3.11)$$

where the parameters are selected as $\omega_3 = 6597$ rad/sec, $\zeta_3 = 0.545$, $\omega_4 = 6157$ rad/sec, and $\zeta_4 = 0.065$ (Appendix C includes the State Space Matrices for $G_{p_2}(s)$).

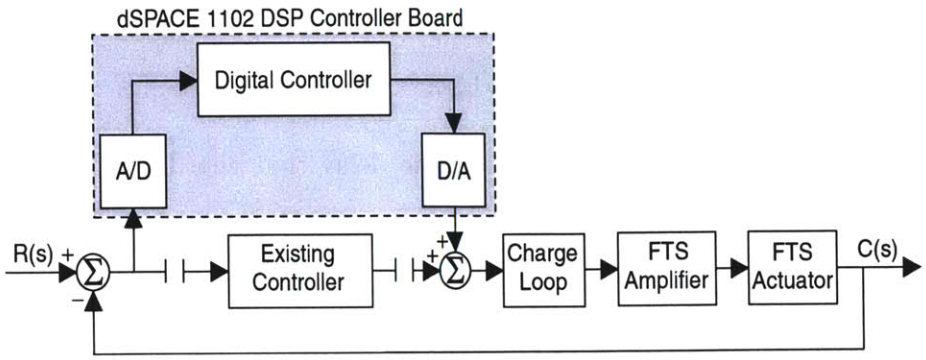

Figure 3-26: dSPACE controller implementation with the on-board inner charge loop implemented.

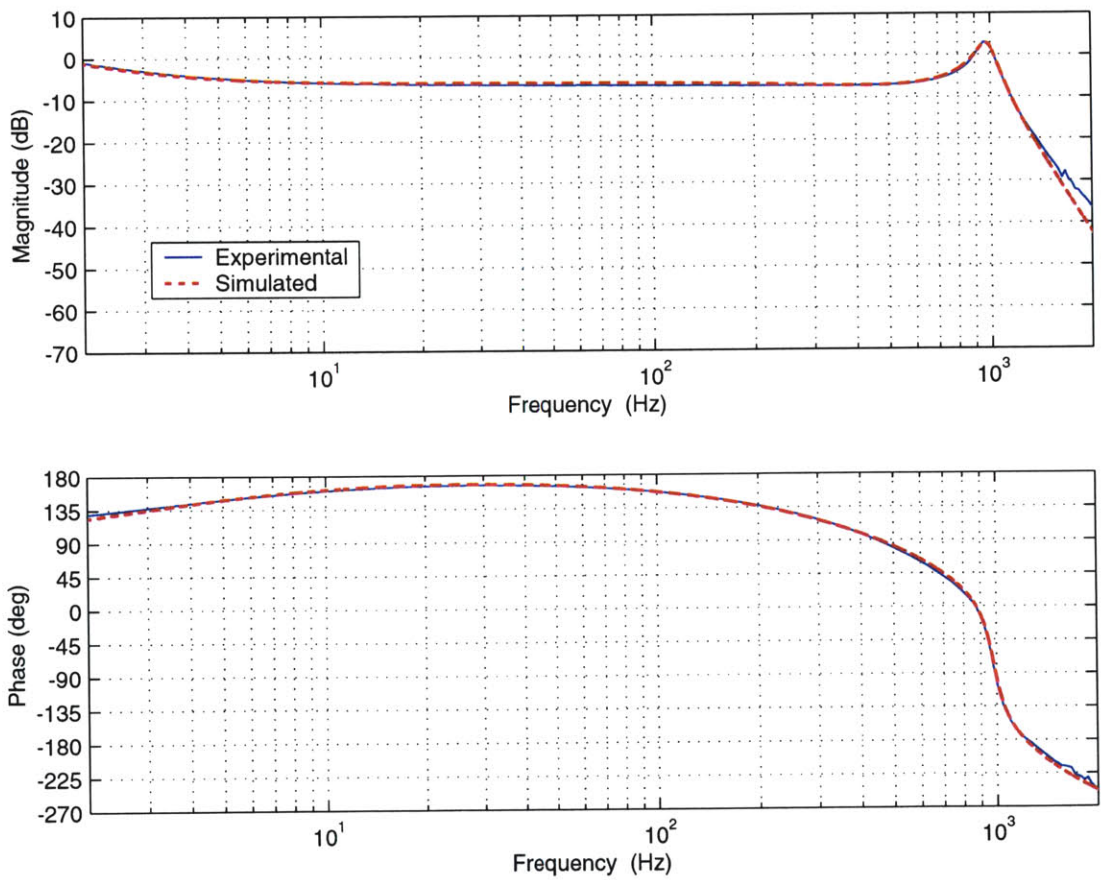

Figure 3-27: Comparison of the experimental and fitted open-loop frequency responses with the on-board inner charge loop implemented. The experimental frequency response was conducted with the Hewlett Packard model #35665A Dynamic Signal Analyzer. (Note, the Bode phase plots as shown are shifted by 180°, since a positive change in the command voltage results in a negative change of the FTS displacement.)

This parametric plant model includes poles at 0, -18850, -400±6144i, -3595±5531i and -2600 rad/sec, with a zero at -18 rad/sec.

Since (3.11) does not model the pure time delay that the dSPACE 1102 board introduces into the experimental closed-loop system, we conducted another open-loop frequency response with the dSPACE DSA, sampled at 25 kHZ, and altered $G_{p_2}(s)$ accordingly to match the new experimental results. The altered plant model with enabled inner charged and modelled pure time delay is given by

$$G_{p_{2DELAY}}(s) = \frac{-9.114(\frac{s}{18.85}+1)e^{-2\times10^{-5}s}}{s(\frac{s}{2600}+1)(\frac{s}{18850}+1)(\frac{s^2}{\omega_3^2}+\frac{2\zeta_3 s}{\omega_3}+1)(\frac{s^2}{\omega_4^2}+\frac{2\zeta_4 s}{\omega_4}+1)}\left[\frac{V}{V}\right], \qquad (3.12)$$

and a comparison between the simulated and experimental Bode plots is shown in Figure 3-28. Note, we did not use $G_{p_{2DELAY}}$(s) during the experimental controller design, due to the fact that we overlooked the dSPACE delay throughout the initial testing period. After conducting the controller experiments, we went back and modelled the delay, as shown in (3.12), to compare the experimental results to predicted models. These results are shown at the end of the section.

The inner charge loop appears to add an integrator and real-axis left hand plane (LHP) zero to original fitted plant model $G_{p_1}(s)$. Thus, we use (3.11) to re-design the experimental dSPACE-based controller and shape the negative of the loop transmission to be comparable in performance to the design in Section 3.3. As Figure 3-28 illustrates, $G_{p_2}(s)$ already provides good low-frequency gain and a -20dB/decade slope but the inner charge loop zero flattens out the Bode magnitude curve around 3 Hz. Thus, we add a first order low-pass filter with break frequency set to the break frequency ω_b of the inner charge loop zero, which provides additional -20dB/decade slope below the 1 kHz resonance. Figure 3-29 illustrates the resulting closed-loop block diagram.

This particular controller design was implemented relatively early in the Variform

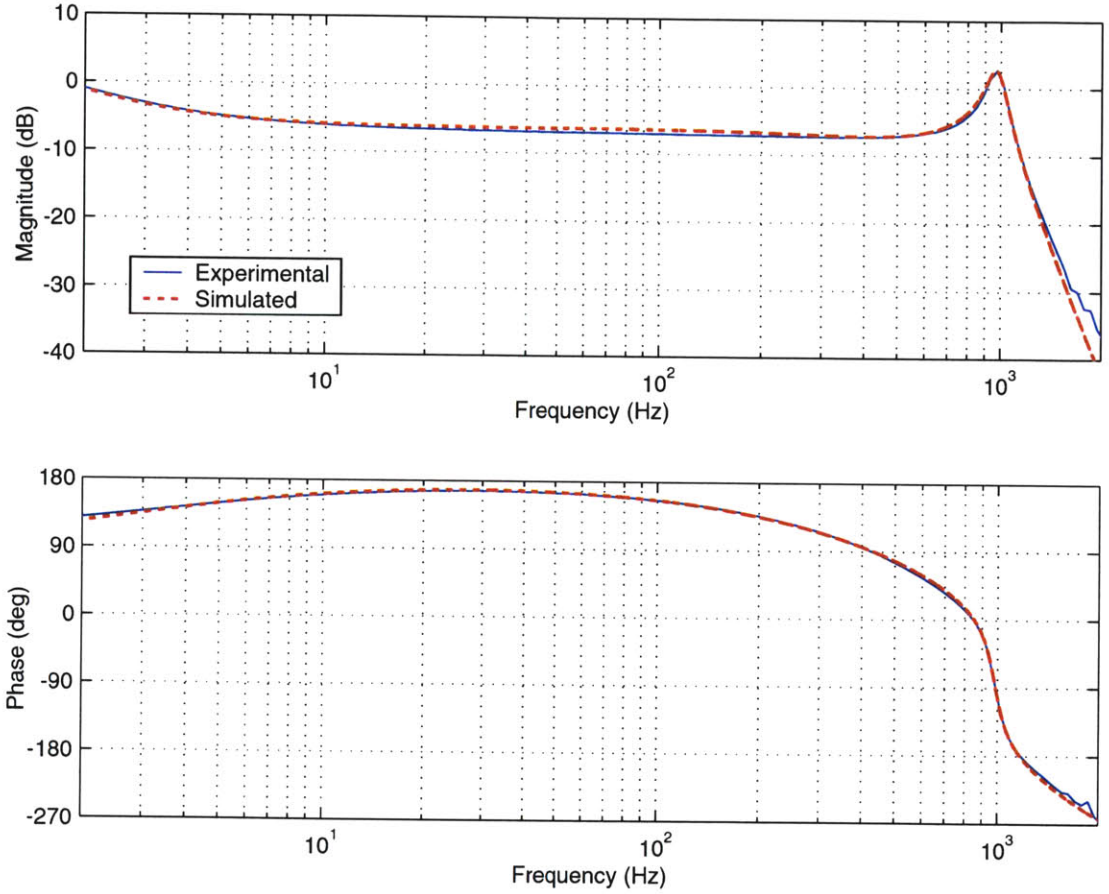

Figure 3-28: Comparison of the experimental and fitted open-loop frequency responses with enabled on-board inner charge loop and modelled pure time delay. The experimental frequency response was conducted with the dSPACE DSA. (Note, the Bode phase plots as shown are shifted by 180°, since a positive change in the command voltage results in a negative change of the FTS displacement.)

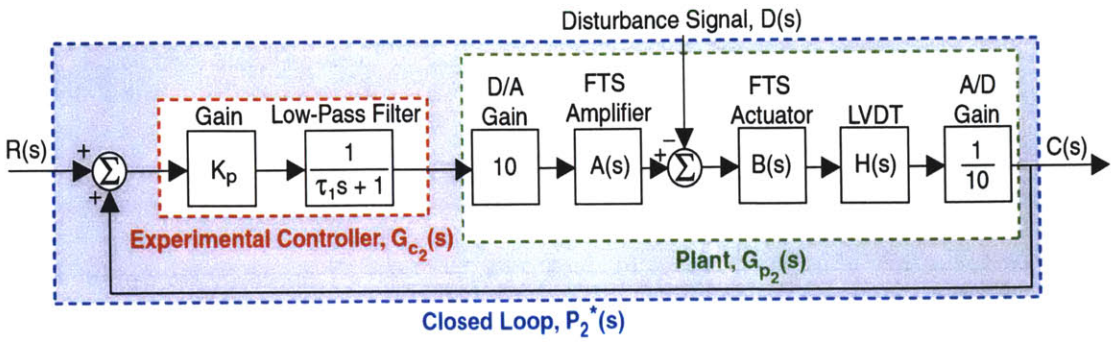

Figure 3-29: Preliminary FTS closed-loop system block diagram with enabled on-board inner charge loop. A plus sign has been placed next to the feedback signal instead of the conventional negative feedback nomenclature, since the output C(s) is 180° out of phase with respect to the reference input R(s). This sign change is required to ensure closed-loop stability. The time constant of the low-pass filter equals $\frac{1}{6\pi}$.

FTS closed-loop experiments. In retrospect, another integral controller would have been a much better design choice, since the low-pass filter does not provide high low-frequency gain for disturbance rejection. Therefore, the reader is referred to Section 3.5 for an improved design, where we remove the low-pass filter and implement an integrator and notch filter to improve upon the closed-loop performance.

Moving forward with this current design, the negative of the loop transmission is given by

$$-L_2(s) = \frac{\text{LVDT Output}}{\text{I/F Board Input}} = G_{c_2}(s)G_{p_2}(s), \tag{3.13}$$

and after determining the appropriate K_p value, equation (3.13) essentially replicates the frequency response of (3.3). Again, notice that we used G_{p_2}(s) instead of $G_{p_{2DELAY}}$(s) in (3.13). This is because we designed this loop before considering the effects of the additional pure time delay. With the sampling rate set to 25 kHz, the dSPACE-based controller will only add an additional few degrees of phase lag at crossover, anf will not significantly affect the closed-loop performance.

With the gain K_p set equal to 90, equation (3.13) predicts an 11.7 dB gain margin, 62° phase margin and 801 rad/sec ($\approx$ 125 Hz) crossover frequency, as shown in Fig-

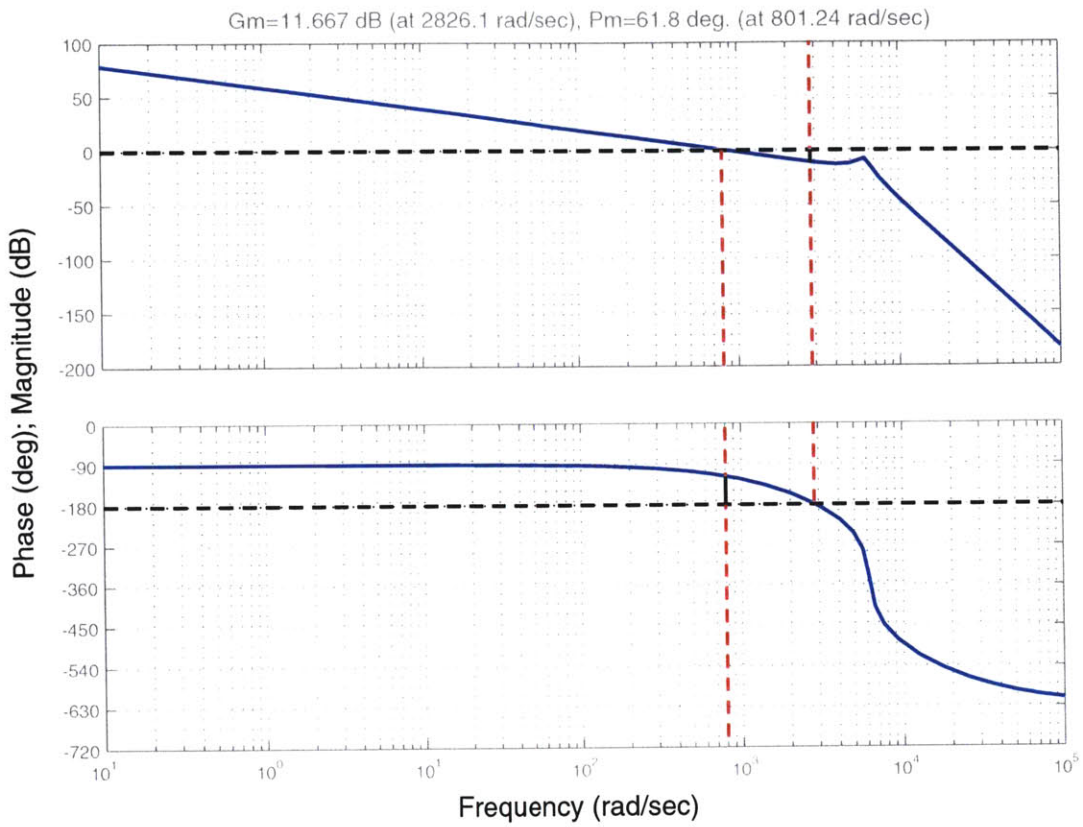

Figure 3-30: Simulated Bode plot indicating the gain and phase margin for preliminary controller with implemented inner charge loop $G_{c_2}(s)$.

ure 3-30. The resulting continuous-time controller transfer function and discrete-time equivalent, sampled at 25 kHz, are given by

$$G_{c_2}(s) = \frac{90}{0.053052s + 1}, \tag{3.14}$$

$$G_{c_2}(z) = \frac{0.033916(z+1)}{z - 0.999246}. \tag{3.15}$$

Figure 3-31 illustrates the experimental Simulink block diagram we use to conduct closed-loop testing with G_{c_2}(z). This system includes an additional on/off switch for the control output signal, as compared to Figure 3-15. The resulting experimental system provides much safer design.

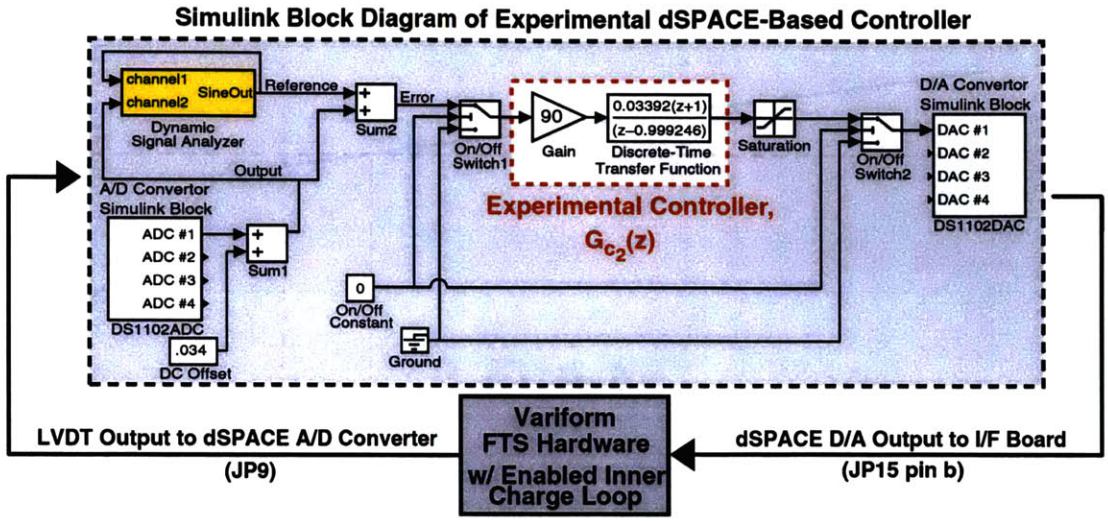

Figure 3-31: Preliminary experimental Simulink closed-loop block diagram. The experimental controller equals $G_{c_2}(z)$.

Figure 3-32 compares the experimental closed-loop frequency response with and without the inner charge loop. As expected, these feedback systems show very similar results. We also perform several experimental closed-loop step responses, to see if the addition of the inner charge loop attenuates the previously observed closed-loop non-linearities. Figure 3-33 compares several experimental step responses to a MATLAB simulated response. The experimental curves show negligible changes in performance with varying input amplitude and good agreement with the predicted model. These results appear to confirm the speculation that the piezoelectric hysteresis is causing the non-linear effects. Then again, $G_{c_1}(z)$ and $G_{c_2}(z)$ provide different frequency responses and will also saturate differently. Ideally, we should have used the same controller design when comparing experimental closed-loop step responses but due to time constraints and the excellent results we obtained in Figure 3-33, we decided to simply leave the inner charge loop enabled and continue improving upon our controller designs.

The Variform FTS literature states that the inner charge loop eliminates the effect of third harmonic distortion. This particular FTS model is designed to operate around

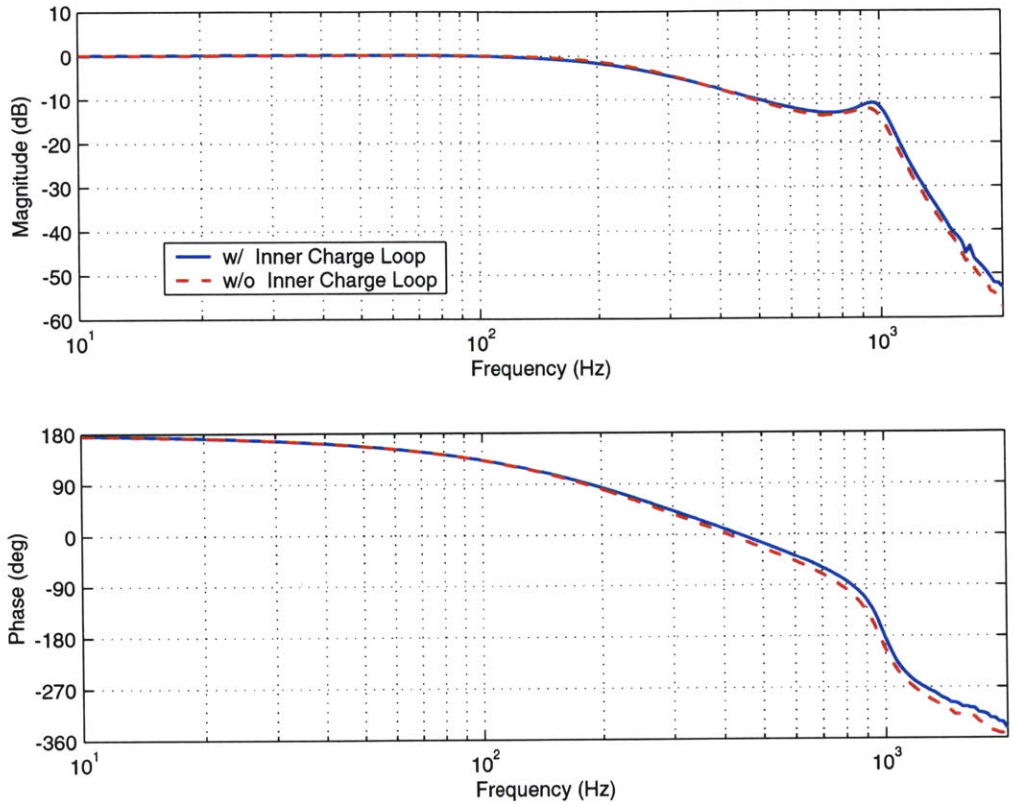

Figure 3-32: Comparison of experimental Bode plots with and without the on-board inner charge loop implemented. (Note, the Bode phase plots as shown are shifted by 180°, since a positive change in the command voltage results in a negative change of the FTS displacement.)

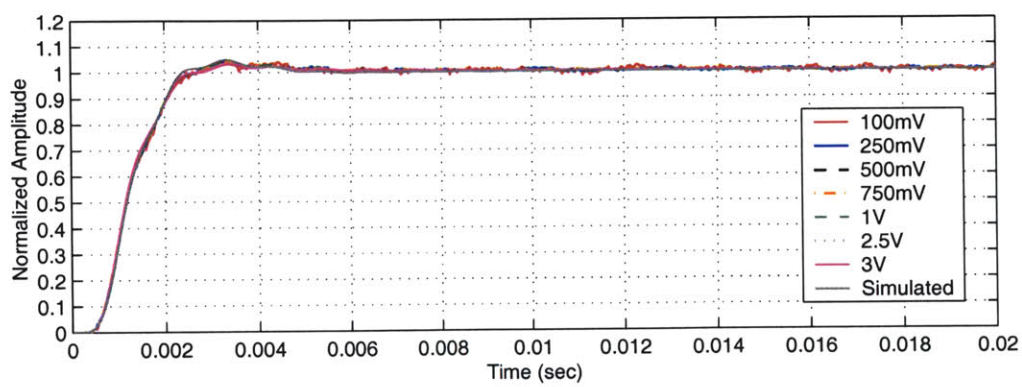

Figure 3-33: Comparison of various input amplitude experimental closed-loop step responses to the predicted response, with enabled on-board inner charge loop. For ease of comparison, all the experimental step responses have been normalized to unity final value.

200 Hz and a significant third harmonic would require a closed-loop bandwidth beyond 600 Hz to be able to control it. HiTek Power claims that the addition of the inner charge loop drives the third harmonic to 40 dB below the fundamental frequency at 200 Hz while the closed-loop -3 dB bandwidth exceeds 500 Hz. Due to time constraints, we were not able to implement the LVDT offset circuit or change the mechanical LVDT offset, as described in Section 3.1. Therefore, we could not verify these results and leave this exercise for future work.

In summary, we only used $G_{c_2}(z)$ to emulate the closed-loop frequency response in Section 3.3. This particular controller provides a comparable closed-loop frequency response to the servo-loop with $G_{c_1}(z)$ but the first order-low pass filter does not produce high low-frequency gain. Thus, $G_{c_2}(z)$ provides inferior disturbance rejection when compared to the preliminary experimental controller design $G_{c_1}(z)$. We improve upon this work in the following section, where we keep the inner charge loop enabled and increase the closed-loop bandwidth.

3.5 Higher Bandwidth Controller Design

In this section, we design and implement two more controllers on the Variform FTS with the dSPACE 1102 controller board. Tables 3.1 and 3.2 list the advertised negative of the loop transmission and closed-loop performance characteristics.

-L(s) Performance Characteristics	
DC Gain	40 dB(min.)
0 dB Crossover Frequency	200 Hz(min.)
gain margin	10 dB(min.)
phase margin	45^o(min.)

Table 3.1: Summary of the Variform FTS advertised negative of the loop transmission performance characteristics.

Using these values as benchmarks, we build upon the previous controller designs to see what kind of closed-loop performance the Variform FTS with a dSPACE-based

Closed-Loop Performance Characteristics	
Small Signal -3 dB Bandwidth	500 Hz(min.)
Normalized Magnitude Peak (M_p)	2.5 dB

Table 3.2: Summary of the Variform FTS advertised closed-loop performance characteristics.

controller can attain. The first design uses the on-board LVDT as the feedback sensor, while the second controller utilizes the Kaman Instrumentation inductive sensor to close the feedback loop.

Figure 3-27 illustrates the preliminary open-loop frequency response with enabled on-board inner charge loop. As mentioned previously, this loop appears to add an integrator and real-axis zero to the original open-loop plant dynamics. Figure 3-34 compares the simulated frequency response of the parametric plant model $G_{p_2}(s)$ to the same model when the inner charge loop dynamics are neglected. These plots show that the magnitude and phase data are approximately equal for frequencies above 100 Hz. Since at least a 200 Hz crossover frequency is desired, we can ignore the inner charge loop dynamics and use a reduced order model to design the following experimental feedback controllers. Reducing the previous plant transfer function gives

$$G_{p_3}(s) = \frac{-0.4835}{s(\frac{s}{2600}+1)(\frac{s}{18850}+1)(\frac{s^2}{\omega_3^2}+\frac{2\zeta_3 s}{\omega_3}+1)(\frac{s^2}{\omega_4^2}+\frac{2\zeta_4 s}{\omega_4}+1)}, \tag{3.16}$$

where the parameters ω_3 , ζ_3, ω_4, and ζ_4 are defined perviously in Section 3.4.

In this section, we want to increase the 0 dB crossover frequency yet still achieve sufficient stability margins. Thus, we must either attenuate the open-loop 1 kHz resonant peaking or ensure that the negative of the loop transmission has less than -180° of phase at the frequencies where the resonant peaking is above the 0 dB magnitude line. Initially, we design a controller with a notch filter and Proportional-plus-Integral (P+I) controller to meet the specifications.

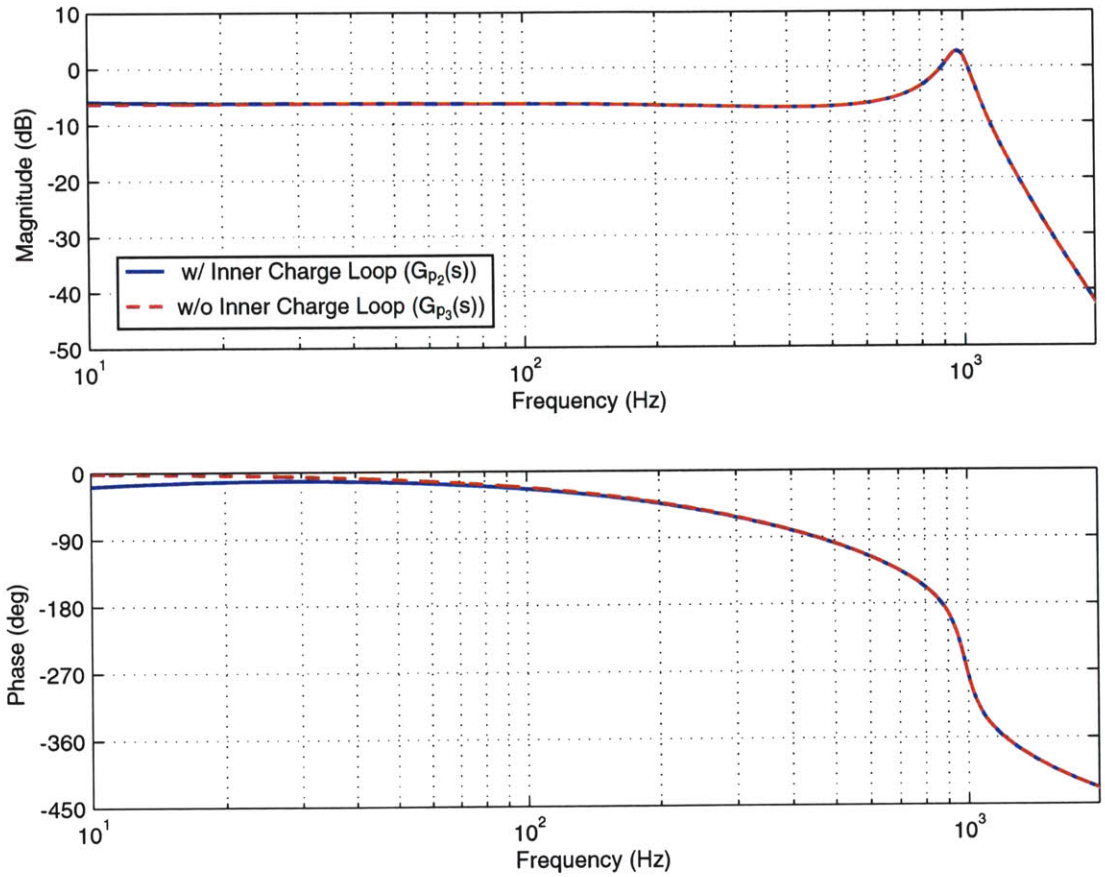

Figure 3-34: Comparison of the simulated frequency response of the plant model $G_{p_2}(s)$ and the reduced order plant model $G_{p_3}(s)$ when the inner charge loop dynamics are neglected.

3.5.1 Controller Design with the LVDT Feedback Sensor

During this experimental controller design, we do not model the additional phase lag from dSPACE. Ideally, these additional dynamics should be taken into consideration but due to time constraints, we did not have time to go back and redesign the controller. However, we modified (3.16) to include the pure time delay for comparisons between the predicted and experimental negative of the loop transmission and closed-loop frequency responses. The altered plant model, with the pure time delay, is given by

$$G_{p_{3DELAY}}(s) = \frac{-0.4835e^{-2\times10^{-5}s}}{s(\frac{s}{2600}+1)(\frac{s}{18850}+1)(\frac{s^2}{\omega_3^2}+\frac{2\zeta_3 s}{\omega_3}+1)(\frac{s^2}{\omega_4^2}+\frac{2\zeta_4 s}{\omega_4}+1)}. \tag{3.17}$$

We begin the experimental controller design with the notch filter, where we isolate the open-loop complex conjugate pole pairs from $G_{p_3}(s)$ and use the natural frequency w_n and damping ratio ζ values to approximate an inverse model of the resonant peak. These values provide the preliminary filter shape but several iterations are required to achieve sufficient magnitude attenuation with minimal phase lag in the vicinity of the desired crossover frequency. Figure 3-35 displays the section of MATLAB code we use to design the fourth order notch filter, while the resulting continuous-time transfer function and discrete-time equivalent, sampled at 20 kHz, are given by

$$G_{Notch}(s) = \left(\frac{s^2+2\zeta_5\omega_5 s+\omega_5^2}{s^2+2\zeta_6\omega_5 s+\omega_5^2}\right)\left(\frac{s^2+2\zeta_7\omega_6 s+\omega_6^2}{s^2+2\zeta_8\omega_6 s+\omega_6^2}\right), \tag{3.18}$$

$$G_{Notch}(z) = \frac{0.910284z^4-3.167813z^3+4.250689z^2-2.59663z+0.61076}{z^4-3.317803z^3+4.2291z^2-2.44664z+0.542644}, \tag{3.19}$$

where the parameters are selected as $\omega_5 = 1950\pi$ rad/sec, $\zeta_5 = 0.0675$, $\zeta_6 = 0.2695$, $\omega_6 = 2090\pi$ rad/sec, $\zeta_7 = 0.555$, and $\zeta_8 = 0.6916$. Equation (3.19) illustrates the final discrete-time transfer function we used in the complete experimental dSPACE-based controller design. However, the notch filter actually should have been implemented

```
%First Notch Filter Parameters
    %Damping Ratio and Natural Frequency
        zeta_n = .0675;   wn_n = (2*pi*975);
    %Second Order System Numerator, Denominator & TF
        num_n = wn_n^2;      den_n = [1 2*zeta_n*wn_n wn_n^2]; Resonance = tf(num_n,den_n);
    %Definition of Resonant Peak 1
        Peak = 1/((2*zeta_n)*(1-zeta_n^2)^.5);
    %Definition of Notch Gain 1
        Magnitude = 3.0;
    %Definition of Pure Differentiator
        s_zero =  tf([1 0],[1]);
    %Definition of First Continuous-Time Notch Filter Transfer Function
        notch1 = 1/(1 + Magnitude*(s_zero*1/(Peak*wn_n)*Resonance));
    %Second Continuous-Time Notch Filter Transformed to Equivalent Discrete-Transfer Function
        notchF_D = C2D( notch1,TS,'tustin');
%Second Notch Filter Parameters
    %Damping Ratio and Natural Frequency
        zeta_n2 = .555; wn_n2 = (2*pi*1045);
    %Second Order System Numerator, Denominator & TF
        num_n2 = wn_n2^2; den_n2 = [1 2*zeta_n2*wn_n2 wn_n2^2]; Resonance2 = tf(num_n2,den_n2);
    %Definition of Resonant Peak 2
        Peak2 = 1.1;
    %Definition of Notch Gain 2
        Magnitude2 = 0.25;
    %Definition of Second Continuous-Time Notch Filter Transfer Function
        notch2 = 1/(1 + Magnitude2*(s_zero*1/(Peak2*(wn_n2*sqrt(1- zeta_n2^2)))*Resonance2));
    %Second Continuous-Time Notch Filter Transformed to Equivalent Discrete-Transfer Function
        notchF_D = C2D( notch2,TS, 'tustin');
```

Figure 3-35: Section of MATLAB code we use to formulate the fourth order notch filter for the higher bandwidth controller $G_{c_3}(s)$.

as two separate transfer functions added in series. The resulting discrete-time z-transform is given by

$$G_{Notch}(z) = \left(\frac{0.944047z^2 - 1.765876z + 0.90666}{z^2 - 1.765876z + 0.850706}\right)\left(\frac{0.964236z^2 - 1.551926z + 0.673638}{z^2 - 1.551926z + 0.637875}\right). \quad (3.20)$$

This representation improves the experimental model's numerical stability.

Figure 3-36 compares the simulated open-loop frequency response with and without the notch filter. We see that (3.18) sufficiently attenuates the 1 kHz resonance and provides a relatively flat Bode plot magnitude curve until the system output breaks with a -120 dB/decade slope. Next, we add an integrator to increase the low-frequency gain and provide the negative of the loop transmission with

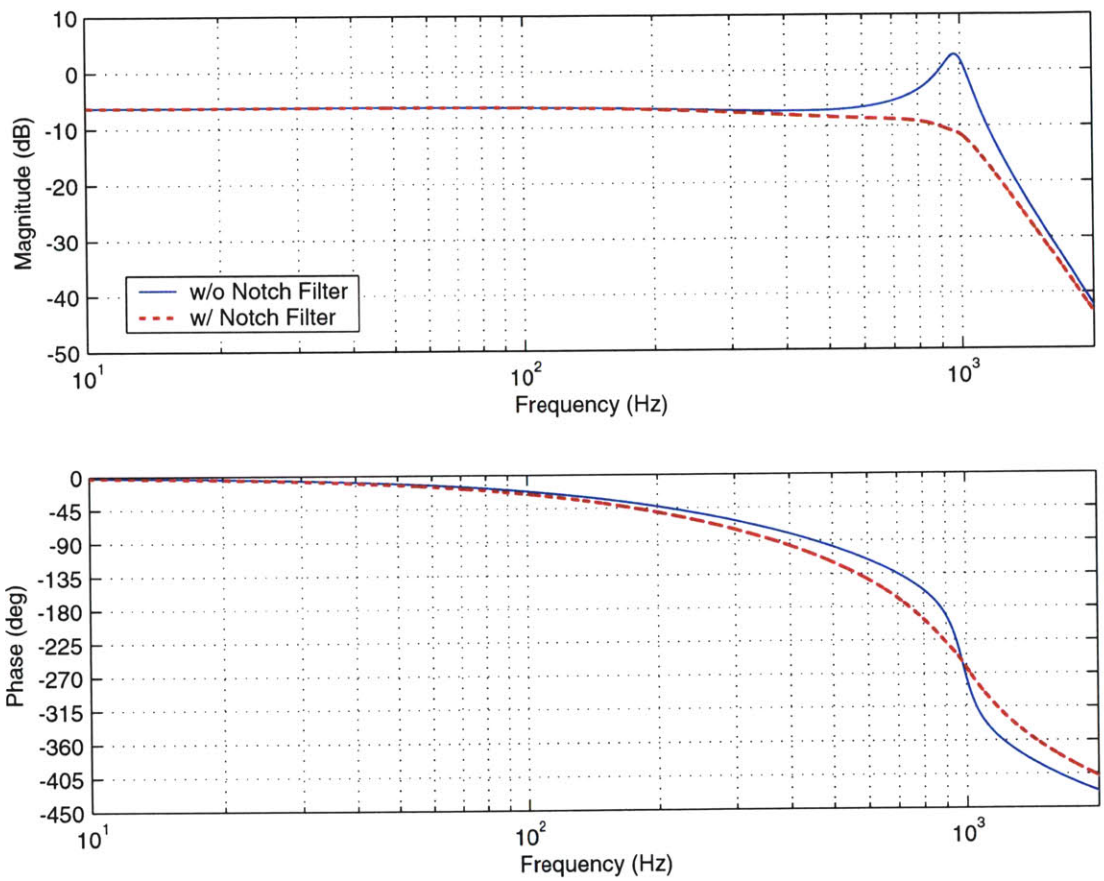

Figure 3-36: Comparison of simulated open-loop plant model $G_{p_3}(s)$ frequency responses with and without the notch filter $G_{notch}(s)$.

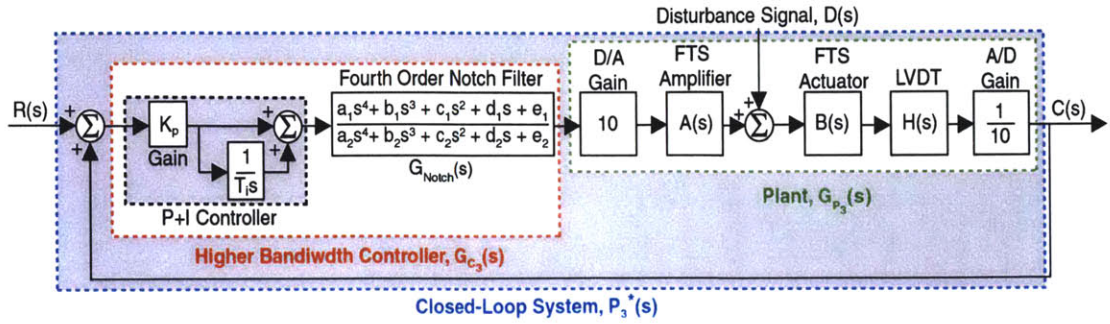

Figure 3-37: Closed-loop block diagram for the variform FTS with a notch filter and proportional plus integral controller. A plus sign has been placed next to the feedback signal instead of the conventional negative feedback nomenclature, since the output C(s) is 180° out of phase with respect to the reference input R(s). This sign change is required to ensure closed-loop stability.

a -20 dB/decade slope at crossover. If we close the loop with only these components, the resulting negative of the loop transmission would have approximately 38° of phase margin at 200 Hz. These characteristics will provide sufficient closed-loop performance, but the advertised FTS literature quotes a minimum 45° of phase margin. Thus, we add a real axis zero to the integrator with a break frequency of 1000 Hz (effectively creating a P+I controller). This configuration provides additional phase lead within the vicinity of the designed crossover frequency. Figure 3-37 illustrates the resulting closed-loop system block diagram.

When we implement this controller on the dSPACE 1102 board, we still want to be able to use the integral anti-windup mentioned previously in Section 3.3. This option is inaccessible unless the integrator is defined as an individual transfer function. Also, Simulink does not allow a real-axis zero be to defined by itself. Thus, we decided to group the P+I zero with a high-frequency pole located at 10 kHz. Figure 3-38 illustrates the resulting closed-loop system block diagram, where the P+I zero plus high-frequency pole continuous-time transfer function and discrete-time equivalent,

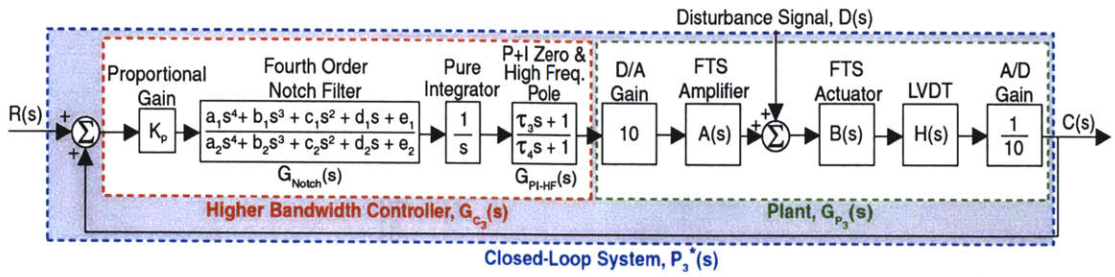

Figure 3-38: Complete closed-loop block diagram for the variform FTS with a notch filter and proportional plus integral controller. A plus sign has been placed next to the feedback signal instead of the conventional negative feedback nomenclature, since the output C(s) is 180° out of phase with respect to the reference input R(s). This sign change is required to ensure closed-loop stability.

sampled at 20 kHz, are given by

$$G_{PI-HF}(s) = \frac{\left(\frac{1}{2000\pi}\right) s + 1}{\left(\frac{1}{20000\pi}\right) s + 1}, \tag{3.21}$$

$$G_{PI-HF}(z) = \frac{4.500861z - 3.27883}{z + 0.22203}. \tag{3.22}$$

With the proportional gain K_p set to 2.733×10^3, the simulated negative of the loop transmission with $G_{c_3}(s)$ predicts an 8 dB gain margin, 49° phase margin, and 1256 rad/sec ($\approx$ 200 Hz) crossover frequency (see Figure 3-40). Figure 3-39 illustrates the complete experimental Simulink block diagram we use to conduct closed-loop testing with G_{c_3}(z).

Figures 3-41 and 3-42 compare the predicted and experimental negative of the loop transmission and closed-loop system frequency responses (we use $G_{p3DELAY}$(s) to calculate the predicted models). These experimental plots show good agreement with the simulated controller model, except for high frequencies and within the vicinity of the 1 kHz resonance. The high-frequency discrepancies are most likely due to un-modelled plant dynamics and the bandwidth of the dSPACE DSA, while the Bode plot 1 kHz waviness is due to sup-optimal notch filter placement. We could

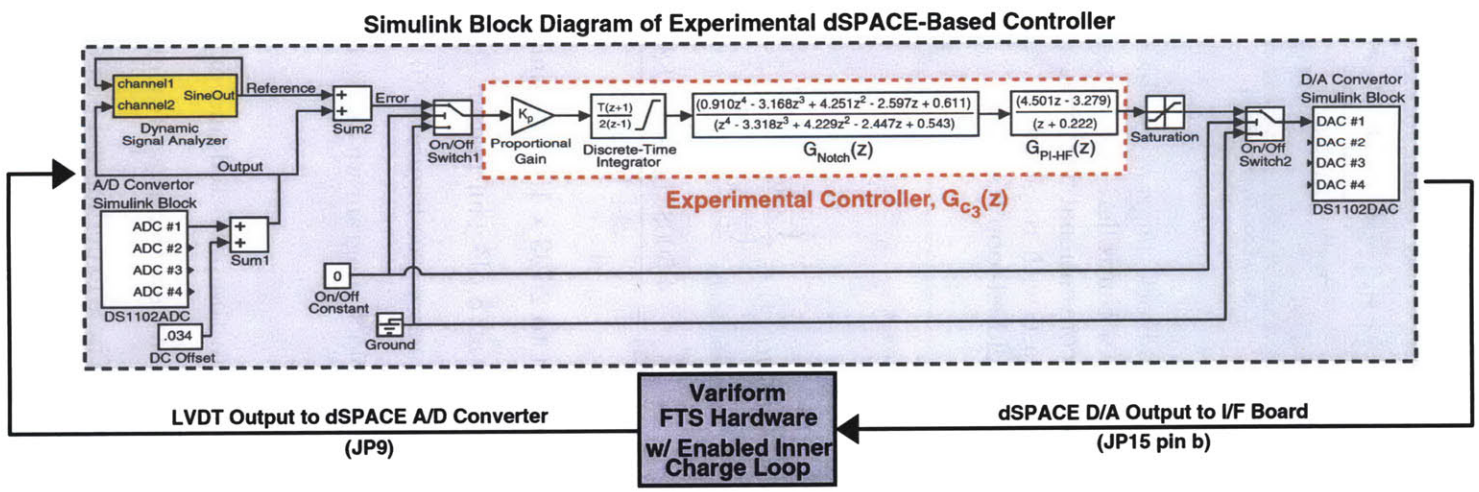

Figure 3-39: Experimental Simulink closed-loop block diagram with the higher bandwidth controller $G_{c_3}(z)$.

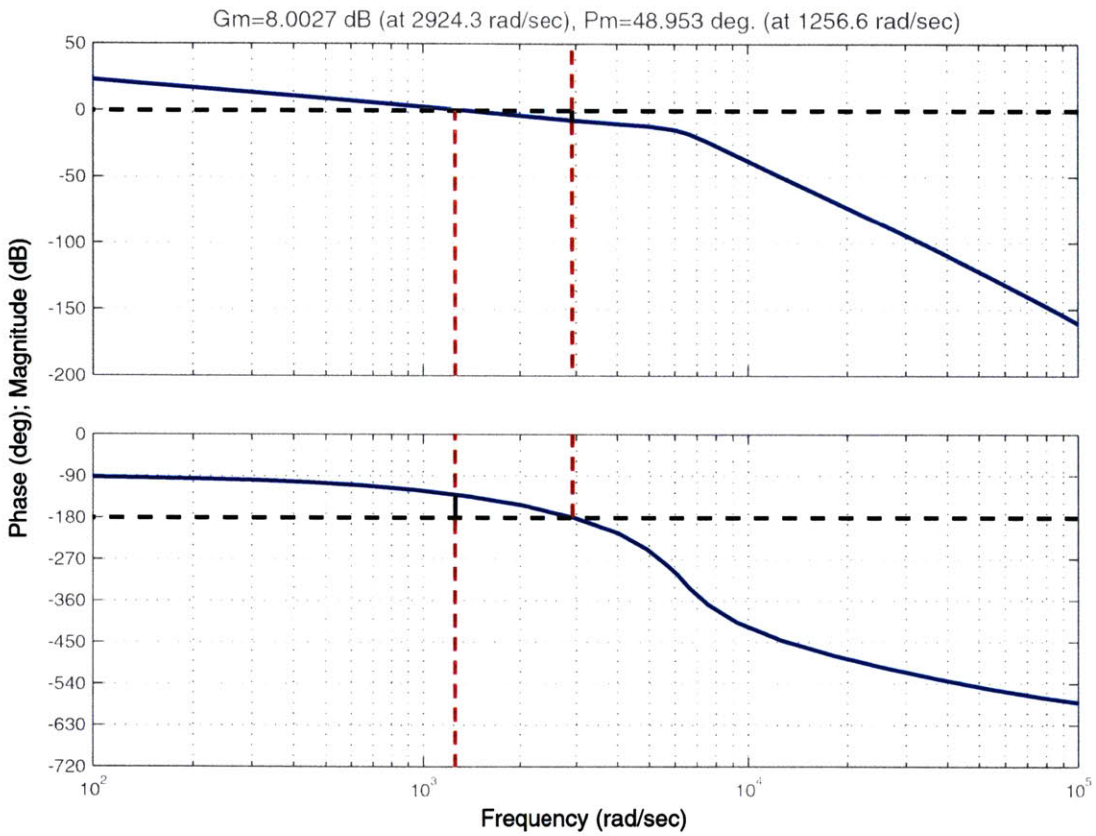

Figure 3-40: Simulated Bode plot indicating the gain and phase margin for the negative of the loop transmission with the higher bandwidth controller $G_{c_3}(s)$.

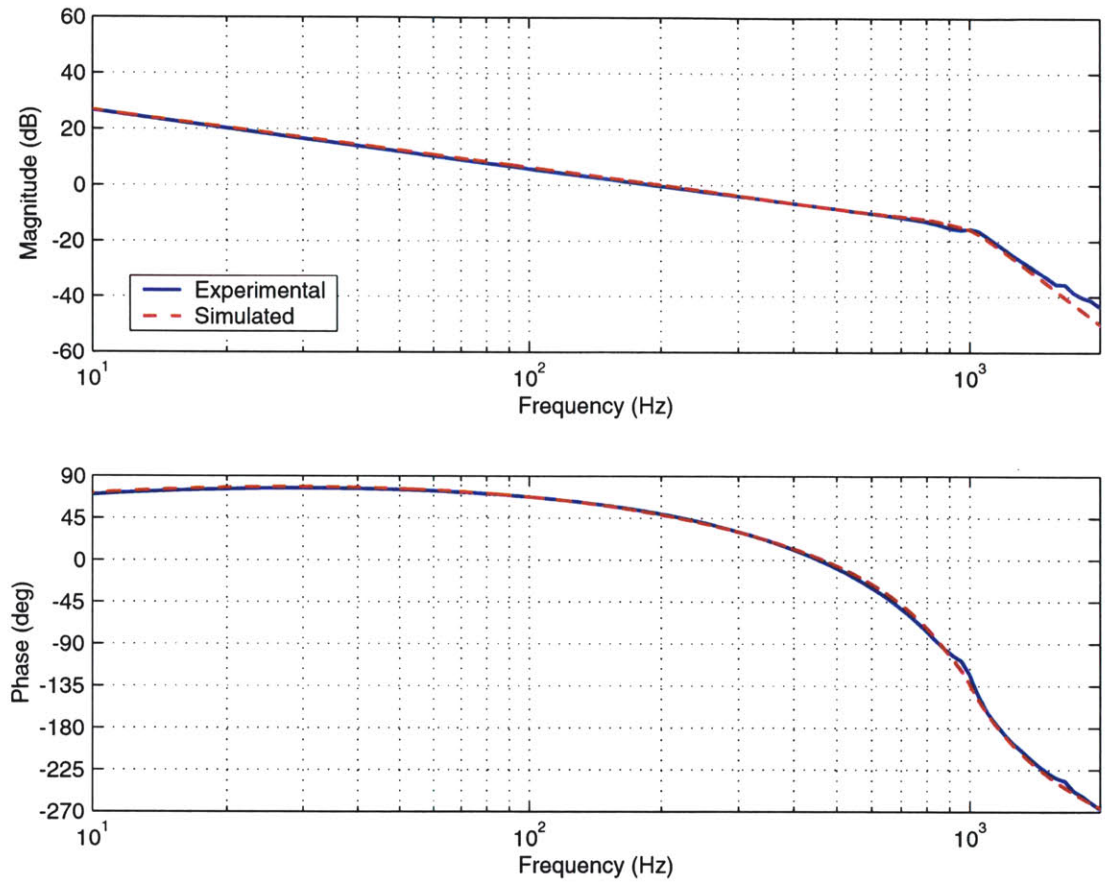

Figure 3-41: Comparison of the experimental and simulated negative of the loop transmission frequency responses with the experimental higher bandwidth controller $G_{c_3}(z)$. (Note, the Bode phase plots as shown are shifted by 180°, since a positive change in the command voltage results in a negative change of the FTS displacement.)

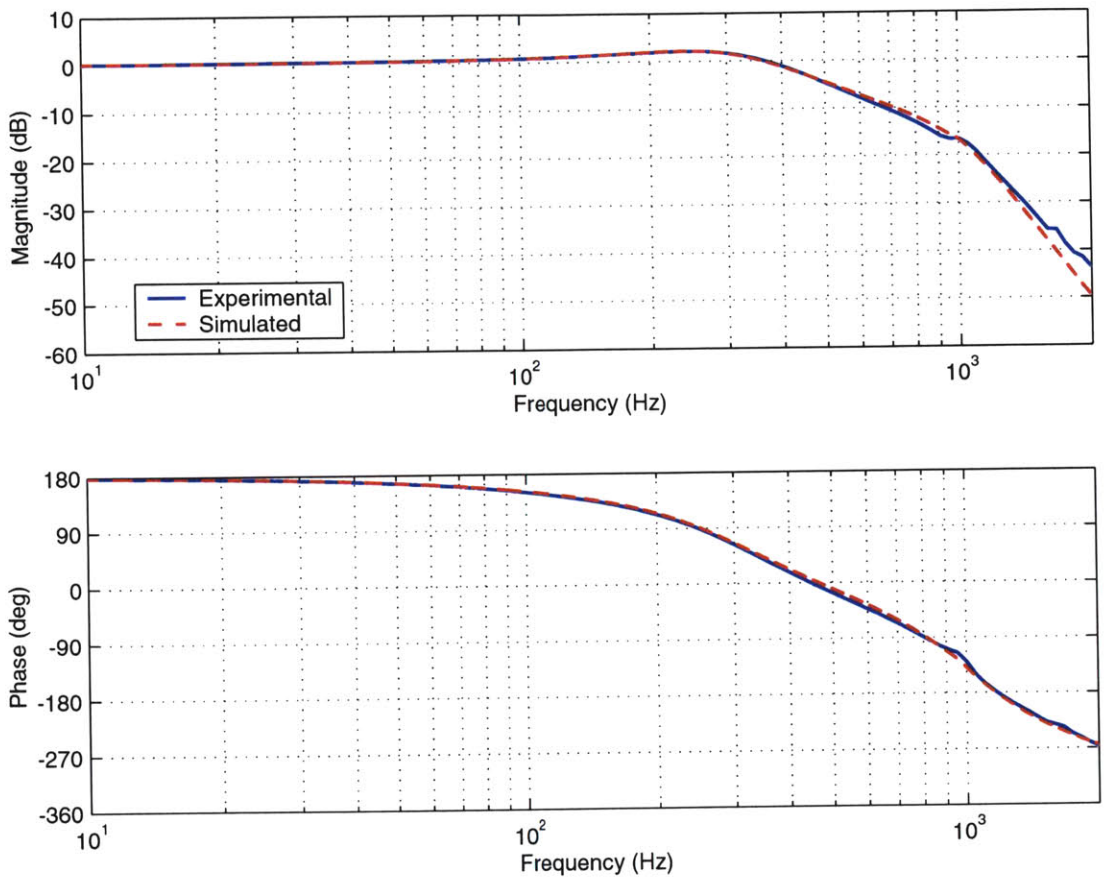

Figure 3-42: Comparison of the experimental and simulated closed-loop system frequency responses with the experimental higher bandwidth controller $G_{c_3}(z)$. (Note, the Bode phase plots as shown are shifted by 180°, since a positive change in the command voltage results in a negative change of the FTS displacement.)

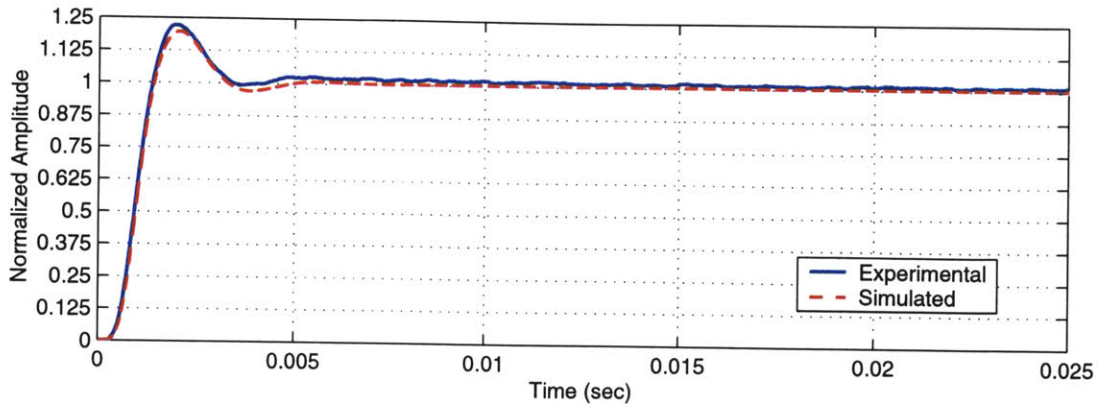

Figure 3-43: Comparison of the experimental and simulated closed-loop step responses with the experimental higher bandwidth controller $G_{c_3}(z)$. The experimental response has been normalized to unity final value for ease of comparison.

re-design (3.18) and try to eliminate these inaccuracies but the errors are relatively small and they do not affect the overall loop stability. Also, the 1 kHz resonance can change shape from day to day, depending on the mass of the cutting tool connected the FTS actuator or system operating temperatures. If the resonant peak deviates significantly from the parametric plant model, $G_{Notch}(\mathrm{s})$ will not provide sufficient attenuation and the system will go unstable. This is one of the inherent problems associated with controllers incorporating notch filters. As a result, we cannot rely on (3.18) to provide robust closed-loop performance and we forego any further design effort here.

Figure 3-43 compares the normalized experimental and simulated closed-loop step response to a 300 mV input. We see very good agreement between the experimental and simulated results but the experimental curve shows a slightly larger percentage overshoot and longer settling time. This is due to the neglected inner charge loop dynamics, which introduce a pole/zero doublet to the negative of the loop transmission. The effect on the closed-loop step response is not highly visible at this scale, since the residue of the additional exponential is small, but the pole/zero doublet does create a long-tail transient that is the most significant dynamic for fine settling.

With the inner charge loop dynamics located at such a low frequency, this problem is unavoidable. We suggest re-designing the inner charge loop with a higher 0 dB crossover frequency than the outer position loop. This will move the inner charge loop dynamics further into the LHP, reducing the effect of the pole/zero doublet on the closed-loop system. In the following section, we design another higher bandwidth controller with the Kaman Instrumentation Inductive Sensor.

3.5.2 Controller Design with the Kaman Instrumentation Inductive Sensor

Figure 3-12 shows the experimental Variform FTS open-loop frequency response using the Kaman Instrumentation inductive sensor. Since our previous controller design with the LVDT is only able to achieve about a 200 Hz crossover frequency, we decided to fit a parametric plant model to this data and see how much more performance we could achieve. The resulting fifth order plant transfer function, ignoring the inner charge loop dynamics, is given by

$$G_{p_4}(s) = \frac{-0.2041}{(\frac{s}{3700\pi}+1)(\frac{s^2}{\omega_7^2}+\frac{2\zeta_9 s}{\omega_7}+1)(\frac{s^2}{\omega_8^2}+\frac{2\zeta_{10} s}{\omega_8}+1)}, \tag{3.23}$$

where $\omega_7 = 6400\pi$ rad/sec, $\zeta_9 = 0.04$, $\omega_8 = 6170$ rad/sec, and $\zeta_{10} = 0.0625$ (Appendix D includes the State Space Matrices for the parametric plant model $G_{p_4}(s)$). If we model the additional time delay of the dSPACE DSA, equation (3.23) becomes

$$G_{p_{4DELAY}}(s) = \frac{-0.2041e^{-2\times10^{-5}s}}{(\frac{s}{3700\pi}+1)(\frac{s^2}{\omega_7^2}+\frac{2\zeta_9 s}{\omega_7}+1)(\frac{s^2}{\omega_8^2}+\frac{2\zeta_{10} s}{\omega_8}+1)}, \tag{3.24}$$

Figure 3-44 compares the experimental and simulated open-loop frequency response with $G_{p_{4DELAY}}$(s). During the following experimental controller design, we actually use G_{p_4}(s) to model the FTS open-loop frequency response with enabled in-

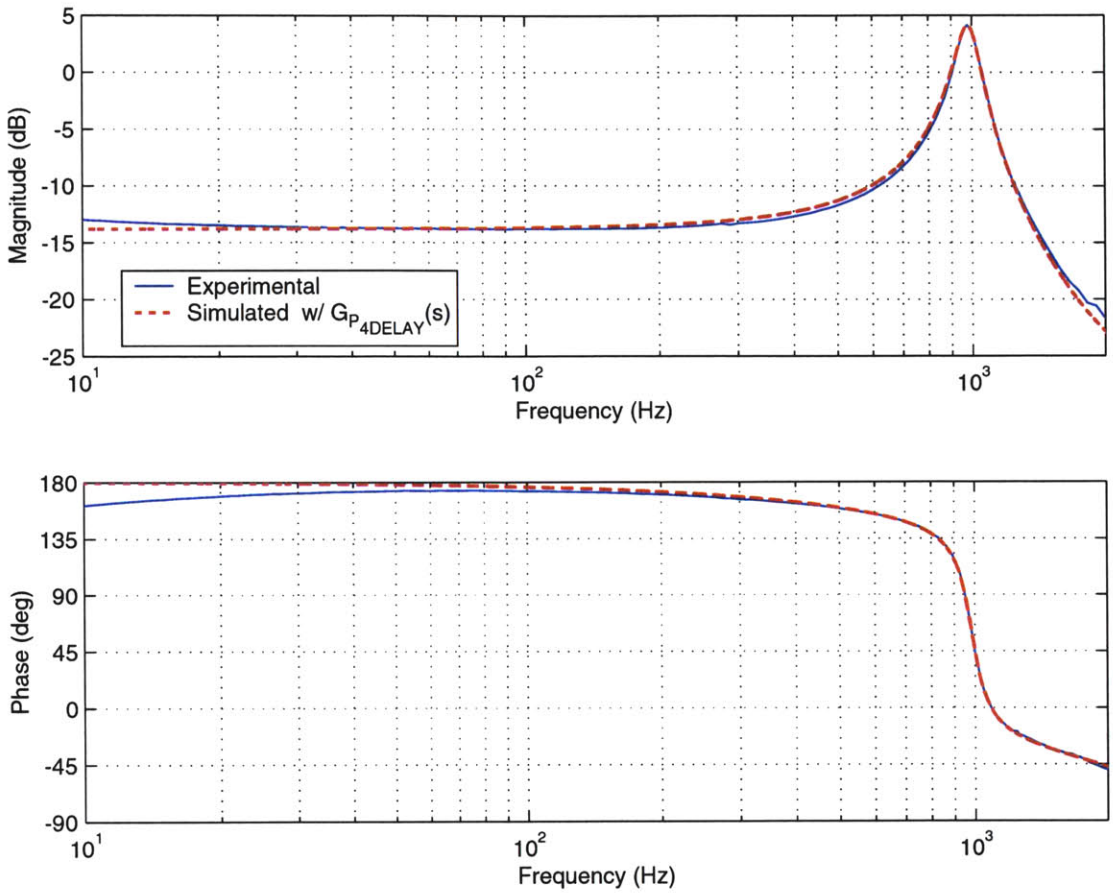

Figure 3-44: Comparison of the experimental and simulated open-loop frequency responses with the Kaman Instrumentation inductive sensor. This frequency response was conducted with the dSPACE DSA. (Note, the Bode phase plots as shown are shifted by 180°, since a positive change in the command voltage results in a negative change of the FTS displacement.)

ner charge loop. We accidently overlooked the pure time delay the during the initial experimental controller design and due to time constraints, were not able to re-iterate the design. Instead, we compare the resulting experimental closed-loop system to the predicted model with the additional phase lag.

We see in Figure 3-44 that the Bode magnitude plot has a relatively flat low-frequency behavior. We decided to place two pure integrators into the loop, providing high low-frequency gain and a -40 dB/decade slope. After choosing 400 Hz as the desired crossover frequency, we add another fourth order notch filter to attenuate the

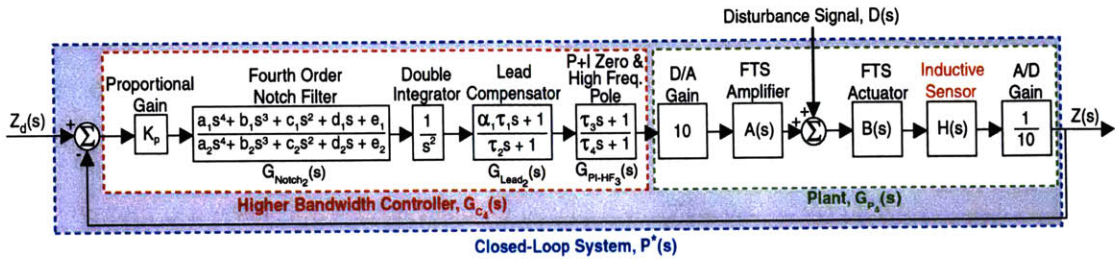

Figure 3-45: Closed-Loop System Block Diagram for the Variform FTS with the higher bandwidth controller $G_{c_4}(s)$ and the Kaman Instrumentation inductive sensor.

1 kHz resonant peaking. With these components in place, the simulated negative of the loop transmission yields approximately -231° of phase at 400 Hz. Analogous to the previous design, we add a real-axis zero to make a P+I controller but group the P+I real-axis zero with a high-frequency pole, since we still want to be able to define each integrator individually and utilize the integral anti-windup option. We mistakenly placed the high-frequency pole at a frequency of 50 kHz, which is not achievable in practice. A better choice would be to place this pole around 10 kHz but do to time constraints, we were not able to redesign this particular controller. Thus, we leave an improved controller design with the Kaman Instrumentation sensor for future work.

With the addition of the P+I zero, the controller still does not provide enough phase margin at a 400 Hz crossover frequency. Thus, we decided to introduce a lead compensator centered about 400 Hz with alpha set equal to ten. Figure 3-45 illustrates the complete closed-loop system block diagram, where we refer to the entire feedback controller as $G_{c_4}(s)$. The fourth order notch filter continuous-time transfer function and discrete-time equivalent, sampled at 20 kHz, are given by

$$G_{Notch}(s) = \left(\frac{s^2 + 2\zeta_{11}\omega_9 s + \omega_9^2}{s^2 + 2\zeta_{12}\omega_9 s + \omega_9^2}\right)\left(\frac{s^2 + 2\zeta_{13}\omega_{10} s + \omega_{10}^2}{s^2 + 2\zeta_{14}\omega_{10} s + \omega_{10}^2}\right), \tag{3.25}$$

$$G_{Notch}(z) = \frac{0.818379z^4 - 2.907765z^3 + 3.996636z^2 - 2.510037z + 0.609664}{z^4 - 3.209985z^3 + 3.951601z^2 - 2.207817z + 0.473078}, \tag{3.26}$$

where $\omega_9 = 6170$ rad/sec, $\zeta_{11} = 0.064$, $\zeta_{12} = 0.575$, $\omega_{10} = 6531$ rad/sec, $\zeta_{13} = 0.4$, and $\zeta_{14} = 0.6182$. Once again, we should have implemented (3.26) as two series z-transforms of the form

$$G_{Notch}(z) = \left(\frac{0.868771z^2 - 1.625433z + 0.835896}{z^2 - 1.625433z + 0.704666}\right)\left(\frac{0.941997z^2 - 1.584552z + 0.729354}{z^2 - 1.584552z + 0.671351}\right), \tag{3.27}$$

which improves the experimental controller's numerical stability. The lead compensator and P+I zero plus high-frequency pole continuous-time transfer functions and discrete-time equivalent, also sampled at 20 kHz, are given by

$$G_{lead}(s) = \frac{\left(\frac{10s}{800\pi\sqrt{10}}\right) + 1}{\left(\frac{s}{800\pi\sqrt{10}}\right) + 1}, \tag{3.28}$$

$$G_{lead}(z) = \frac{8.508185z - 8.176671}{z - 0.668486}, \tag{3.29}$$

$$G_{PI-HF}(s) = \frac{\left(\frac{s}{800\pi}\right) + 1}{\left(\frac{s}{100000\pi}\right) + 1}, \tag{3.30}$$

$$G_{PI-HF}(z) = \frac{15.004998z - 13.230886}{z + 0.774113}. \tag{3.31}$$

With the proportional gain K_p set to 7.183056×10^6, the simulated negative of the loop transmission predicts a 7 dB gain margin, 48° phase margin and 2513 rad/sec ($\approx$ 400 Hz) 0 dB crossover frequency (see Figure 3-47). Figure 3-46 illustrates the complete experimental Simulink block diagram we use to conduct closed-loop testing with G_{c_4}(z).

Figures 3-48 and 3-49 compare the experimental and simulated negative of the loop transmission and closed-loop system frequency responses while Figure 3-50 compares the normalized experimental and simulated closed-loop step response to a 300 mV input. These experimental results agree fairly well with the predicted model but there are several discrepancies between the plots. We speculate that the additional magnitude peaking in the closed-loop frequency response is due to the previously

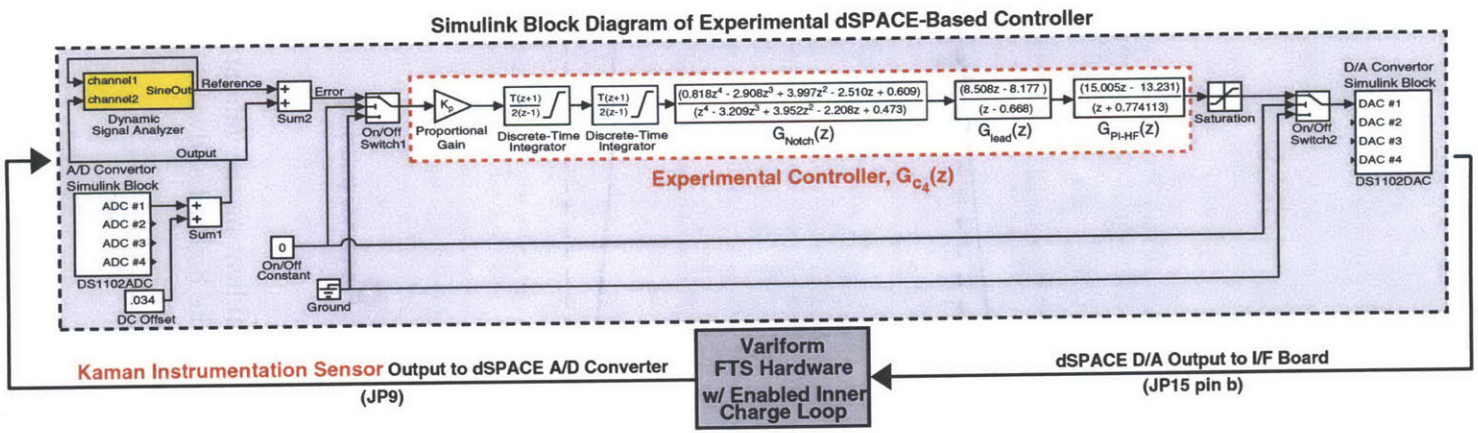

Figure 3-46: Experimental Simulink closed-loop block diagram with the higher bandwidth controller $G_{c_4}(z)$.

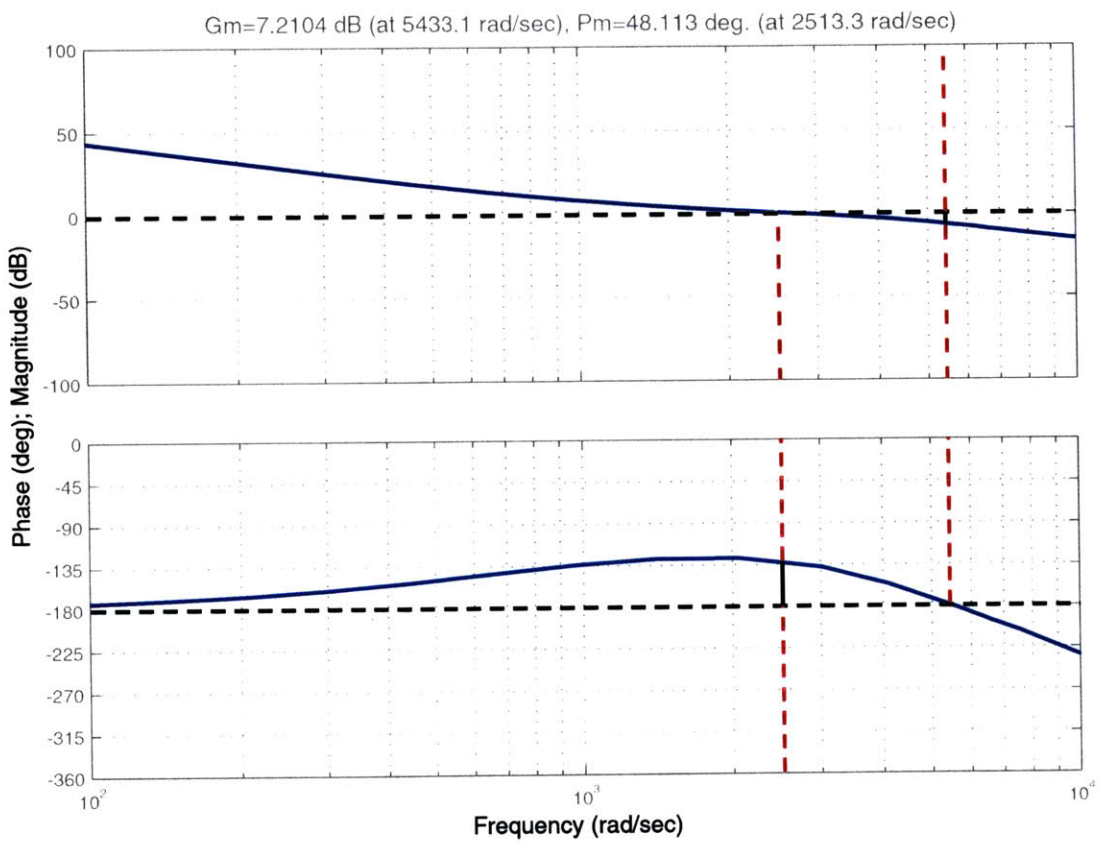

Figure 3-47: Simulated Bode plot indicating the gain and phase margin for the negative of the loop transmission with the higher bandwidth controller $G_{c_4}(s)$ and Kaman Instrumentation inductive sensor.

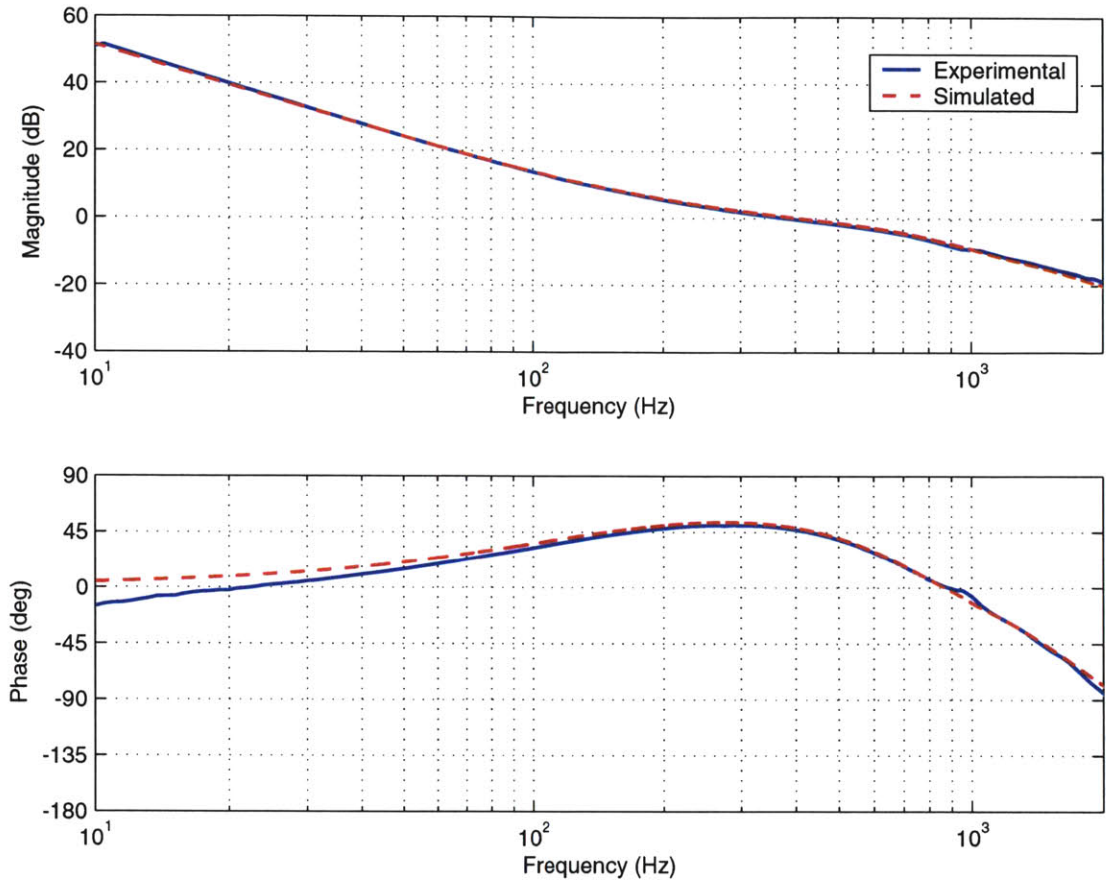

Figure 3-48: Comparison of the experimental and simulated negative of the loop transmission frequency responses with the higher bandwidth controller $G_{p_4}(s)$ and Kaman Instrumentation inductive sensor. (Note, the Bode phase plots as shown are shifted by 180°, since a positive change in the command voltage results in a negative change of the FTS displacement.)

mentioned neglected inner-charger loop dynamics, non-optimal notch filter placement, and pure time delay from the dSPACE 1102 controller board. The experimental closed-loop step response shows an oscillating mode around 1 kHz. We speculate that this is due to the excited mechanical resonance of the FTS actuator, though we did not have time to go back and further analyze the system. Thus, we leave this investigation to future work.

In summary, this particular controller design is by no means a good design choice. It is meant rather to show the superiority of the inductive sensor to the LVDT and

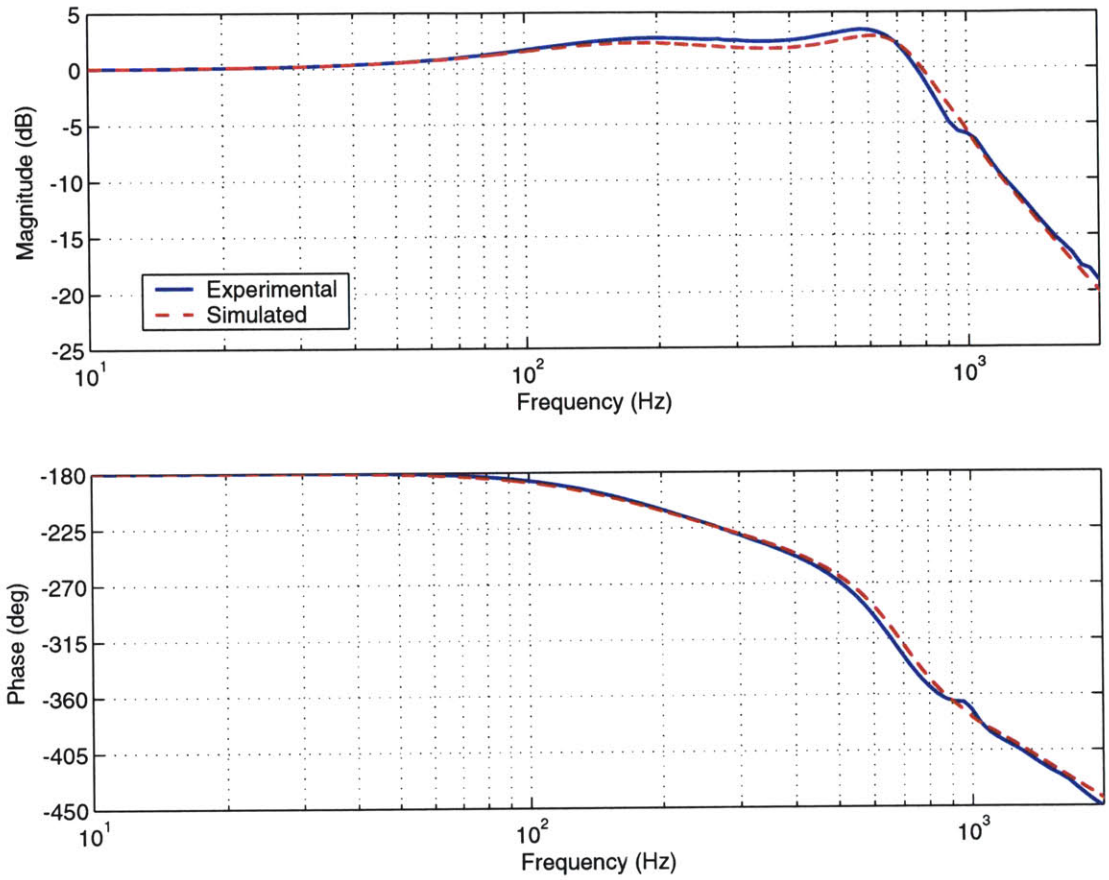

Figure 3-49: Comparison of the experimental and simulated closed-loop frequency responses with the higher bandwidth controller $G_{p_4}(s)$ and Kaman Instrumentation inductive sensor. (Note, the Bode phase plots as shown are shifted by 180°, since a positive change in the command voltage results in a negative change of the FTS displacement.)

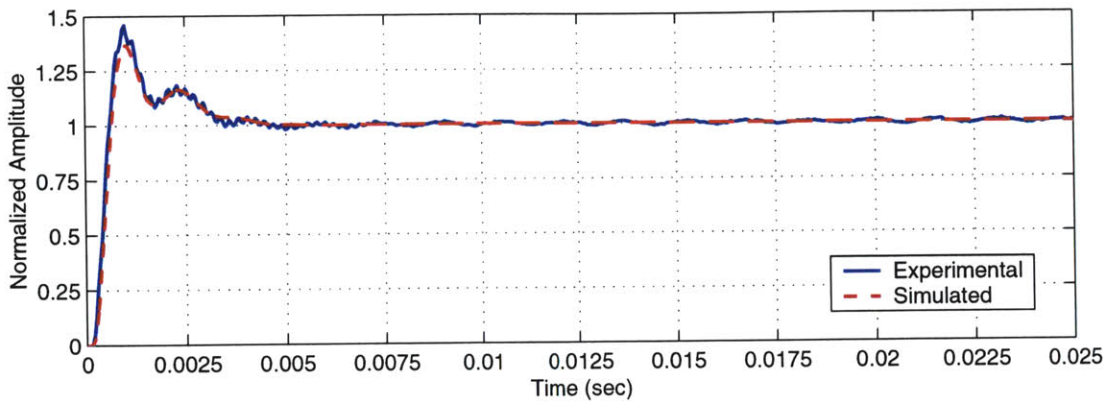

Figure 3-50: Comparison of the experimental and simulated closed-loop step responses with the higher bandwidth controller $G_{p_4}(s)$ and Kaman Instrumentation inductive sensor. The experimental response has been normalized to unity final value for ease of comparison.

one of the many achievable higher bandwidth controller designs. The slope of the negative of the loop transmission in Figure 3-48 is too flat through crossover, which leads to the strange closed-loop dynamics seen in the experimental closed-loop step response. Therefore, further work should be done to investigate the possible closed-loop performance with this particular sensor configuration. In the following section, we detail the experimental design and implementation of several Adaptive Feedforward Cancellation controllers.

3.6 Adaptive Feedforward Cancellation Controller Design

This section details the experimental implementation of several Adaptive Feedforward Cancellation controllers on the Variform FTS. Figure 3-51 illustrates our complete AFC closed-loop block diagram, where the plant and conventional inner-loop compensator transfer functions are given by $G_{p_1}(s)$ and $G_{c_1}(s)$, respectively. Notice the inner and outer AFC loop feedback signals have plus signs instead of the conventional

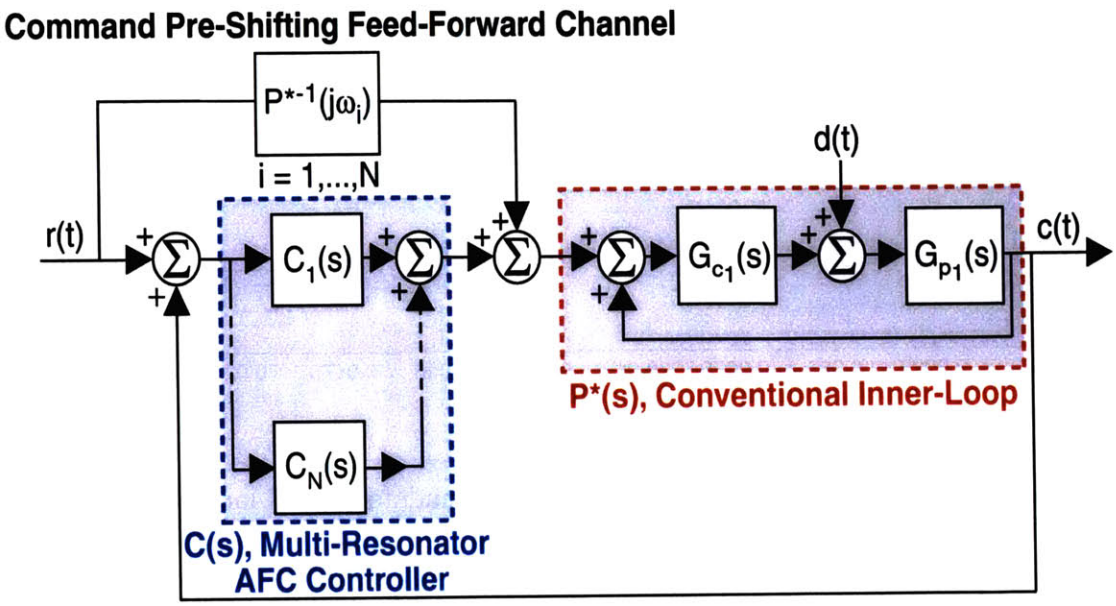

Figure 3-51: Closed-loop block diagram for the Variform FTS Adaptive Feedforward Cancellation experiments. Note, a plus sign has been placed next to the feedback signal in the inner- and outer-loop, since the experimental output c(t) is 180° out of phase with respect to the commanded input r(t).

minus sign. This is due to a negative change in the FTS displacement for a given positive change in the reference input, which causes a 180° phase shift from the reference input (*e.g.*, input to the amplifier I/F board) to the LVDT feedback sensor output. We describe this in detail in Section 3.3.

We utilized the preliminary parametric plant and conventional controller models, which are also detailed in Section 3.3, since the AFC experiments were conducted during the early stages of the thesis and we had not yet investigated further improvements on inner closed-loop performance. It should also be noted that the inner charge loop was not enabled for these tests and we did not take the dSPACE time delay into account, as will be seen in the experimental results. Due to time constraints, we were not able to go back and implement the inner charge loop nor design a higher bandwidth inner-loop with the Kaman Instrumentation sensor, as shown in Section 3.5. Thus, we leave these additions for future work.

3.6.1 Single Resonator AFC Controller

We conducted the following single resonator AFC experiments on the Variform FTS without the command pre-shifting channel. Thus, the inner-loop, negative of the loop transmission, and closed-loop transfer functions are given by

$$
\begin{aligned}
P^*(s) &= \frac{G_{c_1}(s)G_{p_1}(s)}{1 - G_{c_1}(s)G_{p_1}(s)}, && (3.32)\\
-L(s) &= C_i(s)P^*(s) = C_i(s)\left(\frac{G_{c_1}(s)G_{p_1}(s)}{1 - G_{c_1}(s)G_{p_1}(s)}\right), && (3.33)\\
\frac{C(s)}{R(s)} &= \frac{L(s)}{1 - L(s)} = \frac{C_i(s)\left(\frac{G_{c_1}(s)G_{p_1}(s)}{1-G_{c_1}(s)G_{p_1}(s)}\right)}{1 - C_i(s)\left(\frac{G_{c_1}(s)G_{p_1}(s)}{1-G_{c_1}(s)G_{p_1}(s)}\right)},\\
&= \frac{C_i(s)G_{c_1}(s)G_{p_1}(s)}{1 - G_{c_1}(s)G_{p_1}(s) - C_i(s)G_{c_1}(s)G_{p_1}(s)}. && (3.34)
\end{aligned}
$$

We first used dSPACE to provide a constant amplitude disturbance input to the inner-loop of the form

$$d(t) = a_1 \cos(\omega_1 t) + b_1 \sin(\omega_1 t), \tag{3.35}$$

where the parameters are selected as $a_1 = \frac{1}{2}$, $b_1 = \frac{1}{4}$, and $\omega_1 = 360\pi$ rad/sec (180 Hz). The magnitude and phase of the inner-loop, evaluated at s = $j\omega_1$, are

$$
\begin{aligned}
|P^*(j\omega_1)| &= 0.897\ (-0.946\ \text{dB}), && (3.36)\\
\angle P^*(j\omega_1) &= -1.498\ \text{rad}\ (-85.8^o). && (3.37)
\end{aligned}
$$

We see from (3.37) that $|\angle P^*(j\omega_1)| < \frac{\pi}{2}$, which means that we can theoretically design a stable single resonator AFC system to eliminate the disturbance without the use of the phase advance parameter. The resulting AFC controller, with resonator frequency $\omega_i = 360\pi$ rad/sec, is given by

$$C_1(s) = g_i \left[\frac{s}{s^2 + 129600\pi^2}\right], \tag{3.38}$$

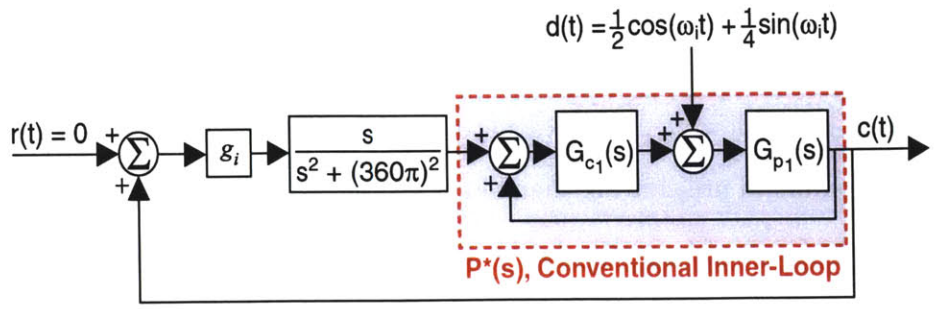

Figure 3-52: Single resonator AFC closed-loop block diagram for the Variform FTS, designed to eliminate a constant amplitude disturbance with frequency $\omega_i = 360\pi$ rad/sec. The phase advance parameter $\phi_i = 0$. Note, a plus sign has been placed next to the feedback signal in the inner- and outer-loop, since the experimental output c(t) is 180° out of phase with respect to the commanded input r(t).

and the LTI equivalent closed-loop block diagram is shown in Figure 3-52. We experimentally implement this system through the previously described AFC modulation/demodulation structure, but convert the integrators into discrete-time equivalents (sampled at 10 kHz). The resulting discrete-time equivalent single resonator AFC controller is shown in Figure 3-53, which also includes an illustration of one of the Simulink closed-loop block diagrams we used during the Adaptive Feedforward Cancellation experiments.

Figure 3-54 shows the experimental transient responses of the Fourier coefficient estimates, $\hat{a_2}(t)$ and $\hat{b_2}(t)$, with the proportional gain g_i set to 10. We see that both of these signals diverge to infinity, indicating an unstable system. This instability is likely due to the additional phase loss from the dSPACE time delay. The predicted negative of the loop transmission, without ϕ_i, only has approximately 4° of phase margin. The actual system includes the additional phase lag from the DSP, as well as any modelling errors in the plant transfer function. Therefore, the resulting closed-loop system is not robust at all. We conducted this particular experiment simply to provide an illustration of the potential dangers in designing an AFC system with insufficient phase margin and not including the phase advance parameter.

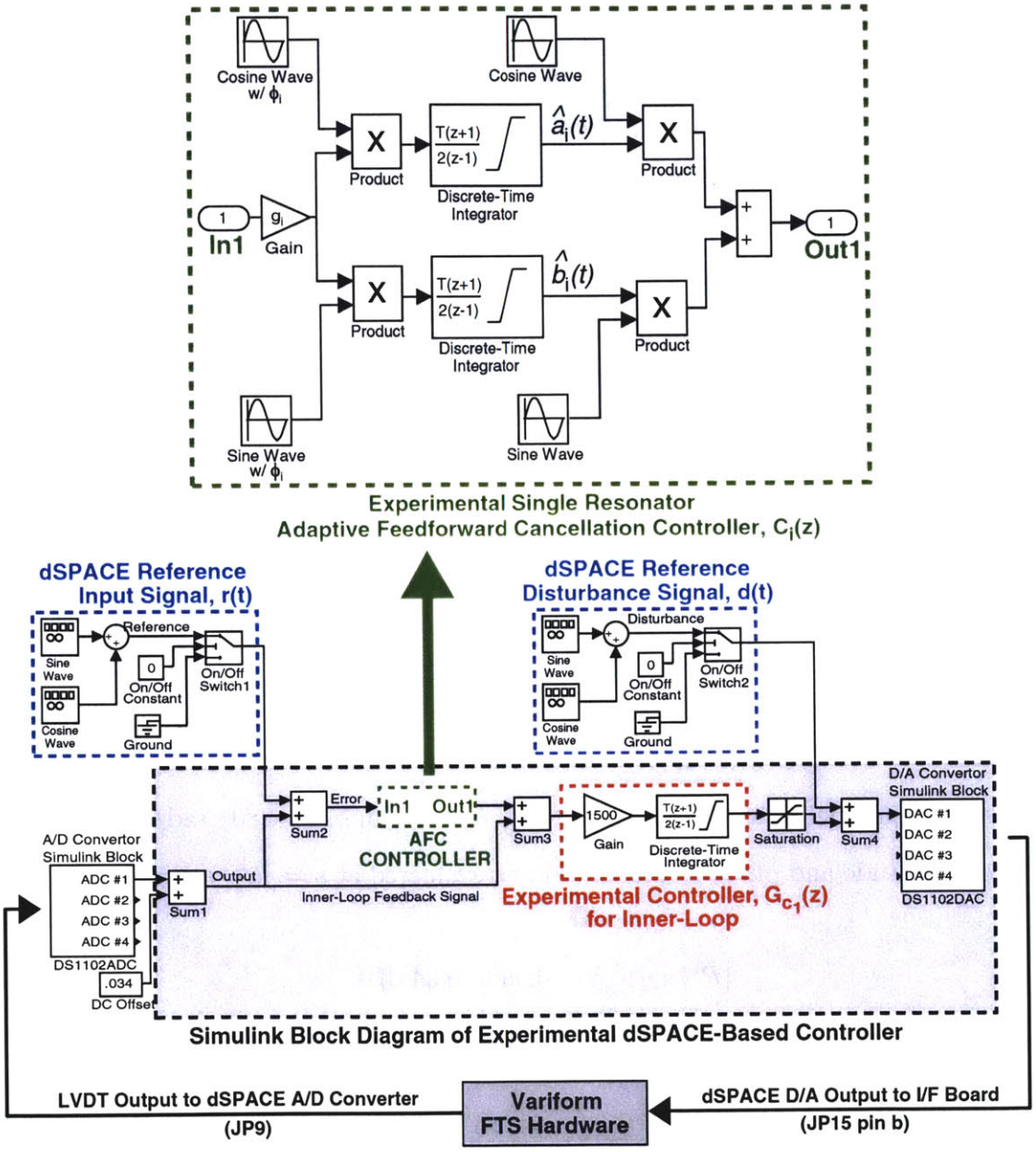

Figure 3-53: Sample Simulink experimental closed-loop block diagram for single resonator AFC testing.

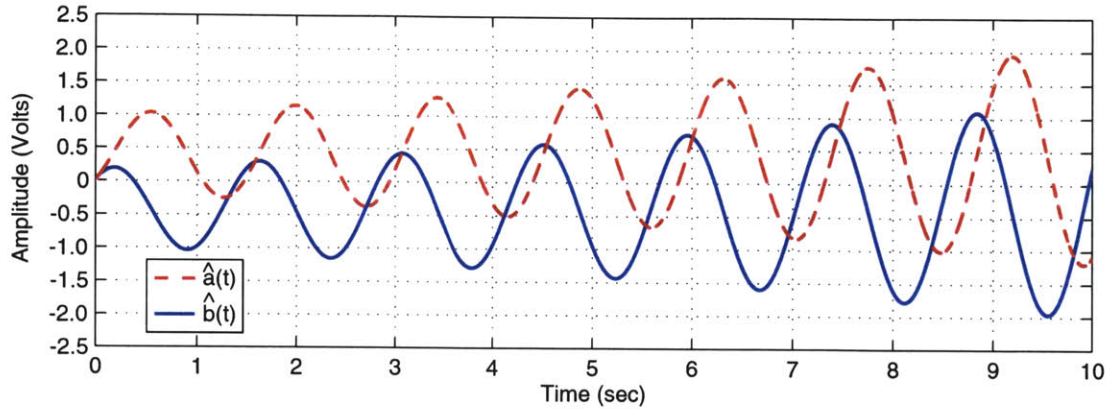

Figure 3-54: Experimental transient responses of the Fourier coefficient estimates, $\hat{a_1}(t)$ and $\hat{b_1}(t)$, for the closed-loop AFC system designed to cancel a disturbance input with frequency $\omega_1 = 360\pi$ rad/sec.

Our next experimental AFC controller is designed to eliminate a constant amplitude disturbance input to the inner-loop of the form

$$d(t) = a_2 \cos(\omega_2 t) + b_2 \sin(\omega_2 t), \tag{3.39}$$

where the parameters are selected as $a_2 = \frac{1}{10}$, $b_2 = \frac{1}{10}$, and $\omega_2 = 280\pi$ rad/sec (140 Hz). The magnitude and phase of the inner-loop, evaluated at s $= j\omega_2$, are

$$|P^*(j\omega_1)| = 0.96\ (-0.34\ \text{dB}), \tag{3.40}$$

$$\angle P^*(j\omega_1) = -1.146\ \text{rad}\ (-65.7^o), \tag{3.41}$$

and the resulting single resonator AFC controllers, with and without the proper phase advance parameter, are given by

$$C_2(s) = g_i \left[\frac{s}{s^2 + 78400\pi^2} \right], \tag{3.42}$$

$$C_{2_{\phi i}}(s) = g_i \left[\frac{(0.412s - 801.6)}{s^2 + 78400\pi^2} \right]. \tag{3.43}$$

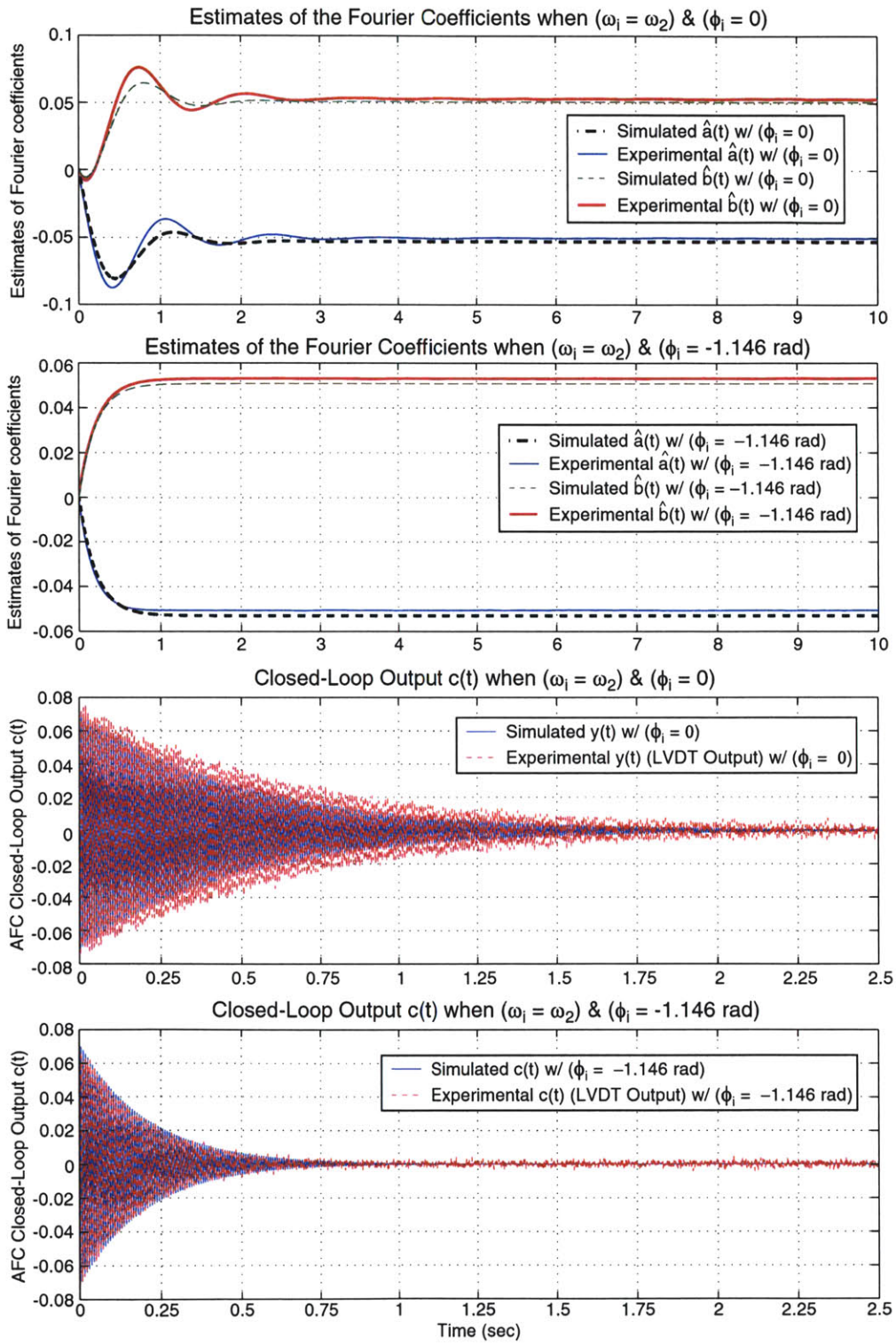

Figure 3-55: Experimental transient responses of the Fourier coefficient estimates, $\hat{a_2}$(t) and $\hat{b_2}$(t), and output c(t) for the closed-loop AFC system designed to cancel a constant amplitude disturbance input with frequency $\omega_2 = 280\pi$ rad/sec.

Figure 3-55 compares the simulated and experimental transient responses for $\hat{a_2}(t)$ and $\hat{b_2}(t)$, and the closed-loop output c(t) to the disturbance input, when $g_i = 10$. We see that our modelled AFC closed-loop system predicts the actual dynamics of the Fourier coefficients and closed-loop output reasonably well. The experimental $\hat{a_2}(t)$ and $\hat{b_2}(t)$ curves actually settle to different values than predicted, and the curves at the top of Figure 3-55 also experience a more oscillatory response. These results are most likely due to the additional phase lag from the experimental dSPACE-based controller and modelling errors in the plant transfer function $G_{p_1}(s)$. The plant non-linearities, as discussed in Section 3.3, may also be a partial cause of these discrepancies.

A comparison of the closed-loop outputs in Figure 3-55 shows that once the proper choice of ϕ_i is implemented, the convergence rate decreases, as described in Section 2.2.5. This is a direct result of the change in the dynamics of the estimates of the Fourier coefficients. Without the phase advance parameter, $\hat{a_2}(t)$ and $\hat{b_2}(t)$ exhibit a rather oscillatory behavior, since the negative of the loop transmission only has approximately 24° of phase margin. With the proper ϕ_i value, the system phase margin approaches 90°, as discussed in Section 2.2.3, and the estimates of the Fourier coefficients experience what appears to be a dominant first-order response, along with a shorter settling time. We present an in depth analysis of these properties in Section 5.4.1, which provides part of the motivation for our Adaptive Feedforward Cancellation viewed from an oscillator amplitude control perspective. Next, we provide an AFC experiment with a two resonator system.

3.6.2 Two Resonator AFC System

This section summarizes the implementation of a two resonator AFC controller on the Variform FTS. Our experiment shows that for multiple resonator systems, we can approximate the dynamics of the error signal by the superposition of the individual dynamics of each resonator to its accompanying reference input frequency component.

This is due to the fact that the multi-resonator AFC algorithm only increases control authority over a selected set of narrow-band frequencies and each resonator dominates the response to the components of the reference/disturbance input within that particular bandwidth. We use this assumption when we view multiple AFC resonator systems from an oscillator amplitude control perspective, as shown in Section 5.4.2.

For this example, we consider a constant amplitude reference trajectory of the form

$$r(t) = a_3 \sin(\omega_3 t) + a_4 \sin(\omega_4 t), \tag{3.44}$$

and select the parameters as $a_3 = \frac{1}{2}$, $\omega_3 = 160\pi$ rad/sec (80 Hz), $a_4 = \frac{1}{4}$, and $\omega_4 = 280\pi$ rad/sec (140 Hz). The magnitude and phase of P^*(s), evaluated at s = $j\omega_3$, are

$$|P^*(j\omega_1)| = 0.9984 \ (-0.014 \text{ dB}), \tag{3.45}$$

$$\angle P^*(j\omega_1) = -0.632 \text{ rad } (-36.2^o), \tag{3.46}$$

while the magnitude and phase of the inner-loop at s = $j\omega_4$ are defined in (3.40) and (3.41). The AFC controllers, with resonator frequency $\omega_i = \omega_3$, are given by

$$C_3(s) = g_i \left[\frac{s}{s^2 + 25600\pi^2} \right], \tag{3.47}$$

$$C_{3_{\phi i}}(s) = g_i \left[\frac{(0.807s - 297.09)}{s^2 + 25600\pi^2} \right]. \tag{3.48}$$

and the AFC controllers, designed for $\omega_i = \omega_4$, are equivalent to (3.42) and (3.43).

Figure 3-56 illustrates The LTI equivalent two resonator closed-loop block diagram, while the comparisons between the predicted and experimental transient responses for $\hat{a_3}$(t), $\hat{b_3}$(t), $\hat{a_4}$(t), $\hat{b_4}$(t), and c(t) are shown in Figure 3-57 and Figure 3-58 (Note, we calculated the predicted model as the superposition of two single AFC resonator systems). We see that, akin to the results obtained in Section 3.6.1, the calculated closed-loop model predicts the dynamics of the Fourier coefficients rea-

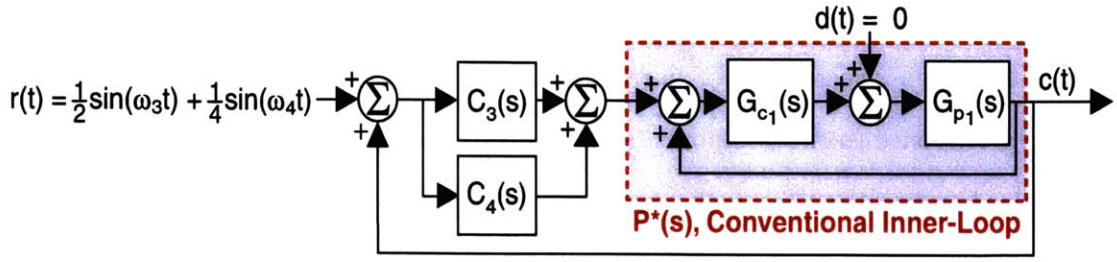

Figure 3-56: Single resonator AFC closed-loop block diagram for the Variform FTS, designed to follow a constant amplitude reference with frequencies with frequencies $\omega_i = 160\pi$ & 280π rad/sec. Note, a plus sign has been placed next to the feedback signal in the inner- and outer-loop, since the experimental output c(t) is 180° out of phase with respect to the commanded input r(t).

sonably well, though the experimental results exhibit a more oscillatory response. We speculate that this is due to the additional dSPACE time delay, plant modelling errors, and/or plant non-linearities.

The closeness of the results in Figure 3-57 and Figure 3-58 (ignoring the additional phase loss due to the unmodelled dSPACE time delay and unmodelled dynamics) confirms the intuition that we can approximate a multiple resonator system as the superposition of N single resonator AFC controllers. However, depending on the size of the g_i and locations of the individual resonators, this assumption does not capture all of the closed-loop dynamics, as shown in Section 5.4.2. These discrepancies are relatively small and do not effect the dominating closed-loop convergence properties Thus, approximating a multiple resonator system as N single resonator systems provides a good approximation of the entire closed-loop performance.

In this example, we again see that once the proper choice of the phase advance parameter is implemented, all of the estimates of the Fourier coefficients experience what appears to be a dominant first-order response and the closed-loop system exhibits a much faster convergence time. Also, we see that without ϕ_i, $\hat{a}_3$(t) and $\hat{b}_3$(t) exhibit a more-damped response than $\hat{a}_4$(t)and $\hat{b}_4$(t). This is because the AFC resonator located at ω_3 has a larger phase margin. We will discuss these characteristics

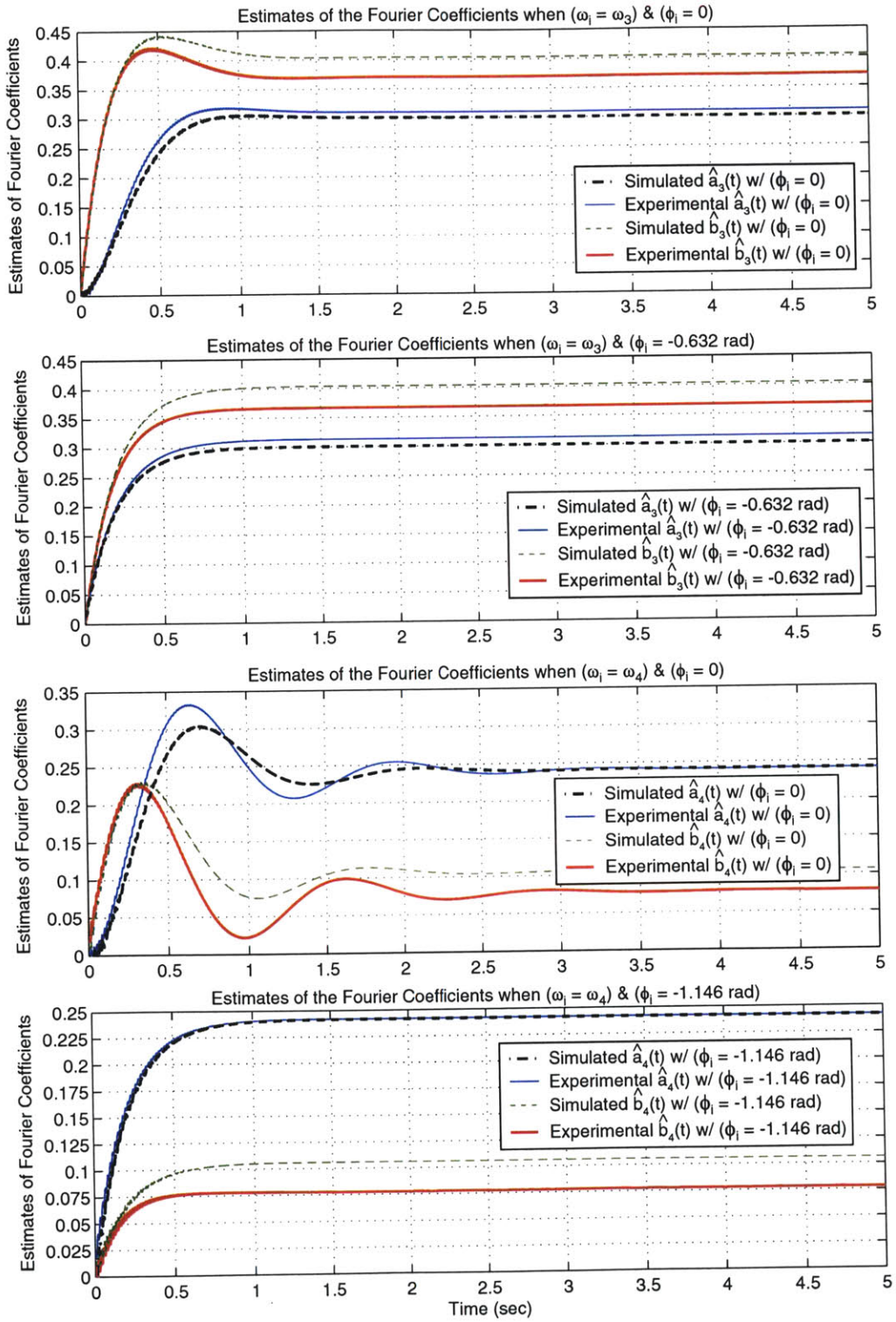

Figure 3-57: Comparison of simulated and experimental transient responses for $\hat{a_3}(t)$, $\hat{b_3}(t)$, $\hat{a_4}(t)$, and $\hat{b_4}(t)$ to the constant amplitude reference input r(t), with and without the phase advance parameter.

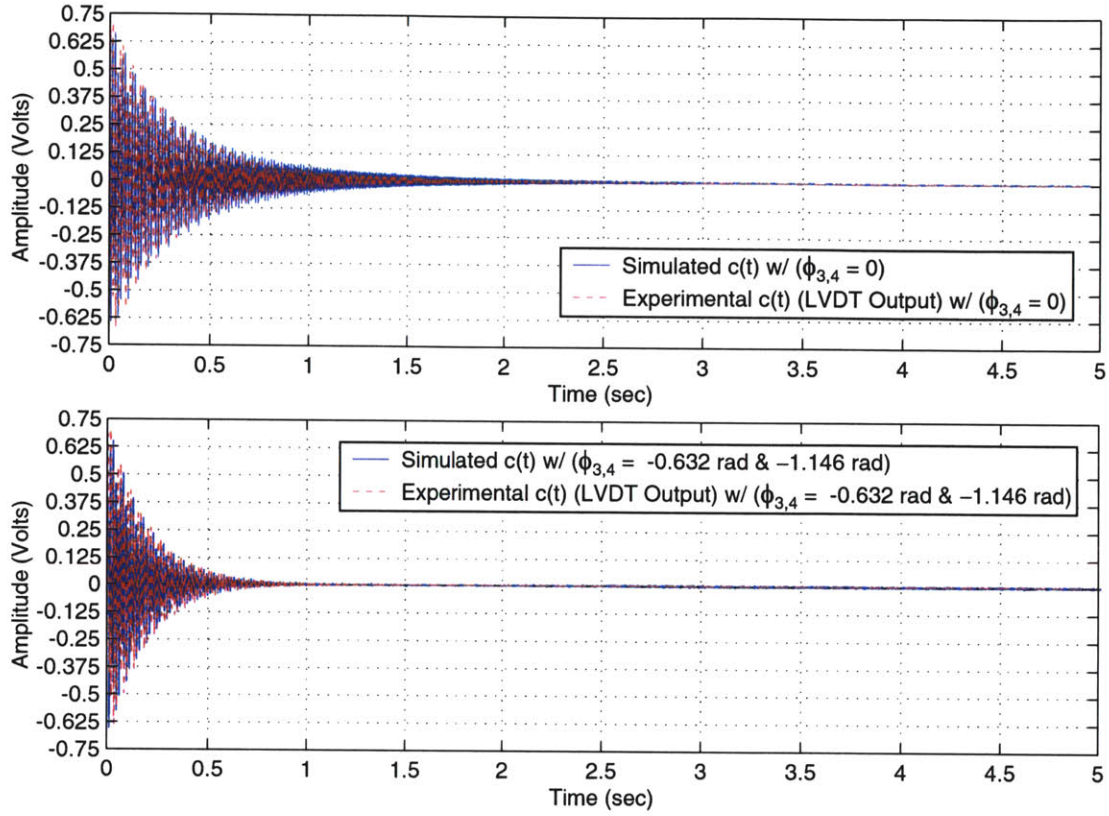

Figure 3-58: Comparison of simulated and experimental transient responses for the closed-loop output c(t) to the reference input r(t), with and without the phase advance parameter.

in detail in Chapter 5. In the following section, we provide the design and testing of our complete multi-resonator AFC controller with command pre-shifting feedforward channel.

3.6.3 Multiple Resonator AFC System with Command Pre-Shifting

In this section, we design our complete multiple resonator AFC controller for the Variform FTS in diamond turning applications, which includes the addition of a command pre-shifting feedforward channel. For this particular design, we again use the conventional compensator $G_{c_1}(z)$ to close the inner-loop and model the Variform

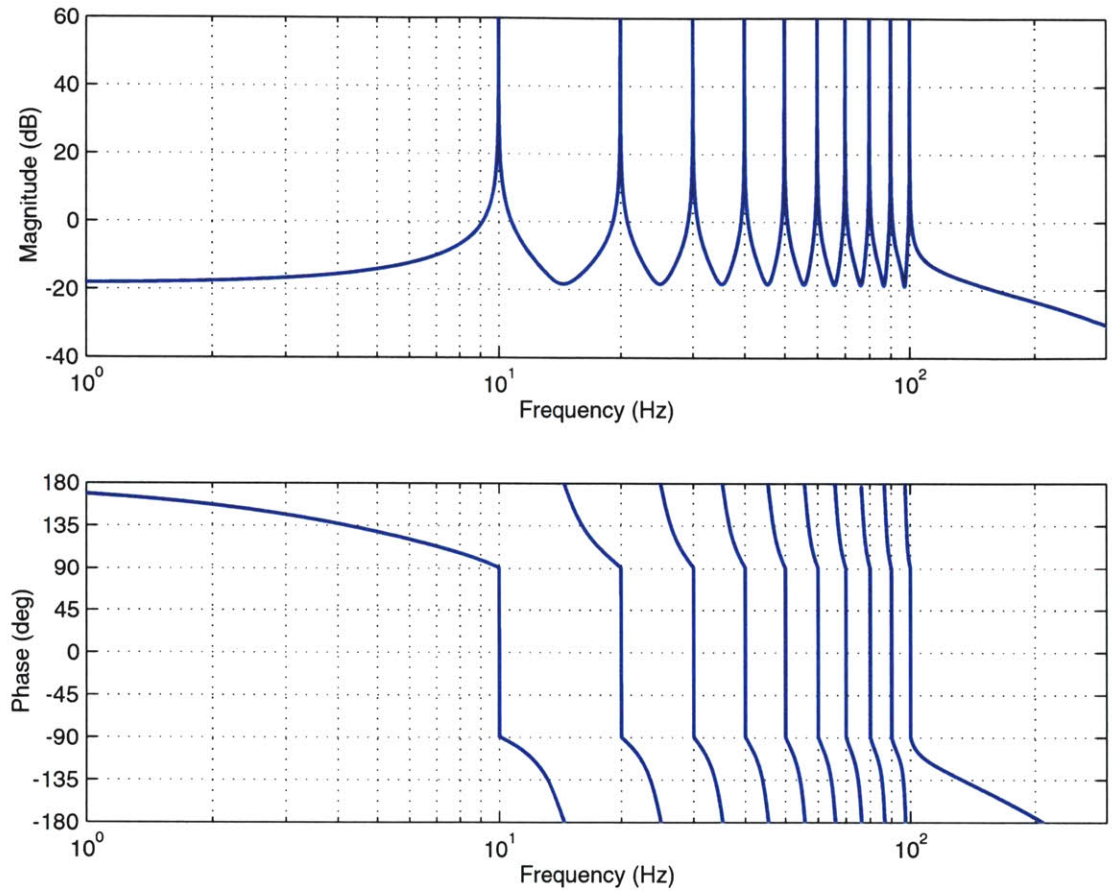

Figure 3-59: Calculated negative of the loop transmission frequency response for the Variform FTS with a ten resonator AFC controller.

FTS hardware with $G_{p_1}(s)$, as described in Section 3.3.

Assuming a spindle rotation speed of 600 RPM, with a desired reference trajectory consisting of the first ten harmonics, we design a ten AFC resonator controller with frequencies at

$$\omega_i = 10 \text{ Hz, } 20 \text{ Hz, ..., and } 100 \text{ Hz.} \tag{3.49}$$

Using the loop-shaping approach, described previously in Section 2.2.6, and a target gain margin of about 20 dB, we set all of the gains g_i equal to 10, while setting each of the phase advance parameters equal to the phase of the inner-loop evaluated at s $= j\omega_i$. A summary of these values is listed in Table F.4 in Appendix F.

Figure 3-59 illustrates the predicted negative of the loop transmission. We see that the system exhibits approximately 20 dB of gain margin and about 80° of phase margin. Thus, this particular controller will provide a stable and robust closed-loop system.

In order to reduce the dSPACE controller complexity and achieve an adequate sampling rate (12.5 kHz), we design this particular controller in MATLAB as a summation of equivalent AFC transfer functions and convert the continuous-time transfer functions into discrete-time equivalents. We do not utilize the single resonator AFC algorithm, as shown in Figure 3-53, since a Simulink model with ten of these structures, along with all of the other Simulink controller blocks, exceeds the limitations of our dSPACE 1102 controller board. A newer dSPACE board (*i.e.*, dSPACE 1103 or 1104) should provide enough computing power to overcome these limitations. Also, the AFC algorithm can be implemented in a much more elegant fashion, which will reduce the size of the resulting C code. Due to the availability in our lab and existing time constraints, we were not able to re-design the AFC controller nor implement the algorithms a newer dSPACE controller board. Thus, we leave these areas for future work.

Figure 3-60 lists the section of MATLAB code we use to calculate the components of the ten resonator AFC controller and convert the continuous-time transfer functions into discrete-time equivalents. The portion of the controller that is designed to eliminate the error at 10 Hz is given by

$$C_1(s) = \frac{\cos\phi_1 s + \omega_1 \sin\phi_1}{s^2 + \omega_1^2}, \tag{3.50}$$

where $\omega_1 = 20\pi$ rad/sec and $\phi_1 = -0.077$ rad. The discrete-time equivalent, sampled

```
% Definition of Variform FTS Plant Characteristics
   num_plant = [3.891703294946617e+022];
   den_plant = [1 2.889311e4 2.91797461837e8 2.4261152947632e12
   1.150193479950049e16 4.498444830832218e19 7.163742834692346e22];
%Definition of Variform FTS Plant P(s)
   plant =tf(num_plant,den_plant);
% Definition of Preliminary FTS Controller Gc(s)
   Gc =tf([1500],[1 0]);
%Sampling Rate for Continuous-Time to Discrete-Time Conversion
   TS = 8e-5;
%Definition of Negative of the Loop Transmission
   LT =   Gc*plant;
%Definition of FTS Conventional Inner-Loop Transfer Function
   CL_LT =   minreal(LT/(1+LT));
%Definition of AFC Oscillation Frequencies
   N = [1:1:10];
   wn = N*2*pi*10;
%Calculation of P(s) Magnitude and Phase at AFC Oscillation Frequencies
   for   i=1:10;
     [m(i),p(i)]=bode(CL_LT,wn(i));
     pr(i) = p(i)*pi/180;
   end
%Calculation of Phase Advance Parameter Values
   for   i=1:10;
     a(i) = cos(pr(i));
     b(i) = wn(i)*sin(pr(i));
   end
%Definition of Continuous-Time AFC Transfer Functions
  for   i=1:10;
       AFC(i) = tf([a(i) b(i)],[1 0 wn(i)^2]);
  end
%Definition of Discrete-Time AFC Transfer Functions
   for   i=1:10;
     AFC_D(i) = C2D(AFC(i),TS, 'tustin');
   end
%Calculation of Num and Den for Discrete-Time AFC Transfer Functions
   for   i=1:10;
     [num,den] = tfdata(AFC_D(i), 'v');
     n_D(i,:) = num;
     d_D(i,:) = den;
   end
```

Figure 3-60: Section of MATLAB code we use to calculate the components of the ten-resonator AFC controller and convert the continuous-time transfer functions into dicrete-time z-transforms using the tustin transformation.

at 12.5 kHz, is

$$C_1(z) = \frac{3.98731 \times 10^{-5} z^2 - 1.549424 \times 10^{-8} z - 3.988855 \times 10^{-5}}{z^2 + -1.999975z + 1}. \tag{3.51}$$

For experimental testing, we take the Simulink closed-loop block diagram, as shown in Figure 3-15, and keep the conventional inner-loop with G_{c_1}(z). Then, we remove the single resonator algorithm and add the ten-resonator AFC controller design C(z) with the command pre-shifting feed-forward loop. This completes the entire experimental multiple resonator AFC controller for the Variform FTS. Figure 3-61 illustrates the resulting Simulink closed-loop block diagram.

Notice that Figure 3-61 includes an altered version of the DSA Simulink block. This new block, along with modified MATLAB code, inputs user provided experimental $P^{*-1}(j\omega_i)$ magnitude and phase lookup tables and produces the approximate command pre-shifted feed-forward values. The list of input frequencies used to perform an experimental frequency response of the complete AFC controller must be the same as those used to obtain the experimental $P^{*-1}(j\omega_i)$ information. If the frequency values in these lists vary, the Preshift and SineOut1 outputs from the new Simulink DSA block will be out of phase with the expected values and yield inaccurate frequency response data. (See Appendix G and Appendix H for a description of the altered MATLAB Simulink DSA block and the listing of the command pre-shifting frequency response MATLAB code.)

Figure 3-62 shows the experimentally measured ten-resonator AFC closed-loop system frequency response with the addition of the experimental command pre-shifting feed-forward loop. Note that the measured input-output transfer function passes through 0 dB and 0° of phase at each of the designed resonator frequencies, and thus that our AFC design works well in practice. A small amount of magnitude and phase shifting still exists at the in-between resonator frequencies, since

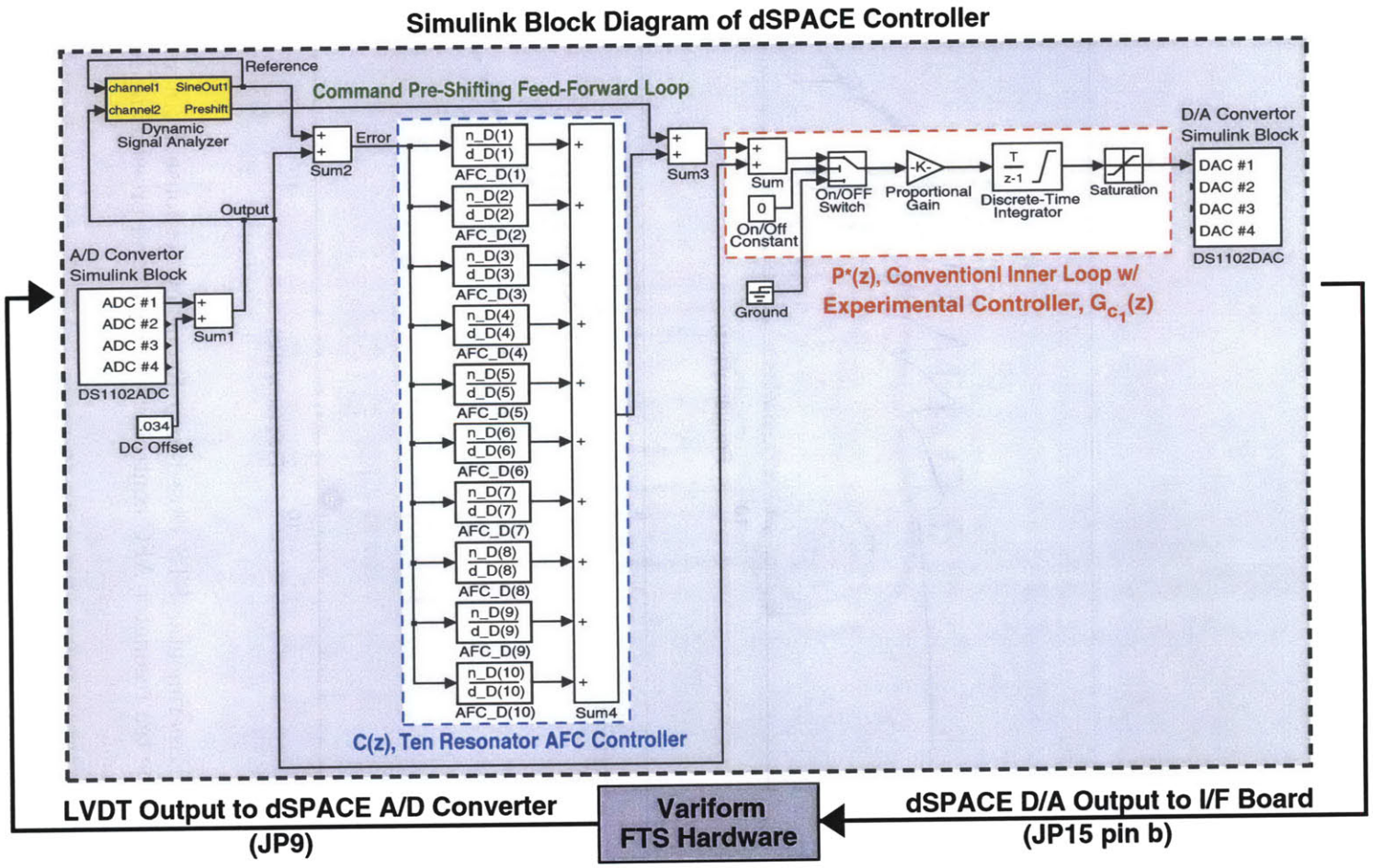

Figure 3-61: Simulink experimental closed-loop block diagram for the Variform FTS with a ten resonator AFC controller, conventional inner-loop, and command pre-shifting feedforward channel.

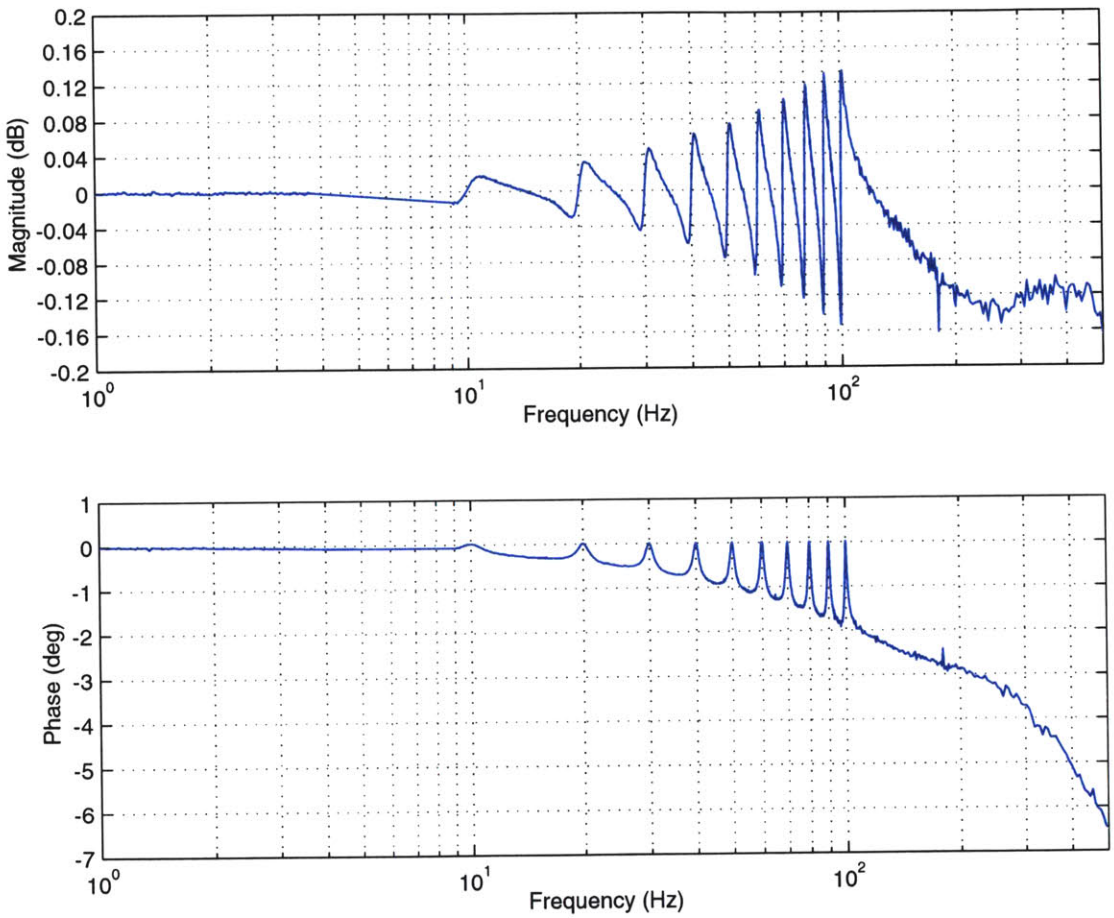

Figure 3-62: Experimental FTS closed-loop frequency response from reference to output with the ten resonator AFC controller and command pre-shifting feedforward channel.

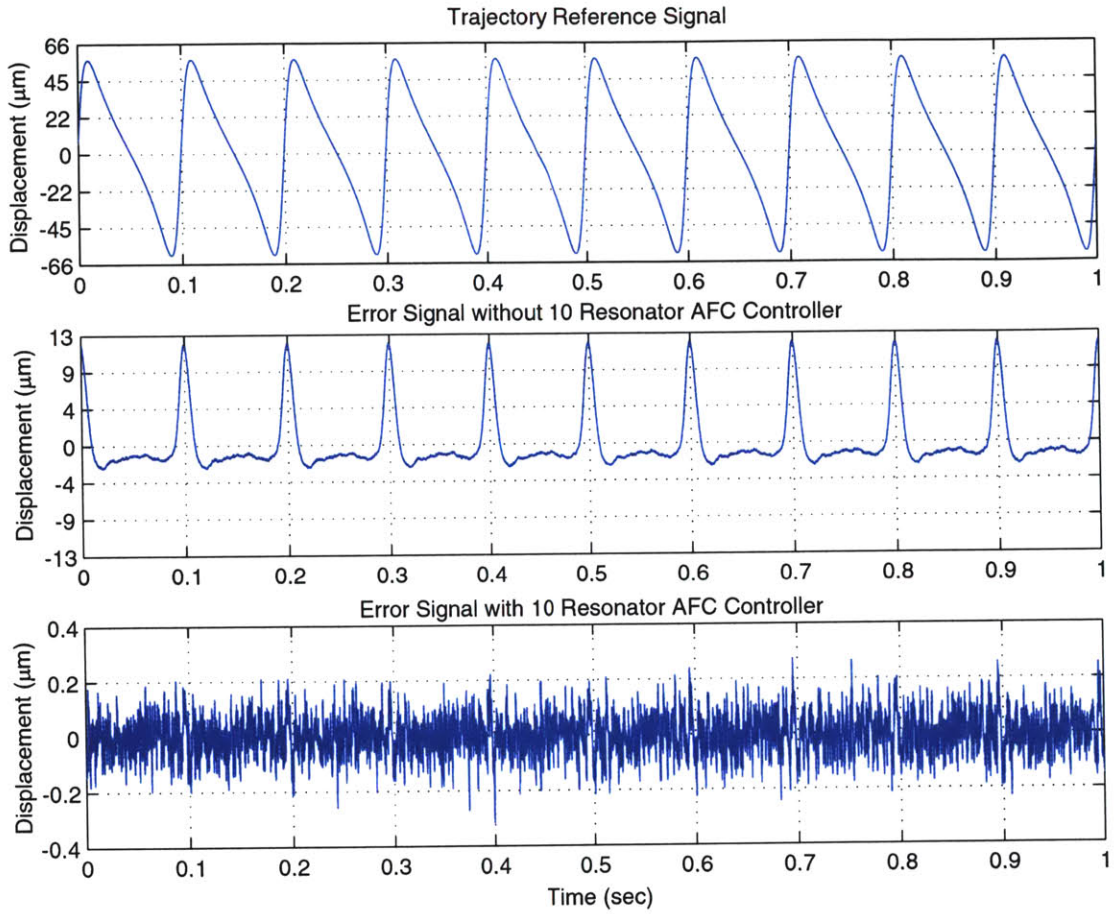

Figure 3-63: Comparison of the experimental closed-loop error signals with and without AFC Control.

the $P^{*-1}(j\omega)$ magnitude and phase data is not 100% accurate relative to the actual system. We speculate that this is due to the dSPACE time delay, discrepancies in the plant model, and non-linearities in the FTS hardware (due to the disabled inner charge loop). However, up to approximately 100 Hz, the experimental results only show about a maximum 2% deviation from the 0 dB line in the Blot magnitude plot and 2° of phase lag. Thus, even with discrepancies in the models, we are able to achieve superior experimental closed-loop performance.

Figure 3-63 shows the experimental Variform FTS closed-loop error signal during an air-cutting experiment, with and without AFC control. A summary of the

components included in the reference trajectory is listed in Table 3.3.

Reference Trajectory Components		
Harmonic	Frequency (Hz)	Amplitude (mV)
1	10	1000
2	60	500
3	20	250
4	70	125
5	30	62.5
6	80	31.25
7	40	15.625
8	90	7.8125
9	50	3.90625
10	100	1.953125

Table 3.3: Summary of frequencies and amplitudes used to create the trajectory reference signal for the Variform FTS air-cutting trajectory following experiments.

The peak-to-peak system error without Adaptive Feedforward Cancellation, measured with the Variform FTS LVDT feedback sensor, amounts to approximately 15% of the trajectory reference signal, while the peak-to-peak system error with AFC control reduces to about 0.5%. It should also be noted that the error signal with AFC control is dominated by the noise of the LVDT and there appears to be no apparent signal left that is correlated to the input reference signal. Therefore, the steady-state tracking error is essentially zero. Due to time and computer memory constraints, we were not able to implement the command pre-shifting channel during this particular test. Then again, we would have had trouble noticing any further improvements in the closed-loop response, since the addition of just the AFC controller apparently reduced the steady-state tracking error to less than the noise of the LVDT. These results illustrate a dramatic improvement in the FTS's steady-state tracking performance to constant amplitude periodic signals.

3.7 Summary

In summary, this chapter investigated the implementation of several conventional controllers, as well as AFC control, on the Variform FTS. We utilized a dSPACE 1102 controller board to implement all of the experimental algorithms and provided

detailed instructions on how to replicate our results. These experiments showed that we can improve upon the conventional on-board servo-loop by using a better feedback sensor, such as the Kaman Instrumentation inductive sensor shown in Section 3.5.2. Also, we showed that we can dramatically increase the Variform FTS's trajectory following capabilities by using Adaptive Feedforward Cancellation with a command pre-shifting feedforward loop.

The experimental single and two AFC resonator system results illustrated the effective decoupling of the sine and cosine AFC channels, as well as a reduction of the convergence time, once the proper choice of phase advance was implemented. Also, these results essentially showed the complete elimination of the error signal. However, we did not perform any experiments with slow-time varying amplitude or frequency components. Thus, we leave this exercise to future work.

In the following chapter, we discuss the background theory on oscillator amplitude control systems. This theory provides the context for our development of viewing Adaptive Feedforward Cancellation from an oscillator amplitude control perspective. From this perspective, we present a simple way of characterizing the stability, robustness, convergence, and error properties for single and multiple resonator AFC systems.

Chapter 4

Oscillator Amplitude Control Systems Theory

This chapter describes oscillator amplitude control systems theory. We use this theory as the basis for our Adaptive Feedforward Cancellation viewed from an oscillator amplitude control perspective, which we present in Chapter 5. Section 4.1 provides a brief introduction to sinusoidal oscillators and illustrates a few oscillator circuit designs. In Section 4.2, we describe oscillator amplitude control and show an example of an OAC system on a quadrature oscillator circuit, an example which has been adapted from Roberge [46].

4.1 Sinusoidal Oscillators

In the classical design and analysis of feedback control systems, we typically want the negative of the loop transmission to have sufficient gain and phase margins. This ensures a stable and robust closed-loop system that will not go unstable and enter into a limit cycle (constant-amplitude periodic oscillations) [46]. However, there are several applications which require the use of limit cycles to operate correctly. One common example is the quartz crystal watch. It is well known that when embedded

in an appropriate circuit, a quartz crystal will produce a stable frequency oscillation that is a function of the crystal's cut and geometry. The oscillating quartz crystal can be made to produce very accurate clocks [72].

Other examples that take advantage of limit cycles include radio tuners, function generators, and micro-controllers. These systems typically include circuits with operational amplifiers, resistors and capacitors that produce stable amplitude sinusoidal outputs. We refer to these types of circuits as sinusoidal oscillators.

4.1.1 Wien-Bridge Oscillator

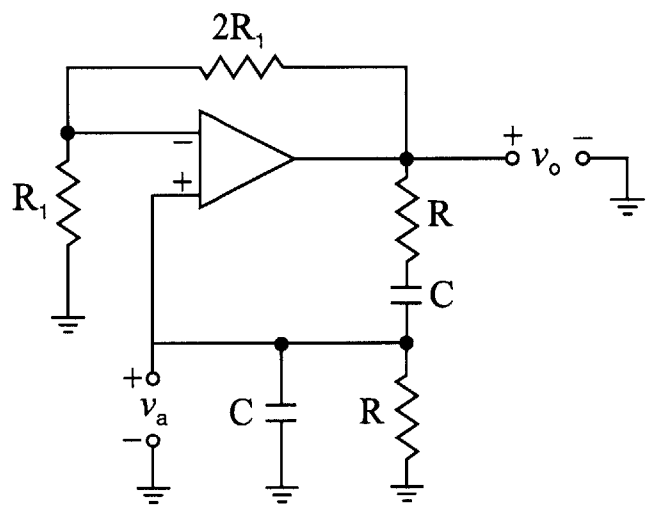

Figure 4-1: Wien-Bridge oscillator circuit diagram. Figure adapted from Roberge [46].

Roberge [46] details several ways to implement a sinusoidal oscillator. One of these circuits is called a Wien-bridge oscillator, which is shown in Figure 4-1. The transfer function from the output of the operational amplifier to the non-inverting input is given by

$$\frac{V_a(s)}{V_o(s)} = \frac{RCs}{R^2C^2s^2 + 3RCs + 1}. \tag{4.1}$$

This amplifier is configured to provide a non-inverting gain of 3 from ν_+ to ν_o. There-

fore, the resulting loop transmission of the positive feedback loop is

$$L(s) = \frac{3RC(s)}{R^2C^2s^2 + 3RCs + 1}, \tag{4.2}$$

and the characteristic equation is thus of the form

$$1 - L(s) = 0, \tag{4.3}$$

which gives

$$R^2C^2s^2 + 1 = 0. \tag{4.4}$$

The roots of (4.4) are

$$s_{1,2} = \pm\frac{j}{RC}, \tag{4.5}$$

and as a result, the Wien-bridge oscillator circuit has a pair of closed-loop poles on the imaginary-axis and is thus capable of producing a constant amplitude sinusoidal output with an oscillation frequency of

$$\omega_{Wien} = \frac{1}{RC} \text{ rad/sec.} \tag{4.6}$$

The amplitude of this oscillation is, however, indeterminate. Techniques to stabilize the oscillation amplitude are discussed in Section 4.2.

4.1.2 Quadrature Oscillator

Another circuit that Roberge [46] presents is called a quadrature oscillator. This circuit, as shown in Figure 4-2, connects an inverting and non-inverting op-amp with three resistors and capacitors to yield a loop transmission given by

$$L(s) = \left[-\frac{1}{R_1C_1s}\right]\left[\frac{R_3C_3s + 1}{(R_2C_2s + 1)R_3C_3s}\right]. \tag{4.7}$$

This circuit is called a quadrature oscillator, since in steady-state oscillation the outputs of the op-amps are 90° out of phase with respect to each other. If all three of the time constants are set equal to one another

$$R_1C_1 \;=\; R_2C_2 \;=\; R_3C_3 \;\equiv\; RC, \tag{4.8}$$

then (4.7) becomes

$$L(s) = \left[-\frac{1}{RCs}\right]\left[\frac{RCs+1}{(RCs+1)RCs}\right] = -\left[\frac{1}{R^2C^2s^2}\right], \tag{4.9}$$

and the characteristic equation is

$$1 - L(s) = 0, \tag{4.10}$$

or

$$R^2C^2s^2 + 1 = 0, \tag{4.11}$$

which produces a pair of complex zeros on the imaginary-axis. Therefore, the resulting closed-loop transfer function contains imaginary-axis poles and is capable of producing a constant amplitude sinusoidal output. Again, the oscillation amplitude is indeterminate.

4.2 Oscillator Amplitude Control

4.2.1 Background

Roberge [46] states a necessary and sufficient condition for the generation of constant amplitude sinusoidal oscillations is that a pair of closed-loop poles must lie on the imaginary axis and that no closed-loop poles lie in the right half s-plane. When im-

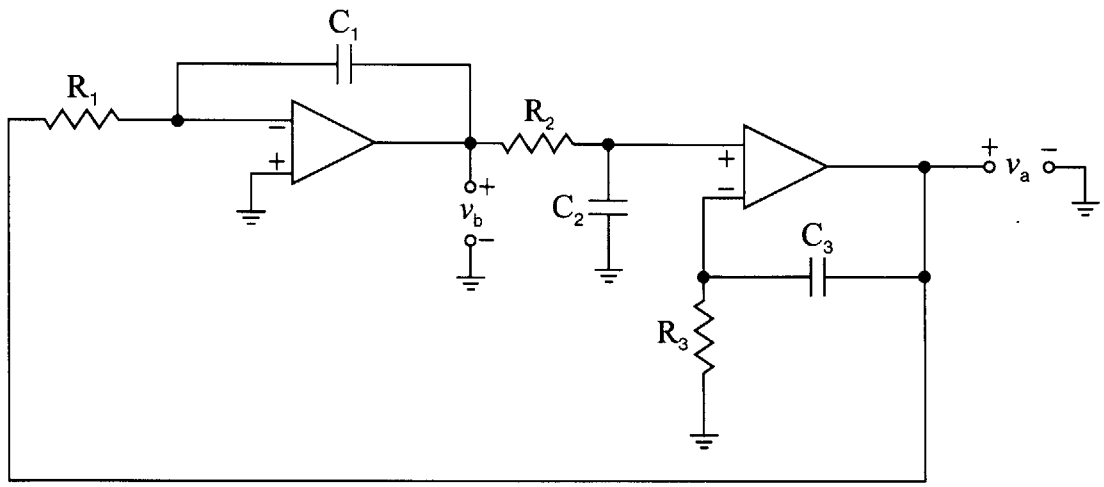

Figure 4-2: Quadrature oscillator circuit diagram. Figure adapted from Roberge [46].

plemented in practice, for such imaginary-axis poles, the oscillator amplitude output is determined by initial conditions . Further, slight changes in the circuit's physical components (*i.e.*, resistors, capacitors, etc.) will shift the locations of the closed-loop poles into the open left or right half s-plane. This shift creates an exponentially decaying or increasing amplitude envelope, which causes either zero steady-state output or some form of limit cycle. The limit cycle amplitude and time-characteristics are determined by op-amp saturation. As such, the output may contain significant harmonic distortion from an ideal sinusoid.

To prevent this from happening, Roberge proposes the addition of another circuit to stabilize the oscillator amplitude output to some desired level. He refers to this circuit as an oscillator amplitude control system. Oscillator amplitude control (OAC) [38] is a particular form of Automatic Gain Control (AGC) [37] which adjusts one of the components of a sinusoidal oscillator to maintain the closed-loop poles directly on the imaginary axis. OAC consists of a secondary feedback loop with an amplitude detector that compares the amplitude of the oscillator to some desired reference level. The resulting error signal causes variation of the selected parameter value until the desired level is obtained. With this feedback active, the closed-loop

poles will be maintained on the imaginary-axis and the oscillator thereby provides a constant amplitude sinusoidal output, with potentially very low distortion.

4.2.2 Quadrature Oscillator Amplitude Control System

In one of Roberge's oscillator amplitude control systems, he varies the resistor R_3 of the quadrature oscillator circuit, as shown in Figure 4-2, to achieve a desired constant amplitude sinusoidal output. He assumes

$$C_1 = C_2 = C_3 \equiv C, \tag{4.12}$$

$$R_1 = R_2 \equiv R, \tag{4.13}$$

$$R_3 \equiv (1+\Delta)R. \tag{4.14}$$

With these definitions, the loop transmission is given by

$$L(s) = -\frac{(1+\Delta)RCs+1}{R^2C^2s^2(1+\Delta)(RCs+1)}, \tag{4.15}$$

and the characteristic equation becomes

$$R^3C^3(1+\Delta)s^3 + R^2C^2(1+\Delta)s^2 + RC(1+\Delta)s + 1 = 0. \tag{4.16}$$

When $|\Delta| \ll 1$, the closed-loop poles can be shown to be approximately given by

$$\left[RC(1+\frac{\Delta}{2})s+1\right]\left[R^2C^2(1+\frac{\Delta}{2})s^2 + RC\frac{\Delta}{2}s+1\right] = 0, \tag{4.17}$$

and the dynamics of the closed-loop oscillator system are dominated by the complex conjugate pole pair at

$$s_{p_1,p_2} = -\zeta\omega_n \pm \omega_n\sqrt{1-\zeta^2}, \tag{4.18}$$

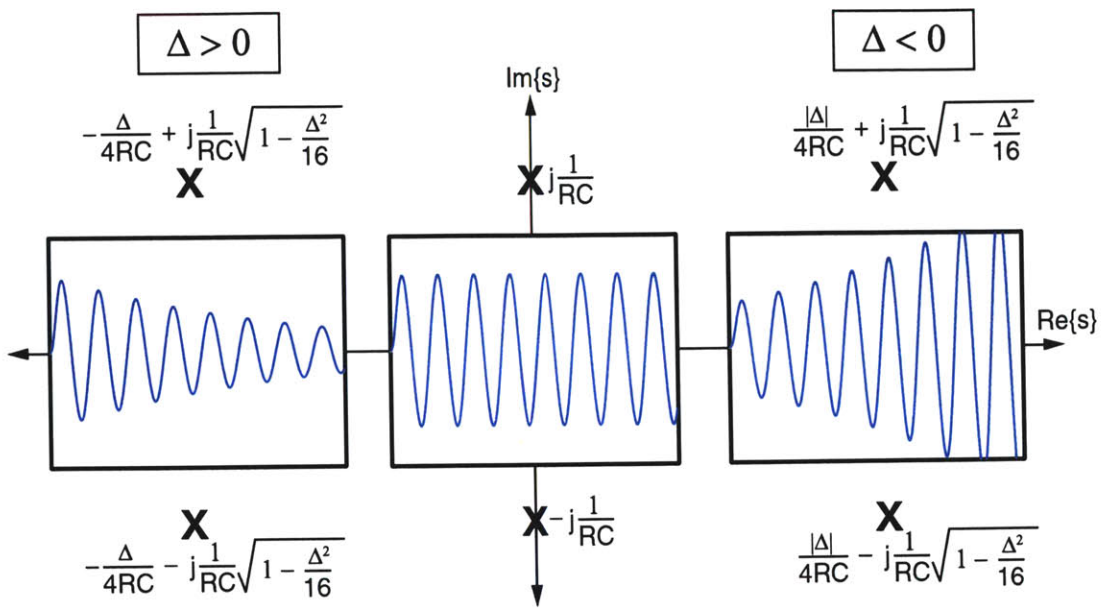

Figure 4-3: Effect on the quadrature oscillator amplitude output when the closed-loop poles on the imaginary-axis are moved into the left or right half s-plane.

where

$$\omega_n \simeq \frac{1}{RC}, \tag{4.19}$$

$$\zeta \simeq \frac{\Delta}{4}. \tag{4.20}$$

Thus, the closed-loop poles on the imaginary-axis can be moved into the left or right half s-plane, as controlled by the value of Δ. An illustration of this is shown in Figure 4-3. The oscillator amplitude output is controlled by moving the closed-loop poles into the left or right half s-plane, depending on whether the amplitude is greater or less than the desired value.

Roberge assumes that the output of the quadrature oscillator $v_A(t)$ is

$$v_A(t) = e_A(t)\sin(\omega_n t), \tag{4.21}$$

where (4.21) is a constant frequency sinusoid with variable amplitude envelope. This

is only an approximation, since the instantaneous frequency of (4.21) is dependent on the value of Δ. Roberge states that as long as the amplitude control feedback loop has a much lower 0 dB crossover frequency than the oscillator frequency, the magnitude changes of $e_A(t)$ will be relatively slow and the sinusoidal portion of the equation can be ignored. As a result, the amplitude envelope can be considered a controlled variable in its own right, independent of the sinusoid. This assumption is akin to the averaging analysis of the AFC algorithm presented in Chapter 5.

Roberge determines the dependence of the oscillator output $v_A(t)$ on the control parameter Δ by assuming that the quadrature circuit is oscillating with $\Delta = 0$ and the closed-loop poles are located directly on the imaginary-axis. Therefore, the operating-point amplitude envelope is a constant E_A and (4.21) becomes

$$v_A(t) = E_A \sin(\omega_n t). \tag{4.22}$$

When the control parameter is changed to some small positive value Δ, the closed-loop poles move into the left half s-plane and (4.22) becomes

$$v_A(t) = E_A e^{-\zeta\omega_n t} \sin(\omega_n t). \tag{4.23}$$

Using (4.19) and (4.20), Roberge shows that (4.23) can be written as

$$v_A(t) = E_A e^{-\frac{\Delta t}{4RC}} \sin(\frac{t}{RC}), \tag{4.24}$$

where the Taylor Series expansion of the amplitude envelope is given by

$$e_A(t) = E_A e^{-\frac{\Delta t}{4RC}} = E_A \left(1 - \frac{\Delta t}{4RC} + \frac{1}{2}\left(\frac{\Delta t}{4RC}\right)^2 - \ldots\right). \tag{4.25}$$

Since $\Delta \ll 1$, he separates e_A(t) into operating point and incremental components of

the form

$$e_A(t) = E_A + e_a(t) \simeq E_A - \frac{E_A \Delta}{4RC} t. \tag{4.26}$$

Note that with this linearized analysis, the output incremental amplitude *integrates* the variable Δ with a gain factor $\frac{E_A}{4RC}$. Said another way, the linearized transfer function relating the output amplitude e_a(t) to the control parameter Δ is

$$\frac{E_a(s)}{\Delta(s)} = -\frac{E_A}{4RCs}. \tag{4.27}$$

Figure 4-4 illustrates Roberge's amplitude control design on the quadrature oscillator in a mixed circuit and block diagram form, where

$$C_1 = C_2 = C_3 \equiv C = 0.01\ \mu F, \tag{4.28}$$

$$R_1 = R_2 \equiv R = 10\ k\Omega, \tag{4.29}$$

$$R_A = 1\ M\Omega, \tag{4.30}$$

$$R_B = 9.5\ k\Omega. \tag{4.31}$$

We can implement the amplitude measuring circuit in several ways (*e.g.*, diode-resistor-capacitor peak detector) but the cost and complexity increases for higher precision (lower harmonic distortion) applications. These details are not particularly relevant to our discussion, assuming the total harmonic distortion is kept to a sufficiently low level. Thus, we will not discuss the amplitude measuring circuit any further.

The difference between the amplitude envelope $v_A(t)$ and the reference amplitude E_R creates the closed-loop error signal e_E(t). The output of the controller $a(s)$ drives a field effect transistor (FET), which acts like a variable resistor and determines the level

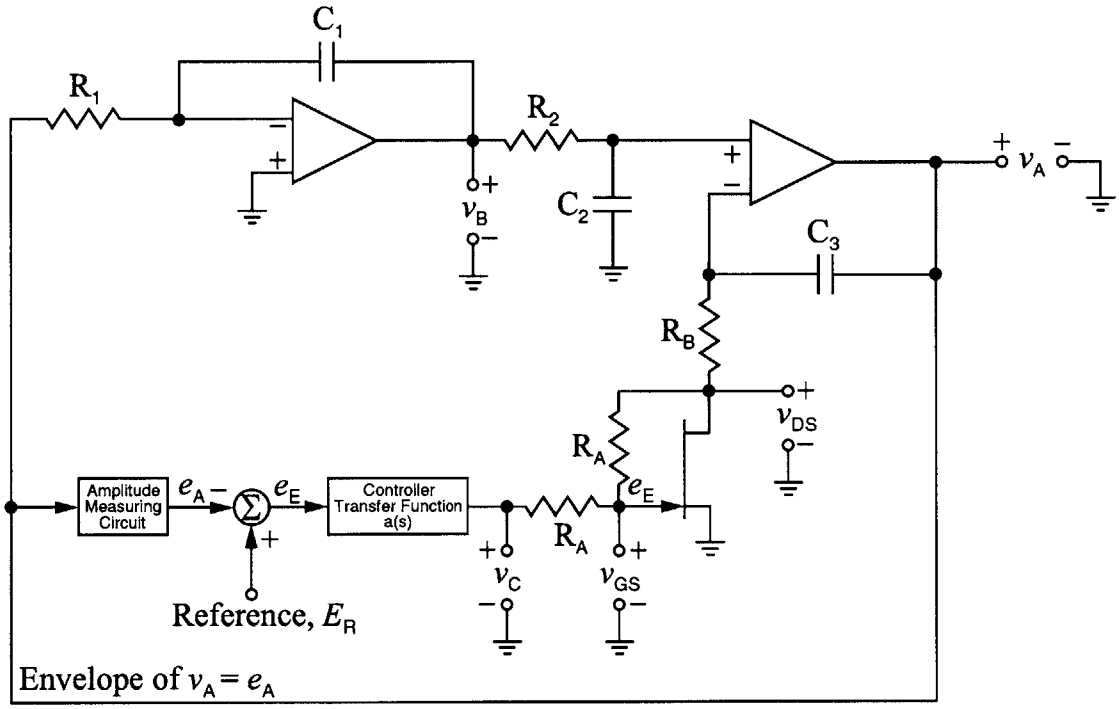

Figure 4-4: Quadrature oscillator with amplitude control circuit. Figure adapted from Roberge [46].

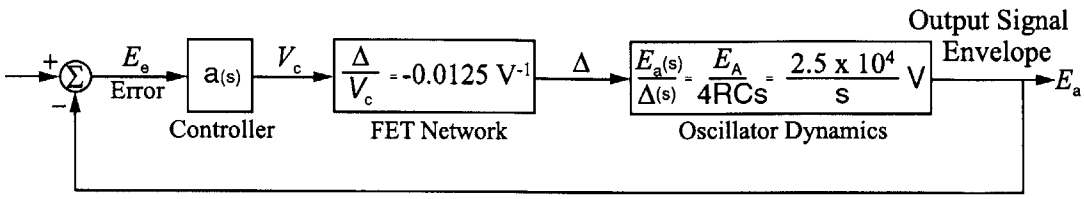

Figure 4-5: Linearized bock diagram for the amplitude control circuit. Figure adapted from Roberge [46].

of the control parameter Δ. Assuming an operating point for the amplitude envelope (*e.g.*, $E_A = 10V$), Roberge determines a linearized block diagram for the amplitude control system, as shown in Figure 4-5, where the resulting loop transmission is given by

$$\frac{E_a(s)}{E_e(s)} = -312.5\frac{a(s)}{s}. \tag{4.32}$$

The details of the controller a(s) will not be discussed here but Roberge recommends designing the circuit to provide additional low-pass filtering, so as to reduce the harmonic distortion from the amplitude measurement circuit and provide a conservative phase margin, since several approximations are made during the formulation of (4.32). The closed-loop performance of this particular oscillator amplitude control system is explored via the following example.

4.2.3 Example of an Oscillator Amplitude Control System

In this section, we consider the previously described quadrature oscillator (including Roberge's oscillator amplitude control circuit) with a constant amplitude oscillation given by

$$v_A(t) = 10\sin(\omega_n \mathrm{t})\ \mathrm{V}, \tag{4.33}$$

where

$$\omega_n = \frac{1}{RC} = 1000\ \mathrm{rad/sec}, \tag{4.34}$$

and we want to change the amplitude output to some desired reference level. In [46], Roberge suggests using a controller of the form

$$a(s) = \frac{3.2(0.1s+1)}{s(10^{-3}s+1)^2}, \tag{4.35}$$

as one of many possible controllers which will provide the previously mentioned frequency response characteristics. Substituting (4.35) into the closed-loop block diagram in Figure 4-5 yields a negative of the loop transmission of

$$-L(s) = -\frac{E_a(s)}{E_e(s)} = \frac{10^3(0.1s+1)}{s^2(10^{-3}s+1)^2}, \tag{4.36}$$

which produces a 100 rad/sec crossover frequency, 26 dB gain margin and more than 70° of phase margin. Figure 4-6 illustrates the calculated frequency response of (4.36), indicating the crossover frequency and stability margins.

Constant Amplitude OAC Reference Input

For this example, we study the response of the oscillator amplitude control circuit to a constant amplitude reference input. We change E_R from 10 V to a constant 15 V input, which introduces an error signal e_E(t) to the controller a(s) and causes the control parameter Δ to develop a small negative value. This moves the closed-loop poles on the imaginary-axis into the RHP, which in the absence of feedback, would create an exponentially increasing amplitude envelope given by

$$e_A(t) = 10e^{\frac{\Delta t}{4RC}} \text{ [V]}. \tag{4.37}$$

As the error signal settles to steady-state, under the action of feedback, the control parameter Δ reduces to zero and the closed-loop poles in the RHP move back onto the imaginary-axis. The oscillator output settles to a constant level and the

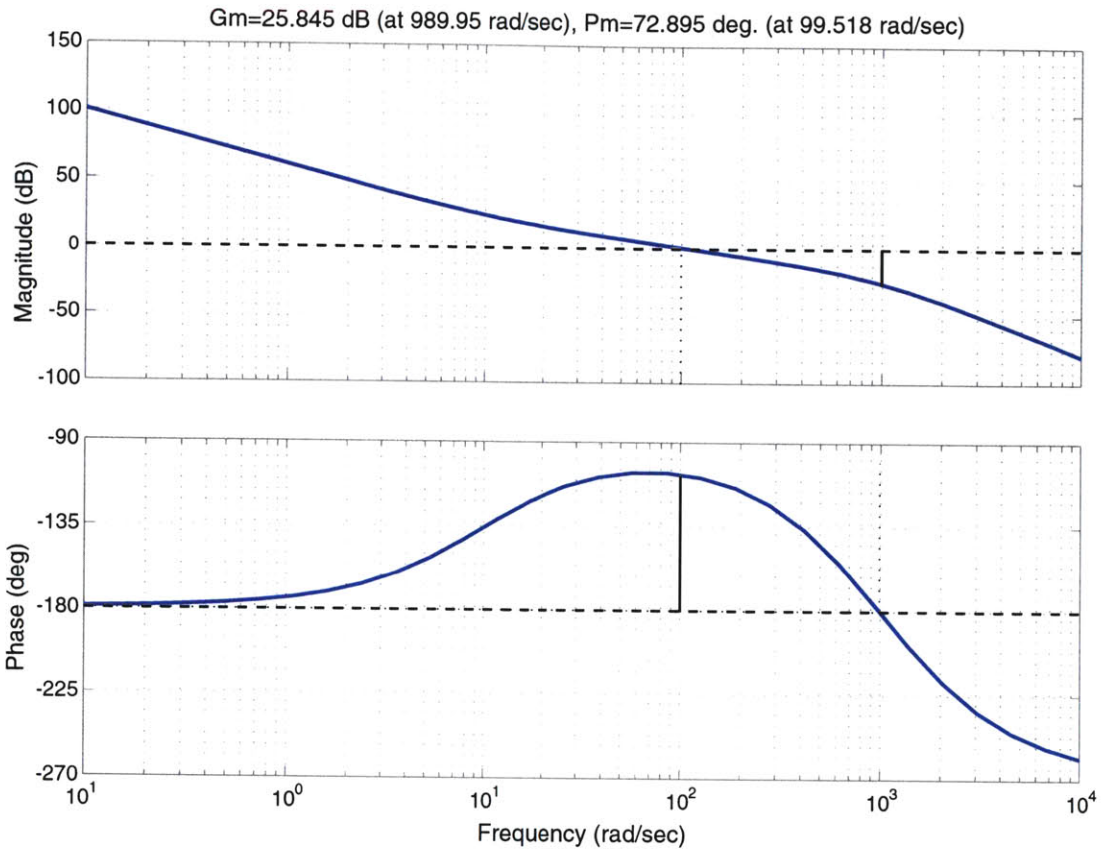

Figure 4-6: Calculated negative of the loop transmission frequency response for the linearized oscillator amplitude control system, indicating the crossover frequency, gain margin, and phase margin.

amplitude output becomes the desired 15 V set-point. Figure 4-7 illustrates the transient responses of the quadrature oscillator amplitude output $\nu_A(\mathrm{t})$, OAC output amplitude envelope $e_A(\mathrm{t})$, error signal $e_E(\mathrm{t})$, and quadrature oscillator error output $(e_A(\mathrm{t})\sin(\omega_n \mathrm{t}))$ when the amplitude reference signal E_R is changed from 10 V to 15 V, at time T_o. This reference change is equivalent to an amplitude step input.

From Figure 4-7, we see that we can approximate the oscillator output and error dynamics from $e_A(\mathrm{t})$ and $e_E(\mathrm{t})$. Thus, for a sufficiently low OAC closed-loop bandwidth, we can determine the dynamics of the quadrature oscillator simply by the examining the negative of the loop transmission, as mentioned previously in Section 4.2.2. The time scale is proportional to the the crossover frequency, while the

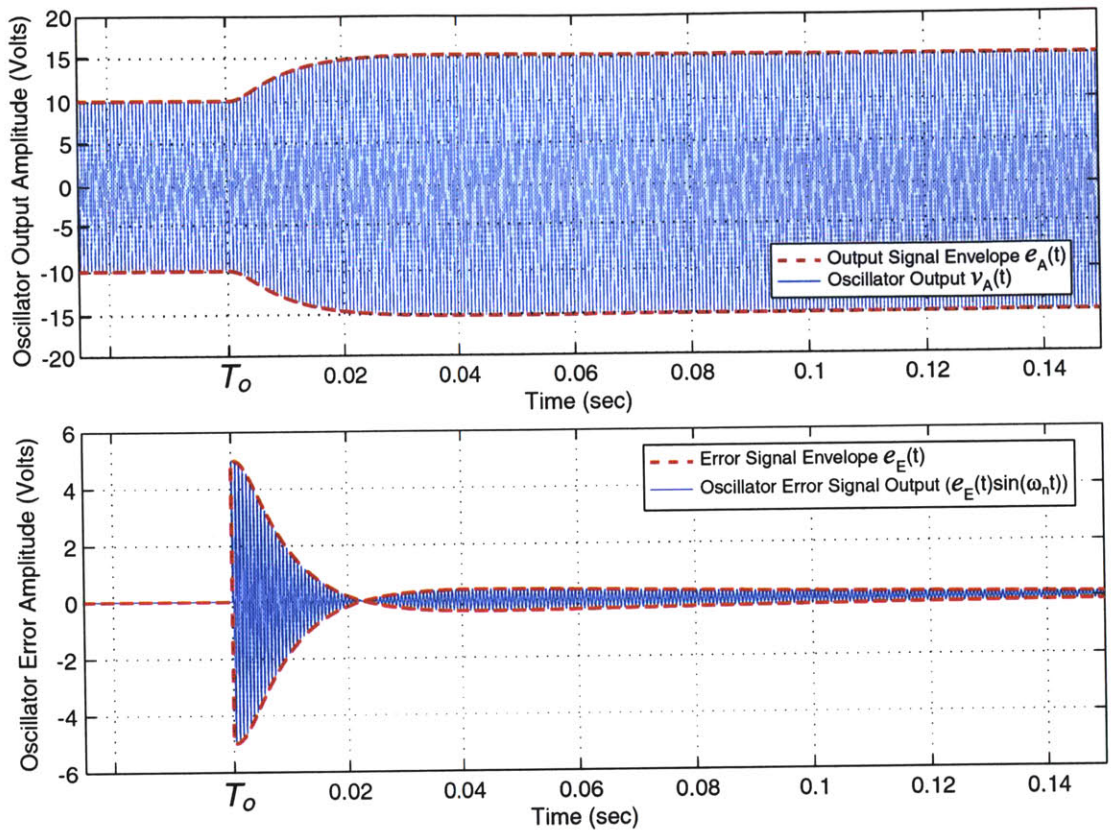

Figure 4-7: Transient response of the quadrature oscillator amplitude output v_A(t) when the amplitude control circuit reference signal E_R is changed from 10 V to 15 V at time T_o.

phase margin predicts the closed-loop damping. More specifically, we can determine the closed-loop convergence properties of the amplitude envelope to changes in the reference input. These properties are analogous to the settling time of a classical feedback system due to a step change in the reference/disturbance input. Notice, Roberge approximates the oscillator dynamics as a integrator. Thus, the OAC closed-loop system will provide approximately zero steady-state error to step change in E_R. In the following example, we modulate the reference input E_R by a low-frequency sinusoid and study the resulting output.

Amplitude Modulated OAC Reference Input

In [46], Roberge states that one of the advantages of the OAC circuit is that we can vary the reference input in a controlled way and thus modulate the amplitude of the oscillator output. However, the time-variation of E_R cannot be too rapid, since the OAC loop has a relatively small closed-loop bandwidth. For this particular example, we simulate a change in the reference input from 10 V to 15sin(ω_rt) V, where

$$\omega_r = 25 \text{ rad/sec.} \tag{4.38}$$

This particular frequency is acceptable, since the predicted oscillator amplitude control loop has a 100 rad/sec crossover frequency, as shown in Figure 4-6. Further, the amplitude frequency is small relative to the oscillation frequency of 1000 rad/sec.

Figure 4-8 illustrates the transient responses of the quadrature oscillator amplitude output ν_A(t), OAC output amplitude envelope e_A(t), error signal e_E(t), and quadrature oscillator error output (e_A(t)sin(ω_nt)) when the amplitude reference signal E_R is changed from 10 V to 15sin(ω_rt) V, at time T_o. Again, we see that we can use e_A(t) and e_E(t) to determine the dynamics of the oscillator amplitude output and error envelopes. Also, since the reference input is not a constant amplitude input, the OAC closed-loop system exhibits a steady-state error, as seen at the bottom of Figure 4-8. For this particular case, we can use the OAC loop transmission to determine the closed-loop convergence properties, as well as an approximate bound on the oscillator amplitude steady-state error envelope, and adjust the controller a(s) accordingly to maximize the quadrature oscillator performance. This is analogous to an AFC system with slowly time-varying amplitude or frequency components. The AFC steady-state error is inversely proportional to the loop gain g_i, which can be explained by a simple magnitude of the loop transmission argument [6].

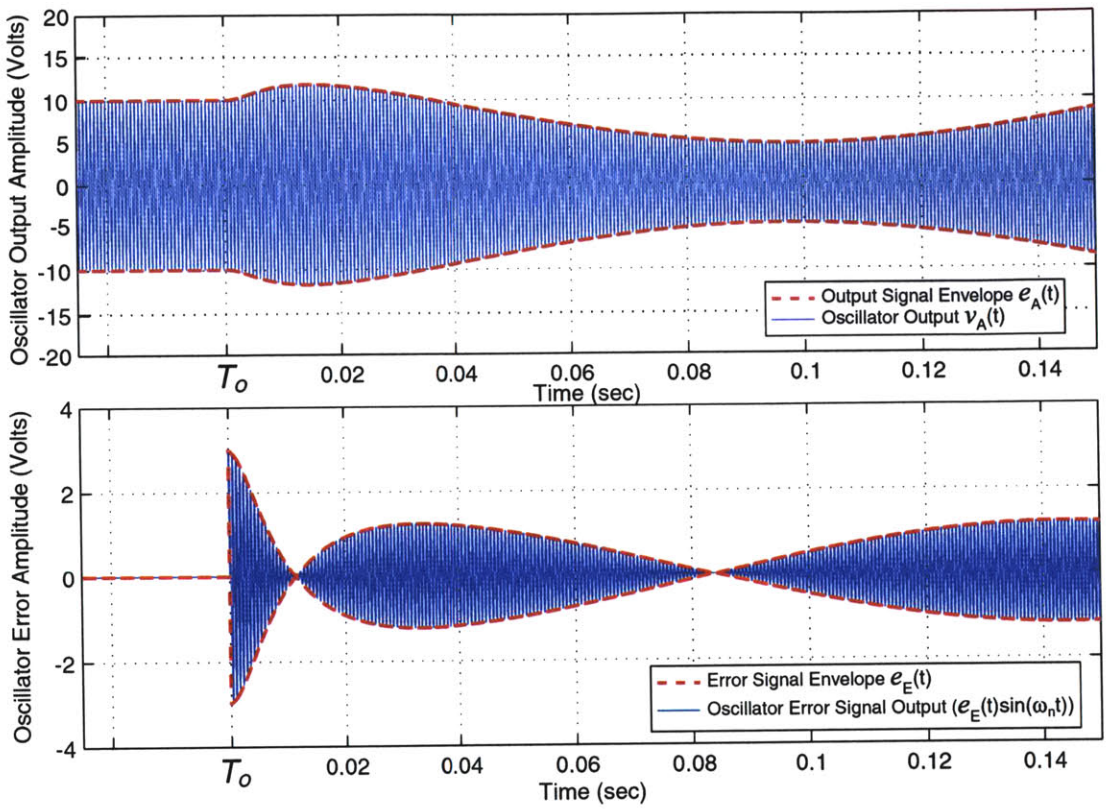

Figure 4-8: Transient response of the quadrature oscillator amplitude output $v_A(t)$ when the amplitude control circuit reference signal E_R is changed from 10 V to $15\sin(25t)$ V at time T_o.

4.3 Summary

In summary, for a sufficiently low oscillator amplitude control bandwidth, we can characterize the dynamics of the oscillator amplitude output from the OAC feedback loop. Therefore, we can use the OAC loop transmission to determine the convergence properties of the oscillator amplitude output and error envelopes, due to changes in the amplitude reference input. Also, we can determine an approximate bound on the oscillator amplitude steady-state error, if the reference input has slowly time-varying characteristics. These formulations are based on a number of approximations. Thus, care must be taken to ensure accurate results. In the following Chapter, we use these assumptions, and the intuition obtained from Roberge's oscillator amplitude

control system, to view the Adaptive Feedforward algorithm from an oscillator amplitude control perspective, and thereby gain an additional perspective on the AFC convergence and error properties.

Chapter 5

Adaptive Feedforward Cancellation Viewed from an Oscillator Amplitude Control Perspective

In the previous chapter, we discussed the background theory of oscillator amplitude control and showed that under certain approximations, the amplitude envelope of a sinusoidal oscillator with an oscillator amplitude control system can be considered a controlled variable by itself, independent of the detailed time variation of the sinusoid. In the following sections, we use this reasoning to develop a method of viewing the Adaptive Feedforward Cancellation algorithm as the combination of multiple oscillator amplitude control systems. From this perspective, we can predict the AFC closed-loop convergence properties and steady-state error using simplified models. Also, we can use classical control techniques to determine the stability and robustness properties of single and multiple-resonator AFC systems.

Figure 5-1 illustrates the single resonator AFC closed-loop block diagram. We view this system as the combination of two oscillator amplitude systems, where the sine and cosine channels correspond to the individual feedback loops. The first sinusoidal

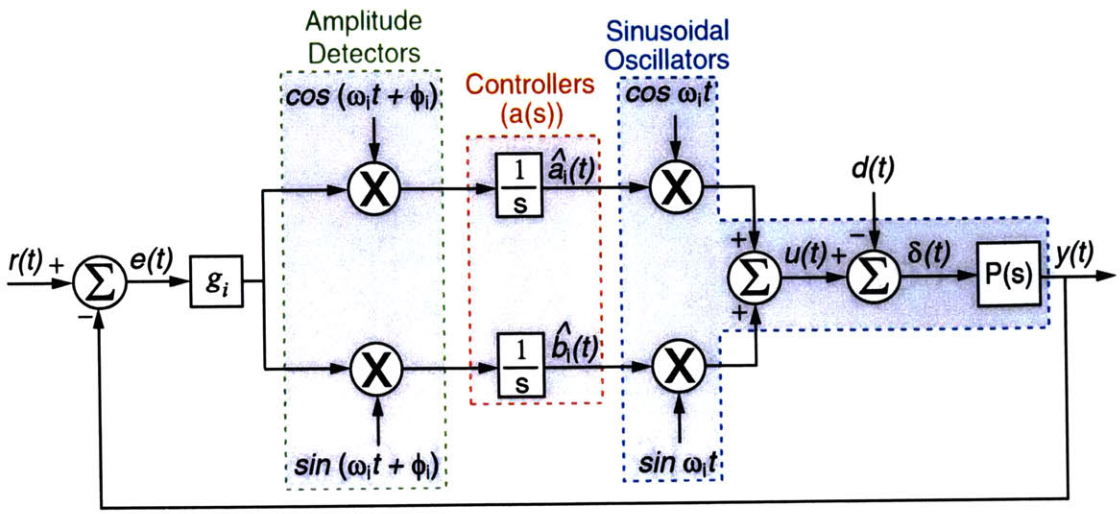

Figure 5-1: Single resonator AFC closed-loop block diagram designed to follow/reject a signal with a frequency ω_i.

modulators in Figure 5-1 are considered the amplitude detectors, and thus serve as sensors. Next, in concert with the gain g_i, the integrators act as the amplitude stabilization controllers, a(s), while the second modulators and plant P(s) can be viewed as sinusoidal oscillators, whose output amplitude in y(t) is to be controlled to a desired level, as set by the component of frequency ω_i in the reference r(t).

The sine and cosine channels in the AFC controller are coupled in a multiple-input multiple-output (MIMO) sense. These two channels can be decoupled via proper selection of ϕ_i relative to the phase of the plant evaluated at s = $j\omega_i$, as shown in Section 5.4. With ϕ_i added to the AFC algorithm, the amplitude dynamics of the sine and cosine AFC channels are essentially equivalent and operate independently. Thus, we can analyze them independently and use superposition to approximate the full AFC closed-loop output.

The rest of this chapter is organized as follows. In Section 5.1, assuming decoupled sine and cosine feedback loops, we simplify the sine channel of the single resonator AFC system into an OAC system and later use the results to view the entire AFC algorithm from an oscillator amplitude control perspective. We only analyze the sine

channel, since the decoupled loops contain equivalent dynamics. Section 5.3 describes the limitations of this perspective, where we use a first order perturbation analysis to determine an approximate bound on the allowable size of the proportional gain and then analyze the effects of slow plant dynamics. Section 5.3 presents the entire Adaptive Feedfoward Cancellation algorithm as a multiple-input multiple-output oscillator amplitude control system, while Section 5.5 discusses the error properties of AFC viewed from an oscillator amplitude control perspective. Finally, in Section 5.6, we summarize viewing AFC from an OAC perspective.

5.1 Simplified Sine Channel of the Single Resonator AFC Controller

Under the assumption that we have implemented the proper phase advance parameter ($\phi_i = \angle P(j\omega_i)$), we can view the sine and cosine channels of the single resonator AFC system independently. These decoupled channels essentially yield equivalent closed-loop dynamics, as shown in Section 5.4. Thus, in the following analysis, we simplify just the sine channel of the AFC controller into an equivalent oscillator amplitude control loop and use the results to view the entire single resonator AFC system from a MIMO oscillator amplitude control perspective.

Figure 5-2 highlights the portion of the single resonator AFC closed-loop block diagram designed to follow/reject the sine component of a signal with frequency ω_i. We will analyze this system by setting the reference signal equal to zero, r(t) = 0, and assume that the feedback loop has an input disturbance signal with a constant amplitude and single frequency component, d(t) = b $\sin(\omega_i t)$. Analogous to Roberge's oscillator amplitude control system approach, we want to be able to analyze the AFC closed-loop output and error signals from the amplitude dynamics alone, independent of the detailed time variation of the sine and cosine waves. In order to do this, a few

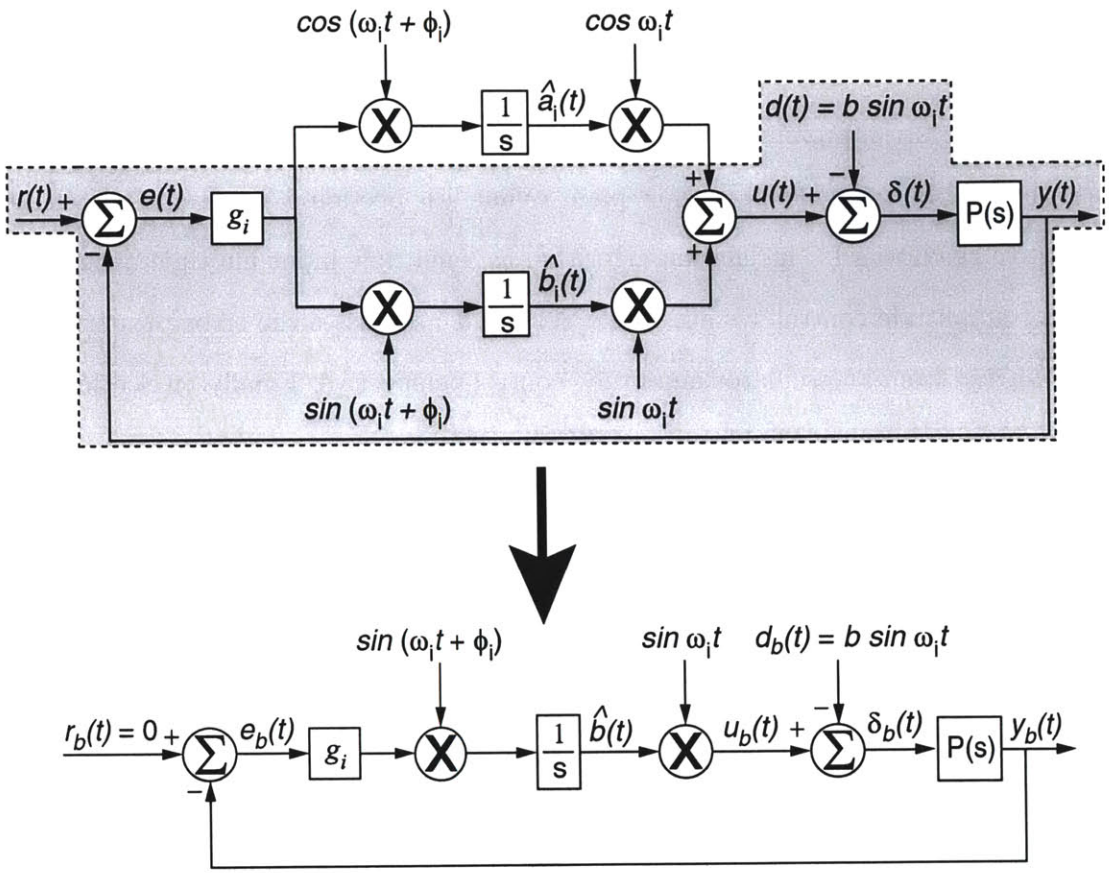

Figure 5-2: Closed-loop block diagram of the portion of the single resonator AFC system designed to follow/reject the sine component of a signal with frequency ω_i.

assumptions must be made.

First, we assume that the sine and cosine channels of the single resonator AFC system consist of multiple times-scales. By this we mean that the dynamics of the plant transfer function P(s) are considered to be much faster than the dynamics of the amplitude control loops. Said another way, the time scales on which the estimates of the Fourier coefficients, $\hat{a}_i$(t) and $\hat{b}_i$(t), vary are slow compared to the plant output y(t). We call y(t) the fast state while $\hat{a}_i$(t) and $\hat{b}_i$(t) are considered slow states [48]. This means that P(s) has essentially settled to steady-state before the AFC feedback loop develops a significant error signal. We can ensure that the estimates of the Fourier coefficients vary relatively slowly when compared to y(t) by

selecting a sufficiently low controller gain value g_i.

Secondly, we assume that the time variations of $\hat{a}_i(\mathrm{t})$ and $\hat{b}_i(\mathrm{t})$ are much slower than the AFC resonator frequency ω_i. The applicability of this statement is presented with the following analysis. Considering just the sine channel of the single resonator AFC system, as shown at the bottom of Figure 5-2, we see that the control input into the plant is

$$\delta_b(t) = \beta(t)\sin(\omega_i t), \tag{5.1}$$

where $\beta(\mathrm{t})$ is some slowly time-varying amplitude. For purposes of discussion, we will assume that $\beta(\mathrm{t})$ is given by

$$\beta(t) = \sin(\alpha t), \tag{5.2}$$

as shown in Figure 5-3, where $\alpha \ll \omega_i$.

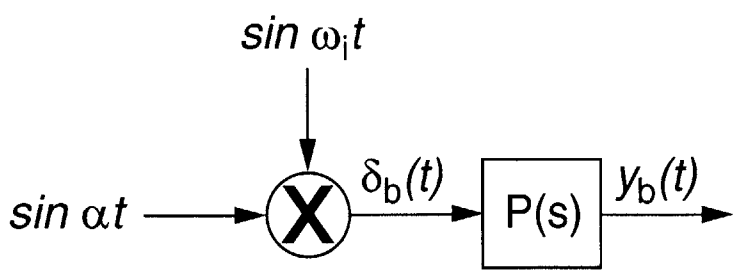

Figure 5-3: Simplification of the closed-loop block diagram for the sine channel of the single resonator AFC system, assuming the amplitude dynamics of the control input $\delta_b(\mathrm{t})$ are amplitude modulated by a low-frequency sinusoid.

Thus, substituting (5.2) into (5.1) gives

$$\delta_b(t) = \sin(\omega_i t)\sin(\alpha t) = \frac{1}{2}\left[\cos(\omega_i - \alpha)t - \cos(\omega_i + \alpha)t\right], \tag{5.3}$$

and if we define the frequencies

$$\omega_- = (\omega_i - \alpha), \tag{5.4}$$

$$\omega_+ = (\omega_i + \alpha), \tag{5.5}$$

then (5.3) becomes

$$\delta_b(t) = \frac{1}{2}\left[\cos\omega_- t - \cos\omega_+ t\right]. \tag{5.6}$$

After reaching steady-state oscillation, the plant output y_b(t), due to control input defined in (5.6), is given by

$$y_b(t) = \frac{1}{2}\left[|\mathrm{P}(j\omega_-)|\cos(\omega_- t + \angle\mathrm{P}(j\omega_-)) - |\mathrm{P}(j\omega_+)|\cos(\omega_+ t + \angle\mathrm{P}(j\omega_+))\right]. \tag{5.7}$$

Now, we assume the frequency α of (5.2) is much less than the frequency ω_i of the modulator, $\alpha \ll \omega_i$, and further that the magnitude and phase of the frequency response of the plant $\mathrm{P}(j\omega)$ do not change significantly in the vicinity of ω_i. Then (5.7) can be approximated by

$$y_b(t) \simeq \frac{1}{2}\left(|\mathrm{P}(j\omega_i)|\cos(\omega_- t + \angle\mathrm{P}(j\omega_i)) - |\mathrm{P}(j\omega_i)|\cos(\omega_+ t + \angle\mathrm{P}(j\omega_i))\right). \tag{5.8}$$

Recalling $\omega_+ = (\omega_i + \alpha)$ and $\omega_- = (\omega_i - \alpha)$, this gives

$$y_b(t) \simeq \frac{1}{2}|\mathrm{P}(j\omega_i)|\left(\cos(\omega_i t + \angle\mathrm{P}(j\omega_i) - \alpha t) - \cos(\omega_i t + \angle\mathrm{P}(j\omega_i) + \alpha t)\right). \tag{5.9}$$

Using the trigonometric relationship

$$\sin\alpha\sin\beta = \frac{1}{2}\left[\cos(\alpha - \beta) - \cos(\alpha + \beta)\right], \tag{5.10}$$

equation (5.9) reduces to

$$y_b(t) \cong |\mathrm{P}(j\omega_i)| \sin(\omega_i t + \angle \mathrm{P}(j\omega_i)) \sin(\alpha t). \tag{5.11}$$

Thus, for a sufficiently slow time-varying $\hat{b}_i(\mathrm{t})$, the output of the sine channel for the single resonator AFC system can be approximated as

$$y_b(t) \cong |\mathrm{P}(j\omega_i)| \sin(\omega_i t + \angle \mathrm{P}(j\omega_i)) b_{AMP}(t), \tag{5.12}$$

where $b_{AMP}(\mathrm{t})$ is the amplitude dynamics of the decoupled sine channel oscillator amplitude control loop. The approximate output of the entire single resonator AFC system is discussed in Section 5.3.2.

The results of (5.12) show that as long as the feedback loops for the sine and cosine channel in Figure 5-1 have a much lower crossover frequency than ω_i, we can analyze the amplitude dynamics of the AFC loop alone, independent of the time-variation of the sinusoids. This approximation is akin to the analysis provided by Roberge [46]. Assuming the previous two assumptions are satisfied, we now proceed to simplify the sine channel of the single resonator AFC system into an oscillator amplitude control system.

Our simplification begins by viewing the control input to the plant $\delta_b(\mathrm{t})$, as shown in Figure 5-2, as the difference between the estimate and actual disturbance signal Fourier coefficient modulated by a sine wave,

$$\delta_b(t) = u_b(t) - d_b(t) = \left[\hat{b}(t) - b\right] \sin(\omega_i t). \tag{5.13}$$

Next, we define the difference between the estimate and actual disturbance signal Fourier coefficient as

$$b_{AMP}(t) = \left[\hat{b}(t) - b\right], \tag{5.14}$$

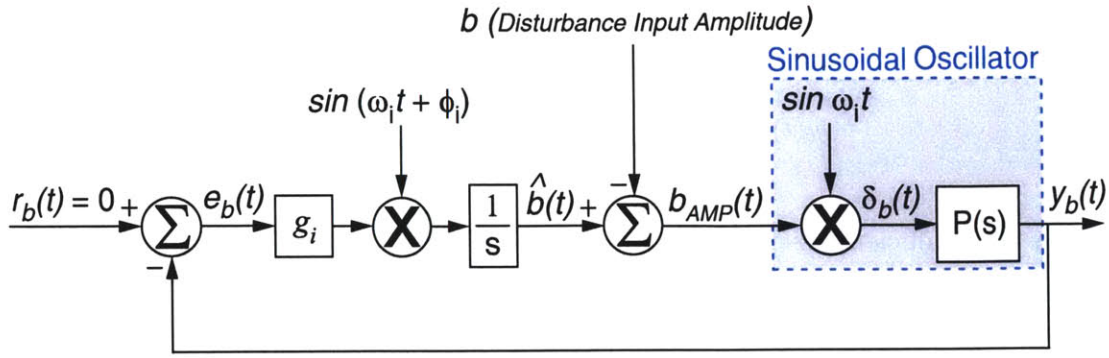

Figure 5-4: Simplification of the closed-loop block diagram for the sine channel of the single resonator AFC system. Here, we view the combination of the plant transfer function and second modulator as the sinusoidal oscillator.

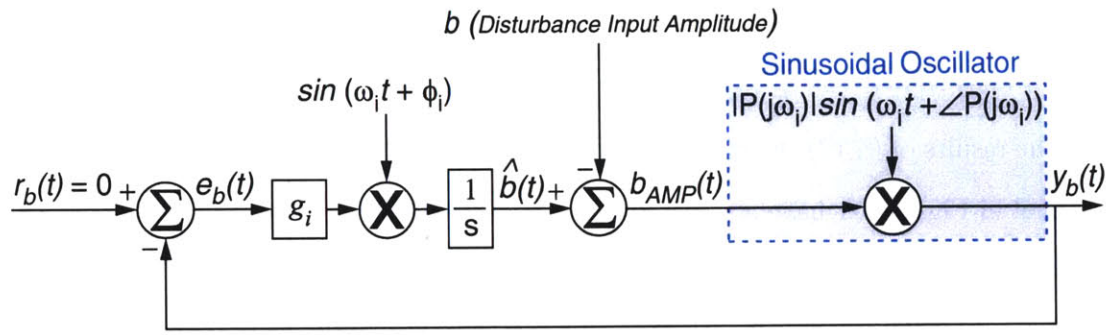

Figure 5-5: Simplification of the closed-loop block diagram for the sine channel of the single resonator AFC system. The second modulating sine wave now includes the magnitude and phase of the plant frequency response P(jω) evaluated at $\omega = \omega_i$, which we view as the sinusoidal oscillator.

where b_{AMP}(t) is the amplitude dynamics of the decoupled sine channel oscillator amplitude control loop, as defined previously in (5.12). Thus, we can group the second sinusoidal modulator and plant transfer function together, as shown in Figure 5-4, and view the combination as a sinusoidal oscillator system.

The results of (5.12) are essentially equivalent to the quasi-steady assumption discussed in [53], where Hall and Wereley model the dynamics of a helicopter rotor-blade as a magnitude attenuation and phase shift of the Higher Harmonic Control algorithm evaluated at s = $jN\Omega$ (see Section 1.3.2). That is, under this assumption,

we remove the plant transfer function from the feedback loop and view the output of the oscillator in Figure 5-4 as a magnitude attenuated and phase shifted sinusoid of frequency ω_i. The resulting simplified block diagram is illustrated in Figure 5-5. From this viewpoint, we see that the resulting oscillator output is given by

$$y_b(t) = b_{AMP}(t)|\mathrm{P}(j\omega_i)| \sin(\omega_i t + \angle \mathrm{P}(j\omega_i)), \tag{5.15}$$

which is equivalent to the results obtained in (5.12).

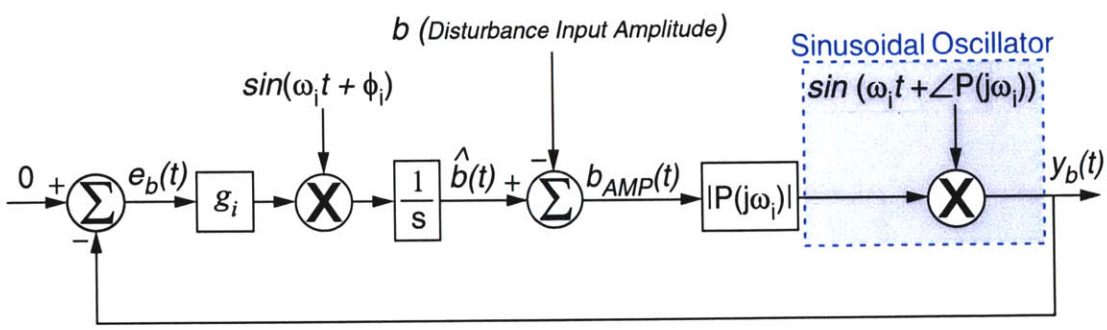

Figure 5-6: Simplification of the closed-loop block diagram for the sine channel of the single resonator AFC system. The magnitude of P(s) evaluated at s =jω_i is viewed as a loop gain, while the second modulator is the sinusoidal oscillator.

Upon removing the plant transfer function from the sine channel of the AFC loop, we view the magnitude of P(s) evaluated at s = $j\omega_i$ as a loop gain, as seen in Figure 5-6. Then, we simplify the loop even further by viewing the first modulator in the sine channel of the AFC loop as an amplitude detector for the sinusoidal oscillator. We proceed to move the second modulator from the output, around the feedback loop and through the beginning summation block and proportional gain g_i, and group it with the modulator in front of the integrator. Figure 5-7 illustrates this process.

Figure 5-8 shows the further simplified sine channel of the single resonator AFC system when the modulators (sinusoidal oscillator & amplitude detector) are grouped

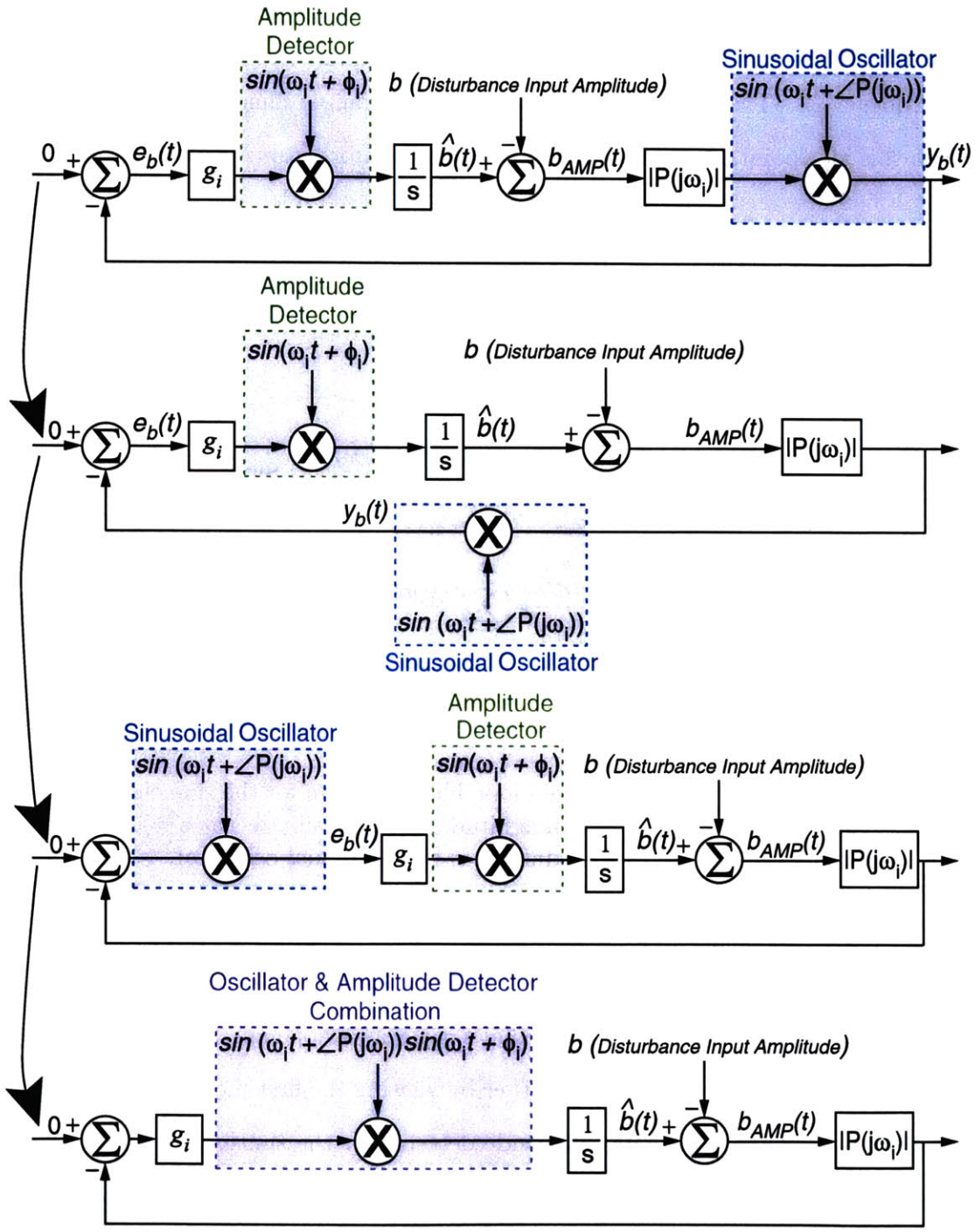

Figure 5-7: Simplification of the closed-loop block diagram for the sine channel of the single resonator AFC system. The second modulator (sinusoidal oscillator) has been moved to the beginning of the feedback loop and grouped with the first modulator (amplitude detector), which includes the phase advance parameter ϕ_i.

together and the phase advance parameter ϕ_i is set equal to

$$\phi_i = \angle P(j\omega_i), \tag{5.16}$$

in order to maximize loop stability, as discussed previously in Chapter 2. Using the following trigonometric relationship

$$\sin^2 \alpha = \frac{1}{2}(1 - \cos 2\alpha), \tag{5.17}$$

the squared modulator term in Figure 5-8 is equivalent to

$$\sin^2(\omega_i t + \angle P(j\omega_i)) = \frac{1}{2}\left[1 - \cos 2(\omega_i t + \angle P(j\omega_i))\right], \tag{5.18}$$

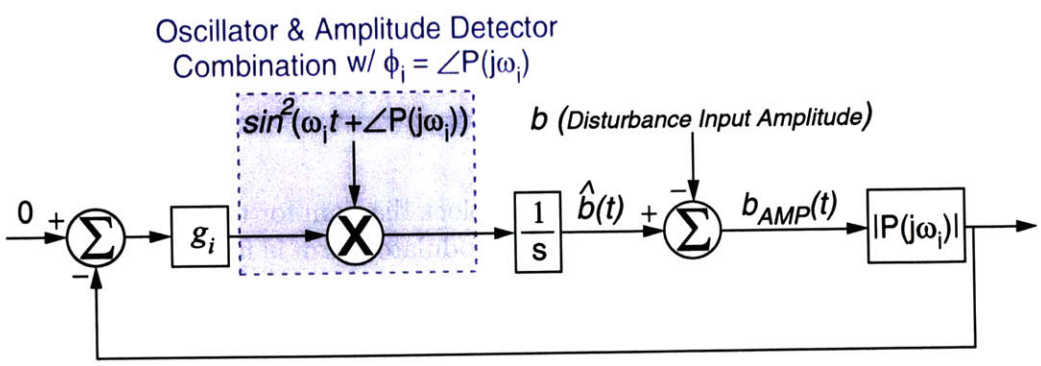

Figure 5-8: Simplification of the closed-loop block diagram for the sine channel of the single resonator AFC system. The second modulating sine wave has been moved to the beginning of the feedback loop and grouped with the first modulator, where the phase advance parameter $\phi_i = \angle P(j\omega_i)$.

which consists of an average DC and second harmonic term. The resulting equivalent closed-loop block diagram is shown in Figure 5-9. Since this feedback loop is inherently low-pass, the high-frequency second harmonic can be removed the analysis, leaving only the average DC component. A more formal presentation is as follows.

In Section 2.2.5, we showed that the averaging equation defined by Bodson [19] is

$$AVG[x] = \lim_{T\to\infty} \frac{1}{T} \int_0^T x(t)dt, \tag{5.19}$$

Thus, averaging (5.18) yields

$$\lim_{T\to\infty} \frac{1}{T} \int_0^T \frac{1}{2} \left[1 - \cos 2(\omega_i t + \angle P(j\omega_i))\right] \; dt = \frac{1}{2}, \tag{5.20}$$

and averaging the simplified feedback loop in Figure 5-9 eliminates the second harmonic term.

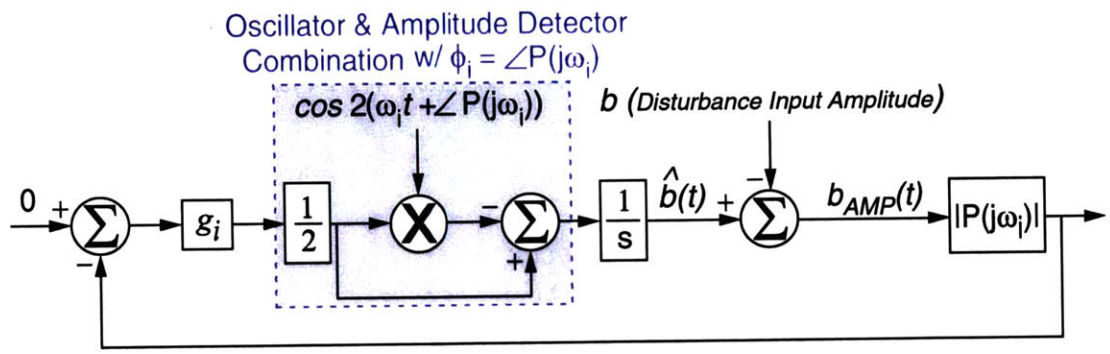

Figure 5-9: Simplification of the closed-loop block diagram for the sine portion of the single resonator AFC system. The squared modulator term is now represented by its average DC and second harmonic terms.

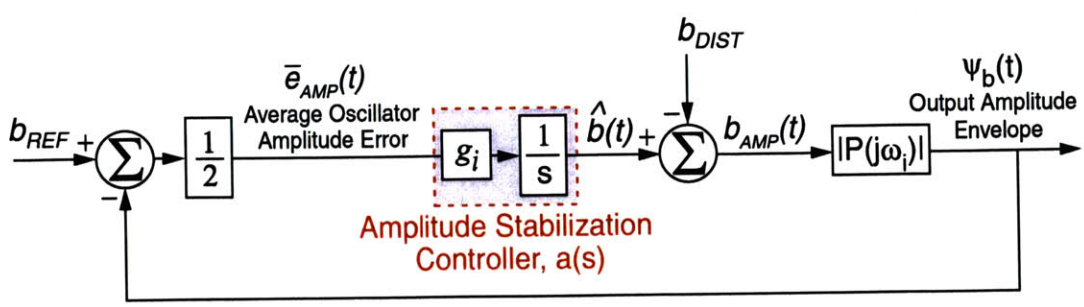

Figure 5-10: Closed-loop block diagram for the sine channel of the single resonator AFC system, simplified into an oscillator amplitude control system.

Figure 5-10 illustrates the final simplified sine channel of the single resonator AFC

closed-loop block diagram. Here, we have defined the reference and disturbance input as b_{REF} and b_{DIST}, respectively. This is due to the fact that this feedback loop now only characterizes the sine channel's amplitude dynamics. Also, we have defined the average oscillator amplitude error and output amplitude envelope as $\bar{e}_{AMP}$(t) and $\Psi_b(t)$, respectively. The average oscillator amplitude error is given by

$$\bar{e}_{AMP}(t) = \frac{1}{2}\left[b_{REF} - b_{AMP}(t)\right], \tag{5.21}$$

which equals the average DC component of the plant output (sinusoidal oscillator output) y_b(t) combined with the first sine wave modulator (amplitude detector), while the oscillator output amplitude envelope is

$$\Psi_b(t) = |\mathrm{P}(j\omega_i)| b_{AMP}(t), \tag{5.22}$$

which is equivalent to the amplitude dynamics of (5.12).

In Figure 5-10, we refer to the combination of the AFC proportional gain g_i and integrator as the OAC amplitude stabilization controller. This controller integrates the average oscillator amplitude error to create the controlled amplitude output envelope $\Psi_b(t)$ which, when modulated with the plant phase shifted sinusoid, provides the approximate AFC closed-loop output to a reference/disturbance sine wave with frequency ω_i.

A summary of the process of simplification of the AFC sine channel into an oscillator amplitude control loop is shown in Figure 5-11. At the bottom of this figure, we define the OAC error as e_{AMP}(t), which is given by

$$e_{AMP}(t) = 2\bar{e}_{AMP}(t), \tag{5.23}$$

while we compensate the resulting loop gain by dividing the proportional gain g_i by

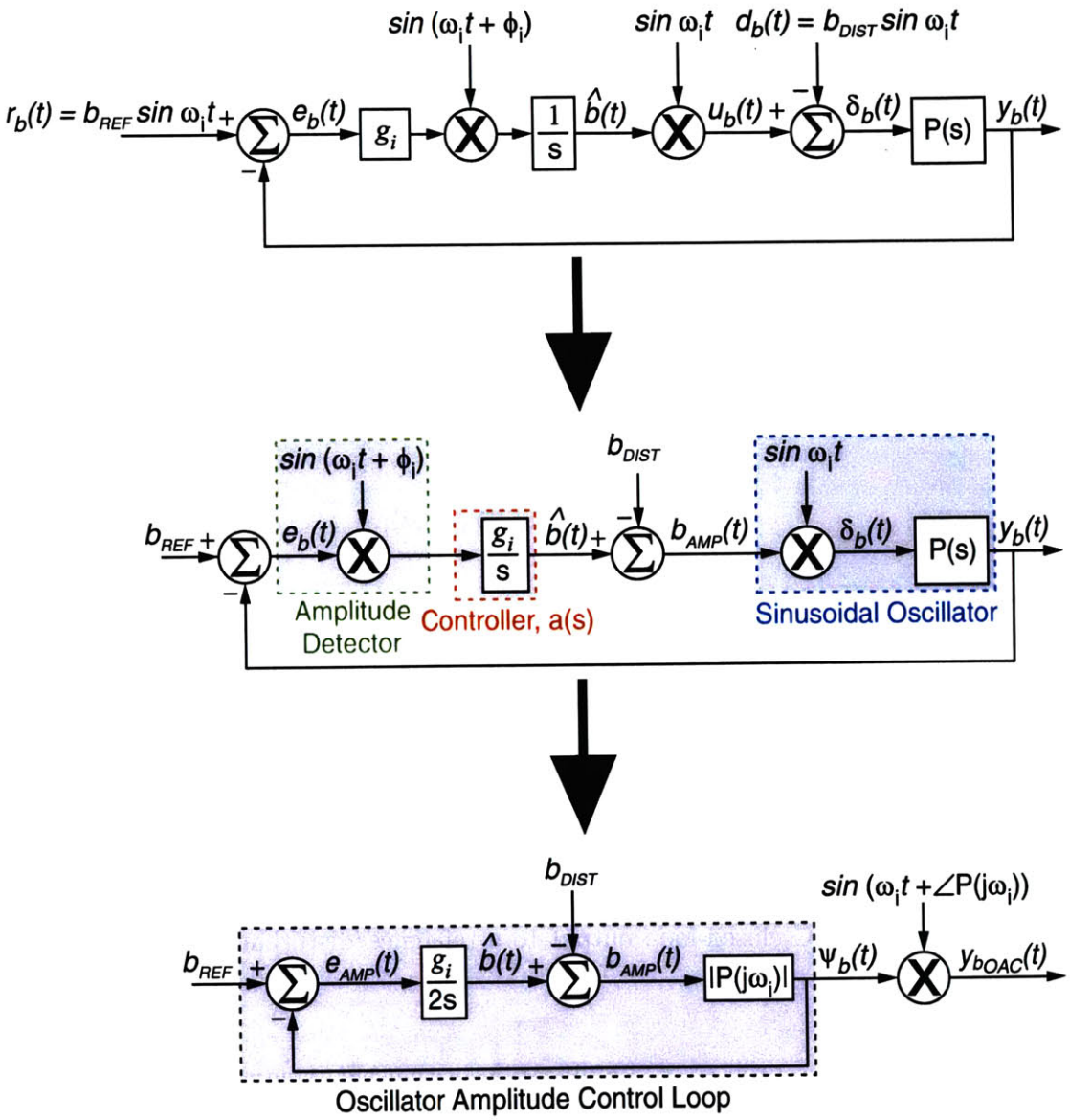

Figure 5-11: Simplification of the sine channel of the single resonator AFC system into an oscillator amplitude control system.

two. Also, the output of the sinusoidal oscillator is

$$y_{b_{OAC}}(t) = \Psi_b(t)\sin(\omega_i t + \angle \mathrm{P}(j\omega_i)), \tag{5.24}$$

which is equivalent the output of the sine channel for the single resonator AFC system, as defined in (5.12). This closed-loop block diagram serves as our OAC perspective for the decoupled sine and cosine channels of the single resonator AFC system.

The loop transmission of the decoupled sine and cosine channels is given by

$$L(s) = -\frac{g_i|P(j\omega_i)|}{2s}, \tag{5.25}$$

and the characteristic equation is of the form

$$1 - L(s) = 0, \tag{5.26}$$

or

$$2s - g_i|P(j\omega_i)| = 0. \tag{5.27}$$

Thus, under the assumption that the dynamics of the feedback loop are slow relative to the oscillation frequency, the dominant OAC closed-loop pole is located at

$$s_{OAC} = -\frac{g_i|P(j\omega_i)|}{2} \ \ \mathrm{sec}^{-1}. \tag{5.28}$$

Further then, for small g_i values, the steady-state settling time t_s is proportional to

$$t_s \sim \frac{2}{g_i|P(j\omega_i)|} \ \ \mathrm{sec}. \tag{5.29}$$

The analysis above assumes that the phase advance parameter is set properly as $\phi_i = \angle \mathrm{P}(j\omega_i)$. In the following analysis, we consider the case where this equality is not

enforced. If we do not use the phase advance parameter in the single resonator AFC controller ($\phi_i = 0$), then the combined sinusoidal modulators, as shown in Figure 5-7, are

$$\sin(\omega_i t + \angle \mathrm{P}(j\omega_i)) \sin(\omega_i t). \tag{5.30}$$

Using the trigonometric relationship

$$\sin\alpha \sin\beta = \frac{1}{2}\left[\cos(\alpha - \beta) - \cos(\alpha + \beta)\right], \tag{5.31}$$

equation (5.30) can thus be re-written as

$$\sin(\omega_i t + \angle \mathrm{P}(j\omega_i)) \sin(\omega_i t) = \frac{1}{2}\left[\cos(\angle \mathrm{P}(j\omega_i)) - \cos(2\omega_i t + \angle \mathrm{P}(j\omega_i))\right]. \tag{5.32}$$

As a result, the loop transmission for the decoupled and simplified sine and cosine channels of the single resonator AFC system is given by

$$L(s) = -\frac{g_i |P(j\omega_i)| \cos(\angle \mathrm{P}(j\omega_i))}{2s}, \tag{5.33}$$

and the dominant closed-loop pole is now located at

$$s_{OAC} = -\frac{g_i |P(j\omega_i)| \cos(\angle P(j\omega_i))}{2} \ \mathrm{sec}^{-1}. \tag{5.34}$$

From (5.34), we see that if the plant contributes 0° of phase lag at the resonator frequency ω_i, then the closed-loop settling time will be the same as given in (5.29). However, with $\phi_i = 0$, as $\angle \mathrm{P}(j\omega_i)$ approaches $\pm 90^o$, then the settling time grows $t_s \longrightarrow \infty$, since

$$\cos(\pm\frac{\pi}{2}) = 0. \tag{5.35}$$

Also, again for $\phi_i = 0$, if $\frac{\pi}{2} < \angle P(j\omega_i) < \frac{3\pi}{2}$, the resulting loop transmission effectively creates positive feedback and hence will be unstable. We thus see another

perspective that in order to maximize the dynamic response of the simplified feedback loop, the phase advance parameter should be used to provide a zero phase difference between the sinusoidal plant output y_b(t) and the first sine wave modulator (*i.e.*, $\phi_i = \angle P(j\omega_i)$) [47]. This result re-emphasizes the importance of using a properly chosen ϕ_i with an AFC controller. This is especially true when the plant model is non-SPR, as otherwise instability will result.

5.2 Example of AFC viewed as an OAC System

In this example, we consider a single resonator AFC system designed to eliminate a constant amplitude disturbance input given by

$$d_1(t) = b_1 \sin(\omega_1 t), \tag{5.36}$$

where the parameters are selected as $b_1 = \frac{1}{2}$ and $\omega_1 = 225$ rad/sec. Assuming a simplified second order plant model

$$P(s) = \frac{\omega_n^2}{s^2 + 2\zeta\omega_n s + \omega_n^2}, \tag{5.37}$$

where the parameters are selected as $\omega_n = 250$ rad/sec and $\zeta = \frac{\sqrt{2}}{2}$, we set g_i equal to 20 and implement the phase advance parameter ($\phi_i = \angle P(j\omega_i)$ = -1.423 rad). Viewing the system from an oscillator amplitude control perspective, we analyze just the sine channel of the closed-loop system, since the disturbance input consists of only a sine term. Thus, the reference and disturbance amplitude inputs are

$$b_{REF} = 0, \tag{5.38}$$

$$b_{DIST} = \frac{1}{2}, \tag{5.39}$$

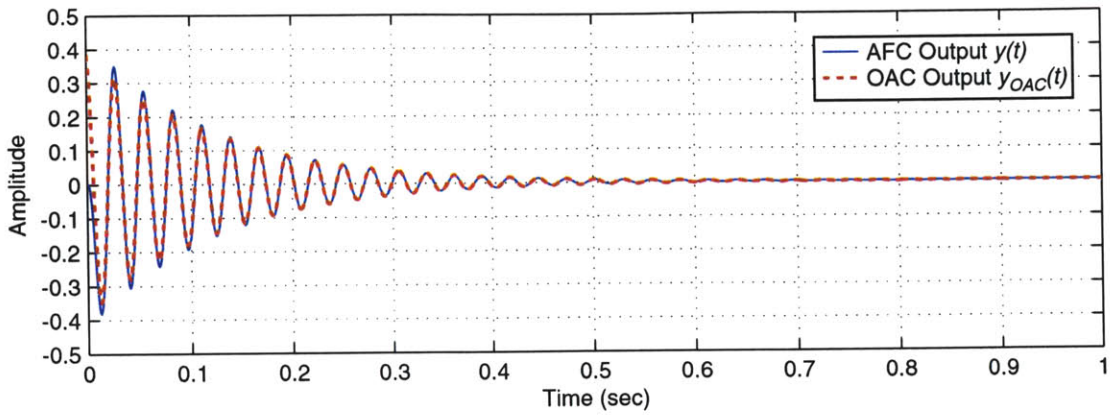

Figure 5-12: Overlay of the predicted output of the single resonator AFC system y(t) and the oscillator amplitude control system output y_{OAC}(t) to a constant amplitude disturbance signal d(t) = $\frac{1}{2}$sin(225t) with the proper phase advance parameter implemented (ϕ_i = -1.423 rad) and g_i = 20.

and the OAC output as a function of time is given by

$$y_{OAC}(t) = \Psi_b(t)\sin(\omega_i t + \angle \mathrm{P}(j\omega_i)). \tag{5.40}$$

Figure 5-12 compares the output of oscillator amplitude control system, as predicted by (5.40), to the exact time simulation of the single resonator AFC system output, which is generated by the algorithm in Figure 5-1. We see that for this particular case, the OAC perspective accurately predicts the behavior of the AFC system. There are some small discrepancies in the initial part of the time response, which we speculate are due to ignoring the transient response of the plant to the sinusoid, but the overall dynamics of the AFC and OAC modulated amplitude envelopes match rather well.

Out of curiosity, due to the initial discrepancies between y_{OAC}(t) and y(t) in Figure 5-12, we decided to add the plant transfer function P(s) to the loop transmission of the oscillator amplitude control loop, as shown in Figure 5-13, and repeat the previous simulation. The results of this simulation are summarized in Figure 5-14. Here,

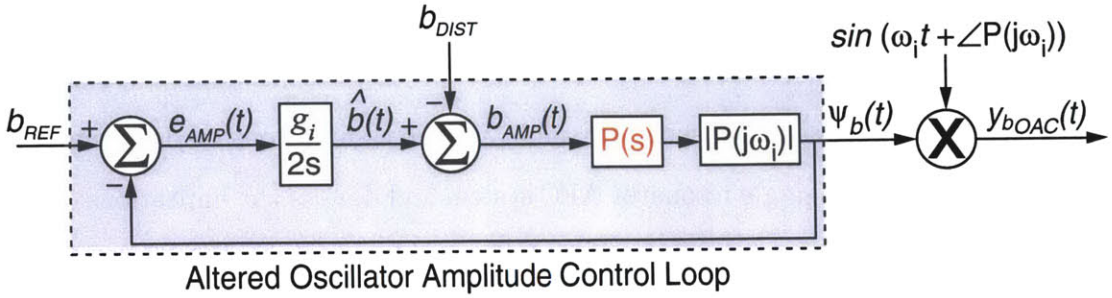

Figure 5-13: Closed-loop block diagram for the sine channel of the single resonator AFC system, simplified into an oscillator amplitude control system. Notice the addition of the plant transfer function to the loop transmission in the OAC loop.

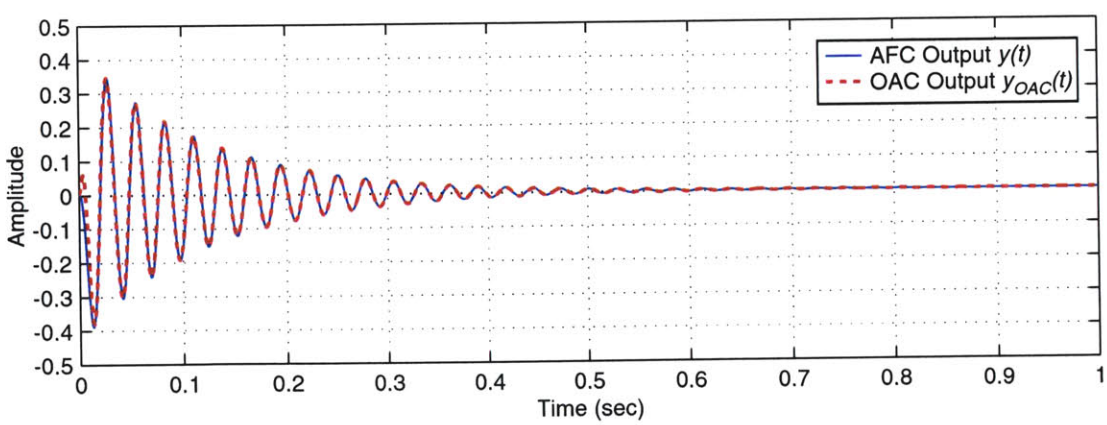

Figure 5-14: Overlay of the simulated output of the single resonator AFC system y(t) and the oscillator amplitude control system output y_{OAC}(t) to the constant amplitude disturbance signal d_1(t) = $\frac{1}{2}$sin(225t) with the proper phase advance parameter implemented (ϕ_i = -1.423 rad), g_i = 20, and the plant model added to the OAC loop.

we actually see more agreement between y_{OAC}(t) and y(t), once P(s) is added to the OAC loop. At the present time, we have not developed a mathematic model which explains these findings but the simulations show very interesting results. Thus, we leave this investigation for future work.

In the following section, we show the validity of the assumptions made to simplify the sine channel of the single resonator AFC system and discuss the limitations of our oscillator amplitude control perspective for large g_i values and slow plant dynamics. During these analyses, we revert back to the original oscillator amplitude control loop, without the addition of the plant transfer function.

5.3 Limitations of the Oscillator Amplitude Control Perspective

As stated previously in Section 5.1, the simplification of the sine channel of the single resonator AFC system relies on the relative speed of the feedback loop in Figure 5-2 compared to the resonator frequency and plant dynamics, as well as the decoupling of the sine and cosine AFC channels. Assuming the proper phase advance has been chosen ($\phi_i = \angle P(j\omega_i)$), the size of the proportional gain g_i dictates, to a large degree, how well the oscillator amplitude control model predicts the AFC closed-loop system's behavior. We use a first order perturbation analysis with averaging to determine an approximate limit on the acceptable size of g_i for a given resonator frequency [29].

5.3.1 First Order Perturbation Analysis

The output of the plant y_b(t), as shown in Figure 5-4, is given by

$$y_b(t) = \mathrm{P}[\delta_b(t)] = \mathrm{P}[b_{AMP}(t)\sin(\omega_i t)], \tag{5.41}$$

where (5.41) is the transfer transform of the plant model operating on the product of b_{AMP}(t) and sin(ω_it). The amplitude envelope b_{AMP}(t), defined previously in (5.14), is

$$b_{AMP}(t) = \left[\hat{b}(t) - b\right], \tag{5.42}$$

and since we assume the Fourier coefficient of the disturbance signal (b) is a constant, the time rate of change of (5.42) is

$$\frac{db_{AMP}(t)}{dt} = \frac{d\left[\hat{b}(t) - b\right]}{dt} = \frac{d\hat{b}(t)}{dt}. \tag{5.43}$$

We see from Figure 5-4 that (5.43) is also given by

$$\frac{db_{AMP}(t)}{dt} = -g_i y_b(t)\sin(\omega_i t + \angle P(j\omega_i)), \tag{5.44}$$

and using the results of (5.12), equation (5.41) can be re-arranged into the form

$$y_b(t) = b_{AMP}(t)|P(j\omega_i)|\sin(\omega_i t + \angle P(j\omega_i)). \tag{5.45}$$

Substituting (5.45) into (5.44) yields

$$\frac{db_{AMP}(t)}{dt} = -g_i b_{AMP}(t)|P(j\omega_i)|\sin^2(\omega_i t + \angle P(j\omega_i)), \tag{5.46}$$

and using the trigonometric relation from (5.17),

$$\frac{db_{AMP}(t)}{dt} = -g_i b_{AMP}(t)|P(j\omega_i)|\frac{1}{2}\left[1 - \cos 2(\omega_i t + \angle P(j\omega_i))\right]. \tag{5.47}$$

For this particular system, b_{AMP} is the dependent variable while time (t) is the independent variable [39]. We can make (5.47) dimensionless with respect to time by

using the resonator frequency ω_i and defining a dimensionless time as

$$T = \omega_i t, \tag{5.48}$$

where

$$\frac{d}{dt} \longrightarrow \omega_i \frac{d}{dT}. \tag{5.49}$$

Substituting (5.48) and (5.49) into (5.47) gives

$$\omega_i \frac{db_{AMP}(T)}{dT} = -g_i b_{AMP}(T)|P(j\omega_i)|\frac{1}{2}\left[1 - \cos 2(T + \angle P(j\omega_i))\right]. \tag{5.50}$$

Thus, equation (5.50) can be rewritten as

$$\frac{db_{AMP}(T)}{dT} = -\epsilon b_{AMP}(T)\left[1 - cos2(T + \angle P(j\omega_i))\right], \tag{5.51}$$

where,

$$\epsilon = \frac{g_i|P(j\omega_i)|}{2\omega_i}. \tag{5.52}$$

ϵ is the ratio of the proportional gain to the resonator frequency and when $2\omega_i \gg g_i|\mathrm{P}(j\omega_i)|$, then ϵ is small and can be used as a perturbation parameter [39]. Solving for the amplitude dynamics directly from (5.51) gives

$$b_{AMP}(T) = b_{AMP}(0)e^{-\int_0^T \epsilon\left[1 - cos(2T + 2\angle P(j\omega_i))\right]dT}, \tag{5.53}$$

or

$$b_{AMP}(T) = b_{AMP}(0)e^{\left(-\epsilon T + \frac{\epsilon}{2}\sin(2T + 2\angle P(j\omega_i))\right)}, \tag{5.54}$$

where

$$b_{AMP}(0) = -b. \tag{5.55}$$

Thus, re-dimensionalizing (5.54) and substituting in (5.52) and (5.55), the amplitude dynamics of the sine channel OAC loop are given by

$$b_{AMP}(t) = -be^{\left(-\frac{g_i|P(j\omega_i)|}{2}t + \frac{g_i|P(j\omega_i)|}{4\omega_i}\sin(2\omega_i t + 2\angle P(j\omega_i))\right)}. \tag{5.56}$$

Assuming ϵ is small, we can average (5.50) over one period before solving for the amplitude dynamics b_{AMP}(t). In doing so, equation (5.56) becomes

$$\hat{b}_{AMP}(t) = -be^{-\left(\frac{g_i|P(j\omega_i)|}{2}\right)t}, \tag{5.57}$$

where,

$$\hat{b}_{AMP}(t) = \text{AVE}[b_{AMP}(t)] = \left[\hat{b}_{ave}(t) - b\right]. \tag{5.58}$$

Sastry and Bodson [48] show that

$$|b_{AMP}(t) - \hat{b}_{AMP}(t)| = e^{-\epsilon\omega_i t}|e^{\frac{\epsilon}{2}\sin 2(\omega_i t + \angle P(j\omega_i))} - 1|, \tag{5.59}$$

which means

$$|b_{AMP}(t) - \hat{b}_{AMP}(t)| \longrightarrow |\frac{\epsilon}{2}\sin 2(\omega_i t + \angle P(j\omega_i))| \quad \text{as } \epsilon \longrightarrow 0. \tag{5.60}$$

Therefore, as $\epsilon \longrightarrow 0$, equations (5.56) and (5.57) become approximately equal to one another.

Equation (5.57) can also be written as

$$\left[\hat{b}_{ave}(t) - b\right] = -be^{-\left(\frac{g_i|P(j\omega_i)|}{2}\right)t}. \tag{5.61}$$

Thus, the average estimate of the Fourier coefficient for the sine channel of the single

resonator AFC system is

$$\hat{b}_{ave}(t) = b\left[1 - e^{-\left(\frac{g_i|P(j\omega_i)|}{2}\right)t}\right]. \tag{5.62}$$

These results are equivalent those shown in (5.28), which state that

$$t_s \sim \frac{2}{g_i|P(j\omega_i)|} \text{ sec.} \tag{5.63}$$

We see from (5.60) that the accuracy of the previous analysis is directly proportional to the size of the perturbation parameter. In calculating the decoupled and simplified AFC loop dynamics, we assume that ϵ is relatively small. Nayfeh [39] shows that the perturbation parameter should be

$$\epsilon \ll 1, \tag{5.64}$$

for the simplified OAC system to produce reasonable results. Thus, in the following section, we simulate a single resonator system and show how increasing the size of ϵ affects the validity of our OAC perspective.

Example of AFC viewed as an OAC System using the First Order Perturbation Analysis

In this example, we consider another single resonator AFC system designed to eliminate a constant amplitude periodic disturbance given by

$$d(t) = \frac{1}{2}\sin(\omega_i t), \tag{5.65}$$

and study the effects of viewing the sine channel from an oscillator amplitude control perspective, as the size of the perturbation parameter increases. Here, the plant being

controlled is the simplified second order transfer function defined previously in (5.37). We design the single resonator AFC controller at four difference resonator frequencies: $\omega_i = 10$, 25, 100, and 250 rad/sec. For each of these frequencies, we set $\phi_i = \angle \mathrm{P}(j\omega_i)$ and $g_i = 25$.

Figure 5-15 compares the transient responses of the control input $\delta_b(\mathrm{t})$ for the sine channel of the single resonator AFC system, as shown in Figure 5-2. These curves correspond to the exact time simulation of the single resonator AFC system control input, which is generated by the algorithm in Figure 5-1, and the modulated amplitude dynamics of the oscillator amplitude control system, which is given by

$$\delta_{b_{OAC}}(t) = b_{AMP}(t)\sin(\omega_i t). \tag{5.66}$$

We see that for $\omega_i = 10$ rad/sec, the perturbation parameter equals $\epsilon = 1.25$ and the OAC perspective does not predict the response of the sine portion of the single resonator AFC system very closely. Note however that the loop settles in less than one cycle of oscillation. In contrast, when $\omega_i = 250$ rad/sec, $\epsilon = 0.0354$ and the AFC and OAC responses overlap one another quite well. Here, loop settling requires about 10 cycles of oscillation.

The results of Figure 5-15 confirm the intuition that the accuracy (η) of viewing the sine channel of the single resonator Adaptive Feedforward Cancellation system from an oscillator amplitude control perspective is proportional to

$$\eta \sim \frac{g_i}{\omega_i}. \tag{5.67}$$

For a large resonator frequency and relatively small proportional gain, OAC provides a valid representation of the amplitude envelope dynamics. On the other hand, for slow periodic signals (small ω_i values) and large g_i levels, this approach does not accurately capture the underlying system dynamics. For example, for the value ω_i

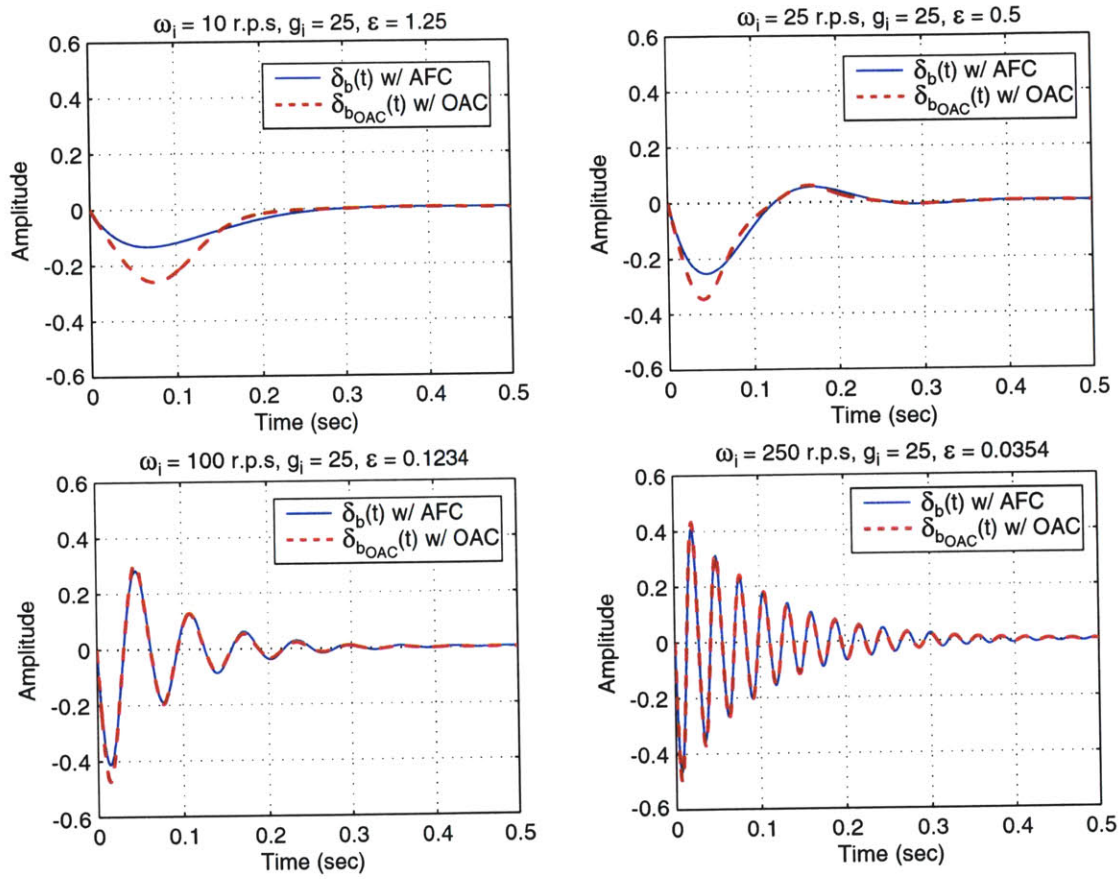

Figure 5-15: Comparison of the transient responses of the control input δ_b(t) for the sine channel of the single resonator AFC system and the resulting oscillator amplitude control input $\delta_{b_{OAC}}$(t) with $g_i = 25$ and $\omega_i = 10$, 25, 100, and 250 rad/sec.

$= 100$ rad/sec, $\epsilon = 0.1234$ and the simulated OAC output follows the AFC curve reasonably well but there are still small discrepancies between the curves. Thus, it appears that ϵ should be at least an order of magnitude less than unity to approximate the sine channel of the single resonator AFC system with an OAC system. In other words, the approximate bound on the size of g_i for a given resonator frequency is given by

$$g_i < \frac{2\omega_i}{10|P(j\omega_i)|}. \tag{5.68}$$

Throughout these previous simulations, we chose resonator frequencies that were either slower than or equal to the bandwidth (ω_b) of the plant transfer function. This means that the magnitude of the plant $|P(j\omega_i)|$ was approximately equal to or on the same order of magnitude as unity. We proved in Section 2.2.3 that an AFC controller can be stabilized with the phase advance parameter for any resonator frequency, even if ω_i is higher than the plant's bandwidth. However, if the resonator frequencies are chosen such that

$$\omega_i \gg \omega_b, \tag{5.69}$$

then $|P(j\omega_i)|$ will have a considerable effect on the speed of the amplitude envelope and accuracy of the OAC model, as shown in (5.52). Another issue also arises when the dynamics of the plant are approximately the same order of magnitude as the dynamics of the simplified OAC feedback loop. We illustrate such effects in the following section.

5.3.2 Oscillator Amplitude Control Perspective with Slow Plant Dynamics

In this section, we use the simplified second order plant model

$$P(s) = \frac{\omega_n^2}{s^2 + 2\zeta\omega_n s + \omega_n^2}, \tag{5.70}$$

where the parameters are selected as $\omega_n = 5$ rad/sec and $\zeta = \frac{\sqrt{2}}{2}$, to design a single resonator AFC system. With a periodic disturbance of the form

$$d_1(t) = b_1 \sin(\omega_1 t), \tag{5.71}$$

where the amplitude and frequency are chosen as $\omega_1 = 40$ rad/sec and $b_1 = \frac{3}{4}$, the magnitude and phase of the plant transfer function at ω_1 are

$$\begin{aligned} |P(j\omega_1)| &= 0.0156\ (-36.125\ \text{dB}), \\ \angle P(j\omega_1) &= -2.964\ \text{rad}\ (-169.82^o). \end{aligned} \tag{5.72}$$

For this particular example, the resonator frequency is approximately an order of magnitude faster than the bandwidth of the plant transfer function. This results in a large attenuation and phase shift of the second modulating sine wave, as shown in (5.72). Thus, without the use of the phase advance parameter, this system will be unstable, since the phase of the plant at s = $j\omega_i$ is more negative than -90°. If we set $\phi_i = \angle P(j\omega_1)$ = -2.964 rad and $g_i = 250$, the closed-loop system is stable and the perturbation parameter becomes

$$\epsilon = 0.049. \tag{5.73}$$

Notice that the proportional gain has been set relatively high. We do this in order to offset the attenuation due to $|P(j\omega_1)|$ and provide the closed-loop with a reasonable convergence time.

Looking at the size of the perturbation parameter in (5.73), it appears that we should be able to use the simplified OAC model to accurately predict the dynamics for the sine channel of the single resonator AFC system. Figure 5-16 compares the transient responses for the estimate of the Fourier coefficient $\hat{b}$(t) and AFC control input δ_b(t), using the exact time simulation of the single resonator AFC system and

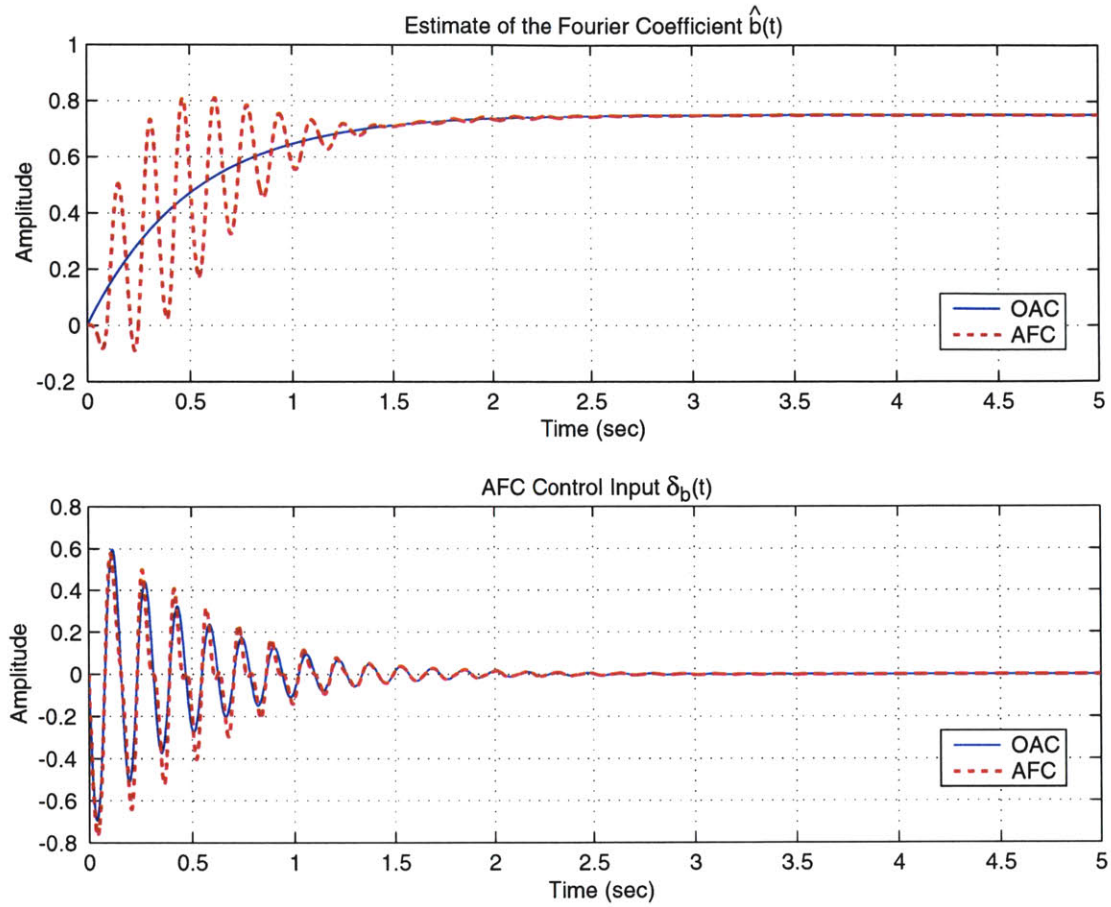

Figure 5-16: Comparison of the estimate of the Fourier coefficient $\hat{b}(t)$ and AFC control input $\delta_b(t)$ for the sine channel of the single resonator AFC system and simplified OAC loop with $\omega_n = 5$ rad/sec, and $g_i = 250$.

simplified oscillator amplitude control loop. We see that both of these plots show noticeable variations between the AFC and OAC simulations. These discrepancies are due to the closeness of the poles of the second order plant transfer function to the oscillator amplitude control dynamics.

The poles of the plant transfer function P(s) are

$$s_{1,2} = -3.535 \pm 3.535j \text{ sec}^{-1}, \tag{5.74}$$

while the approximate dominant OAC close-loop pole is

$$s_{OAC} = -1.953 \text{ sec}^{-1}. \tag{5.75}$$

Since these poles are of the same order of magnitude, the results of the first order perturbation analysis are not highly accurate. This analysis is based on the assumption that the plant dynamics are much faster than the bandwidth of the decoupled sine and cosine OAC loops. If we change the natural frequency of the plant tranfer function to $\omega_n = 50$ rad/sec, set $g_i = 8$ and alter the rest of the system parameters accordingly, the poles of P(s) and the approximate dominant OAC closed-loop pole are now

$$s_{1,2} = -35.35 \pm 35.35j \text{ sec}^{-1}, \tag{5.76}$$

$$s_{OAC} = -3.37 \text{ sec}^{-1}. \tag{5.77}$$

These poles are now separated by more than an order of magnitude, and the resulting perturbation parameter equals $\epsilon = 0.0842$.

Figure 5-17 compares the resulting simulated AFC and OAC transient responses for the estimate of the Fourier coefficient $\hat{b}$(t) and AFC control input δ_b(t). With $\epsilon < 0.1$ and the plant poles an order of magnitude faster than the dominant OAC closed-loop pole, we see that viewing the sine channel of the single resonator AFC system from an OAC perspective is quite accurate. Thus, as a rule of thumb, the poles of the plant being controlled with an AFC system should always be at least an order of magnitude faster than the amplitude envelope dynamics to be able to use oscillator amplitude control theory with high accuracy. It should also be noted that these discrepancies usually only appear when the AFC controller is designed to follow/reject signals with frequencies greater than the plant's bandwidth. Care must always be taken to ensure AFC closed-loop stability when $\omega_i \gg \omega_b$ and the results of

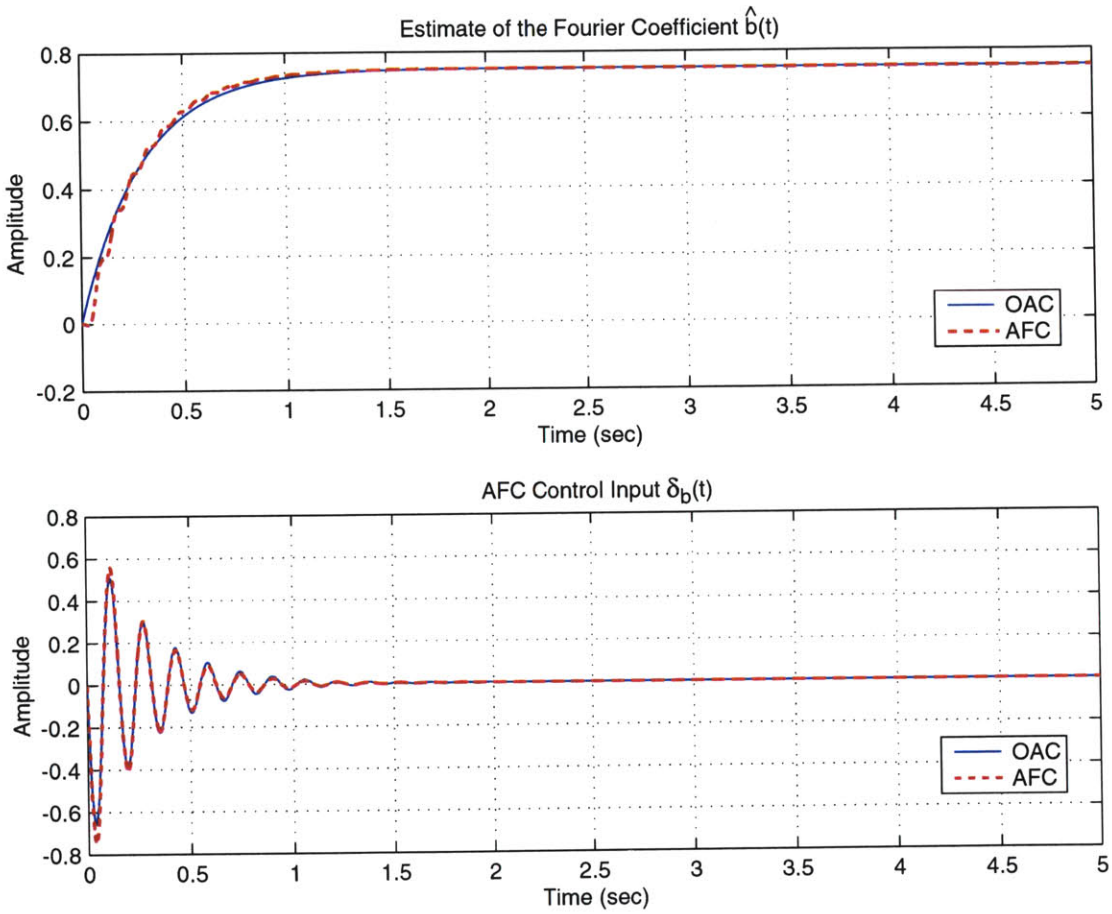

Figure 5-17: Comparison of the estimate of the Fourier coefficient $\hat{b}(\mathrm{t})$ and sine wave modulated amplitude envelope $\delta_b(\mathrm{t})$ for the sine portion of the single resonator AFC system and oscillator amplitude control loop with $\omega_n = 50 rad/sec$, and $g_i = 8$.

this section show that Adaptive Feedforward Cancellation viewed from an oscillator amplitude control perspective can become erroneous when $\frac{\omega_i}{\omega_b} \gg 1$.

5.4 Adaptive Feedforward Cancellation viewed as a Multiple-Input Multiple-Output Oscillator Amplitude Control System

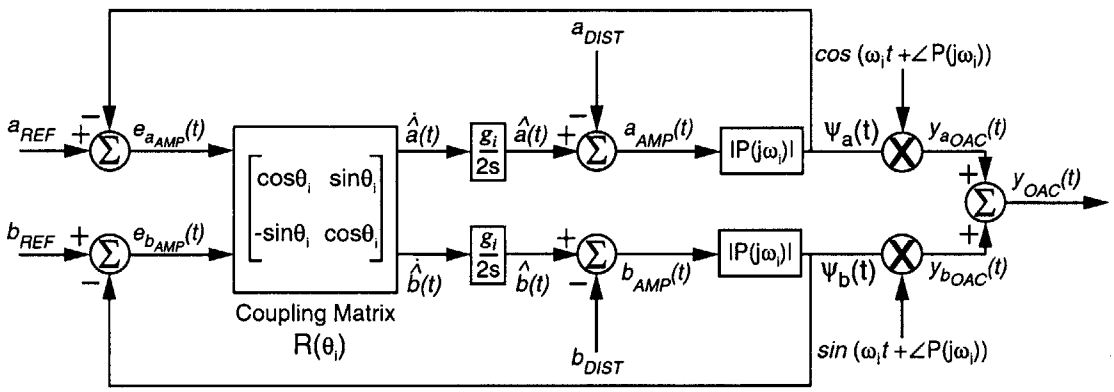

Figure 5-18: Closed-loop block diagram for the single resonator AFC system viewed as a multiple-input multiple-output (MIMO) oscillator amplitude control system.

Using the results from Sections 5.1 and 5.3, we develop a model for the entire single resonator AFC system by viewing the feedback loop in Figure 5-1 as a multiple-input multiple-output (MIMO) oscillator amplitude control system. Figure 5-18 illustrates the resulting closed-loop block diagram, which is essentially equivalent to the block diagram Tamisier *et al* use to explain the principle of Automatic Vibration Reduction (see Figure 1-18). Here, a_{REF}, b_{REF}, a_{DIST}, and b_{DIST} are the Fourier coefficients of the periodic reference and disturbance input signals, respectively. $\Psi_a(\mathrm{t})$ and $\Psi_b(\mathrm{t})$ represent the oscillator amplitude outputs of the sine and cosine channels of the single resonator AFC system, while $y_{a_{OAC}}(\mathrm{t})$ and $y_{b_{OAC}}(\mathrm{t})$ are the corresponding full oscillator outputs, respectively. The superposition of these outputs equals the approximate

AFC closed-loop output, given by

$$y_{OAC}(t) = y_{a_{OAC}}(t) + y_{b_{OAC}}(t). \tag{5.78}$$

Without the addition of the phase advance parameter ($\phi_i = 0$), we model the MIMO OAC system as two single-input single-output (SISO) oscillator amplitude control loops coupled by a rotation matrix $\mathrm{R}(\theta_i)$. The coupling matrix is of the form

$$\mathbf{R}(\theta_\mathrm{i}) = \begin{bmatrix} \cos\theta_i & \sin\theta_i \\ -\sin\theta_i & \cos\theta_i \end{bmatrix}, \tag{5.79}$$

where

$$\theta_i = \angle P(j\omega_i). \tag{5.80}$$

Section 2.2.3 shows that the phase advance parameter ϕ_i can be implemented through a rotation matrix of the form

$$\mathbf{R}(\phi_\mathrm{i}) = \begin{bmatrix} \cos\phi_i & -\sin\phi_i \\ \sin\phi_i & \cos\phi_i \end{bmatrix}, \tag{5.81}$$

and when $\phi_i = \angle P(j\omega_i)$, this phase advance matrix equals the inverse of the coupling matrix. Thus, equation (5.81) essentially diagonalizes the coupling matrix $\mathrm{R}(\theta_i)$ and separates the single resonator AFC system into two independent SISO OAC loops. Skogestad and Postlethwaite [40] refer to this type of approach as *Decoupling Control*, where a compensator is chosen such that the MIMO system is diagonalized at a selected frequency. This allows us to analyze the sine and cosine channels of the AFC system independently and utilize classical controls techniques to measure the closed-loop convergence, stability, and robustness properties.

5.4.1 Single Resonator AFC System viewed from an OAC Perspective

In this section we study the validity of viewing the single resonator Adaptive Feedforward Cancellation system from an oscillator amplitude control perspective and show how we can use the approximate dominant OAC closed-loop pole to approximate the closed-loop convergence properties, for sufficiently low g_i values. Specifically, we analyze the transient response of the single resonator AFC system designed to eliminate a constant amplitude disturbance input of the form

$$d_1(t) = a_1 \cos(\omega_1 t) + b_1 \sin(\omega_1 t), \tag{5.82}$$

where the parameters are selected as $\omega_1 = 180$ rad/sec, $a_1 = \frac{1}{8}$, and $b_1 = \frac{3}{4}$. We model the plant transfer function P(s) as the well-known simplified second order model, and select the parameters as $\omega_n = 250$ rad/sec and $\zeta = \frac{\sqrt{2}}{2}$. A state-space model of the complete MIMO OAC system is given in Appendix I.

With the proper phase advance parameter chosen ($\phi_i = \angle P(j\omega_1)$), we analyze the closed-loop system as the superposition of the decoupled AFC sine and cosine channels. The eigenvalues of the plant and approximate dominant OAC closed-loop pole are given by

$$\lambda_{1,2} = -176.78 \pm 176.78j \text{ sec}^{-1}, \tag{5.83}$$

$$s_{OAC} = -4.439 \text{ sec}^{-1}, \tag{5.84}$$

while the resulting perturbation parameter is

$$\epsilon = 0.0247. \tag{5.85}$$

We see that these results meet the specifications of Section 5.3. Therefore, the MIMO

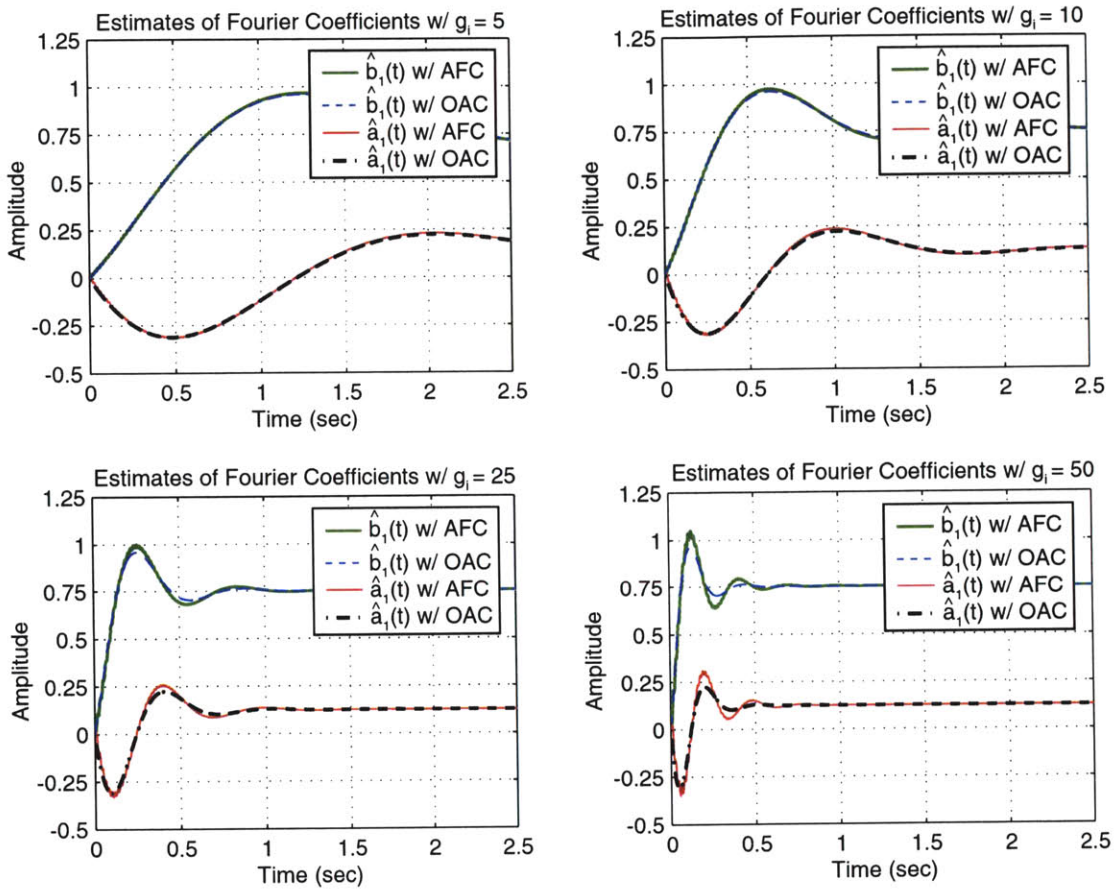

Figure 5-19: Comparison of the estimates of the Fourier coefficients $\hat{a}_1(t)$ and $\hat{b}_1(t)$ of the disturbance signal $d_1(t)$ using AFC and OAC, without the phase advance parameter ($\phi_i = 0$).

OAC perspective can be used to predict the dynamics of the entire single resonator AFC system quite well.

Figure 5-19 compares the transient responses for the estimates of the Fourier coefficients, $\hat{a}(t)$ and $\hat{b}(t)$, using the exact time simulation of the single resonator AFC system and simplified oscillator amplitude control system, with $g_i = 5$, 10, 25, and 50. Without the phase advance parameter implemented (*i.e.*, $\phi_i = 0$), we see that $\hat{a}_1(t)$ and $\hat{b}_1(t)$ show an oscillatory response. There even appears to be a RHP zero in the dynamics of $\hat{b}_1(t)$. Notice though, in Figure 5-19, as we increase the AFC gain g_i, the predicted $\hat{a}(t)$ and $\hat{b}(t)$ curves from the decoupled and simplified sine and cosine

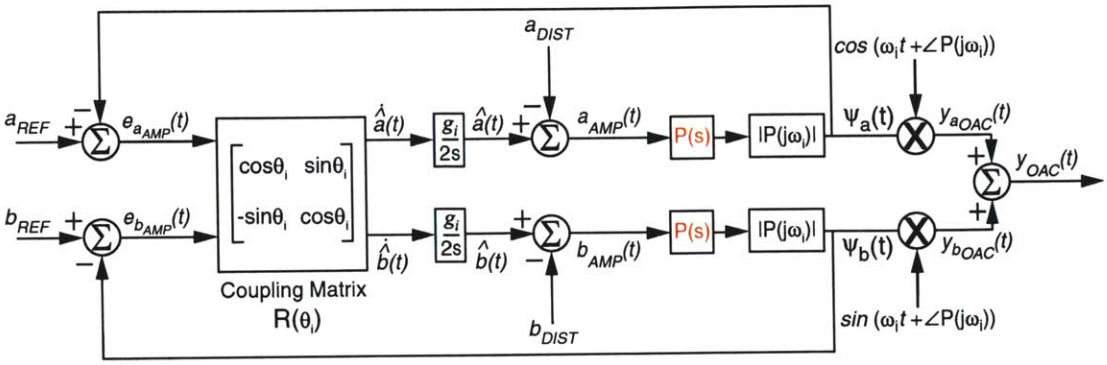

Figure 5-20: Altered closed-loop block diagram for the single resonator AFC system viewed as a multiple-input multiple-output (MIMO) oscillator amplitude control system. A model of the plant has been added to the sine and cosine OAC loops.

OAC simulations deviate from the exact time simulations of the single resonator AFC system. Thus, we decided to add the plant transfer function into the OAC loops, as done previously in Section 5.2, and repeat the simulations with the four g_i values.

Figure 5-20 illustrates the altered closed-loop block diagram for the single resonator AFC system viewed from an oscillator amplitude control perspective, with the addition of the plant transfer function in the sine and cosine OAC loops, while Figure 5-21 compares the resulting estimates of the Fourier coefficients. The altered state-space model of the complete MIMO OAC system is given in Appendix J. We see that the resulting transient responses show the same oscillatory behavior as Figure 5-19, but as g_i increases, the OAC curves do not diverge from the exact time simulations nearly as much. Thus, as the bandwidth of the OAC loops increases, the validity of the results in (5.12) become less accurate. An explanation of these results is provided below.

As mentioned previously in Section 5.1, for sufficiently low g_i values, the output of the AFC closed-loop is given by

$$y_b(t) \cong b_{AMP}(t)|\mathrm{P}(j\omega_i)|\sin(\omega_i t + \phi_i). \tag{5.86}$$

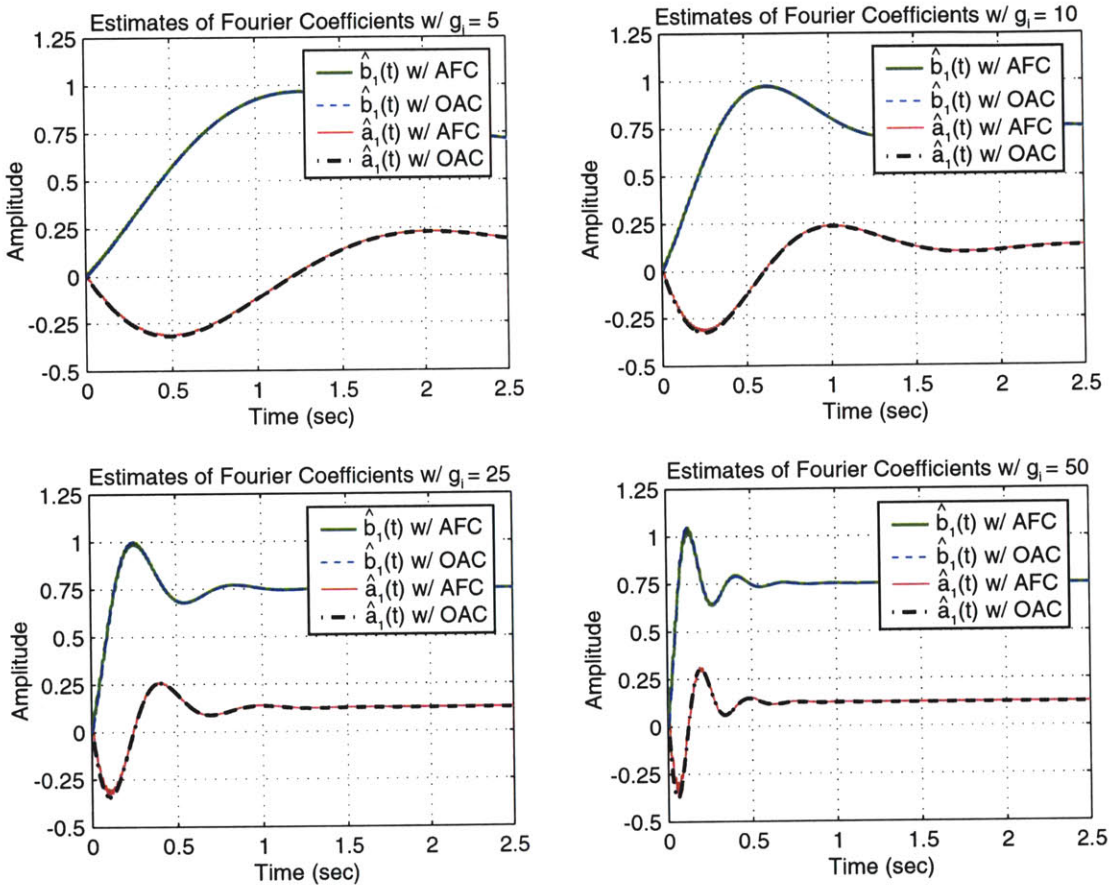

Figure 5-21: Comparison of the estimates of the Fourier coefficients $\hat{a}_1(\mathrm{t})$ and $\hat{b}_1(\mathrm{t})$ of the disturbance signal $d_1(\mathrm{t})$ using AFC and OAC without the phase advance parameter ($\phi_i = 0$). These curves correspond to the altered OAC loops with the additional plant model.

However, as the time-variation of b_{AMP}(t) increases (bandwidth of the sine channel OAC loop increases), the output of (5.86) becomes less accurate. This is due to the assumptions made in the derivation.

In deriving (5.86), we assumed that the control input to the plant was given by

$$\delta_b(t) = \sin(\omega_i t)\sin(\alpha t) = \frac{1}{2}\left[\cos(\omega_i - \alpha)t - \cos(\omega_i + \alpha)t\right], \tag{5.87}$$

where $\alpha \ll \omega_i$. Thus, the magnitude and phase of the frequency response $\mathrm{P}(j(\omega_i \pm \alpha))$ are approximately given by

$$|\mathrm{P}((j\omega_i \pm \alpha))| \approx |\mathrm{P}(j\omega_i)|, \tag{5.88}$$

$$\angle\mathrm{P}((j\omega_i \pm \alpha)) \approx \angle\mathrm{P}(j\omega_i). \tag{5.89}$$

Figure 5-22 illustrates the Fourier spectrum of the AFC closed-loop output y_b(t), assuming the amplitude dynamics of the control input δ_b(t) are amplitude modulated by a low-frequency sinusoid. We see that this spectrum consists of magnitude attenuated and phase shifted cosine spectrums, centered about $+\omega_i$ and -ω_i. As the frequency of the low-frequency sinusoid α increases, the distances between $\pm\omega_i$, $\pm\omega_A$, and $\pm\omega_B$ increase. Also, the accompanying plant magnitude attenuation and phase shifts increase. Thus, for a large α, the results of (5.88) and (5.89) become less accurate, since the resulting frequency response $\mathrm{P}(j(\omega_i \pm \alpha))$ contributes considerably more magnitude attenuation and phase shift to the cosine spectrums.

Figure 5-23 compares the estimates of the Fourier coefficients for the original sine and cosine OAC loops, once the proper phase advance parameter ($\phi_i = \angle\mathrm{P}(j\omega_i)$) has been implemented, while Figure 5-24 shows the same plots when the additional plant model is added to the OAC loop transmission. All of these curves illustrate a dominant first order response, due to an approximate 90° of phase margin. However, upon closer inspection of the predicted $\hat{a}_1$(t) and $\hat{b}_1$(t) curves in the original OAC

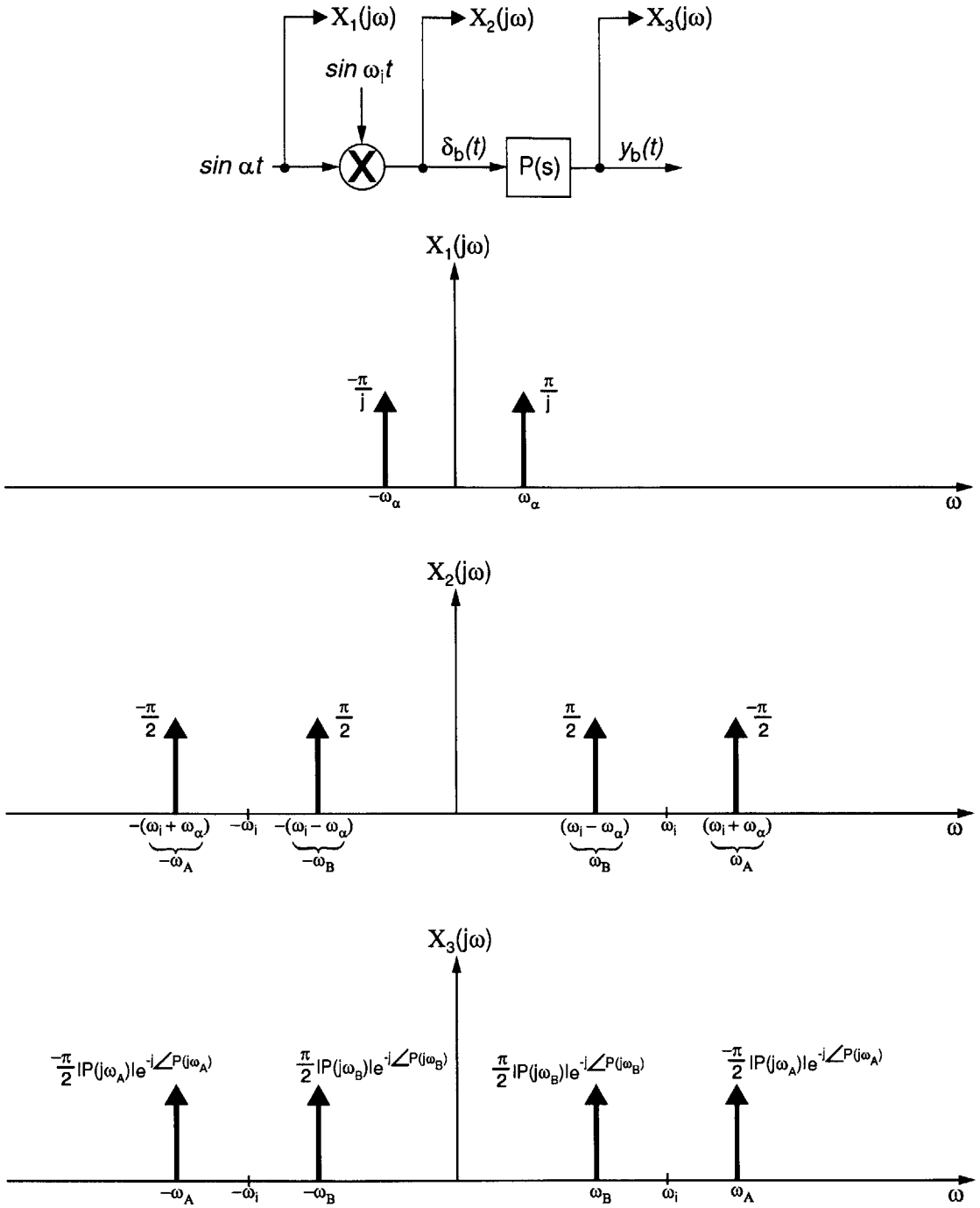

Figure 5-22: Fourier Spectrum of the simplification of the closed-loop block diagram for the sine channel of the single resonator AFC system, assuming the amplitude dynamics of the control input $\delta_b(t)$ are amplitude modulated by a low-frequency sinusoid.

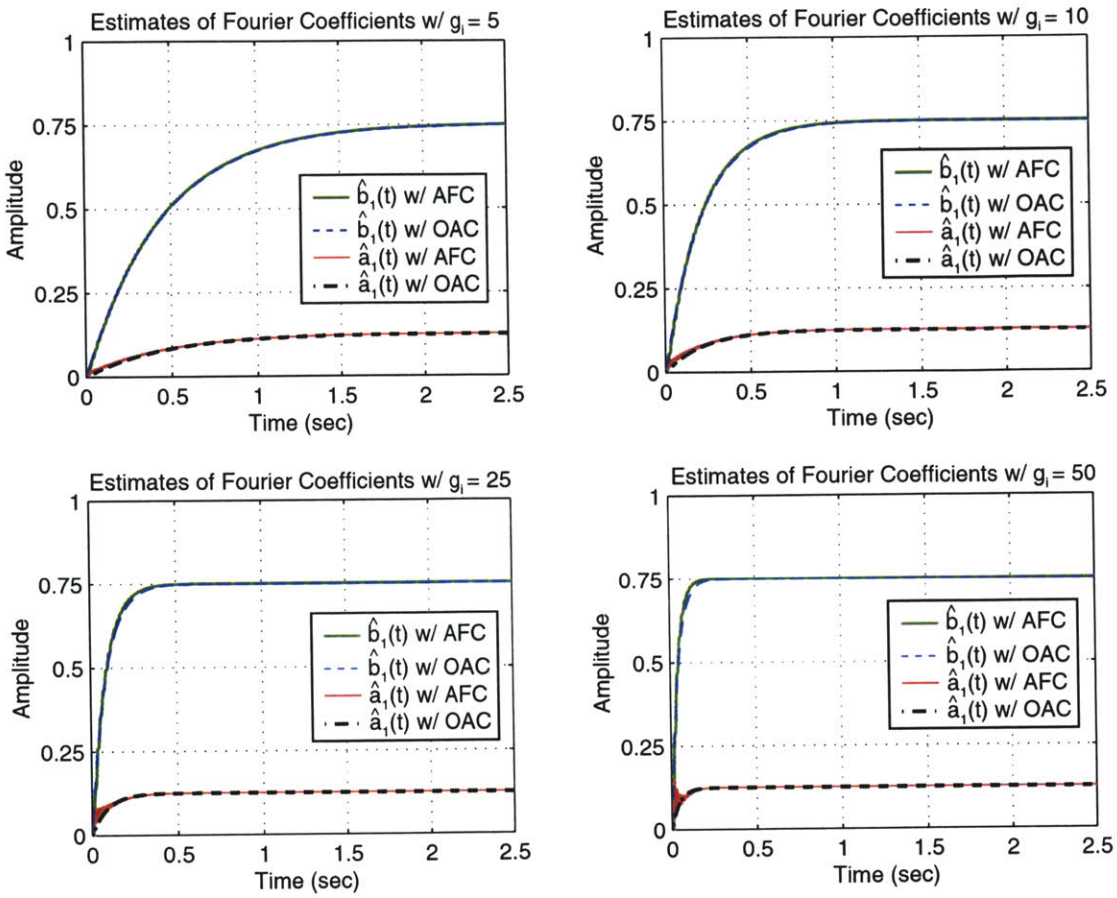

Figure 5-23: Comparison of the estimates of the Fourier coefficients $\hat{a}_1(\mathrm{t})$ and $\hat{b}_1(\mathrm{t})$ of the disturbance signal $d_1(\mathrm{t})$ using AFC and OAC with the phase advance parameter ($\phi_i = \angle \mathrm{P}(j\omega_i)$).These curves correspond to the altered OAC loops with the additional plant model.

model, we see slightly less agreement with the exact time simulations of the single resonator AFC system, for higher g_i levels. It should also be noted that we see the second harmonic appear in the initial $\hat{b}_1(\mathrm{t})$ responses. We speculate that this is due to the increased bandwidth of the OAC loop, which reduces low-pass filtering, and the additional plant phase shift, which couples the sine and cosine channel.

It appears from Figure 5-19 and Figure 5-23 that as g_i increases, the resulting OAC system phase margin decreases. The is most clearly seen in Figure 5-19, since the dynamics of estimates of the Fourier coefficients exhibit an apparent reduction in

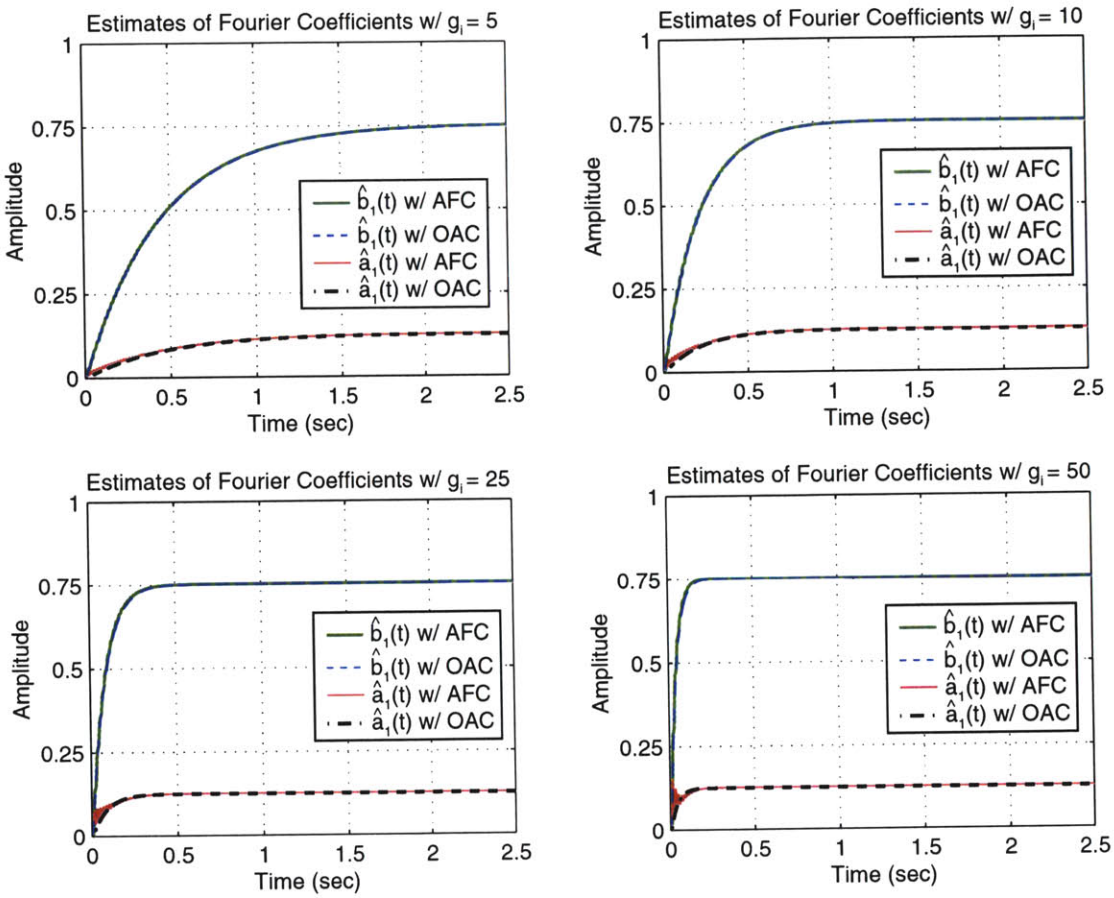

Figure 5-24: Comparison of the estimates of the Fourier coefficients $\hat{a}_1(t)$ and $\hat{b}_1(t)$ of the disturbance signal $d_1(t)$ using AFC and OAC with the phase advance parameter ($\phi_i = \angle P(j\omega_i)$).These curves correspond to the altered OAC loops with the additional plant model.

damping. Once we included the additional plant model P(s) to the sine and cosine OAC loops, the resulting $\hat{a}_1(t)$ and $\hat{b}_1(t)$ curves follow the exact time simulations of the single resonator AFC system much closer, even for larger g_i values.

As g_i increases, the sine and cosine OAC loop transmissions will observe additional magnitude attenuation and phase shift, due to the time varying characteristics of $\hat{a}_1(t)$ and $\hat{b}_1(t)$ as shown in Figure 5-22. However, due to time constraints, we were not able to develop a mathematical model for these findings but the results of including P(s) in the OAC loop show promising results. Thus, we leave this investigation for

future work.

The oscillatory behavior of $\hat{a}_1(t)$ and $\hat{b}_1(t)$, as seen in Figure 5-19 and Figure 5-21, is a direct result of the coupling between the sine and cosine channels of the single resonator AFC system, due to the phase of P(s) at the resonator frequency ($\angle P(j\omega_1) = -64.69^o$). The averaging analysis performed by Sacks *et al* [26] on the single resonator AFC system, derived in Section 2.2.5, shows that the averaged system eigenvalues (without ϕ_i) are given by

$$\lambda_{1,2} = -\frac{g_i|P(j\omega_i)|}{2}\left[\cos(\angle P(j\omega_i)) \pm j\sin(\angle P(j\omega_i))\right]. \tag{5.90}$$

These eigenvalues provide an approximate measure of the dynamics of the estimates of the Fourier coefficients.

Equation (5.90) shows that as $\angle P(j\omega_i) \longrightarrow -\frac{\pi}{2}$, $\hat{a}_1(t)$ and $\hat{b}_1(t)$ will experience a more under-damped response. In theory, when $|\angle P(j\omega_i)| = \frac{\pi}{2}$, the averaged eigenvalues lie on the imaginary-axis and the estimates of the Fourier coefficients will oscillate. If

$$-\frac{3\pi}{2} < \angle P(j\omega_i) < -\frac{\pi}{2}, \tag{5.91}$$

the averaged system eigenvalues lie in the RHP and the AFC and OAC system is unstable. However, when $\angle P(j\omega_i) = 0^o$, then the averaged system eigenvalues coalesce on the LHP real-axis. Sacks *et al* state that for this particular case, the responses of the estimates of the Fourier coefficients are critically damped. We have determined that $\hat{a}_1(t)$ and $\hat{b}_1(t)$ actually experience equivalent dominant first order responses, where the dominant poles are approximated by (5.28). Figure 5-23 and Figure 5-24 show than once the phase advance parameter is implemented ($\phi_i = \angle P(j\omega_i)$), the phase of the plant is essentially eliminated and $\hat{a}_1(t)$ and $\hat{b}_1(t)$ undergo a dominant first order response.

Figure 5-25 illustrates an example of the root contour of the averaged system

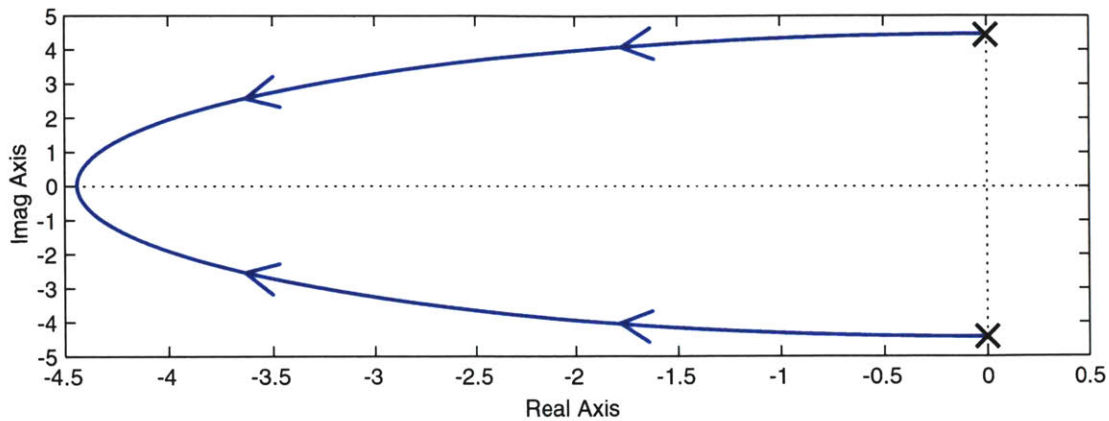

Figure 5-25: Sample root contour of a single resonator AFC system's averaged system eigenvalues as $\angle P(j\omega_i)$ is varied from $\pm\frac{\pi}{2}$ to 0°.

eigenvalues for the single resonator AFC system when the phase of the plant is varied between $-\frac{\pi}{2}$ and 0°. As $\angle P(j\omega_i) \longrightarrow 0^o$, the real part of the eigenvalues move further into the LHP and the imaginary part approaches zero. If $\angle P(j\omega_i) = 0^o$, equation (5.90) has a zero imaginary component and the largest negative real value, which corresponds to the shortest convergence time. This result is equivalent to (2.159), where the averaging analysis takes into account the phase advance parameter $\phi_i = \angle P(j\omega_i)$.

As stated previously in Section 2.2.3, the proper choice of phase advance parameter essentially inverts the phase of the plant at the resonator frequency. This means that ϕ_i decouples the MIMO OAC system and produces critically damped averaged system eigenvalues for the single resonator AFC system, regardless of the phase of the plant. The phase advance parameter eliminates the oscillatory $\hat{a}_1(\mathrm{t})$ and $\hat{b}_1(\mathrm{t})$ responses and produces the fastest closed-loop convergence time. Also, the decoupled oscillator amplitude control loops each exhibit approximately 90° of phase margin and are robust to modelling errors in the phase of the plant transfer function by as much as $\pm\frac{\pi}{2}$ before the feedback loops become unstable.

Figure 5-26 illustrates the transient response of the plant output y(t) to the dis-

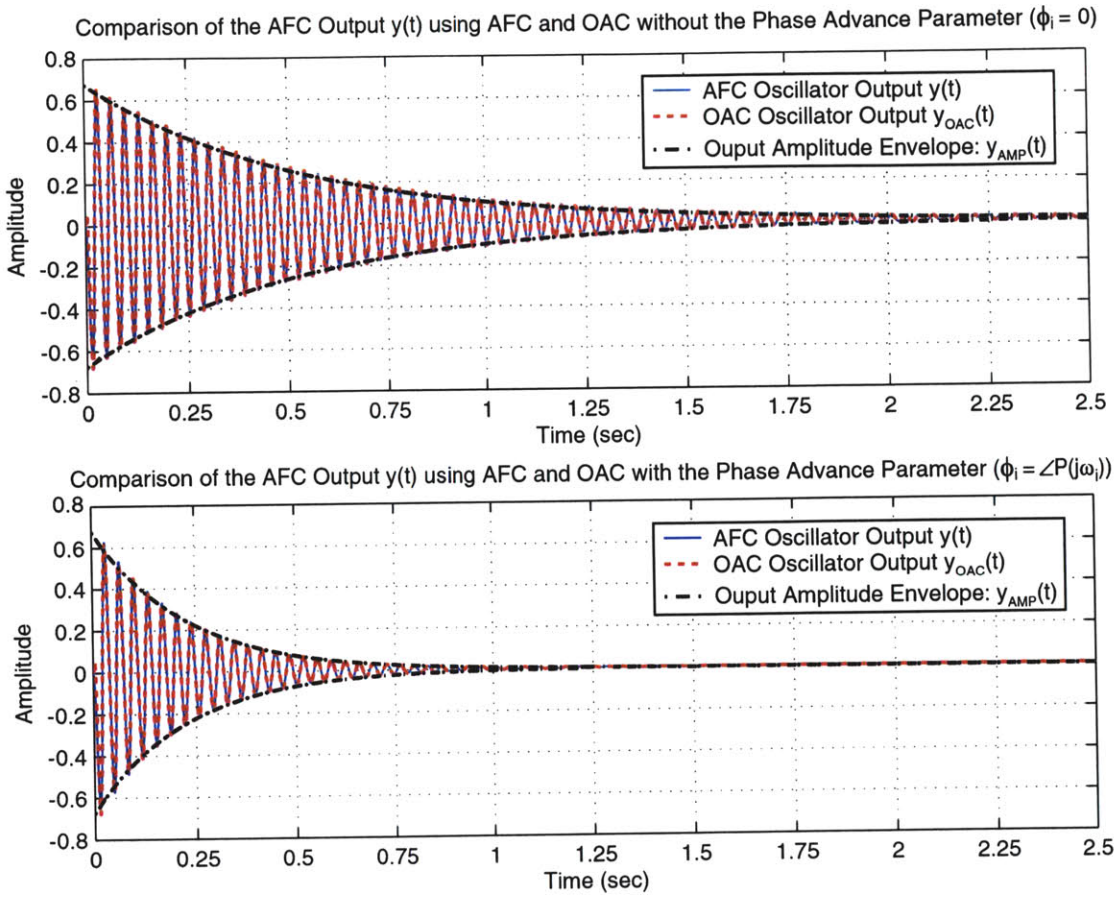

Figure 5-26: Comparison of the plant output y(t) using AFC and OAC with and without the phase advance parameter ϕ_i implemented. The first order amplitude decay envelope y_{AMP}(t) is also included in the plots.

turbance signal d_1(t). This figure includes the simulated AFC, OAC, and dominant first order amplitude decay envelope output with and without the addition of the phase advance parameter. These plots show close agreement between the AFC and OAC curves, as well as good correlation with the dominant first order amplitude decay envelope. Since this example includes the output of both the sine and cosine channels of the single resonator AFC system, the amplitude output decay envelope is given by

$$y_{AMP}(t) = y_{AMP}(0)e^{s_{OAC}t}, \tag{5.92}$$

where s_{OAC} is defined by (5.28) or (5.34) (depending on whether or not the proper choice of phase advance parameter is implemented) and

$$y_{AMP}(0) = |P(j\omega_i)|\sqrt{a_{AMP}{}^2 + b_{AMP}{}^2}. \tag{5.93}$$

These results show that under the assumptions described in Section 5.1, we can approximate the dynamics of the single resonator AFC system by using the MIMO oscillator amplitude control perspective. Also, we can obtain a good approximation of the convergence properties by using the dominant OAC closed-loop poles. This analysis can easily be expanded to analyze an AFC system designed to follow/reject more than one frequency, as described in the following section.

5.4.2 Multiple Resonator AFC System viewed from an OAC Perspective

In order to view a multiple resonator AFC system from an oscillator amplitude control perspective, we look at each AFC resonator individually, analyze those particular amplitude dynamics, and then use superposition to approximate the entire closed-loop response. For a multiple resonator AFC system designed to follow/reject N frequency components, there exist 2N estimates of Fourier coefficients with N values of g_i, ω_i and ϕ_i. Implementing the phase advance parameter ($\phi_i = \angle$ P(jω_i)) effectively decouples the system into 2N individual OAC loops, where the dynamics of the sine and cosine channels of each AFC resonator are identical and characterized by (5.28). Thus, the entire approximate amplitude error envelope is given by

$$e_{AMP}(t) \approx \sum_{i=1}^{N} e_{AMP_i}(0)e^{s_{OAC_i}t}. \tag{5.94}$$

Let's re-analyze the previous oscillator amplitude control example but change the AFC controller design to to follow a periodic reference signal of the form

$$r_A(t) = \sum_{i=1}^{3} \left[a_i \cos(\omega_i t) + b_i \sin(\omega_i t)\right], \tag{5.95}$$

where a_i, b_i, and ω_i are listed in Table 5.1. This requires placing three AFC resonators in parallel and setting $\phi_i = \angle P(j\omega_i)$ for each resonator. Again, for this example, we use the simplified second order plant model given by

$$P(s) = \frac{\omega_n^2}{s^2 + 2\zeta\omega_n s + \omega_n^2}, \tag{5.96}$$

where the parameters are selected as $\omega_n = 250$ rad/sec and $\zeta = \frac{\sqrt{2}}{2}$. Table 5.2 provides the values of each resonator's proportional gain, frequency, and phase advance parameter. The g_i values are arbitrarily chosen for this example and do not necessarily optimize the closed-loop system response.

r_A(t) Parameters			
i	a_i	b_i	ω_i (rad/sec)
1	1	0.75	150
2	0.5	0.375	200
3	0.25	0.125	250

Table 5.1: Listing of the parameters for the periodic reference input signal r_A(t).

AFC Resonator Parameter Vaues			
i	g_i	ϕ_i	ω_i (rad/sec)
1	10	-52.97^o	150
2	15	-72.35^o	200
3	20	-90°	250

Table 5.2: List of proportional gains, resonator frequencies, and phase advance parameters for the multi-resonator AFC system designed to follow r_A(t).

The simulated negative of the loop transmission frequency response is shown in Figure 5-27 while Table 5.3 lists all of the perturbation parameters and approximate

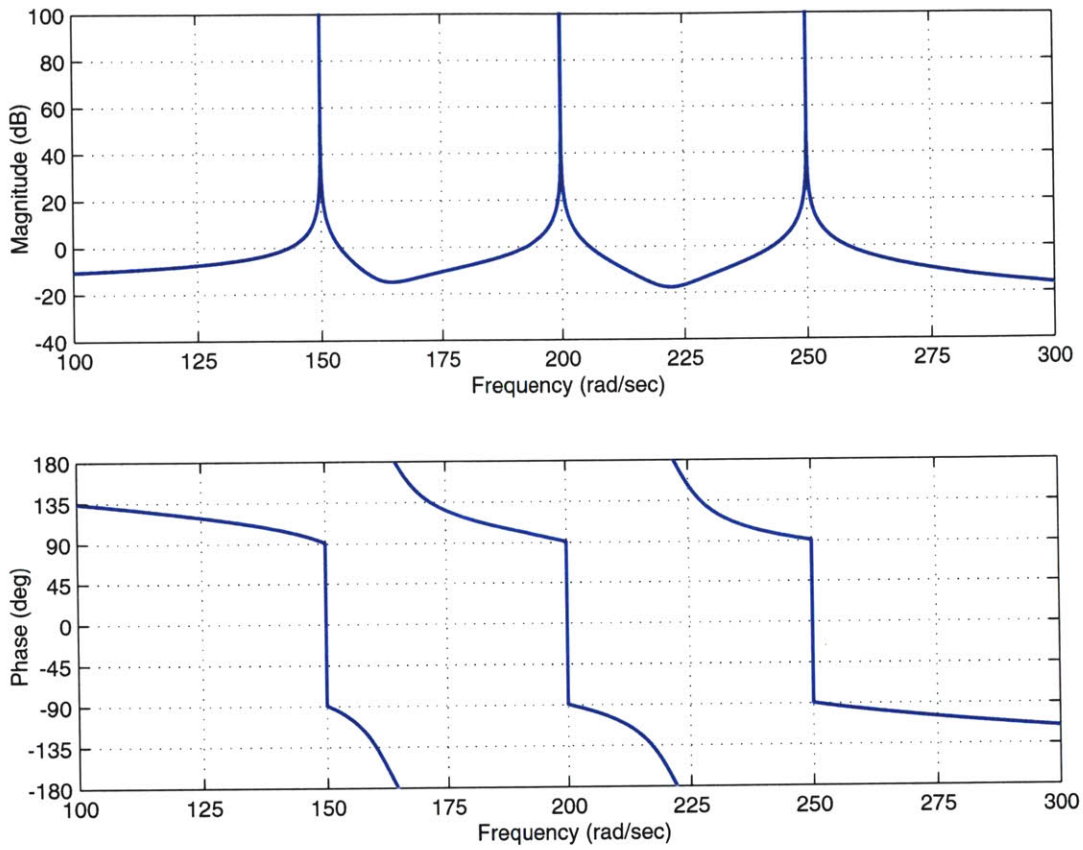

Figure 5-27: Simulated negative of the loop transmission for the multi-resonator AFC system designed to follow $r_A(\mathrm{t})$.

dominant oscillator amplitude control closed-loop pole locations. Since all of the ϵ and s_{OAC} values meet the specifications of Section 5.3, this multi-resonator AFC system can be approximated by a 2N loop OAC system.

Figure 5-28 compares two closed-loop AFC error signals to the resulting OAC amplitude error envelope $e_{AMP}(\mathrm{t})$. The first curve simulates the error signal of the entire multiple resonator AFC system designed to follow $r_A(\mathrm{t})$, while the second curve equals the superposition of the three individual AFC error signals. The second simulation views the reference signal $r_A(\mathrm{t})$ as a summation of three frequency components, where three separate single resonator AFC controllers are required to achieve zero steady-state tracking error. We simulate the transient response of each single resonator AFC

ϵ & s_{OAC} Values		
i	ϵ	s_{OAC}
1	0.0314	-4.704
2	0.0316	-6.317
3	0.0283	-7.071

Table 5.3: List of perturbation parameters and approximate dominant oscillator amplitude control closed-loop poles for the three AFC resonator frequencies.

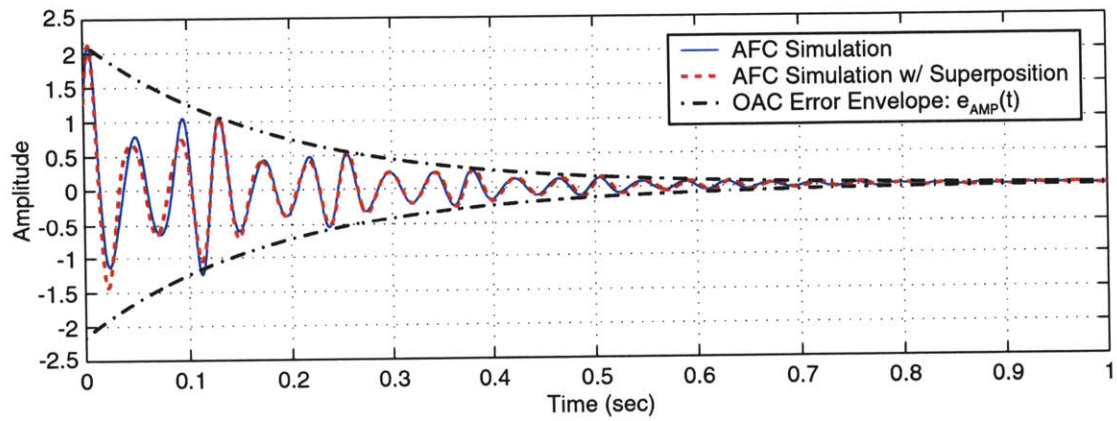

Figure 5-28: Closed-loop system error signal e(t) for the multi-resonator AFC controller designed to follow r_A(t). This figure compares e(t) for the entire closed-loop system to the approximate error signal when taking the superpostion of each resonator's error signal.

system to the associated reference input signal and use superposition to approximate the entire closed-loop response to r_A(t).

Essentially, we view the reference signal as

$$r_A(t) = r_{A_1}(t) + r_{A_2}(t) + r_{A_3}(t), \tag{5.97}$$

where the resulting error signal is given by

$$e(t) = e_1(t) + e_2(t) + e_3(t). \tag{5.98}$$

Each component of the error signal corresponds to a single resonator AFC system

designed to follow each frequency component of the periodic reference input signal (Table 5.2 lists each AFC resonator's parameters). The superposition of $e_1(t)$, $e_2(t)$, and $e_3(t)$ approximates the entire multi-resonator response fairly well but there are small discrepancies between the two curves.

Figure 5-29 compares the transient responses of each single resonator AFC system to the complete multi-resonator AFC system. We see that the dynamics of the single resonator AFC systems dominate the transient responses but the dynamics of the other two resonators in the multi-resonator system also have an observable effect on the overall response. These differences are relatively small and do not have a considerable affect on the amplitude error envelope. As a result, we approximate the N AFC resonator system as the superposition of N single resonator AFC systems and proceed to simplify the loop into the superposition of 2N OAC systems.

Figure 5-30 compares the transient responses of the multi-resonator system viewed as the superposition of N single resonator AFC controllers to the superposition of 2N OAC systems. Since the multi-resonator AFC system has relatively small perturbation parameters and approximate dominant OAC closed-loop poles (see Table 5.3), the oscillator amplitude control perspective predicts the AFC error response very well. This means that we can use (5.94) to approximate the dynamics of the AFC amplitude error envelope.

Figures 5-28 and 5-30 include the OAC amplitude error envelope $e_{AMP}(t)$ for the multi-resonator AFC system. These plots show that (5.94) does not characterize all of the underlying system dynamics. Depending on the frequency and phase difference between the individual error signals (*i.e.*, $e_1(t)$, $e_2(t)$, and $e_3(t)$) the actual envelope can be greater or less than $e_{AMP}(t)$. However, equation (5.94) does provide a good approximation of the convergence properties of the amplitude decay envelope.

The results of the previous example show that under certain approximations, we can obtain a fairly good approximation of the convergence properties of an N

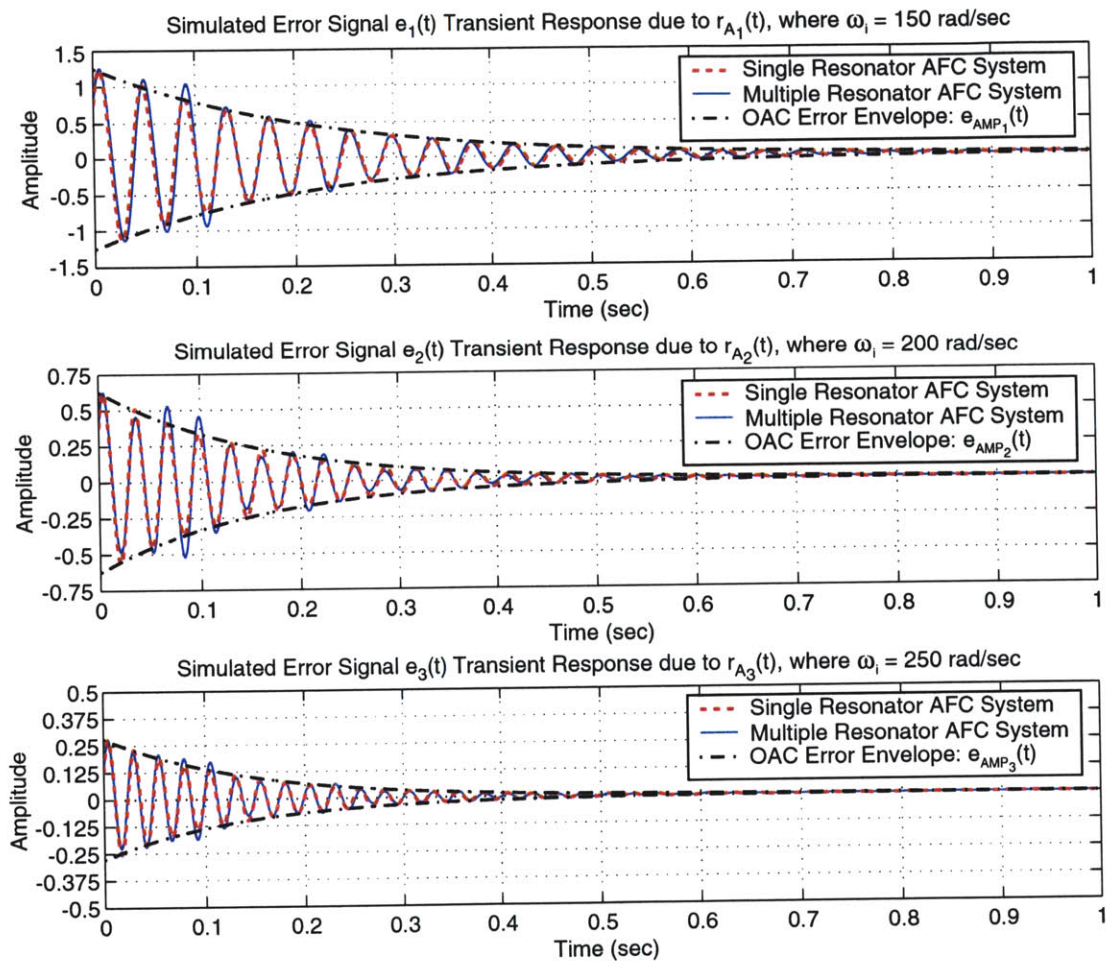

Figure 5-29: Comparison of the transient responses of the closed-loop system error signal e(t) due to each frequency component of the reference input signal r_A(t). The comparison is between each single resonator AFC system used to approximate the entire system output through superposition and the entire multi-resonator AFC system.

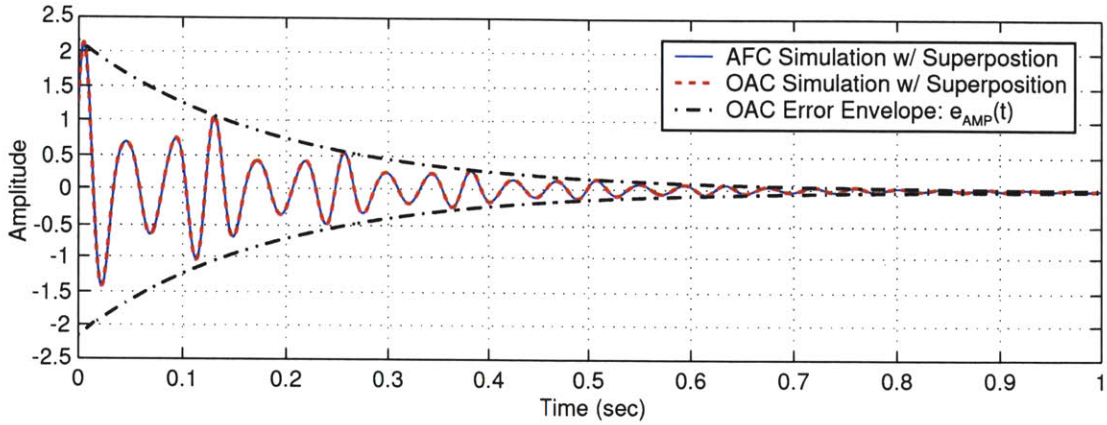

Figure 5-30: Comparison of the closed-loop system error signal e(t) using AFC with superposition versus the OAC perspective with superposition.

resonator AFC system with 2N OAC systems. Up to now, we have only investigated the AFC closed-loop response to constant amplitude reference and disturbance signals. In the following section, we investigate the AFC closed-loop response to reference/disturbance signals which consist of time-varying amplitude or frequency components.

5.5 Error Properties of AFC viewed from an OAC Perspective

In the previous analyses, we simulated the transient responses of various AFC systems to constant amplitude reference/disturbance inputs. We determined, in Chapter 2, that an AFC controller will provide zero steady-state error to either one of these signals, and we can use s_{OAC} to determine the approximate convergence properties. However, once the reference/disturbance signal consists of time-varying amplitude or frequency components, a conventional AFC controller can not completely eliminate the error signal. Analogous to the results of Section 4.2.3, we can use the OAC perspective of AFC to analyze the closed-loop response to time-varying amplitude

and/or frequency components, and provide an approximate measure of the size of the amplitude error envelope. We illustrate these results with the following example.

5.5.1 Example of a Single Resonator AFC System with Time-Varying Input Amplitude Components

In this example, we repeat the single resonator AFC controller simulation from Section 5.4.1, except we now study the steady-state error properties of the closed-loop system to a disturbance input given by

$$d_2(t) = a_2 \cos(\omega_2 t) + b_1 \sin(\alpha t) \sin(\omega_2 t), \tag{5.99}$$

where the parameters are selected as $\omega_2 = 180$ rad/sec, $a_2 = \frac{1}{8}$, $b_2 = \frac{1}{4}$, and $\alpha = 15$ rad/sec. From an oscillator amplitude control perspective, the inputs into the sine and cosine OAC loops are

$$a_{REF} = b_{REF} = 0, \tag{5.100}$$

$$a_{DIST} = \frac{1}{8}, \tag{5.101}$$

$$b_{DIST} = \frac{3}{4} \sin(15t) \text{ rad/sec.} \tag{5.102}$$

Since the previous example with these same design parameters met the specifications of Section 5.3, we can use the MIMO OAC perspective to predict the dynamics of the single resonator AFC system. For this example, we implement the proper phase advance parameter ($\phi_i = \angle P(j\omega_2)$), and analyze the transient response of the closed-loop for $g_i = 10$, 25, 50, and 75.

Figure 5-31 compares the error signal of single resonator AFC system, as predicted by the superposition of the decoupled and simplified sine and cosine OAC loops, to the exact time simulation generated by the algorithm in Figure 5-1. Notice, we have

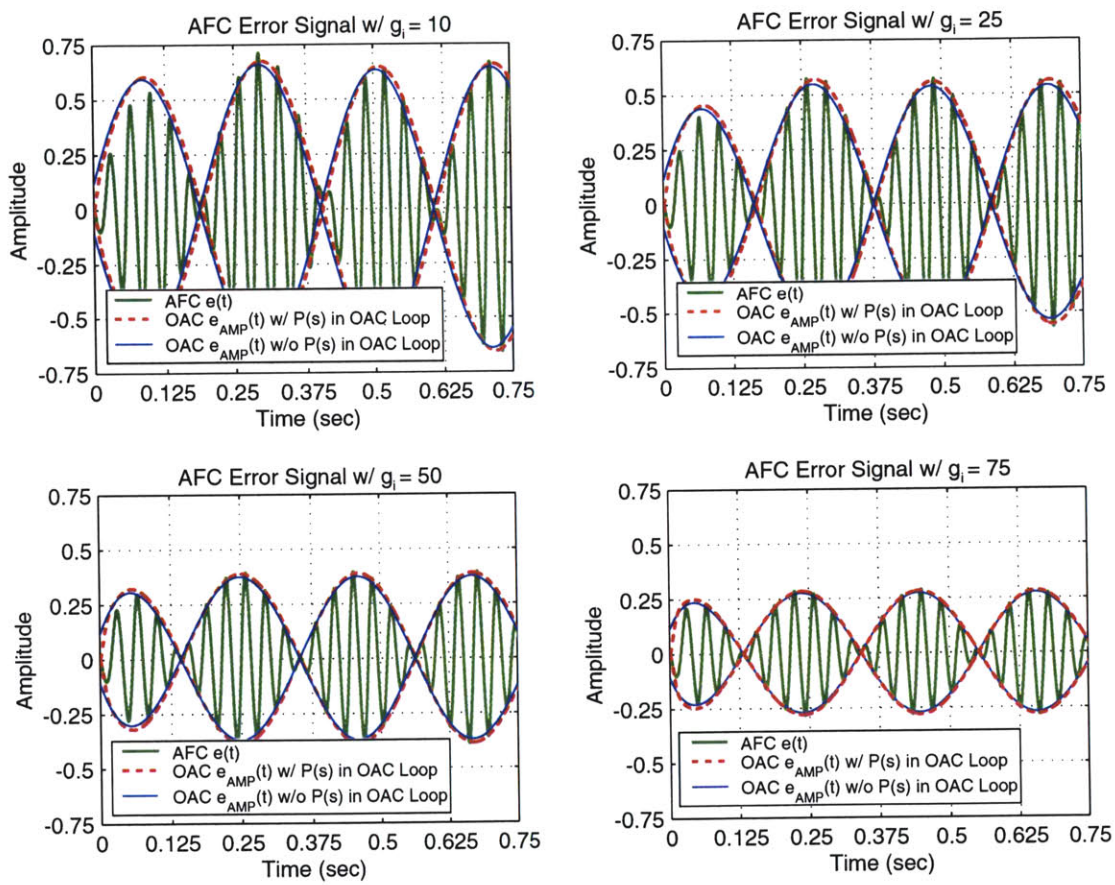

Figure 5-31: Comparison of the closed-loop system error signal using our OAC perspective to the exact time simulation of the single resonator AFC system. Notice, we have included the OAC error signal with and without the addition of the plant transfer function to the OAC loops.

included the resulting e_{AMP}(t) curves with and without the addition of P(s). We see that for this particular case, the OAC perspective provides a good approximation of AFC amplitude error envelope. It also appears that the inclusion of the plant transfer function provides a more accurate representation of the actual system response. This observation re-emphasizes the need for further investigation into a more detailed model of our OAC perspective.

Figure 5-31 shows that there is an inverse relationship between g_i and the AFC steady-state error decreases, as shown previously in Section 2.2.5. However, viewing the AFC loop from an OAC perspective lets us approximate the trajectory following and/or disturbance rejection properties directly with the OAC loop transmission. For example, with $g_i = 50$, the negative of the loop transmission and transfer function relating E(s) to D(s) (with the addition of P(s) in the OAC loop) are given by

$$\begin{aligned} -L(s) &= \frac{g_i\omega_n^2|P(j\omega_i)|}{2s(s^2+2\zeta\omega_n s+\omega_n^2)}, \\ &= \frac{13.87\times 10^{5LT}}{s(s^2+353.55s+625000)}, \end{aligned} \tag{5.103}$$

$$\begin{aligned} \frac{E(s)}{D(s)} &= \frac{2\omega_n|P(j\omega_i)|s}{2s^3+4\zeta\omega_n s^2+2\omega_n^2 s+g_i|P(j\omega_i)|\omega_n^2}, \\ &= \frac{55487.34s}{s^3+353.55s^2+62500s+13.87\times 10^5}. \end{aligned} \tag{5.104}$$

Figure 5-32 and Figure 5-33 illustrate the corresponding calculated frequency responses. We see that the negative of the loop transmission frequency response predicts a 22 rad/sec crossover frequency, 24 dB gain margin and approximately 83° of phase margin. Thus, this particular system provides some disturbance rejection to d_2(t) but since α is close to the bandwidth of the OAC loop, there is an appreciable steady-state error. For $g_i = 10$ and $g_i = 25$, α actually exceeds the bandwidth of the OAC loops, and hence produces even poorer disturbance rejection. As a result of these observations, we always want to try and keep the time-variations of the

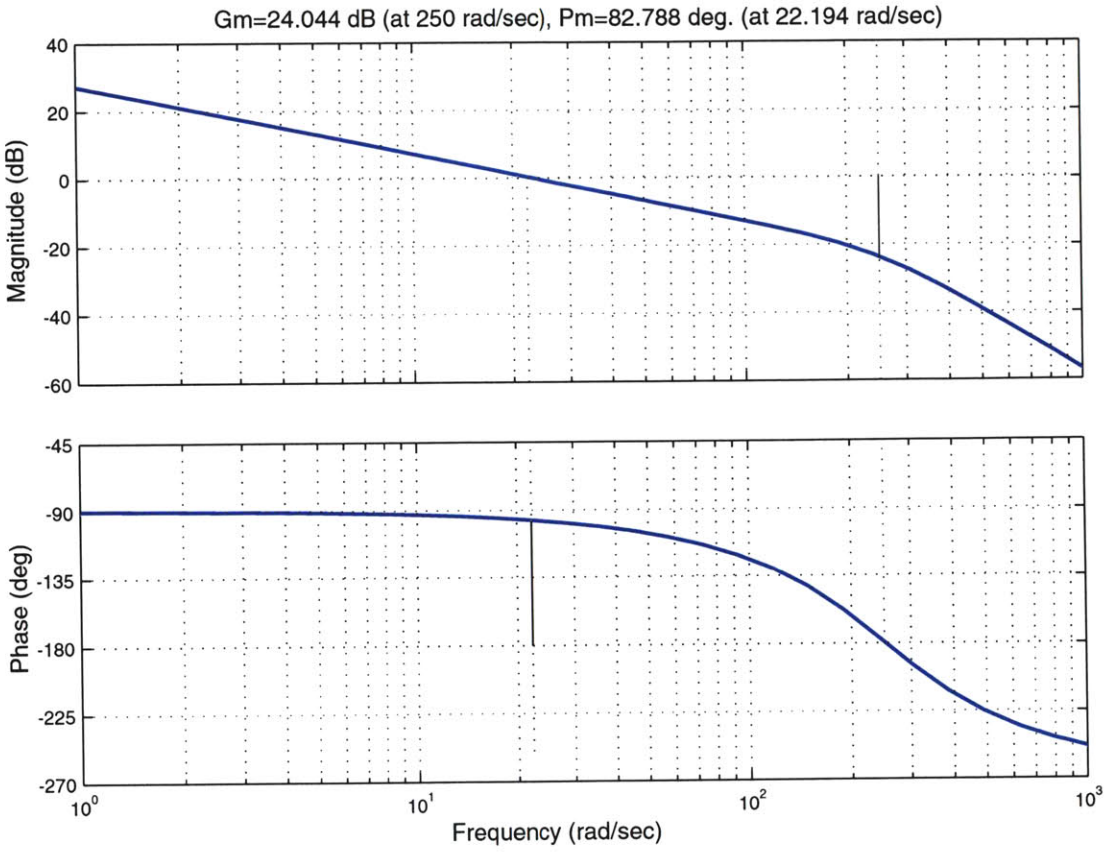

Figure 5-32: Calculated negative of the loop transmission frequency response for the decoupled and simplified sine and cosine OAC loops. Here, the plant P(s) has been added to the feedback loops.

reference/disturbance input below the bandwidth of the OAC loops. This involves maximizing the gains at different resonator frequencies and keeping the machining feedrate as slow as possible.

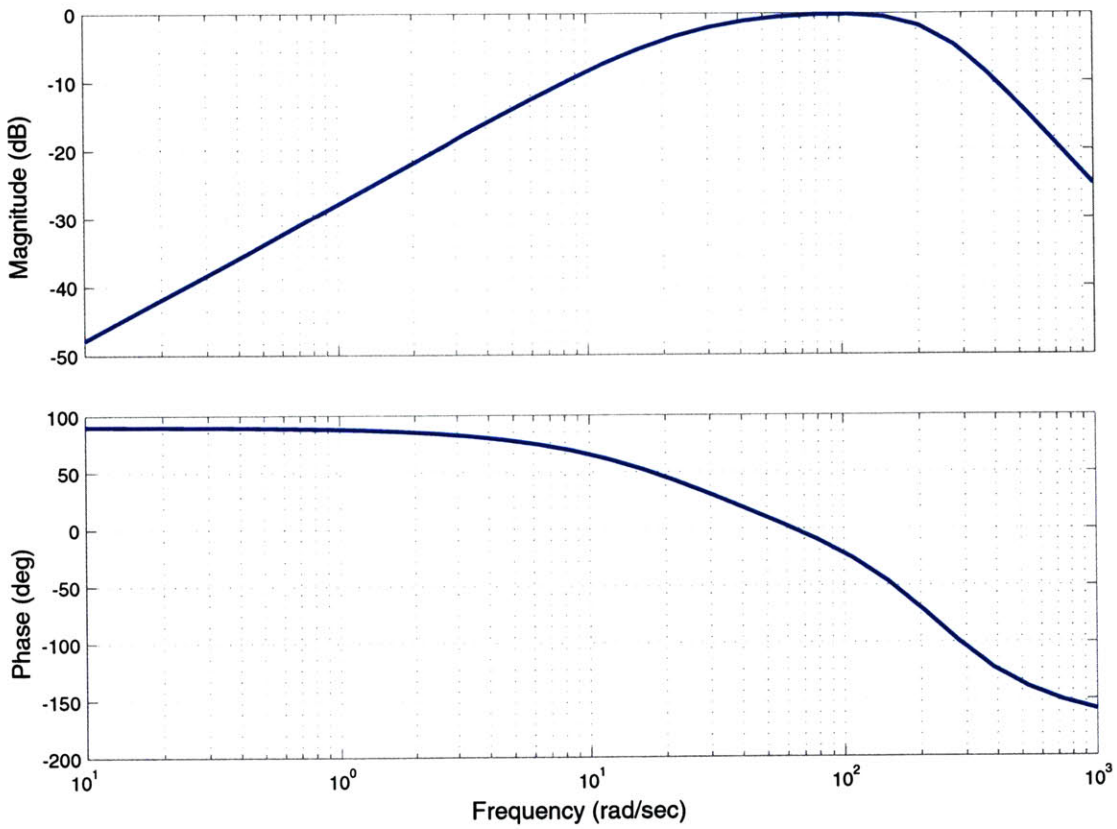

Figure 5-33: Calculated frequency response for $\frac{E(s)}{D(S)}$. Here, the plant P(s) has been added to the feedback loops.

5.6 Summary

In summary, this chapter described our method of viewing Adaptive Feedforward Cancellation from an oscillation amplitude control perspective. We looked at the sine and cosine channels of the AFC algorithm as two OAC loops, coupled by the phase of the plant evaluated at the resonator frequency. With the proper choice of the phase advance parameter, these loops are effectively decoupled, yielding equivalent OAC loops which operate independently. Under the assumptions that the bandwidth of the since and cosine OAC loops are much smaller that the plant bandwidth and resonator frequency ω_i, we can analyze the amplitude dynamics of these AFC loops alone, independent of the detailed time-variation of the sinusoids. From this viewpoint, we can approximate the convergence and error properties of Adaptive Feedforward Cancellation systems directly from the OAC loop transmission. This approach is very advantageous when we want to optimize the closed-loop performance of single and multiple resonator AFC systems.

Consider the example taken from Byl *et al* [6], as shown in Section 2.2.6. This example details the design of a multiple resonator controller for use on a rotary fast tool servo in diamond turning applications. Byl *et al* go through multiple gain-tuning iterations in order to try an optimize the closed-loop performance for several low-frequency harmonics. However they are not able to provide a rational measure of the convergence or error properties at these particular frequencies. Our OAC perspective allows direct examination of each resonator frequency, to determine the approximate AFC convergence and error properties of the entire closed-loop. Thus, if an AFC system experiences time-varying amplitude and/or frequency components (*i.e.*, most practical systems) our oscillator amplitude control approach can be used, along with the loop shaping method of Byl *et al*, to individually tune the resonator gains and achieve the maximum closed-loop performance, yet still provide adequate stability margins.

For example, one particular harmonic of the reference/disturbance signal may experience relatively large time-varying amplitude dynamics, while the adjacent harmonics do not. Thus, gain can be sacrificed at the adjacent resonator frequencies so that we can increase g_i at the frequency under question, which reduces this particular error component. The convergence time of the entire closed-loop may increase, which we can approximate with our OAC method, but the steady-state tracking error will be minimized to achieve optimal trajectory following.

In the next chapter, we summarize the work presented in thesis thesis and highlight some areas of possible future work.

Chapter 6

Conclusions and Suggestions for Future Work

6.1 Summary

This thesis described the theory and design of Adaptive Feedforward Cancellation control systems. We have focused primarily on the applicability of AFC for reducing/eliminating the steady-state tracking errors of fast tool servos in high-precision diamond turning applications. However, this particular algorithm is also well suited for applications such as hard disk and optical disk track following, vibration rejection in spindle and magnetic bearing systems, and camshaft and piston machining. In this thesis, we also summarized the loop-shaping method developed by Byl, Ludwick, and Trumper [6] for designing multiple resonator AFC controllers. We used this approach to experimentally implement a ten resonator AFC controller on a commercially-available fast tool servo using a PC-based digital control system. The results of these experiments showed a significant improvement in the FTS's steady-state tracking performance over conventional controller designs. Determination of the convergence and error properties of the closed-loop system to changes in the reference

or disturbance signal, though, were not an obvious output of these analyses. Thus, we developed a method of viewing Adaptive Feedforward Cancellation from an oscillator amplitude control perspective.

6.2 Suggestions for Future Work

During the course of this thesis, we gained valuable insight on the stability, robustness, and performance properties of Adaptive Feedforward Cancellation control systems. As mentioned previously, we experimentally implemented several AFC controllers on a commercially-available fast tool servo and showed that these designs work well in practice. Also, our perspective of AFC as an oscillator amplitude control system provided additional insight into the convergence and error properties of the closed-loop systems, for sufficiently low gains. There were several results, however, which we were not able to explain or did not have time to investigate further. Thus, we offer the following suggestions to improve upon our AFC controller designs and our view of AFC from an OAC perspective.

6.2.1 Variform FTS Experimental Controller Design

In Chapter 3, we detailed the complete design and implementation of several conventional and Adaptive Feedforward Cancellation controllers on the Variform FTS. We were able to achieve good results, though several improvements can be made to our designs to improve the closed-loop performance. In the following sections, we offer several suggestions.

Variform FTS On-Board Controller

During the initial experimental controller testing, we completely bypassed the Variform FTS's on-board controller, due to apparent controller instability. Thus, we

used a dSPACE 1102 controller board to conduct all of our closed-loop experiments. After performing some initial tests, we observed rather significant non-linear effects, as shown in Section 3.3, and decided to re-enable the inner charge loop. This loop attenuated the non-linear effects of the piezoelectric stacks in the FTS actuator, but it appears to have added some low-frequency dynamics to the experimentally plant transfer function, when compared to the fully open-loop plant dynamics. Further work should be done to investigate the design of this inner charge loop and possibly redesign it to have a higher bandwidth than the outer position loop. This change would greatly improve the long-term convergence properties of the entire closed-loop system.

Also, the LVDT DC offset circuit, mentioned previously in Section 3.1, should be integrated onto the amplifier interface board. This would allow the LVDT DC offset to be adjusted electronically, eliminating the time consuming task of opening up the FTS actuator and adjusting the offset mechanically.

Conventional Controller Design

While using the dSPACE 1102 board to implement our experimental control algorithms, and the on-board LVDT as the feedback sensor, we were able to achieve comparable closed-loop performance to the advertised on-board controller specifications. From our experimental results, it appears that this particular configuration can only achieve about a 200 Hz crossover frequency, due to the additional dynamics the LVDT and its associated electronics introduces to the system.

However, by switching the feedback to Kaman Instrumentation inductive sensor, we were able to achieve about a 400 Hz crossover frequency, as shown in Section 3.5.2. Thus, further work should be done to investigate the practical implementation of another feedback sensor on the Variform FTS (possibly the Kaman sensor) to push the mechanical limits of the closed-loop performance. Also, while performing the

conventional controller experiments, we observed rather significant noise from the LVDT sensor. Therefore, to achieve superior tracking performace, a much cleaner sensor should be implemented on the Variform FTS hardware. These changes would allow both higher bandwidth and lower noise propagation.

Adaptive Feedforward Cancellation Controller Design

While conducting the single and double resonator AFC controller experiments, described in Section 3.6.1 and Section 3.6.2, we were able to use the modulator/demodulator AFC algorithm in our experimental control designs. However, with the ten resonator system, we had to implement the design as a parallel of Internal Model Principle controller transfer functions, as described in Section 2.1.2. This is due the limited computing capacities of the dSPACE 1102 controller board, and the rather inefficient control algorithm C code we used.

In all of our controller experiments, we simply used Simulink's control system block-set and MATLAB's Real-Time-Workshop to design and implement all of the control algorithms. We did not spend any time trying to optimize our method of controller implementation nor size of the equivalent C code. Thus, future work would include determining the most computationally efficient method of implementing the AFC algorithm, as well as the command pre-shifting feedforward channel. This would reduce computing power requirements, and thereby allow higher achievable sampling rates, or the use of lower-cost controllers.

6.2.2 Adaptive Feedforward Cancellation

In this thesis, we showed that AFC essentially provides zero steady-state tracking error to a constant amplitude sinusoidal input signal. However, once the amplitude and/or frequency components include time-varying characteristics, the closed-loop system will develop a steady-state error signal. There are many times when

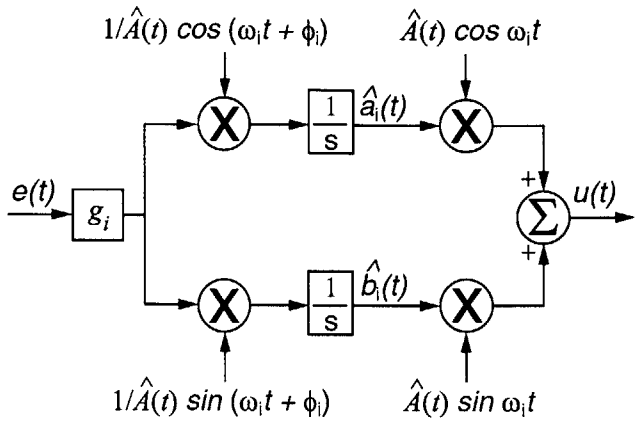

Figure 6-1: Amplitude Modulated Adaptive Feedforward Cancellation block diagram.

we know (or at least partially know) the time-varying characteristics of the reference/disturbance signal in diamond turning applications. Thus, we can use this information in a feedforward fashion to improve the AFC closed-loop steady-state tracking performance.

Amplitude Modulated Adaptive Feedforward Cancellation

Our lab has begun the development of a new form of AFC, known as Amplitude Modulated Adaptive Feedforward Cancellation (AMAFC), which uses the time-varying characteristics of the reference/disturbance signal to amplitude modulate the AFC algorithm. This work was started by Joe Calzaretta during the time that he was a student in the Precision Motion Control Laboratory.

This altered AFC configuration is based on the Internal Model Principle, as discussed in Section 2.1.1, which states that in order to achieve zero steady-state error to an input, the controller must include a model of that signal. Thus, AMAFC essentially adds a model of the time-varying amplitude and/or frequency components to the original AFC algorithm, and increases the trajectory following and disturbance rejection properties, under certain limited conditions.

Figure 6-1 illustrates the AMAFC algorithm in block diagram form, where $\hat{A}$(t)

represents the time-varying amplitude components. It is also feasible to vary the frequency ω_i to track, for instance, a varying spindle speed. As a cut progresses across a surface, the amplitude and phase of the trajectory change in a known way. It is advantageous to build this deterministic variation into the AFC controller. Future work on AMAFC would include determining the practical implementation of this particular configuration, general tuning rules, and the closed-loop stability, robustness, and performance characteristics.

6.2.3 Adaptive Feedforward Cancellation viewed from Oscillator Amplitude Ccontrol Perspective

In our development of AFC from an OAC perspective, we relied on several approximations to come to our final results. Specifically, we assumed that if the proper choice of the phase advance parameter was used, the sine and cosine channels of the AFC algorithm were effectively decoupled. This led to 2 independent feedback loops with equivalent dynamics. However, if the phase advance parameter is not 100% accurate, or if our plant model includes modelling errors, the sine and cosine OAC loops are actually coupled in a MIMO sense. We have shown in Section 5.4.1 that we can approximate the closed-loop convergence properties with the dominant OAC closed-loop poles, even if the proper phase advance parameter is not used. Also, we have shown in Section 5.5 that we can determine the AFC closed-loop steady-state error to signals with slowly time-varying amplitude and/or frequency components, once the proper phase advance parameter was implemented. However, if the sine and cosine channels are still coupled, the dynamics of the estimates of the Fourier coefficients, and steady-state error properties, cannot be accurately approximated without using MIMO control techniques. Thus, future work would include characterizing the dynamics of the sine and cosine channel OAC loops when they are still coupled. This perspective will provide an approximate measure of the dynamics of the estimates of

the Fourier coefficients, as well as the steady-state error properties, when the proper phase advance parameter is not chosen, or there are large modelling errors designed system.

Finally, while developing our simplified OAC model, we saw an improvement in the simulated closed-loop responses if we added an additional model of the plant to the feedback loops. We speculate that this is due to the magnitude attenuation and phase shift from the time-variations of the estimates of the Fourier coefficients, $\hat{a}(t)$ and $\hat{b}(t)$. We saw in Section 5.1 that as the gain g_i increased, the OAC model with the additional plant model provided more accurate results. Thus, further work needs to be done on determining the validity of using the additional P(s) transfer function in our OAC perspective.

6.3 Conclusions

The main contribution of this thesis is the development of viewing Adaptive Feedforward Cancellation from an oscillator amplitude control perspective. From this viewpoint, we can analyze the amplitude dynamics of the AFC loop alone, independent of the time-variation of the sinusoids. Thus, we can utilize classical control techniques to determine the stability, convergence, error, and robustness properties of AFC systems. More work needs to be done on viewing AFC from an OAC perspective, especially when the proper choice of phase advance parameter is not used. However, the results presented in this thesis do provide a good starting point on how to characterize AFC closed-loop performance.

Appendix A

Variform FTS Pictures & I/F Board Schematic

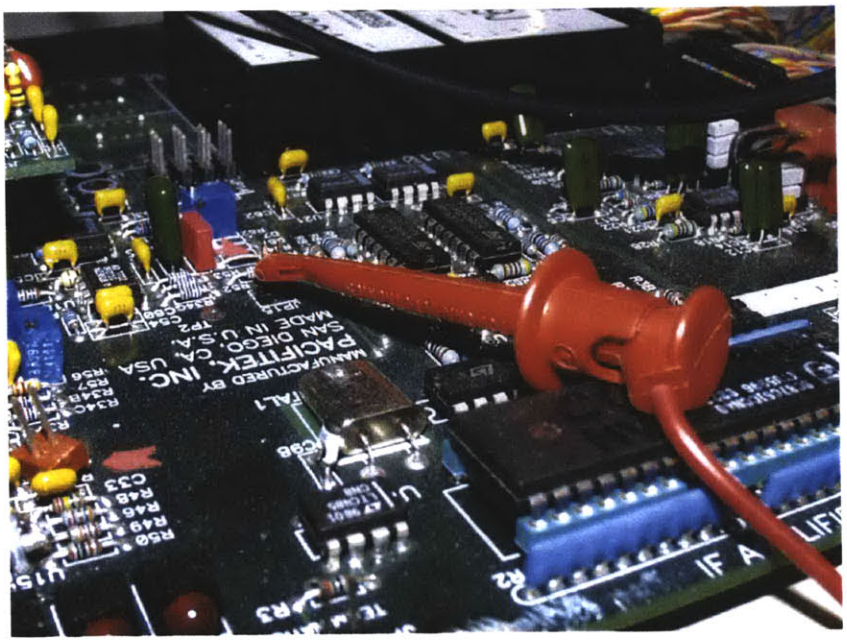

Figure A-1: Signal input connection JP15 (pin b) on the amplifier interface board.

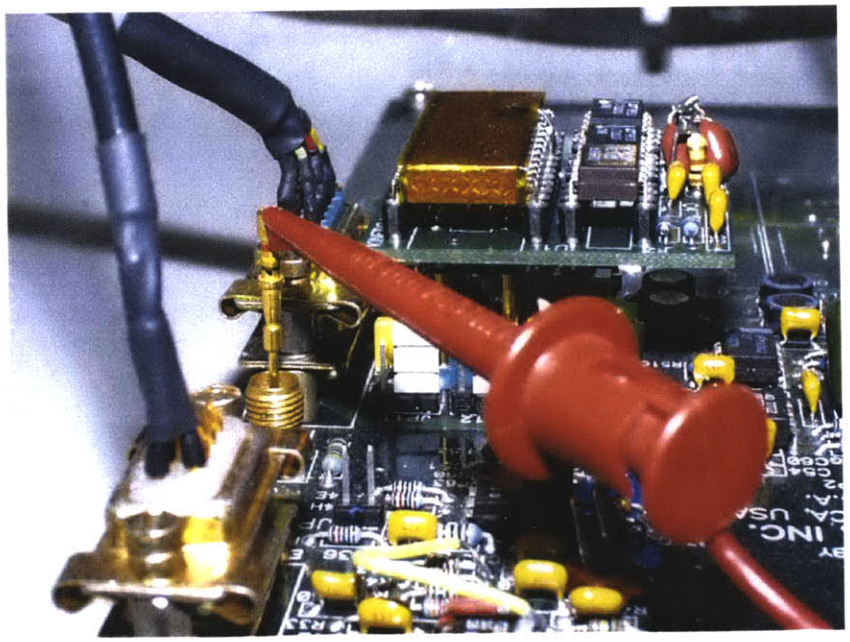

Figure A-2: Signal output connection JP9 on the amplifier interface board.

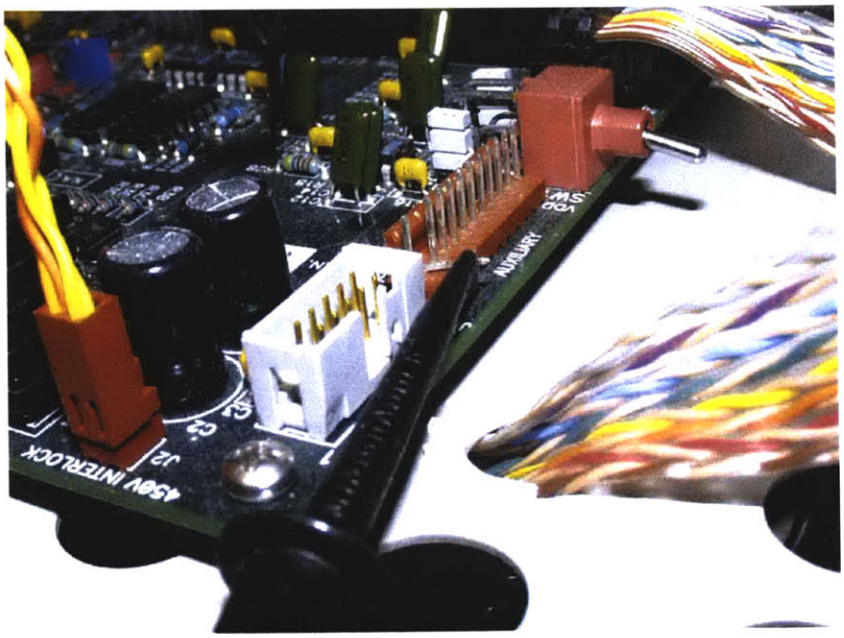

Figure A-3: Reference ground connection JP2 (pin 2) on the amplifier interface board.

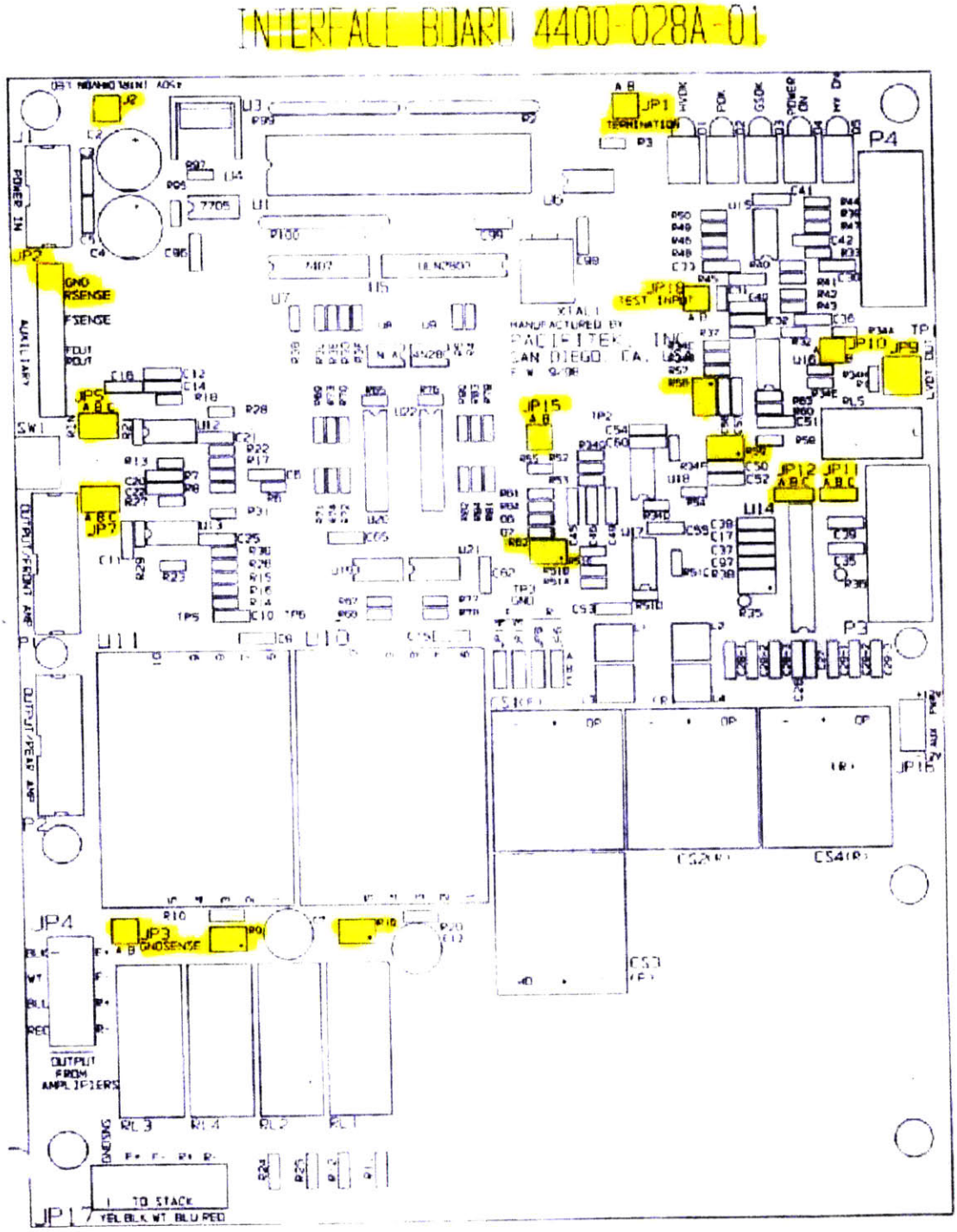

Figure A-4: Amplifier interface board schematic illustrating all of the pertinent jumper locations.

Appendix B

State Space Matrices for $G_{p_1}(s)$

$$A = \begin{bmatrix} -2600 & 0 & 0 & 0 & 0 & 0 \\ 0 & -18850 & 0 & 0 & 0 & 0 \\ 0 & 0 & -3204.3 & 5404.5 & 0 & 0 \\ 0 & 0 & -5404.5 & -3204.3 & 0 & 0 \\ 0 & 0 & 0 & 0 & -517.23 & 6063 \\ 0 & 0 & 0 & 0 & -6063 & -517.23 \end{bmatrix}$$

$$B = \begin{bmatrix} 757.87e{-3} \\ 119.04e{-4} \\ 551.64e{-3} \\ -108.46e{-2} \\ -1.345 \\ 0 \end{bmatrix}$$

$$C = \begin{bmatrix} 2600 & -1969.3 & -1821.9 & 866.52 & 159.28e{-2} & -1183.1 \end{bmatrix}$$

$$D = \begin{bmatrix} 0 \end{bmatrix}$$

Appendix C

State Space Matrices for $G_{p_2}(s)$

$$A = \begin{bmatrix} -2600 & 0 & 0 & 0 & 0 & 0 & 0 \\ 0 & -18850 & 0 & 0 & 0 & 0 & 0 \\ 0 & 0 & -3595.6 & 5531.5 & 0 & 0 & 0 \\ 0 & 0 & -5531.5 & -3595.5 & 0 & 0 & 0 \\ 0 & 0 & 0 & 0 & -400.24 & 6144.5 & 0 \\ 0 & 0 & 0 & 0 & -6144.5 & -400.24 & 0 \\ 0 & 0 & 0 & 0 & 0 & 0 & 0 \end{bmatrix}$$

$$B = \begin{bmatrix} 682.92 \times 10^{-3} \\ 122.61 \times 10^{-4} \\ 427.16 \times 10^{-3} \\ -864.17 \times 10^{-3} \\ -1.2206 \\ -372.92 \times 10^{-5} \\ 1 \end{bmatrix}$$

$$C = \begin{bmatrix} 2600 & -1969.3 & -1763 & 1023.4 & 103.99 & -1037.7 & 9.1136 \end{bmatrix}$$

$$D = \begin{bmatrix} 0 \end{bmatrix}$$

Appendix D

State Space Matrices for $G_{p_4}(s)$

$$A = \begin{bmatrix} -804.25 & -20090 & 0 & 0 & 0 \\ 20090 & -804.25 & 0 & 0 & 0 \\ 0 & 0 & -385.63 & -6157.9 & 0 \\ 0 & 0 & 6157.9 & -385.63 & 0 \\ 0 & 0 & 0 & 0 & -11624 \end{bmatrix}$$

$$B = \begin{bmatrix} -468.88 \times 10^{-5} \\ -975.57 \times 10^{-5} \\ -797.22 \times 10^{-3} \\ -436.83 \times 10^{-3} \\ 1.295 \end{bmatrix}$$

$$C = \begin{bmatrix} 0 & -20106 & 19.596 & 1390.6 & 329.67 \end{bmatrix}$$

$$D = \begin{bmatrix} 0 \end{bmatrix}$$

Appendix E

State Space Matrices for Rotary Fast Tool Servo

$$A = \begin{vmatrix}
-1632.2 & 753.98 & 753.98 & 0 & 0 & 0 & 0 & 0 & 2530 & 0 & 0 & 0 & 0 \\
0 & 0 & 188.5 & 0 & 0 & 0 & 0 & 0 & 632.5 & 0 & 0 & 0 & 0 \\
0 & 0 & 0 & 0 & 0 & 0 & 0 & 0 & 632.5 & 0 & 0 & 0 & 0 \\
-2.69e6 & 1.87e6 & 1.87e6 & -498.1 & -13744 & -557 & -4710 & 0 & 6.26e6 & 15000 & 0 & 6985 & -1632 \\
0 & 0 & 0 & 16384 & 0 & 0 & 0 & 0 & 0 & 0 & 0 & 0 & 0 \\
0 & 0 & 0 & 0 & 8192 & 0 & 0 & 0 & 0 & 0 & 0 & 0 & 0 \\
0 & 0 & 0 & 0 & 0 & 8192 & 0 & 0 & 0 & 0 & 0 & 0 & 0 \\
0 & 0 & 0 & 0 & 0 & 0 & 64 & 0 & 0 & 0 & 0 & 0 & 0 \\
0 & 0 & 0 & 0 & 0 & 0 & 0 & 32 & 0 & 0 & 0 & 0 & 0 \\
4.31e7 & -2.99e7 & -2.99e7 & 0 & 0 & 0 & 0 & 0 & -1.0e8 & -1.2e5 & -9.16e5 & -5.59e5 & 2.61e5 \\
0 & 0 & 0 & 0 & 0 & 0 & 0 & 0 & 0 & 6.55e5 & 0 & 0 & 0 \\
0 & 0 & 0 & 0 & 0 & 0 & 0 & 0 & 0 & 0 & 3.28e5 & 0 & 0 \\
-1.80e6 & 1.24e6 & 1.24e6 & 0 & 0 & 0 & 0 & 0 & 4.17e6 & 0 & 0 & 0 & -1632
\end{vmatrix}$$

$$B = \begin{vmatrix} 0 \\ 0 \\ 0 \\ -32 \\ 0 \\ 0 \\ 0 \\ 0 \\ 0 \\ 512 \\ 0 \\ 0 \\ 0 \end{vmatrix} \quad C = \begin{vmatrix} -2.81e5 & 1.94e5 & 1.94e5 & 0 & 0 & 0 & 0 & 0 & 6.52e5 & 0 & 0 & 0 & 0 \end{vmatrix} \quad D = [0]$$

Appendix F

AFC resonator Values

AFC Resonator Tuning Values										
n	1	2	3	4	5	6	7	8	9	10
ω_n **(rad/sec)**	125.7	251.3	377	502.7	628.3	754.0	879.7	1005	1131	1256
g_n	1	1	1	1	1	1	1	1	1	1
ϕ_n(deg)	-7.7	-11.2	-17.4	-30.7	-50.3	-70.7	-87.4	-100.3	-110.8	-119.7

Table F.1: AFC resonator tuning values for a ten resonator AFC system with $g_1 = ... = g_i \equiv 1$ and $\phi_i = \angle \mathrm{P}(j\omega_i)$. Table adapted from Byl *et al* [6].

AFC Resonator Tuning Values										
n	1	2	3	4	5	6	7	8	9	10
ω_n **(rad/sec)**	125.7	251.3	377	502.7	628.3	754.0	879.7	1005	1131	1256
g_i	5.18	5.18	5.18	5.18	5.18	5.18	5.18	5.18	5.18	5.18
ϕ_n(deg)	-7.7	-11.2	-17.4	-30.7	-50.3	-70.7	-87.4	-100.3	-110.8	-119.7

Table F.2: AFC resonator tuning values for a tean resonator AFC system with $g_1 = ... = g_i \equiv 5.18$ and $\phi_i = \angle \mathrm{P}(j\omega_i)$. Table adapted from Byl *et al* [6].

AFC Resonator Tuning Values										
n	1	2	3	4	5	6	7	8	9	10
ω_n **(rad/sec)**	125.7	251.3	377	502.7	628.3	754.0	879.7	1005	1131	1256
g_n	31.1	20.7	5.1	2.59	2.59	2.59	5.18	5.18	5.18	5.18
ϕ_n(deg)	-7.7	-11.2	-17.4	-30.7	-50.3	-70.7	-87.4	-100.3	-110.8	-119.7

Table F.3: AFC resonator tuning values for a ten resonator AFC system with g_i modified by hand and $\phi_i = \angle \mathrm{P}(j\omega_i)$. Table adapted from Byl *et al* [6].

AFC Resonator Tuning Values										
n	1	2	3	4	5	6	7	8	9	10
ω_n **(rad/sec)**	62.83	125.7	188.5	251.3	314.2	377.0	439.8	502.7	565.5	628.3
g_n	10	10	10	10	10	10	10	10	10	10
ϕ_n(deg)	-4.42	-8.85	-13.3	-17.8	-22.3	-26.9	-31.5	-36.2	-40.9	-45.8

Table F.4: AFC resonator tuning values for the ten resonator AFC system for the Variform FTS $g_1 = ... = g_i \equiv 10$ and $\phi_i = \angle \mathrm{P}(j\omega_i)$.

Appendix G

Description of Altered MATLAB Simulink DSA Block

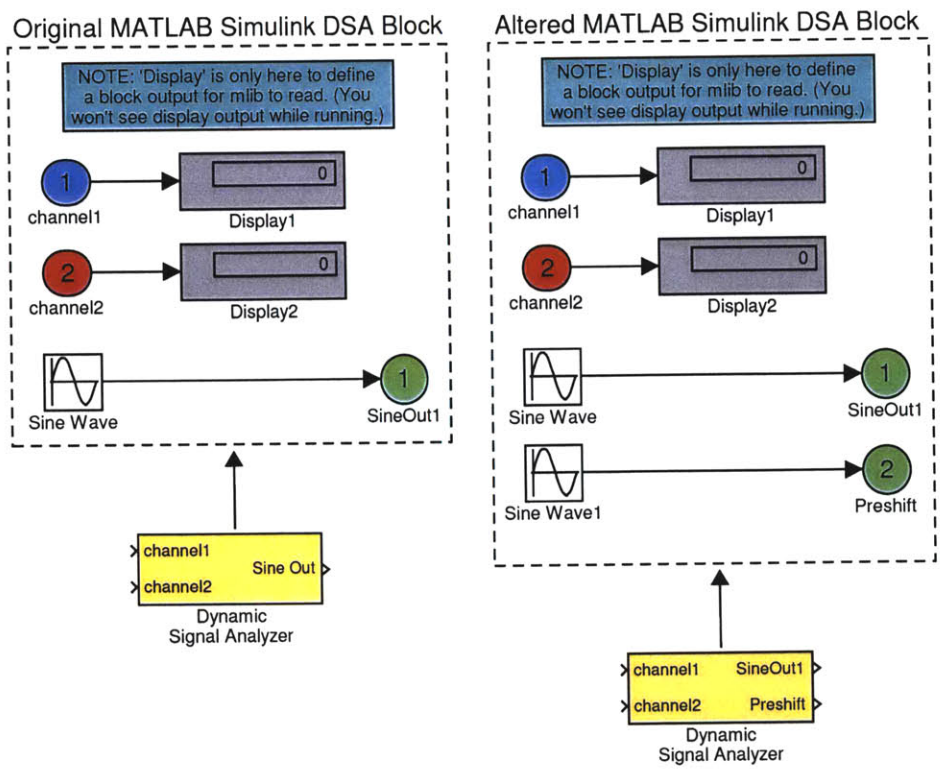

A comparison between the original and altered MATLAB Simulink DSA block shows that the altered block includes an extra sine wave signal generator. When

the altered block is placed into a Simulink model, compiled on the dSPACE 1102 controller board, and run with the accompanying command pre-shifting frequency response MATLAB code, the user input frequency, magnitude, and phase $P^{*-1}(j\omega_i)$ information is read from MATLAB and written to the associated dSPACE memory locations. The code writes the $P^{*-1}(j\omega_i)$ information directly to the amplitude, frequency, and phase memory locations of the extra sine wave signal generator and produces the command pre-shifting output. We assume that both of the sine wave generators produce the same output if provided the same amplitude, frequency, and phase values. This may in fact be untrue but due to the time constraints and rather good experimental results, we decided not to refine the model.

Appendix H

Listing of Command Pre-Shifting Frequency Response MATLAB Code

```
function [AFC_data] = dsa_1102b(w_list,amp_list,sval,datestamp,m_list,p_list)
% This program is a new version of dsa_tf.m modified to apply to
% sub-Herz frequency. 12/10/99 T.SATO
%
% function [AFC_data] = dsa_1102b(w_list,amp_list,sval,datestamp,m_list,p_list)
% w_list : optional vector of INPUT FREQUENCY values at which to find TF
% amp_list : optional vector of INPUT AMPLITUDE values at which SINE
%          output will sweep.  (If amp_list is a scalar, the same
%          amplitude will be used at ALL frequencies...)
% sval : optional string value for the plot (e.g. 'r*' would plot
%          red *'s at points on figure(1)
% datestamp: optional 4th argument (not shown above).
%          If a non-zero 4th argument is used in calling the
%          function dsa_tf, the program will 'time stamp' the
%          output figure.  This will NOT WORK unless you have
%          the time-stamping MATLAB function 'get_date.m'
%          as well, however!!!
% m_list: List of P^-1(s) Magnitude Values
%         for Command Preshifting
% p_list: List of P^-1(s) Phase Values for
%         for Command Preshifting
%
%-----------------------------------------------------------------------
% OUTPUTs: The output is an (N x 3) matrix. 'N' is the length of w_list.
%    Column 1:  Returned FREQUENCY list (w_list values)
%    Column 2:  GAIN, as the ratio of channel2/channel1 (not in db)
%    Column 3:  PHASE, in degrees
%-----------------------------------------------------------------------
% NOTES:
%  (1) You must be running a SIMULINK model on the ds1102 board
%      for the MATLAB function dsa_tf() to work, and the simulink
%      model must include a special block called 'Dynamic Signal Analyzer'
%  (2) This program will overwrite figures 1 and 2 (in matlab)!!
%      Before running dsa_tf(), make sure you do not have images/plots
%      in either figure which should not be destroyed.

%-----------------------------------------------------------------------
% Section 0: Define number of samples and default siggen amplitude.
if ~exist('datestamp')
   do_date=0;
else
   do_date=(datestamp~=0);
end
N=10000;       % N: number of points to sample.
w_rad=0;       % indicates frequencies are NOT in rad/sec by default (Hz default)
dsa_A=.01;      % default AMPLITUDE of Swept Sine from DSA
exitval=0;     % program will exit if this is non-zero.
%-----------------------------------------------------------------------
% Section 1: Make sure all frequencies and amplitudes are set for this run:
fprintf(1,'\nNote: Make sure your (DSA) model is built and running.\n');
fprintf(1,'      This program will erase any images or plots in figure 1 and figure 2.\n
\n');
fprintf(1,'      If you would like to STOP this program now, enter ''q'' to quit,\n');
isok=input('      otherwise, just hit enter to continue : ','s');
if strcmpi(isok,'q')
   fprintf(1,'\nOK, bye.\n')
else
   if ~exist('sval') % default symbol for Bode plot
      sval='bo-';
   end
   if ~exist('w_list')
      w0=1:(1/10):3;
      w_use=10.^w0;
      fprintf('\nRunning %d points.\n  [Range = %.2f [Hz] (min) to %.2f [Hz] (max)]
\n',length(w_use),min(w_use),max(w_use));
   else
      is_rad=input('\nThe list of frequencies you entered was in:\n HERTZ (h) or RAD/SEC
(r) [default to Hertz]? ','s');
```

```
   if strcmpi(is_rad,'r')
      fprintf('\n--> using RAD/SEC\n');
      w_use=(1/(2*pi))*w_list;
      w_rad=1;
   elseif strcmpi(is_rad,'h')
      fprintf('\n--> using HERTZ\n');
      w_use=w_list;
   else
      fprintf('\n...hmmm, I don''t understand, so I''m going to use
      HERTZ (by default).\n');
      w_use=w_list;
   end
end
if ~exist('amp_list')
   A=dsa_A;            % initial SINE WAVE amplitude
   amp_list=A+(0*w_use);
else
   if length(amp_list)<length(w_use)
      fprintf('Using %.4f as SINE WAVE amplitude as ALL frequencies...\n');
      amp_list=amp_list(1)+(0*w_use);
      A=amp_list(1);
   end
end
%-----------------------------------------------------------------------
% Section 2: Get dSPACE board parameter addresses with mlib().
mlib('SelectBoard','ds1102');
mlib('SelectBoard','ds1102');
amp_addr=mlib('GetSimAddr','P[Model Root/Dynamic Signal Analyzer/Sine Wave.Amplitude]');
freq_addr=mlib('GetSimAddr','P[Model Root/Dynamic Signal Analyzer/Sine Wave.Frequency]');
MAG=mlib('GetSimAddr','P[Model Root/Dynamic Signal Analyzer/Sine Wave1.Amplitude]');
PHASE=mlib('GetSimAddr','P[Model Root/Dynamic Signal Analyzer/Sine Wave1.Phase]');
FREQ=mlib('GetSimAddr','P[Model Root/Dynamic Signal Analyzer/Sine Wave1.Frequency]');
phi_last=0; B=1;
%-----------------------------------------------------------------------
% Section 3: Begin outputting the frame for a TABLE to the matlab screen.
fprintf('\n---------------------------------------- :: -----------------------\n');
fprintf('_________Frequency_________   _SineAmp__  ::  __GAIN___      _PHASE_\n');
fprintf('   Hertz        [rad/sec]                 ::     db         Degrees\n');
fprintf('---------------------------------------- :: -----------------------\n');
%-----------------------------------------------------------------------
% Section 4: Run through all requested FREQUENCY values; find gain and phase at each.
f1=figure(1); set(f1,'Position',[465,210,450,520]);
f2=figure(2); clf; set(f2,'Position',[10,210,450,520]);
patch([-.5 1.5 1.5 -.5 -.5],[-.5 -.5 1.5 1.5 -.5],[0 0 0])
patch([0 0 1 1 0],[0 1 1 0 0],[0 1 0])
axis([-.5 1.5 -.5 1.5])
t1=text(.5,.65,'COLLECTING'); set(t1,'HorizontalAlignment','center');
t1=text(.5,.5,'FIRST'); set(t1,'HorizontalAlignment','center');
t1=text(.5,.35,'DATA SET...'); set(t1,'HorizontalAlignment','center');
axis off
u1=uicontrol(2,'Position',[10 10 150 30],...
            'String','HIT to BREAK',...
            'Callback','stopval=1;',...
            'Enable','on','Value',5);
i=1;
while (i<=length(w_use)) & (exitval==0)
   w=w_use(i);       % frequency for this data set
   w_hz = 2*pi*w;    % frequency turned to rad/sec
   A=amp_list(i);    % NOTE: amplitude must be 'reasonable'...
                     % USER must visually check that OUTPUT is not saturated!!!
   m_dsa = m_list(i); % MAGNITUDE FROM PHESHIFT TABLE
   p_dsa = p_list(i); % PHASE FROM PHESHIFT TABLE
   fprintf('%9.4f     [%10.4f]    %9.6f   ::  ',w,2*pi*w,A);
```

```
drawnow;
mlib('Writed',freq_addr,w_hz); mlib('Writed',amp_addr,A);
mlib('Writed',MAG,m_dsa); mlib('Writed',PHASE,p_dsa); mlib('Writed',FREQ,w_hz);
tic                                  % give system some time to settle...
%while (toc<(150/w)) & (get(u1,'Value')>1)
while (toc<(10/w)) & (get(u1,'Value')>1)

   drawnow
end
%-----------------------------------------------------------------------
% Section 4-1: Here is the actual procedure to get gain and phase at
% a particular frequency.  This would be more elegantly implemented
% as a separate function.  Instead, it is included within this loop
% so that the dynamic signal analyzer can be run from a SINGLE FILE.
% (Otherwise, the user has to worry about having all files needed.)
%k=[0:(N-1)]';
A=mlib('Readf',amp_addr); w=(mlib('Readf',freq_addr))/(2*pi); T=1/w;
mlib('SelectBoard','ds1102');
y_addr=mlib('GetAddr','rti B[Model Root/Dynamic Signal Analyzer/channel1]',...
   'rti B[Model Root/Dynamic Signal Analyzer/channel2]',...
   'rti B[Model Root/Dynamic Signal Analyzer/Sine Wave]');
mlib('TraceVars',y_addr);
samp_per=mlib('GetSimAddr','Task Info/Timer Task 1/sampleTime');
dt=mlib('ReadF',samp_per);

if w>10              % by T.SATO 12/10/99
   ds=1;
else
   ds=ceil(1/w)+1;   % by T.SATO 12/10/99
end

ncyc=floor(w*dt*ds*N);        % by T.SATO 12/10/99
Nlast=round(ncyc/(w*dt*ds));  % by T.SATO 12/10/99

%ncyc=floor(w*dt*N);          % Use an INTEGRAL number of sine waves!!
%Nlast=round(ncyc/(w*dt));
if ncyc>10                   % Display no more than this number of sine waves
   Nplot=round(10/(w*dt*ds)); % by T.SATO 12/10/99
   %Nplot=round(10/(w*dt));   % for the user to observe during the run...
else
   Nplot=Nlast;
end
tic
while (toc<2) & (get(u1,'Value')>1) % settle time pause...
   drawnow
end
if (get(u1,'Value')>1)
   % !@!!! set frame in desired way!!!
   mlib('SetFrame',[],ds,0,Nlast*ds); % by T.SATO 12/10/99
   %mlib('SetFrame',[],1,0,N);
   %mlib('SetFrame',dt,1,0,dt*(N));
   mlib('SetTrigger',y_addr(3,:),0,1);
   mlib('LockProgram');
   mlib('StartCapture');
   while mlib('CaptureState')~=0
      drawnow;
   end
   my_data=mlib('FetchData');
   % Take an INTEGRAL number of sine waves, total:
   k=[0:(Nlast-1)]';
   %ncyc=floor(w*dt*Nlast);         %12/15/99 T.Sato
   %y_out=my_data(2,1:Nlast);
   %y_in=my_data(1,1:Nlast);
   %t_out=dt*[1:Nlast];
   %ncyc=floor(w*dt*Nlast);         %12/15/99 T.Sato
   y_out=my_data(2,1:Nlast);
   y_in=my_data(1,1:Nlast);
   t_out=dt*ds*[1:Nlast];
```

```
   mlib('UnlockProgram');
end
set(u1,'Enable','off');  % do not allow a break until new data presented
if (get(u1,'Value')<1)
   i=max(1,(i-1));
   w=w_use(i);       % frequency for this data set
   w_hz = 2*pi*w;    % frequency turned to rad/sec
   A=amp_list(i);    % NOTE: amplitude must be 'reasonable'...
   m_dsa = m_list(i); % MAGNITUDE FROM PHESHIFT TABLE
   p_dsa = p_list(i); % PHASE FROM PHESHIFT TABLE
   % USER must visually check that OUTPUT is not saturated!!!
   fprintf(1,'\nBREAK: going back to previous frequency.\n');
   fprintf(1,' * Use COCKPIT to reset Amplitude.\n');
   fprintf(1,' * USE TRACE to view resulting sine waves.\n');
   fprintf(1,'Restart DSA by hitting RESTART button in figure 2.\n');
   %fprintf('%9.4f     [%10.4f]    %9.6f   ::  ',w,2*pi*w,A);
   drawnow;
   mlib('Writed',freq_addr,w_hz); mlib('Writed',amp_addr,A);
   mlib('Writed',MAG,m_dsa); mlib('Writed',PHASE,p_dsa); mlib('Writed',FREQ,w_hz);
   startval=0; exitval=0;
   subplot(3,1,3); cla;
   patch([0 30 30 0 0],[2 2 7 7 2],[0 1 0]);
   axis off; axis([0 30 2 7]);
   text(.5,6,'You can use COCKPIT and TRACE to reset');
   my_str=num2str(w_use(i),'%.1f');
   text(.5,5,['Amplitude and then CONTINUE at ' my_str ' Hz...']);
   text(.5,4,'...or you can EXIT to completely rerun DSA.');
   text(.5,3,'[choose EXIT or CONTINUE]');
   set(u1,'String','HIT to EXIT','Callback','exitval=1;');
   u2=uicontrol('Position',[200 10 150 30],'Value',5,...
      'String','CONTINUE','Callback','startval=1;');
   set(u1,'Enable','on','Value',5);
   while (get(u1,'Value')~=0) & (get(u2,'Value')~=0)
      drawnow;  % wait for user to hit a button...
   end
   if get(u1,'Value')==0
      exitval=1;     % exit the dsa
   else
      startval=1;    % restart the dsa
      A=mlib('Readd',amp_addr);
      amp_list=A+(0*amp_list);  % reset amp_list for current and future freqs
      figure(2); clf;
      patch([-.5 1.5 1.5 -.5 -.5],[-.5 -.5 1.5 1.5 -.5],[0 0 0])
      patch([0 0 1 1 0],[0 1 1 0 0],[0 1 0])
      axis([-.5 1.5 -.5 1.5])
      t1=text(.5,.65,'COLLECTING'); set(t1,'HorizontalAlignment','center');
      t1=text(.5,.5,[my_str ' Hz']); set(t1,'HorizontalAlignment','center');
      t1=text(.5,.35,'DATA SET...'); set(t1,'HorizontalAlignment','center');
      axis off
      u1=uicontrol(2,'Position',[10 10 150 30],...
         'String','HIT to BREAK',...
         'Callback','stopval=1;',...
         'Enable','on','Value',5);
   end
else
   % user did NOT request a break, so analyze this data set:
   if exist('y_out')
      if (max(y_out)<0.95) & (min(y_out)>-.95) & (max(y_in)<.95) & (min(y_out)>-.95)
         warncolor=[1 1 0];        % Amplitude not 'saturated'. OK to use this data.
      else
         warncolor=[1 0 0];
      end
      %          y_sin=(dt*(w*2*pi)*(k))';
      y_sin=((w*2*pi)*t_out);       % Ideal SINE at this freq
      Bc=(2/(length(y_out)))*sum((y_out).*cos(y_sin));
```

```
   Bs=(2/(length(y_out)))*sum((y_out).*sin(y_sin));
   B_=sqrt(Bc^2+Bs^2);            % Amplitude of OUTPUT at this freq
   Ac=(2/(length(y_out)))*sum((y_in).*cos(y_sin));
   As=(2/(length(y_out)))*sum((y_in).*sin(y_sin));
   A_=sqrt(Ac^2+As^2);            % Amplitude of INPUT at this freq (check)
   Gain=B_/A_;
   phi_out=atan2(Bc,Bs);
   phi_in=atan2(Ac,As);
   phi=phi_out-phi_in;      % Difference in phase (input->output) (rad)
   figure(2); clf
   subplot(311)
   plot(t_out(1:Nplot),y_out(1:Nplot),'r.');
   hold on; grid on; title('RED: channel2'); %xlabel('seconds')
   subplot(312)
   plot(t_out(1:Nplot),y_in(1:Nplot),'b.');
   hold on; grid on; title('BLUE: channel1 (input)'); xlabel('seconds')
   subplot(313)
   patch([0 30 30 0 0],[2 2 7 7 2],warncolor);
   axis off; axis([0 30 2 7]);
   text(.5,6,'Check that the OUTPUTS above are :');
   text(1.5,5,'* NOT SATURATED.');
   text(1.5,4,'* Not buried in noise.');
   text(.5,3,'otherwise, BREAK and run with new AMPLITUDEs.');
   u1=uicontrol(2,'Position',[10 10 150 30],...
      'String','HIT to BREAK',...
      'Callback','stopval=1;',...
      'Enable','on', 'Value',5);
   stopval=0;   % insure 'stopval' is reset to show 'OK' state
   %else
   %   A=A*3/4;   % REDUCE INPUT AMPLITUDE AND RETAKE DATA!
   %   fprintf('Reducing input amplitude from %5.3f volts to %5.3f volts...\n',
      (4/3)*A,A);
   %   mlib('SelectBoard','ds1102');
   %   mlib('WriteF',amp_addr,A);
   %end
   %end
end
if phi>phi_last
   while (phi-phi_last)>(pi)
      phi=phi-(2*pi);
   end
else
   while (phi-phi_last)<(-pi)
      phi=phi+(2*pi);
   end
end

AFC_data(i,:)=[w Gain phi];
fprintf(1,'%8.3f     %9.2f\n',20*log10(Gain),(180/pi)*phi);
figure(1)
subplot(2,1,1); semilogx(AFC_data(1:i,1),20*log10(AFC_data(1:i,2)),sval); hold on;
%semilogx(AFC_data(1:i,1),20*log10(AFC_data(1:i,2)),'-');
axis auto; grid on;
xlabel('Frequency (Hertz)');
ylabel('Gain (db)'); title('Transfer Function (channel2/channel1)');
subplot(2,1,2); semilogx(AFC_data(1:i,1),(180/pi)*AFC_data(1:i,3),sval);hold on;
%semilogx(AFC_data(1:i,1),(180/pi)*AFC_data(1:i,3),'-');
axis auto; grid on;
if do_date==1
   s_xlabel=get_date;
else
   s_xlabel=' ';
end
s_xlabel2='                              ';
s_xlabel2=s_xlabel2(1:length(s_xlabel));
xlabel([s_xlabel2 '  Frequency (Hertz)  ' s_xlabel]);
ylabel('Phase (Degrees)');
```

```
        %if ((180/pi)*(max(AFC_data(1:i,3))-min(AFC_data(1:i,3))))>80
        %   set(gca,'YTick',[45*floor((180/pi)*min(AFC_data(1:i,3))):45:45*ceil((180/pi)
           *max(AFC_data(1:i,3)))]);
        %elseif (((180/pi)*(max(AFC_data(1:i,3))-min(AFC_data(1:i,3))))>40) & (get
        (gca,'YTickMode')=='manual')
        %   set(gca,'YTick',[15*floor((180/pi)*min(AFC_data(1:i,3))):15:15*ceil((180/pi)
        *max(AFC_data(1:i,3)))]);
        %end
        drawnow
        phi_last=phi;
        figure(2)  % PUT FIGURE 2 ON TOP TO FORCE USER TO LOOK AT SINE WAVE DATA
        i=i+1;
      end
      %if startval==0
      %   i=max(1,(i-1));
      %end

   end
   if exitval==0
      if w_rad==1
         fprintf(1,'\nThe TF created has 3 columns:  Frequency (rad/sec), Magnitude
         (absolute), Phase (radians)\n')
         AFC_data(:,1)=(pi/180)*AFC_data(:,1);
      else
         fprintf(1,'\nThe TF created has 3 columns:  Frequency (Hz), Magnitude (absolute),
         Phase (radians)\n')
      end
      fprintf(1,'To replot GAIN in Bode format:  semilogx(tf(:,1),20*log10(tf(:,2))\n');
      fprintf(1,'To replot PHASE in Bode format: semilogx(tf(:,1),(180/pi)*tf(:,3)\n');
   else
      fprintf(1,'\n\n   ************************************************\n');
      fprintf(1,     '   *** Program exited by user during run.... bye. ***\n');
      fprintf(1,     '   ************************************************\n\n');
   end  % ends user query if 'ok' to continue
   mlib('Writed',freq_addr,w_use(1));
   mlib('Writed',amp_addr,0);

end
return
function y = setstop()
y=1;
return
```

Appendix I

State Space Matrices for MIMO OAC Model

For the MIMO OAC example in Section 5.4, we use the second order plant model

$$P(s) = \frac{\omega_n^2}{s^2 + 2\zeta\omega_n s + \omega_n^2}, \tag{I.1}$$

where the natural frequency $\omega_n = 250$ r.p.s and damping ratio $\zeta = \frac{\sqrt{2}}{2}$. The simulated frequency response $P(j\omega)$ is shown in Figure I-1. The state-space state and output equations are defined as

$$\dot{\mathbf{x}} = \mathbf{A}\mathbf{x} + \mathbf{B}\mathbf{u} + \mathbf{E}\mathbf{x}_o, \tag{I.2}$$

$$\mathbf{y} = \mathbf{C}\mathbf{x} + \mathbf{D}\mathbf{u}, \tag{I.3}$$

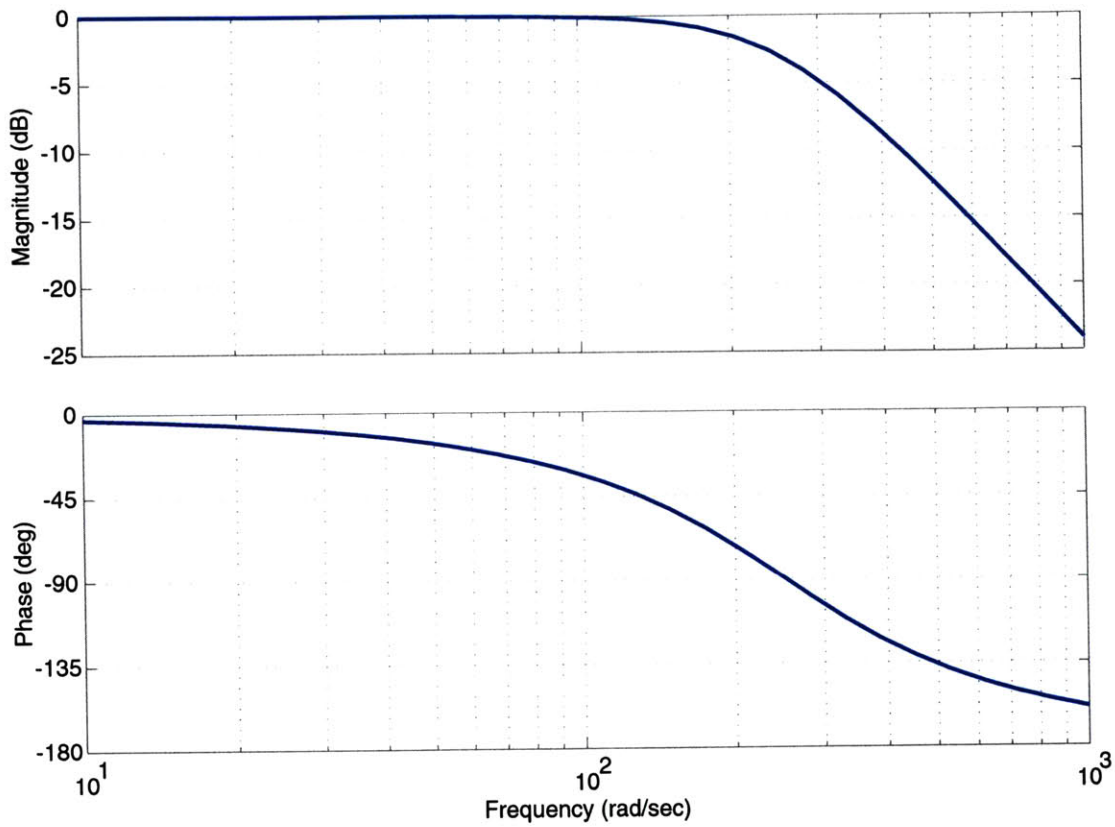

Figure I-1: Simulated frequency response for the simplified second order plant model with $\omega_n = 250$ rad/sec and $\zeta = \frac{\sqrt{2}}{2}$.

where

$$\mathbf{x} = \text{state vector}, \tag{I.4}$$

$$\mathbf{u} = \text{input vector}, \tag{I.5}$$

$$\mathbf{x}_o = \text{disturbance vector}, \tag{I.6}$$

$$\mathbf{y} = \text{output vector}. \tag{I.7}$$

Figure I-2 illustrates the resulting MIMO OAC closed-loop block diagram, while (I.8) through (I.12) give the state-space matrices.

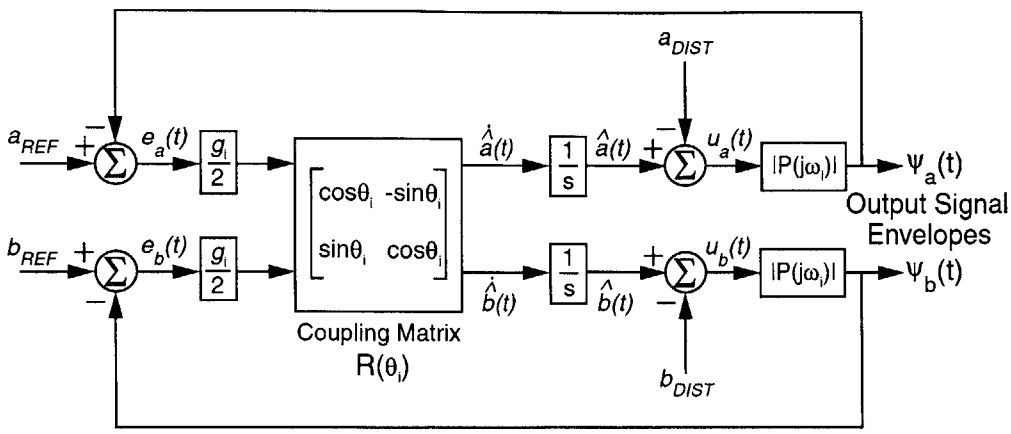

Figure I-2: Closed-loop block diagram for the single resonator AFC system viewed as a multiple-input multiple-output (MIMO) oscillator amplitude control system.

$$A = \begin{bmatrix} -\frac{g_i|P(j\omega_i)|}{2}\cos\phi_i & \frac{g_i|P(j\omega_i)|}{2}\sin\phi_i \\ -\frac{g_i|P(j\omega_i)|}{2}\sin\phi_i & -\frac{g_i|P(j\omega_i)|}{2}\cos\phi_i \end{bmatrix} \tag{I.8}$$

$$B = \begin{bmatrix} \frac{g_i}{2}\cos\phi_i & -\frac{g_i}{2}\sin\phi_i \\ \frac{g_i}{2}\sin\phi_i & \frac{g_i}{2}\cos\phi_i \end{bmatrix} \tag{I.9}$$

$$C = \begin{bmatrix} |P(j\omega_i)| & 0 \\ 0 & |P(j\omega_i)| \end{bmatrix} \tag{I.10}$$

$$D = \begin{bmatrix} 0 \end{bmatrix} \tag{I.11}$$

$$E = \begin{bmatrix} \frac{g_i}{2}\cos\phi_i & -\frac{g_i}{2}\sin\phi_i \\ \frac{g_i}{2}\sin\phi_i & \frac{g_i}{2}\cos\phi_i \end{bmatrix} \tag{I.12}$$

Appendix J

State Space Matrices for Altered MIMO OAC Model

Figure J-1 illustrates the altered MIMO OAC closed-loop block diagram with the second order plant transfer function, with the addition of the plant transfer function, while (J.1)-(J.5) equal the state-space matrices.

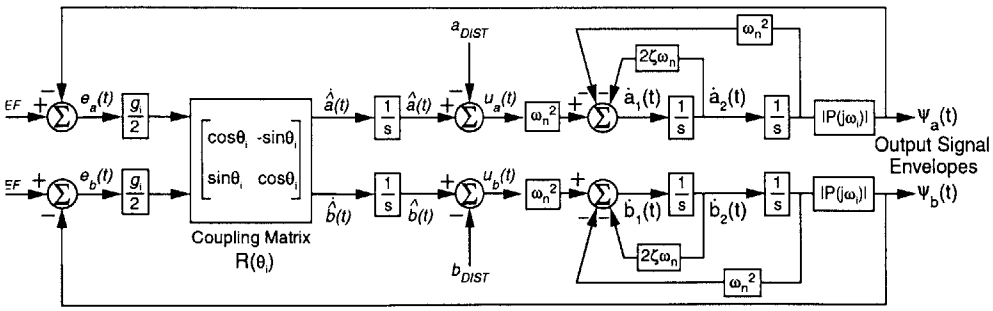

Figure J-1: Altered closed-loop block diagram for the single resonator AFC system viewed as a multiple-input multiple-output (MIMO) oscillator amplitude control system. The plant model has been added to the sine and cosine OAC loops.

$$A = \begin{bmatrix} 0 & 1 & 0 & 0 & 0 & 0 \\ -\omega_n^2 & -2\zeta\omega_n & \omega_n^2 & 0 & 0 & 0 \\ -\frac{g_i|P(j\omega_i)|}{2}\cos\phi_i & 0 & 0 & \frac{g_i|P(j\omega_i)|}{2}\sin\phi_i & 0 & 0 \\ 0 & 0 & 0 & 0 & 1 & 0 \\ 0 & 0 & 0 & -\omega_n^2 & -2\zeta\omega_n & \omega_n^2 \\ -\frac{g_i|P(j\omega_i)|}{2}\sin\phi_i & 0 & 0 & -\frac{g_i|P(j\omega_i)|}{2}\cos\phi_i & 0 & 0 \end{bmatrix} \tag{J.1}$$

$$B = \begin{bmatrix} 0 & 0 \\ 0 & 0 \\ \frac{g_i}{2}\cos\phi_i & -\frac{g_i}{2}\sin\phi_i \\ 0 & 0 \\ 0 & 0 \\ -\frac{g_i}{2}\sin\phi_i & \frac{g_i}{2}\cos\phi_i \end{bmatrix} \tag{J.2}$$

$$C = \begin{bmatrix} |P(j\omega_i)| & 0 & 0 & 0 & 0 & 0 \\ 0 & 0 & 0 & |P(j\omega_i)| & 0 & 0 \end{bmatrix} \tag{J.3}$$

$$D = \begin{bmatrix} 0 \end{bmatrix} \tag{J.4}$$

$$E = \begin{bmatrix} 0 & 0 \\ \omega_n^2 & 0 \\ 0 & 0 \\ 0 & 0 \\ 0 & \omega_n^2 \\ 0 & 0 \end{bmatrix} \tag{J.5}$$

Appendix K

Vendors

dSPACE Inc.
28700 Cabot Drive – Suite 1100
Novi, MI 48377
Telephone — (248) 567-1300
Web address — http://www.dspaceinc.com/index.htm
Product used: ACE Kit DS1102

The MathWorks, Inc.
3 Apple Hill Dr.
Natick, MA 01760-2098
Telephone — (508) 647-7000
Web address — http://www.mathworks.com
Products used: MATLAB, Simulink

Kaman Instrumentation
3450 N. Nevada Ave.
Colorado Springs, CO 80907
Telephone — (800) 552-6267
Web address — http://www.kamansensors.com/html/core.htm
Product used: SMU 9000-15N Sensor Systems

HITEK POWER
10221 Buena Vista
Santee CA, 92071
Telephone — (619)-258-7700
Web address — http://www.hitekp.com
Product used: Variform Fast Tool Servo

Kinetic Ceramics, Inc.
26240 Industrial Blvd.
Hayward CA, 94545
Telephone — (510)-264-2140
Web address — http://www.kineticceramics.com
Product used: Variform (9000-064 REVE) Technical Manual

Tektronix, Inc.
P.O. Box 500, M-S 55-230
Beaverton, Oregon 97077
Telephone — (800)-833-9200
Web address — http://www.tektronix.com
Product used: TDS 420 Digital Oscilloscope

Bibliography

[1] Stephen J. Ludwick. A Rotary Fast Tool Servo for Diamond Turning of Asymmetric Optics. Ph.D. Thesis, Department of Mechanical Engineering, Massachusetts Institute of Technology, Cambridge, MA, 1999.

[2] David C. Ma. Design and Implementation of a Rotary Fast Tool Servo for a Turning Machine. S.M. Thesis, Department of Mechanical Engineering, Massachusetts Institute of Technology, Cambridge, MA, 1998.

[3] David A. Chargin. Rotary Fast Tool Servo Component Design. S.M. Thesis, Department of Mechanical Engineering, Massachusetts Institute of Technology, Cambridge, MA, 1999.

[4] Stephen J. Ludwick, David A. Chargin, Joseph A. Calzaretta, and David L. Trumper. Design of a Rotary Fast Tool Servo for Ophalmic Lens Fabrication.*Precision Engineering*, vol. 23, no. 4, pp. 253-252, October, 1999.

[5] Joseph A. Calzaretta, Stephen J. Ludwick, Martin F. Byl, and David L. Trumper. Repetitive Control of a Fast-Tool Servo for Asymmetric Diamong Turning.*Mechatronics 2000, the 7th Mechatronics Forum International Conference*, Atanta, GA, September 2-8, 2000.

[6] Marten F. Byl, Stephen J. Ludwick, and David L. Trumper. A Loop Shaping Perspective for Tuning Controllers with Adaptive Feedforward Cancellation.....*submitted to ASPE for review*

[7] B.A. Francis and W.M. Wonham. The Internal Model Principle for Linear Multivariable Regulators. *Applied Mathematics and Optimization*, vol. 2, no. 2, pp. 170-194, 1975.

[8] B.A. Francis and W.M. Wonham. The Internal Model Principle of Control Theory. *Automatica*, vol. 12, pp. 457-465, 1976.

[9] Shinji Hara, Yutaka Yamamoto, Tohru Omata, and Michio Nakano. Repetitive Control System: A New Type Servo System for Periodic Exogeneous Signals. *IEEE Transactions on Automatic Control*, vol. 33, no. 7, pp. 659-668, July, 1988.

[10] Maarten Steinbuch. Repetitive control for systems with uncertain period-time. *Automatica*, vol. 38, no. 12, pp. 2103-2109, 2002.

[11] Jung-Ho Moon, Moon-Noh Lee, and Myung Jin Chung. Repetitive Control for the Track-Following Servo System of an Optical Disk Drive. *IEEE Transactions on Control Systems Technology*, vol. 6, no. 5, pp. 663-670, September, 1998.

[12] Manabu Yamada, Zaier Riadh, and Yasuyuki Funahashi. Design of Discrete-Time Repetitive Control System for Pole Placement and Application. *IEEE/ASME Transactions on Mechatronics*, vol. 4, no. 2, pp. 110-118, June, 1999.

[13] Jianwu Li and Tsu-Chin Tsao. A Two Parameter Robust Repetitive Control Design Using Structured Singular Values. *Proceedings of the* 37th *IEEE Conference on Decision and Control*, pp. 1230-1235, December, 1998.

[14] Wook Sok Chang, Il Hong Suh, and Jae-Hyuk Oh. Synthesis and Analysis of Digital Multiple Repetitive Control Systems. *Proceedings of the American Control Conference*, pp. 2687-2691, June, 1998.

[15] Byung-Sub Kim and Tsu-Chin Tsao. Robust Repetitive Controller Design with Improved Performance. *Proceedings of the American Control Conference*, pp. 2027-2032, June, 2001.

[16] Tsu-Chu Tsao, Masayoshi and Tomizuka, M. Robust adaptive and repetitve digital tracking control and application to hydraulic servo for noncircular machining. *ASME Journal of Dynamic Systems, Meaurement, and Control*, Vol.116, pages 24-32, 1994.

[17] M. Crudele and T. Kurfess. Implementation of a fast tool servo with repetitive control for diamond turning. *Mechatronics*, vol. 13:243-257, 2003.

[18] Thomas J. Manayathara, Tsu-Chin Tsao, Joseph Bentsman, and Douglas Ross. Rejection of Unknown Periodic Load Disturbances in Continuous Steet Casting Process Using Learning Repetitive Control Approach. *IEEE Transactions on Control Systems Technology*, vol. 4, no. 3, pp. 259-265, May, 1996.

[19] Marc Bodson. Effect of the Choice of Error Equation on the Robustness Properties of Adaptive Control Systems. *International Journal of Adaptive Control and Signal Processing*, vol. 2, pp. 249-257, 1988.

[20] Marc Bodson, Alexei Sacks, and Pradeep Khosla. Harmonic Generation in adaptive feedforward cancellation schemes. *IEEE Transactions on Automatic Control*, 39(9):1939-1944, September, 1994.

[21] Alexei Sacks, Marc Bodson, and Pradeep Khosla. Experimental Results of Adaptive Periodic Disturbance Cancellation in a High Performance Disk Drive. *Proceedings of the 1993 American Control Conference*, pp. 686-690, San Fransisco, CA, June, 1993.

[22] Alexei Sacks, Marc Bodson, and Pradeep Khosla. Experimental Results of Adaptive Periodic Disturbance Cancellation in a High Performance Disk Drive. *ASME Journal of Dynamic Systems, Measurement, and Control*, vol. 118, no. 3, pp. 416-424, September, 1996.

[23] Alexei Sacks, Marc Bodson, and William Messner. Advanced Methods for Repeatable Runout Compensation. *IEEE Transactions on Magnetics*, vol. 31, no. 2, pp. 1031-1036, March, 1995.

[24] William Messner, and Marc Bodson. Design of Adaptive Feedforward Algorithms using Internal Model Equivalence. *International Journal of Adaptive Control and Signal Processing*, 9:199–212, 1995.

[25] Marc Bodson, Alexei Sacks, and Pradeep Khosla. Harmonic Generation in Adaptive Feedforward Cancellation Schemes. *Proceedings of the 31st IEEE Conference on Decision and Control*, pp. 1261-1266, Tuscon, AZ, 1992.

[26] Andrew John Stein. A Metrological Atomic Force Microsope. S.M. Thesis, Mechanical Engineering Dept., Massachusetts Institute of Technology, September, 2002.

[27] Michael Kevin Liebman. Rotary-Linear Axes for High Speed Machining. Ph.D. Thesis, Mechanical Engineering Dept., Massachusetts Institute of Technology, September, 2001.

[28] Joseph A. Calzaretta, Personal Correspondance.

[29] Justin Verdirame, Personal Correspondance.

[30] Katie A. Lilienkamp and David L. Trumper. Dynamic Signal Analyzer for dSPACE. In *Proceedings of the dSPACE User's Conference*, May 2000.

[31] R.F. Schenz, S.R. Patterson, and T.T. Saito. Direct Machining of a Non-Axisymmetric Phase Corrector. *Proc. SPIE - Int. Soc. Opt. Eng*, vol. 966, pp. 43-59, 1989.

[32] Masayoshi Tomizuka. Zero phase error tracking algorithm for digital control. *Journal of Dynamic Systems, Measurement, and Control*, vol. 109 pp. 65-68, 1987.

[33] J. Bollinger, N. Duffie. *Computer Control of Machines and Processes*, Addison-Wesley Co., Section 4.4, 1988.

[34] R. Herzog, P. Bühler, C. Gähler, and R. Larsonneur. Unbalance compensation using generalized notch filters in the feedback of magnetic bearings. *IEEE Trans. on Control Systems Technology*, vol.4, no.5, pp. 580-586, 1996.

[35] Vincent Tamisier, Francois Carrère, and Stéphane Font. Synchronous Unbalance Cancellation Across Critical Speed Using A Closed-Loop Method. *Proceedings of the 8th International Symposium on Magnetic Bearings*, pp. 399-404, August, 2002.

[36] Lichuan Li, Tadahiko Shinshi, Xiaoyou Zhang, and Akira Shimkohbe. A Simple Method for Rotation about the Inertial Axis of a Rigid AMB Motor. *Proceedings of the 8th International Symposium on Magnetic Bearings*, pp. 405-410, August, 2002.

[37] Paul H. Young. *Electronic Communication Techniques, Fourth Edition*, Prentice-Hall Inc., New Jersey, 1999.

[38] Bernabé Linares-Barrance. Comparing the Traditional Oscillator Amplitude Control Loop (with 'zero') and L-Tsividis's Direct-Q Control Loop. *Personnal Report*, bernabe@imse.cnm.es.

[39] Ali Hasan Nayfeh. *Introduction to Perturbation Techniques*, John Wiley & Sons Inc., New York, 1981.

[40] Sigurd Skogestad and Ian Postlethwaite. *Mutivariable Feedback Control: Analysis and Design*, John Wiley & Sons Inc., West Sussex, England, 1996.

[41] Norman S. Nise. *Control Systems Engineering: Third Edition*, John Wiley & Sons Inc., New York, 2000.

[42] Benjamin C. Kuo. *Automatic Control Systems, Seventh Edition*, Prentice-Hall Inc., New Jersey, 1995.

[43] L.A Gould, W.R. Markey, J.K. Roberge, and D.L. Trumper. *Control Systems Theory.* MIT 6.302 Class Notes, Massachusetts, 1997.

[44] B.D.O Anderson, R.R. Bitmead, C.R. Johnson, Jr., P.V. Kokotovic, R.L. Kosut, I.M.Y. Mareels, L. Praly, and B.D. Riedle. *Stability of Adaptive Systems: Passivity and Averaging Analysis*, The MIT Press, Massachusetts, 1986.

[45] Jean-Jacques E. Slotine and Weiping Li. *Applied Nonlinear Control*, Prentice-Hall Inc., New Jersey, 1991.

[46] James K. Roberge. *Operational Amplifiers: Theory and Practice*, John Wiley & Sons Inc., 1975.

[47] Alan V. Oppenheim, Alan S. Willsky, with S. Hamid Nawab. *Signals and Systems: Second Edition*, Prentice-Hall Inc., New Jersey, 1997.

[48] Shankar Sastry and Marc Bodson. *Adaptive Control: Stability, Convergence , and Robustness*, Prentice-Hall Inc., New Jersey, 1989.

[49] Gene F. Franklin, J. David Powell, and Abbas Emami-Naeini. *Feedback Control of Dynamic Systems*, Addison-Wesley Publishing Company, Reading, Massachusetts, 1987.

[50] Katsuhiko Ogata, *Modern Control Engineering*, Prentice Hall of India, 1998.

[51] F. McHugh and J. Shaw. Helicopter Vibration Reduction with Higher Harmonic Blade Pitch. *Journal of the American Helicopter Society*, vol. 23, no. 4, pp. 26-34, 1978.

[52] J. Shaw and N. Albion. Active Control of Rotor Blade Pitch for Vibration Reduction: A Wind Tunnel Demonstration. *Vertica*, vol. 4, no. 1, pp. 3-11, 1980.

[53] Steven R. Hall and Norman M. Wereley. Linear Control Issues in the Higher Harmonic Control of Helicopter Vibrations. *Proceedings of the 45th Annual Forum of the American Helicopter Society*, pp. 955-971, 1989.

[54] Steven R. Hall and Norman M. Wereley. Performance of Higher Harmonic Control Algorithms for Helicopter Vibration Reduction. *Journal of Guidance and Control*, vol. 16, no. 4, pp. 793-797, 1992.

[55] Kartik B. Ariyur and Miroslav Krstić. Feedback Attenuation and Adaptive Cancellation of Blade Vortex Interaction on a Helicopter Blade Element. *IEEE Transactions on Control Systems Technology*, vol. 7, no. 5, pp. 596-605, 1999.

[56] A.R. Kashani and J.W. Sutherland. Adaptive Feedforward Control for Periodic Disturbance Rejection with Application to Machining Processes. *Proceedings of the 24th North American Manufacturing Research Conference.*

[57] Yoshikazu Onuki, Hideaki Ishoiaka, and Hiroaki Yada. Repeatable Runout Compensation for Disk Drives Using Multi-Loop Adaptive Feedforward Cancellation. *Proceedings of the 37th SICE Conference*, pp. 1093-1098, 1998.

[58] Yoshikazu Onuki and Hideaki Ishoiaka. Compensation for Repeatable Tracking Errors in Hard Disk Drives Using Discrete-Time Repetitive Controllers. *IEEE/ASME Transactions of Mechatronics*, vol. 6, no. 2, pp. 132-136, 2001.

[59] Ho Seong Lee. Implementation of Adaptive Feedforward Cancellation Algorithms for Pre-Embossed Rigid Magnetic (PERM) Disks. *IEEE Transactions on Magnetics*, vol. 33, no. 3, pp. 2419-2423, 1997.

[60] H.-S. Na and Y. Park. An Adaptive Feedforward Controller for Rejection of Periodic Disturbances. *Journal of Sound and Vibration*, 201(4), pp. 427-435, 1997.

[61] K.B. Scribner, L.A. Sievers, and A.H. von Flotow. Active Narrow-Band Vibration Isolation of Machinery Noise from Resonant Structures. *Journal of Sound and Vibration*, 167(1), pp. 17-40, 1993.

[62] Lisa A. Sievers and and Andreas H. von Flotow. Comparison and Extensions of Control Methods for Narrow-Band Disturbance Rejection. *IEEE Transactions on Singal Processing*, vol. 40, no. 10, pp. 2377-2391, October, 1992.

[63] David S. Bayard. A General Theory of Linear Time-Invariant Adaptive Feedforward Systems with Harmonic Regressors. *IEEE Transactions on Automatic Control*, vol. 45, no. 11, pp. 1983-1996, November, 2000.

[64] David S. Bayard, John Spanos, and Zahidul Rahman. A Result on Exponential Tracking Error Convergence and Persistent Excitation. *IEEE Transactions on Automatic Control*, vo. 43, no. 9, pp. 1334-1338, 1998.

[65] Dennis R. Morgan and Charles Sanford. A Control Theory Approach to the Stability and Transient Analysis of the Filtered-X LMS Adaptive Notch Filter. *IEEE Transactions on Signal Processing*, vol. 40, no. 9, pp. 2341-2346, September, 1992.

[66] X. Qiu and C.H. Hansen. An Algorithm for Active Control of Transformer Noise with On-Line Cancellation Path Modelling Based on the Perturbation Method. *Journal of Sound and Vibration*, vol. 240, no. 4, pp. 647-665, 2001.

[67] Neil J. Bershad and Jośe Carlos M. Bermudez. Sinusoidal Interference Rejection Analysis of an LMS Adaptive Feedforward Controller with a Noisy Periodic Reference. *IEEE Transactions on Signal Processing*, vol. 46, no. 5, pp. 1298-1313, May, 1998.

[68] Glover, John R. Jr. Adaptive Noise Canceling Appied to Sinusoidal Interferences. *IEEE Transactions on Acoustics, Speech, and Signal Processing*, vol. ASSP-25, no. 6, pp. 484-491, December, 1977.

[69] H.C. So. Adaptive Algorithm for Sinusoidal Interference Cancellation. *Electronics Letters*, vol. 33, no. 22, pp. 1910-1912, October, 1997.

[70] Lisa Paige Fowler. Application of the Filtered-X LMS Algorithm for Disturbance Rejection in Time-Periodic Systems. S.M. Thesis, Mechanical Engineering Dept., Virginia Polytechnic Institute and State University, May, 1996.

[71] J.E. Mason, E.W. Bai, L.-C. Fu, M. Bodson, and S.S. Sastry. Analysis of Adaptive Identifiers in the Presence of Unmodeled Dynamics: Averaging and Tuned Parameters. *IEEE Transactions on Automatic Control*, vol. 33, no. 10, pp. 969-976, 1988.

[72] "The Quatz Watch." May 2, 2003. < http://www.si.edu/lemelson/Quartz/index.html >.

[73] Kinetic Ceramics, Inc. 26240 Industrial Blvd. Hayward, Ca 94545, Tel:(510)-264-2140, Url: < http://www.kineticceramics.com >.

3571-109